CURVED LIQUID JETS: EFFECT OF SCALE, RHEOLOGY AND FORCED DISTURBANCES

by

VICTORIA LOUISE HAWKINS

A thesis submitted to
University of Birmingham
for the degree of
DOCTOR OF PHILOSOPHY

School of Chemical Engineering
College of Engineering and Physical Sciences
University of Birmingham
September 2010

Abstract

The creation of drops and sprays from the growth of surface tension instabilities on the surface of liquid jets has been exploited in both industrial applications and scientific research. Curved jets are relevant to the *prilling* process, which is used in industry to create small spherical pellets from molten material. There is a need to optimise the process in order to produce pellets of uniform size.

The dynamics of the break-up of curved jets is examined, with experiments performed to investigate the effects of scale, rheology and surface tension, with a particular focus on pseudo-plastic (shear thinning) liquids, using both a laboratory and pilot-scale facility. The experiments were compared to previous work on Newtonian fluids, as well as with existing numerical simulations, which use the method of finite differences to solve the non-linear evolution equations for jet radius and axial velocity

The effect of non-Newtonian rheology on the trajectory of the jet and its linear instability are determined using a mixture of computational and asymptotic methods. The sizes of the droplets produced by this instability are determined by considering the most unstable wave mode. This again enables a quantitative comparison with the experiments to be made.

The influence of multiple disturbance frequencies (imparted by mechanical vibrations) on the break-up of curved Newtonian jets is investigated. Numerical models show that regions where satellite drop are eliminated can be obtained.

The pilot scale rig was modified to force mechanical vibrations at the orifice, so that both the frequency and the amplitude of the vibration can be controlled. Experimental data was compared with existing numerical models, to see if it is possible to predict conditions where satellite droplets are eradicated.

ACKNOWLEDGEMENTS

I would like to thank my supervisors Prof. Stephen Decent and Dr. Mark Simmons for their guidance and inspiritment throughout my postgraduate studies. I would also like to thank Dr. Jamal Uddin and Dr. Chris Gurney for their invaluable assistance.

As ever I am indebted to my family, and in particular my parents Jackie and Chris, for their support and encouragement throughout my whole academic career. Without them, this thesis would never have reached completion and as such, I would like to dedicate this thesis to them.

I would also like to offer my thanks and appreciation to all my friends and colleagues who have offered me support, both at the University and outside of it, and not forgetting Maxim who has always been there.

I would also like to acknowledge the financial support from EPSRC which made this work possible.

Table 1: Nomenclature

Symbol	Usual meaning	Unit
Q	Flowrate	kg s^{-1}
V	Volume of drum	m^3
U	Jet exit speed	m s^{-1}
a	Radius of the orifice	m
s_0	Radius of drum	m
ϵ	Aspect ratio	-
D	Diameter of can	m
H	Height of liquid in drum	m
k, κ	Wavenumber	m^{-1}
λ	Growth rate, wavelength	s^{-1}, m
δ	Amplitude of initial perturbation	
t	Time	s
σ	Surface tension	N m^{-1}
ρ	Density	kg m^{-3}
p	Pressure	Pa
g	Gravity	m s^{-2}
μ	Dynamic viscosity	Pa s
η	Apparent (effective) viscosity	Pa s
k	Flow consistency number	Pa s^{α}
α	Flow index number	s
τ	Shear stress	Pa
$\dot{\gamma}$	Shear rate	s^{-1}
$\boldsymbol{\tau}$	Stress tensor	
Π	Total stress tensor	
$\boldsymbol{\gamma}$	Rate of strain tensor	
s	Arclength	m
$\mathbf{r}$	Position vector	
$\mathbf{n}$	Unit normal pointing away from the jet	
I	Second order identity tensor	
$R(s, \phi, t)$	Radius of the jet	
$\mathbf{u}$	Velocity vector	
u, v, w	Components of the velocity vector	
s, n, ϕ	Components of curvilinear co-ordinate system	
$\mathbf{e}_s$, $\mathbf{e}_n$, $\mathbf{e}_\phi$	Unit vectors in the curvilinear coordinate system	
$X(s,t)$, $Y(s,t)$, $Z(s,t)$	Coordinates of the centreline	
κ	Curvature of free surface	m^{-1}
Ω	Rotation rate	rad s^{-1}
$\mathcal{W}e$	Weber number	
$\mathcal{R}b$	Rossby number	
$\mathcal{O}h$	Ohnesorge number	
$\mathcal{F}r$	Froude number	
$\mathcal{R}e$	Generalised Reynolds number based on radius of the jet, a	
$\mathcal{R}e_\alpha$	Reynolds number based on radius of the can, s_0	
k^*, κ^*	Most unstable wavenumber	m^{-1}
ω^*	Frequency corresponding to most unstable wavenumber	s^{-1}
γ	Amplitude of additional forced disturbance	
ω	Frequency of additional forced disturbance	

CONTENTS

LIST OF FIGURES

LIST OF TABLES

CHAPTER 1

INTRODUCTION

Liquid jets and the creation of drops and sprays from surface tension driven flows are ubiquitous in modern engineering, and have been of interest to the scientific community for over a century, with the earliest classical studies dating back to Savart (1833), Plateau (1873) and Rayleigh (1879a,b). The practical importance of droplet formation in industrial processes ensures that studies into the break-up of liquid jets are still undertaken and are continually advancing.

Jet disintegration is not only a classic example of hydrodynamic stability theory (Kowaleski, 1996) but, due to its practical importance, has also become the subject of a variety of studies with numerous industrial applications. Whilst the rupture of a liquid jet is easily identifiable in processes such as ink-jet printing and agricultural irrigation, there are many more scenarios, such as those involved in silicon chip technology and modern fuel injection devices, where the properties of a liquid jet are used to the advantage of the application. More novel and emerging applications include developments in the fields of biotechnology and pharmaceutics. Examples include the technique of electrospraying, which is commonly used for the production of fine mono- and polydispersed drops and can also be used to introduce biomaterial into cells for gene transformation and gene therapy (Okubo et al., 2008). In the treatment of asthma, the use of electrohydrodynamic atomisation has emerged as a way to produce monodisperse aerosols which improve the therapeutic quality of the dispersed drug (Ijsebaert et al., 2001).

Hydrodynamic focusing is a technique used by microbiologists to provide more accurate results from flow cytometers for determining the size of bacteria or cells. Hydrodynamic fo-

cusing creates a monodisperse dropstream, each droplet containing a tiny cell, which is then interrogated and sorted based on its properties. A common task in the fabrication of enzyme electrodes and other types of bio/chemosensors is the deposition of proteins and other biospecific molecules onto an electrode surface. In Morozov and Morozova (1999) the possibility of using electrospray deposition to create these microarrays is explored. Recent developments in the area of electrospraying jets primarily focus on the encapsulation of particles, as micro- and nanoencapsulation is of particular importance for food additives and targeted drug delivery.

However, industrial applications of these phenomena have suffered from the fact that the break-up of jets can produce a non-uniform distribution of drop sizes due to non-linearity in the wave growth on the surface of the jet. A distribution of wavelengths can be found on the surface of the jet which leads to the production of smaller satellite droplets in between the larger main droplets.

This widespread use of liquid jets provides new challenges in appreciating how different types of fluids behave in such applications and also necessitates a greater understanding of liquid jet dynamics. The work presented in this thesis focuses on the industrially important process of prilling, which is widely used in industry to enable the production of small spherical pellets from molten material in many different applications, such as in the manufacture of fertiliser (urea), aluminium and magnesium pellets.

1.1 Prilling

> "The action or process of forming a substance, esp. a fertiliser, into prills."
> *Oxford English Dictionary*

The term prilling is generally used to describe the production of granular solids by spray crystallisation. Molten material is either sprayed through a system of fixed orifices, or dropped into a perforated vertical cylindrical drum which is suspended at the top of a tower and rotates about its vertical axis. It is this second method which is the focus of this thesis. Due to centrifugal forces, the melt is flung outwards towards the wall of the drum and thousands of long curved jets are produced from the perforations on the surface of the drum. These break up due to

the growth of surface tension driven instabilities on the surface of the jet. In either case, the droplets produced by break-up fall against a counter current of cool air and solidify to form pellets. Prilling was originally used for the production of lead shot (Land, 2004), however more recently the most common prills are solid ammonium nitrate or other fertilisers (urea and copper treated urea). The process is also used to produce particulate aluminum sulfate hydrate, which is used in the paper industry and in potable and waste water treatment. Aluminum sulfate with very low iron content is also used in the food industry and in the manufacture of deodorants, astringents, catalysts and metal alum (Ornek et al., 2000). Inorganic products, such as sodium hydroxide and iodine as well as certain organic compounds, like stearic acid, are also prilled.

Within industry there is a need to optimise the process in order to produce pellets of uniform size and hence suppress the formation of fine particles, which are formed by the creation of small satellite droplets during break-up. Fines are undesirable from both an emissions viewpoint and due to the possibility of dust explosions.

Norsk Hydro is a leading Norwegian manufacturer of fertiliser pellets. Understanding the prilling process is essential in order to be able to deliver a high quality product whilst minimising costs. With the initial support from *Norsk Hydro* and the ongoing support of EPSRC, it has been possible to investigate the prilling process both theoretically and experimentally, both in the School of Chemical Engineering and the School of Mathematics, at the University of Birmingham. The prilling plant at *Norsk Hydro*, in Porsgrunn, Norway measures 30 m in height and 24 m in diameter, which is one of the largest in the world. Suspended near the top of the prilling tower is a cylindrical drum, which is approximately 1 m tall and 0.5 m in diameter. A photograph of a prilling drum is shown in Figure 1.1. There are 2000 holes of 4 mm diameter on the drum. Molten fertiliser is pumped into the drum at a rate of approximately 120 tons per hour. The volume of the drum is about $V = 0.0625\pi$ m^3, and the flow rate of the molten fertiliser is $Q = 33.3$ kg s^{-1}. The drum is rotated at a controlled velocity between $320 - 450$ rpm, so the rotation frequency is between $\omega = 10\pi$ s^{-1} $- 15\pi$ s^{-1}. The exit speed at which a jet leaves an orifice has been calculated in Wallwork (2001) to be 11.85 m s^{-1}. The average size of one of the droplets processed in the prilling plant at *Norsk Hydro* is approximately 1.2 mm in radius.

Figure 1.1: Photograph of a prilling can. Courtesy of GEA Niro A/S.

At the University of Birmingham, initial experiments were carried out using a small can to simulate the prilling process. Wallwork et al. (2002) examined the trajectory of curved liquid jets to enable a comparison to be made with theoretical work. A mathematical formulation of the problem for an inviscid fluid was introduced in Wallwork et al. (2002), where these initial experimental studies were shown to display reasonable agreement with the theory. Wong et al. (2004) performed a more comprehensive experimental study on the laboratory scale, where he found four different modes of break-up that depend on jet exit conditions. Partridge et al. (2005) also performed experiments on a pilot scale rig.

The inclusion of the effects of gravity and viscosity were introduced by Decent et al. (2002, 2009) who used a temporal and spatial stability analysis to determine break-up lengths and droplets sizes. Non-linear effects have been considered by Părău et al. (2006, 2007).

The effects of prilling non-Newtonian fluids was examined theoretically, both linearly and non-linearly in Uddin et al. (2006, 2008a) respectively. The inclusion of gravity was introduced

in Uddin and Decent (2008).

The effect of a surfactant was investigated by Uddin et al. (2008b), while in Uddin and Decent (2009), the instability of a rotating liquid jet, having a power law rheology with a layer of surfactants along its free surface was investigated.

Gurney et al. (2010) performed a comprehensive comparison of both the linear and non-linear models for Newtonian fluids. He also investigated the effect of an additional forced disturbance at the orifice.

In this thesis, a number of techniques for controlling the break-up of liquid jets are investigated. These include the use of non-Newtonian liquid jets, the use of soluble surfactants and forcing a particular mode of break-up by the use of a vibrating nozzle.

1.2 Aims and objectives

This thesis extends previous experimental and theoretical work on the behaviour of curved liquid jet break-up and drop formation. The primary objectives are

- To determine the break-up behaviour of curved liquid jets for non-Newtonian fluids on both the pilot and laboratory scale and to compare these results to previous work on Newtonian fluids.
- To compare experimental studies completed to both new and existing numerical models.
- To develop theoretical work to include non-Newtonian effects in the linear instability model for curved liquid jets.
- To carry out novel work on forced disturbances at the orifice to try and control droplet formation and force a particular mode of break-up.

1.3 Novelty of the work

This thesis builds on previous work performed mostly on Newtonian fluids. Curved non-Newtonian liquid jets are examined experimentally, with the focus on shear thinning fluids,

although shear thickening fluids and fluids containing surfactant are also studied. Break-up is examined and compared to previous experiments on Newtonian work and existing theoretical models that can be used for simulations of curved non-Newtonian liquid jets.

Previous techniques used in experimental analysis are improved upon through the use of MATLAB. A linear dispersion relation for curved liquid jets, incorporating the effects of a power law fluid has been obtained that can be solved computationally to establish the behaviour of wave modes as they propagate along a curved liquid jet. This has also been compared to experimental work performed on non-Newtonian liquid jets.

Finally, by modification of the pilot scale rig, a vibrating nozzle is attached, enabling forced disturbances to be generated in an attempt to control drop formation. This was found to be successful in some cases in controlling liquid jets and changing the mode of break-up. Work was also performed to see if it is possible to use existing numerical models to predict when this change in break-up mode would occur.

1.4 Structure of the thesis

This thesis is arranged in the following manner. The first chapter of this thesis provides an introduction into industrial processes using liquid jets, and why the formulation and control of them is important. This particularly focuses on the process of prilling. A review of work done at the University of Birmingham is briefly outlined. The aims and objectives and novelty of this thesis are also clarified.

The classical linear instability work is briefly recapped in the next chapter, as this forms the basis of more recent non-linear analysis. A review of the most prominent experimental and theoretical work in the field of both straight and curved liquid jets is then explored, with particular attention given to relevant experimental and theoretical studies that are directly applicable to this thesis. The concept of a non-Newtonian fluid and the power law model are then introduced, with some prominent work being explored. Relevant studies on surfactant jets are also briefly recapped.

Chapter 3 details the materials and methods used to carry out experiments on both a pilot

and laboratory scale rig. Experiments have been performed using both non-Newtonian fluids and fluids containing surfactants. Details of data analysis methods are also given in this chapter.

Chapters 4 - 7 detail the experimental and theoretical results obtained throughout the course of this thesis. In Chapter 4 the results of experiments performed on both shear thinning and shear thickening fluids on the laboratory scale rig are presented. This section discusses the results of these experiments and also makes comparisons with the laboratory scale work of Wong et al. (2004).

In Chapter 5 the dynamics of the break-up of curved jets of pseudoplastic (shear thinning) liquids are examined in more detail using experimental and numerical methods. A pilot scale experimental facility is used and images of the jet trajectory, break-up and of the drops formed are captured using a high speed camera. Significant features of the break-up dynamics will be shown to be attributed to the shear-thinning effects of the fluid. Experiments performed on the pilot scale will be compared with simulations of the shape of the jet's free surface, generated from the non-linear finite difference model of Uddin et al. (2008a). It will be shown that the model can be used with reasonable accuracy to predict primary drop size, but that it is less accurate when used to predict the size of satellite droplets. The results of a brief study examining the influence of varying surface tension along the jet through the use of surfactants are also presented.

Chapter 6 presents a model determining the linear instability of the non-Newtonian rheology on the trajectory of the jet, using a mixture of computational and asymptotic methods. The sizes of the droplets produced by this instability are determined by considering the most unstable wave mode. This enables a quantitative comparison between the theoretical and experimental results of Chapter 5 to be made, by comparing droplet sizes predicted from the theory with experimental measurements.

In Chapter 7, the work of Gurney et al. (2010) is explored, where a secondary disturbance is introduced through the boundary conditions at the orifice in the non-linear model of Părău et al. (2007). This is done to investigate the possibility of mechanical instabilities affecting the break-up of the liquid jets. It is noted that satellite droplets are eradicated by the application of

certain frequencies and amplitudes and the idea of applying a secondary disturbance in order to force a certain break-up mode is investigated further, by exploiting the results found in Gurney et al. (2010) and applying these. Modifications are made to the pilot scale rig to enable the use of a vibrating nozzle to force mechanical vibrations at the orifice, so that both the frequency and the amplitude of the vibration can be controlled. Experiments are performed on aqueous glycerol (0-80% glycerol) solutions of varying viscosity, with a full range of forced disturbances being applied, varying both the amplitude and frequency of the secondary disturbance to see if it is possible to alter the mode of break-up and eliminate satellite droplets. These results are compared with the numerical simulations developed in Gurney et al. (2010), to determine whether the model can be used to accurately predict conditions using forced disturbances, where satellite droplets are eradicated.

Finally in Chapter 8 a brief summary of all the results obtained in the previous chapters are given. Future directions of the work performed in this thesis are explored.

1.5 Publications arising from this thesis

- Hawkins, V.L., Gurney, C.J., Decent, S.P., Simmons, M.J.H. & Uddin, J. (2010) *Unstable waves on a curved non-Newtonian liquid jet.* J. Phys. A.: Math. Theor. 43, 055501.

- Gurney, C.J., Hawkins, V.L., Simmons, M.J.H. & Decent, S.P. (2010) *The impact of multi-frequency and forced disturbances upon drop size distributions in prilling.* Chem. Eng. Sci, doi:10.1016/j.ces.2010.02.030

- Marston, J.O., Hawkins, V.L, Decent, S.P. & Simmons, M.J.H. (2009) *Influence of surfactant upon air entrainment hysteresis in curtain coating.* Exp. Fluids, 46:549-558

1.5.1 Conference Proceedings

- Hawkins, V.L., Simmons, M.J.H., Uddin, J. & Decent, S.P. (2009) *Experimental and Theoretical Description of Curved Non-Newtonian Liquid Jets* 8th World Congress of Chemical Engineering, WCCE 2009, Montreal, Canada, August 23-27 2009 (paper on Proceedings memory stick)

- Hawkins, V.L., Simmons, M.J.H., Uddin, J. & Decent, S.P. (2007) *Break up of spiralling non-Newtonian liquid jets* 6th International Conference on Multiphase flow, ICMF 2007, Leipzig, Germany, July 9-13 2007 (paper on Proceedings CDROM)

CHAPTER 2

LITERATURE REVIEW

2.1 Review of previous work on liquid jets

2.1.1 Classical work

The earliest experiments were carried out by Savart (1833), who investigated the decay of liquid jets. Savart developed a stroboscopic technique, and by illuminating the jets with sheets of light was able to produce images such as Figure 2.1, where it is possible to observe both tiny undulations growing on the jet of water, as well as the appearance of smaller satellite droplets in between the main droplets, which can only be understood by considering the non-linear dynamics of jet break-up. Savart also noted that break-up occurs spontaneously, independently of any external force or direction in which the jet is projected, therefore must be a feature intrinsic to jet dynamics. Despite these fundamental insights, Savart did not recognise that the source of the instability which led to the eventual break-up of these liquid jets was surface tension. This discovery was left to Plateau (1849). It was discovered that any perturbation that leads to a reduction in surface area is favoured by surface tension and will thus grow. This makes all sinusoidal perturbations with wavelength longer than 2π unstable (Eggers, 2006).

Figure 2.1: A figure from Savart (1833), showing the break-up of a straight liquid jet from a 6 mm orifice. Reproduced from Eggers and Villermaux (2008).

Previously, Plateau had developed his own experimental technique to study drop break-up (Plateau, 1843), by observing the decay of columns of fluids in density matched surrounding, in a so-called 'Plateau tank', thus eliminating the effects of gravity. This research was focused on predicting whether a particular configuration would be stable or not (Eggers, 2006), however Plateau also included some experimental sketches that offered interesting insight into the non-linear dynamics of break-up for a viscous fluid.

It was the seminal work of Rayleigh (1879a,b) who proposed that capillary jet break-up is caused by the wavemode which grows most quickly with time, or the mode of maximum instability, and he was able to show that an optimal wavelength ($\lambda \approx 4.5$ jet diameters), at which perturbations grew fastest existed.

Rayleigh analysed the linear stability of an infinitely long axisymmetric cylinder of an inviscid incompressible fluid, with initial radius $r = R$, which is subjected to small sinusoidal disturbances of wavelength λ_w from its equilibrium. This leads to the radius having the form $r = R + \delta\cos(kz)\cos(n\phi)$, where δ is a small initial disturbance, k is the wavenumber, where $k = 2\pi/\lambda_w$, n is an integer, z represents the distance along the central axis of the cylinder and ϕ is the azimuthal co-ordinate. Using the standard equations of motion and assuming that disturbances can be written in the form $\exp(i(kz - n\phi) + \lambda t)$, where t is time, Rayleigh was able to derive a dispersion relation. That

$$\lambda^2 = \frac{\sigma(kR)}{\rho R^3}(1 - n^2 - k^2R^2)\frac{I_n^{'}(kR)}{I_n(kR)}, \tag{2.1}$$

where σ is the surface tension, ρ is the density of the liquid, I_n is the modified Bessel function of the n^{th} order and $I_n^{'}$ is the derivative, defined by $I_n^{'} = \left(\frac{d}{dr}I_n(kr)\right)\Big|_{r=R}$.

Values of $\mathrm{Re}(\lambda) > 0$ cause the amplitude of the disturbance to grow with time, and so $\mathrm{Re}(\lambda)$ is defined as the growth rate of the disturbance. $\mathrm{Im}(\lambda)$ is the wave frequency. The integer n is the periodicity of the motion around the jet's circumference. For values of $n \neq 0, \lambda^2 < 0$; this corresponds to neutrally stable waves, where λ is purely imaginary and $\mathrm{Re}(\lambda) = 0$. Waves for which $\mathrm{Re}(\lambda) < 0$ are stable. However, for $n = 0$, $\mathrm{Re}(\lambda) > 0$, corresponding to a growing

amplitude for $0 < kR < 1$. This mode is axisymmetric and it is possible to use the recurrence formulae for Bessel functions,

$$I_{n-1}(x) + I_{n+1}(x) = \frac{2n}{x} I_n(x), \qquad I_n^{'}(x) = \frac{1}{2}(I_{n-1}(x) + I_{n+1}(x)),$$

to arrive at the dispersion relation for the unstable axisymmetric disturbances

$$\lambda^2 = \frac{\sigma(kR)}{\rho R^3}\left(1 - k^2R^2\right)\frac{I_1(kR)}{I_0(kR)}. \tag{2.2}$$

The most unstable mode is the value of k corresponding to the maximum of Re(λ). The disturbance which grows most rapidly occurs for $kR \approx 0.697$, which has a wavelength $\lambda_w \approx 2\pi R/0.697 \approx 9R$, the so-called famous Rayleigh mode. At this wavenumber the perturbation grows fastest and kR governs the size of the droplets produced. The corresponding growth rate is $Re(\lambda) \approx 0.34(\sigma/\rho R^3)^{\frac{1}{2}}$, which yields a characteristic break-up time, $t_b \approx 1/\text{Re}(\lambda) \approx 2.94(\rho R^3/\sigma)^{\frac{1}{2}}$. For $kR > 1, \lambda$ is imaginary and the disturbances do not grow with time.

This famous result was checked directly against the experiments of Savart (1833), whose experiments from some 50 years earlier give remarkably good agreement.

Inclusion of viscosity

Weber (1931) considered the effects of the liquid viscosity as well as the density of the ambient fluid. Viscosity is a damping force on capillary wave growth, hence the dispersion relation that describes wave behaviour must be dependent on viscosity. The above analysis can be repeated with viscosity to arrive at a similar characteristic equation for $n = 0$, namely

$$\lambda^2 + \lambda\frac{2\mu k^2}{I_0(kR)}\left[I_1^{'}(kR) - \frac{2k\tilde{k}(kR)I_1^{'}(\tilde{k}R)}{(k^2+\tilde{k}^2)I_1(\tilde{K}R)}\right] = \frac{\sigma kR^2}{\rho\mu^2}\left(1 - k^2R^2\right)\frac{(k^2-\tilde{k}^2)I_1(kR)}{(k^2+\tilde{k}^2)I_0(kR)}, \tag{2.3}$$

where $\tilde{k}^2 = k^2 + \lambda/\mu$ and μ is the viscosity of the fluid.

His theoretical prediction did not agree well with experimental data, as pointed out by Sterling and Sleicher (1975), who improved Weber's theory with partial success (Lin and Reitz, 1998).

While linear stability analysis and Rayleigh's seminal work is, even today, a useful tool and quite a good predictor of important quantities like the continuous length of the jet, it only permits a description of the initial growth of instabilities as they initiate near the nozzle. The drop shapes determined by linear stability analysis would be of a single harmonic waveform. Rayleigh himself observed that this was often not the case, but instead small spherules formed between the main drops (Rayleigh, 1882). Close to break-up, non-linear effects become important and thus, linear stability analysis fails to describe the details of drop break-up which lead to the formation of satellite drops. For a full review on significant early work the reader is referred to Bogy (1979). An extensive and detailed review on the work done on liquid jets is given by Eggers (1997) and Eggers and Villermaux (2008). Other sources include Lin and Reitz (1998) and books by Middleman (1995), Yarin (1993) and Anno (1977).

2.2 Reviews of experimental work on liquid jets

2.2.1 Straight liquid jets

Analytically, the cornerstone of most work on liquid jets is linear stability. For a hundred years after Rayleigh's original work, theoretical research focused on extending his results using this mathematical approach. However, experimental results accumulated that probed the dynamics of free surfaces beyond the validity of linear theory. Experimental studies investigating the phenomena of break-up and drop formation of liquid jets tend to fall into three categories; those which consider a liquid jet emerging from a nozzle, a dripping faucet (where jets do not form, but pendant shapes emerge, neck and detach from a nozzle), and a liquid bridge. These experiments have much in common especially near the locality of the singularity where the radius goes to zero and the jet ruptures. Early work tended to focus either on the early stages of drop formation, or on the size and number of the resulting drops.

The features of non-linear dynamics were revealed in increasingly sophisticated experiments, including those of Savart (1833) and Lenard (1887). Lenard (1887) observed the drop oscillations that remain after break-up, already noted by Savart. To record the drop oscillations, Lenard (1887) used a stroboscopic method and was able to record a sequence showing the dy-

namics close to break-up, leading to the separation of a drop. It is here that the origin of a satellite drop is shown for the first time (Eggers, 2006).

Edgerton et al. (1937) examined a drop of fluid of different viscosities falling from a faucet. Whilst rediscovering some of the features initially observed by Lenard (1887), they also found that a high viscosity fluid, like glycerol, forms extremely long threads that break up into myriads of satellite drops.

Experimentally, advances in high speed digital photography and cinematography that enable insight into the immediate vicinity of the point of break-up have revived the subject. While photographic methods were introduced by Rayleigh (1891), these observations were only qualitative in nature. The first quantitative experiments were those of Haenlein (1931), Baird and Davidson (1962), Donnelly and Glaberson (1965) and Goedde and Yuen (1970).

Baird and Davidson (1962), who studied straight annular liquid jets without gravity, noted that a singularity occurs when the Weber number is around 1, where the Weber number is defined as $\mathcal{W}e = \rho U^2 a/\sigma$, where ρ is the density of the fluid, U is the jet exit velocity, a is the size of the orifice and σ is the surface tension. Thus, the Weber number is an index of the inertial force to the surface tension force acting on a fluid element. Baird and Davidson (1962) also concluded that short jets have large menisci at the orifice which alters the jet profile.

The first accurate measurement of the complete dispersion relation was by Donnelly and Glaberson (1965). Stroboscopic flash pictures were taken which enabled a direct determination of the growth of disturbances, which could then be compared to the theory. A jet of water was excited by a loudspeaker and it was observed how perturbations grew from one wave crest to another. For stability purposes, a water jet may be considered inviscid and excellent agreement with Rayleigh's dispersion relation was found. It should be mentioned that Crane et al. (1964), who used an electrical vibrator to induce mechanical vibrations of different wavelengths, had found deviations from linear theory based on both the break-up length and direct analysis of photographs. This was attributed to the large disturbance amplitude used in their experiment, making linear theory inapplicable.

The viscous dispersion relation was also tested by Donnelly and Glaberson (1965) and

Goedde and Yuen (1970), who both found good agreement with the results of Chandrasekhar (1961). Goedde and Yuen (1970) investigated jets falling under gravity and induced a range of perturbations at the orifice using a variety of methods. Experiments were carried out using a short vertical nozzle, which allowed the velocity profile to remain uniform on exit, and jet speeds were chosen to be small enough so that the surrounding effects could be ignored and a laminar flow assumed, but high enough so that effects of gravity could be neglected. They produced one of the first papers to consider the non-linear effects of jet instability in detail. They observed the very complex behavior of the process of satellite drop formation. While incorrect in the assertion that break-up of satellite droplets always occurs downstream of the ligament, which was contradicted in later experiments by Pimbley and Lee (1977), they found that the satellite-drop size increases with decreasing wavenumber. On this point the experimental results of Rutland and Jameson (1971) concurred with those of Goedde and Yuen (1970). Rutland and Jameson (1971) investigated the decay of a water jet falling under gravity; to induce perturbations at the nozzle they used a 10W speaker, which is similar to the method used by Donnelly and Glaberson (1965). They also reported that the size of the drops was unaffected by the disturbance amplitude, a result contradicted by later experiments (Bogy, 1979).

Aside from Pimbley and Lee (1977) noting that a ligament may first separate downstream, upstream, or simultaneously from both ends, they also observed that the satellite droplet receives a relative net acceleration towards the end of the ligament that remains attached longer, so it may merge forwards or backwards with the adjacent main drop. If the ligament separates simultaneously from both ends, the velocity of the satellite drop remains equal to that of the main drops and no merging occurs. They were thus able to control the formation of satellite droplets by increasing the amplitude of the initial disturbance, so that the satellites merge forward in fewer and fewer wavelengths, until finally a point is reached at which the satellite drop does not occur. Lindblad and Schneider (1965) also noted that droplet size can be controlled by using a piezo-electric transducer.

Many of the more recent studies (Peregrine et al., 1990; Vassallo and Ashgriz, 1991; Shi et al., 1994; Zhang and Basaran, 1995; Kowaleski, 1996; Clanet and Lasheras, 1999) have been

on the structure of the jet at the point of break-up, including necking and satellite formation under both jetting and low-velocity dripping conditions. As experimental techniques improved and became available for observing the actual evolution of a liquid jet throughout drop formation, common features began to emerge. The last stages of break-up are dominated by the properties of the pinch singularity. This idea was first enunciated clearly by Peregrine et al. (1990), whose paper also contained the first high-resolution pictures of water falling from a faucet. For higher viscosities, this work was extended and corresponding pictures were taken by Shi et al. (1994). Zhang and Basaran (1995) and Brenner et al. (1997) produced time-resolved motion pictures of the bifurcation. From those, the temporal dependence of neck radius and neck length could be measured.

There have also been many studies that focus on obtaining methods to reduce the formation of satellites. The need for this was catalyzed in the late 1970's by the introduction of inkjet printers into the market. Inkjet printers work by first charging a drop and then using an electric field to deflect the drop towards the desired position. A bimodal drop size distribution is a problem, as drops of different sizes are deflected differently in the electric field, leading to a reduction in quality. Chaudhary and Maxworthy (1980a,b) performed extensive experimental investigations into satellite formation. The work of Chaudhary and Maxworthy (1980b) agrees qualitatively with that of Pimbley and Lee (1977), that there is a transition from rear merging to forward merging as the driving amplitude is increased, and that the critical amplitude that corresponds to the no-merge condition increases with wavenumber. The Weber number has also been shown by Vassallo and Ashgriz (1991) to have a significant effect. Rear merging, no merging and forward merging satellites are shown in Figure 2.2.

A large body of experiments studying the break-up of jets into drops have been undertaken, usually with a sinusoidal periodic frequency disturbances applied at the nozzle tip using acoustic, electromagnetic, or piezo-electric-induced pressure vibrations or a vibrating impinging needle (Donnelly and Glaberson, 1965; Goedde and Yuen, 1970; Pimbley and Lee, 1977; Chaudhary and Maxworthy, 1980b; Kowaleski, 1996; Taub, 1976); by applying some sort of mechanical or sonic disturbance a particular break-up mode is forced. More recently Chauhan

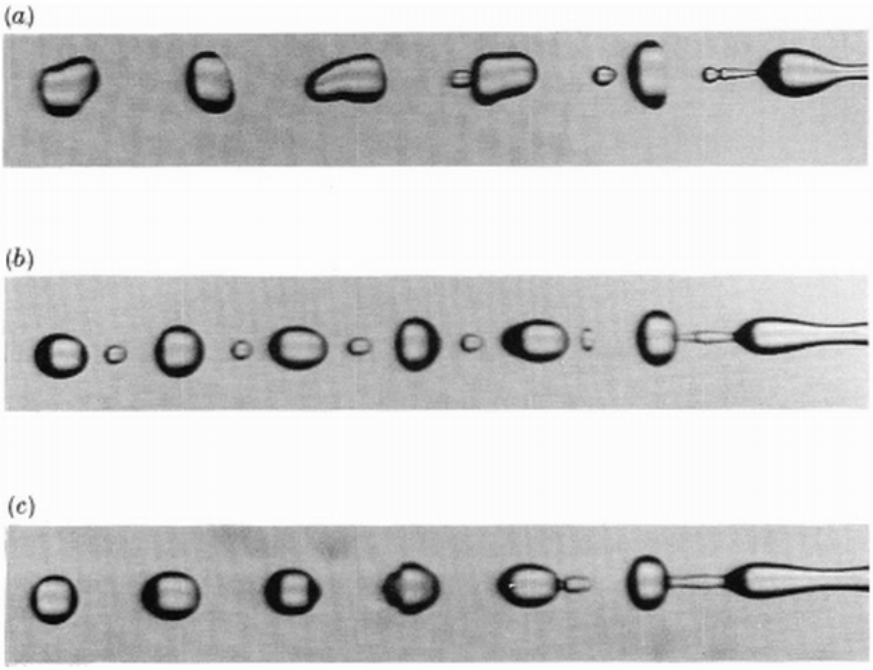

Figure 2.2: Example of rear merging, no merging and forward merging satellite droplets. Image taken from Vassallo and Ashgriz (1991).

et al. (2003) used a piezo crystal to generate these disturbances. Early devices used for the production of monodisperse drops, suggested by Schneider and Hendricks (1964), Dabora (1967) and Berglund and Liu (1973) amongst others, used electrically driven piezoceramic vibrators to excite liquid jets using capillary glass tubes or pinhole orifices. An extension of this work was achieved by Orme and Muntz (1987, 1990, 1991), who proposed the application of amplitude-modulated electrical signals for driving the piezovibrators which control the jet break-up. They were able to show that this technique leads to the formation of droplets which tend to merge with one another as they move away from the nozzle. Brenn and Lackermeier (1997) also showed that laminar liquid jets emerging from the nozzle of a vibrating orifice drop generator may be excited by a piezovibrator driven by modulated electrical signals to produce monodisperse drops over an extended range of wavenumbers.

As well as the break-up mode being very sensitive to the amplitude of the initial perturbation, it also depends on the presence of higher harmonics (Chaudhary and Maxworthy, 1980b). The existence of higher harmonic components in the driving by real world nozzles has also been recognised and measured by Taub (1976) and Torpey (1989).

Shield et al. (1987) and Bousfield and Denn (1987) developed the 'drop-on-demand' technique, a method which generates individual droplets by pulsing the liquid flow. This technique is limited to a lower droplet production rate than the continuous methods of droplet generation where droplets are formed by the growth of surface tension driven instabilities on the surface of a continuous jet.

Exploiting high speed photographic techniques, Kowaleski (1996) observed that just before a jet separates, a long thin liquid ligament is created, which connects the swell with the preceding droplet. Typical jet diameters were up to eighty times smaller ($50 - 900\mu$m) than those considered by Rutland and Jameson (1971) and typical break-up lengths were between 100-200 jet radii. The ligament characteristics are a function of liquid viscosity, orifice diameter, jet perturbation amplitude and frequency. If the viscosity is increased it is possible to make this region more visible. Shortly before rupture, a fine secondary filament, a 'micro-thread,' is created, which connects the ligament with the droplet. Once the jet ruptures, a satellite droplet is created due to the jet-droplet filament moving rapidly back towards the jet and the surface disturbances of the main liquid jet propagating in the opposite direction. While the maximum length of this micro-thread is strongly influenced by viscosity, causing its length to vary from micrometres to several millimetres, the minimum diameter of the jet before break up, which is approximately 1 μm, appears to be relatively impervious to changes in liquid parameters. The pinch off process appears to be unaffected by external initial conditions.

2.2.2 Curved liquid jets

When compared to straight jets, there is a contrastive shortage of experimental work performed on curved liquid jets.

At the University of Birmingham, experimental work has been undertaken which attempts to directly simulate the prilling process at various scales. As a first attempt, a laboratory scale rig was set up by Wallwork et al. (2002) to examine the trajectory and break-up of slender, curved liquid jets of water, to enable a comparison with theoretical work done by the same group which is discussed in more detail in $\oint$ 2.3.2. Results from these preliminary studies showed reason-

able agreement with theoretical work. Wong et al. (2004) performed a more comprehensive experimental study on the laboratory scale, using the same equipment as Wallwork et al. (2002) over a wider range of viscosities. Newtonian aqueous solutions of glycerol were used as the working fluid ($0.001 < \mu < 0.09$ Pa s).

A photograph of the laboratory scale facility is shown in Figure 2.3. The apparatus consists

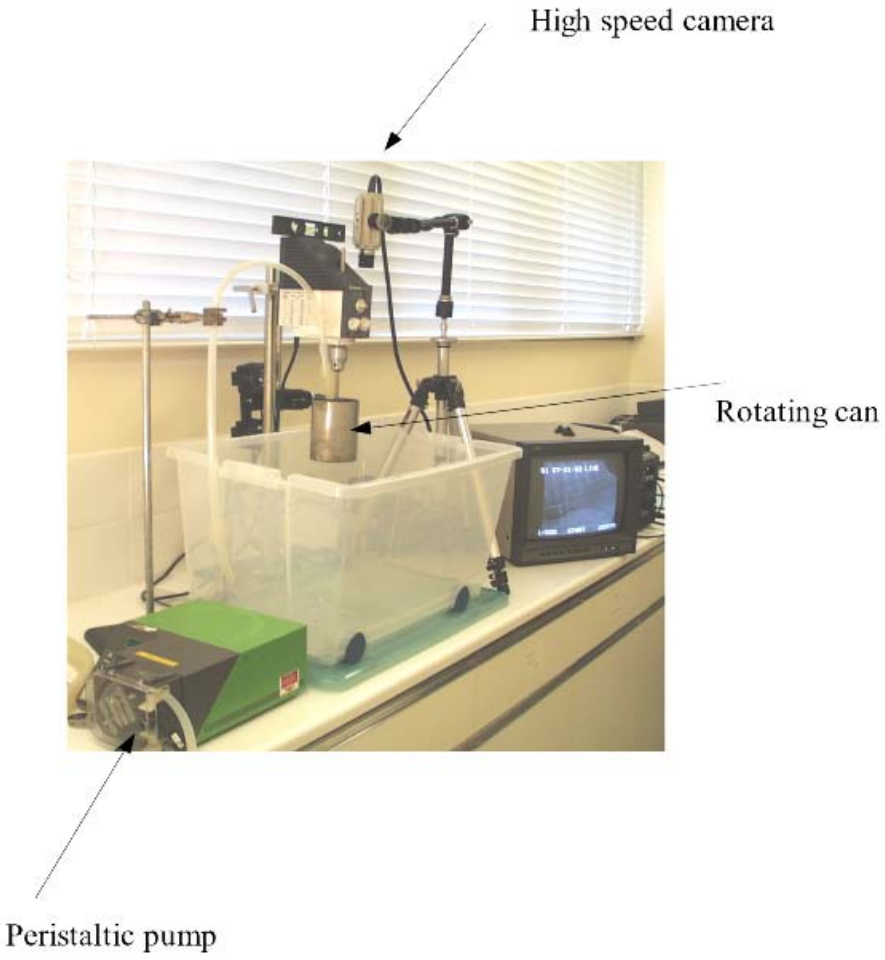

Figure 2.3: Photograph of the laboratory scale facility.

of a cylindrical can with a diameter, D, of 0.85 m and a height of 0.115 m, that contains two diametrically opposed orifices of radius, a, of 0.0005 m and 0.0015 m respectively. The can was partially filled with liquid to a height, H, to give liquid aspect ratios, H/D, ranging from $2/3 - 5/4$. To maintain a constant hydrostatic pressure, the liquid level was kept constant by the use of a peristaltic pump (Waltson-Marlow 505s) which continuously supplied fresh fluid to the can. The rotation rate was varied from $50 - 300$ rpm, which corresponds to an angular

speed of $\Omega = 5.24 - 31.4$ rad s^{-1}. The apparatus was all contained in a transparent tank that enables the collection of excess fluid. The average exit velocity of the jet, U, leaving the orifice was calculated by dividing the total volume of liquid collected over a period of 1 minute by the cross-sectional area of the orifice.

The trajectory of a jet was captured by means of a high speed digital camera (Photron Fastcam Super 10k), capable of recording up to $10,000$ frames per second. The images from the camera were downloaded into a personal computer for analysis. Digital measurements were then obtained from the images using Image-Pro Express software (Datacell Ltd., UK). At least 35 frames were examined to ascertain the break-up length from origin to detachment. Wong et al. (2004) also produced drop size distributions, these were obtained by assessing at least 200 individual droplets. The physical properties of the fluid were altered by using different concentrations of solutions of water and glycerol ($0-80\%$ w/v) which gave dynamic viscosities, μ, ranging from $0.001 - 0.09$ Pa s.

Over the range of experimental parameters studied, Wong et al. (2004) identified four different modes of break-up, denoted as M1, M2, M3 and M4. For each mode, considerable differences in the mechanism of break-up and in the drop size distributions produced were observed. Full definitions of these modes are given in Wong et al. (2004), however a brief description of each mode is given here.

M1 break-up is shown in Figure 2.4, and is characterised by disturbances with a short wavelength (approximately equal to the jet diameter), leading to the production of a unimodal drop size. Examples of M1 drop size distributions taken from Wong et al. (2004) are shown in Figure 2.5(a). Varicose surface tension driven disturbances on the jet surface are convected downstream until they are sufficiently large that the primary drops form by capillary pinch-off. The primary aim of this research into curved liquid jets concerns the formation and eradication of satellite droplets. As such, M1 break-up is a desirable mode of break-up. However, typically this mode occurs for jets with a low exit velocity and low viscosity and so is difficult to reproduce in the prilling industry due to the large rotation rates present. Wong et al. (2004) suggested that the formation of occasional random satellite droplets may be caused by external disturbances acting

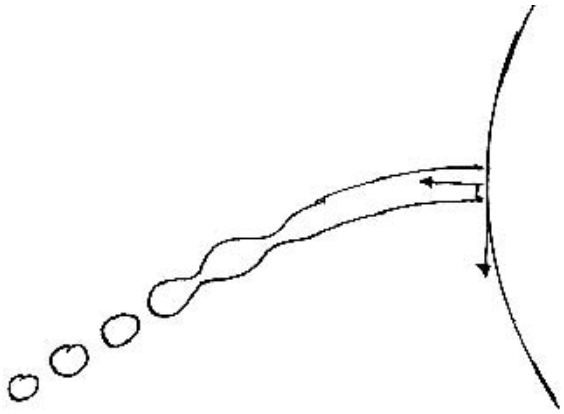

(a) Sketch showing M1 break-up.

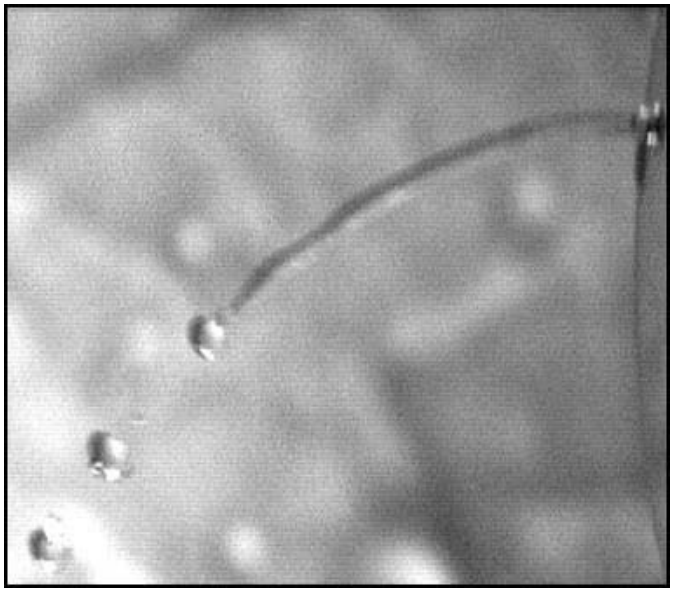

(b) Photograph showing M1 break-up.

Figure 2.4: M1 break-up (Wong et al., 2004).

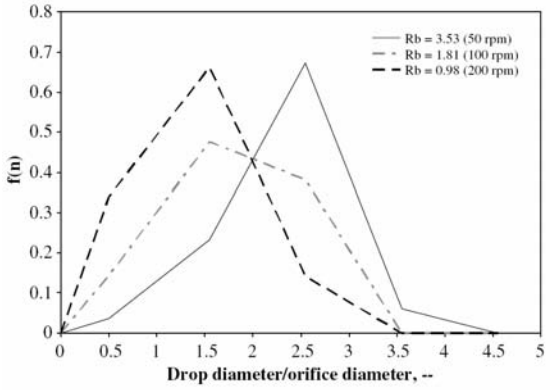

(a) Drop size distribution for three rotational rates: $\mathcal{R}b = 3.53, 1.81, 0.98(50, 100, 200$ rpm) in break-up M1 ($400 < \mathcal{R}e < 500; \mathcal{W}e < 10; \mathcal{O}h = 0.005(\mu = 0.001$ Pa s, $\rho = 998.1$ kg m^3)).

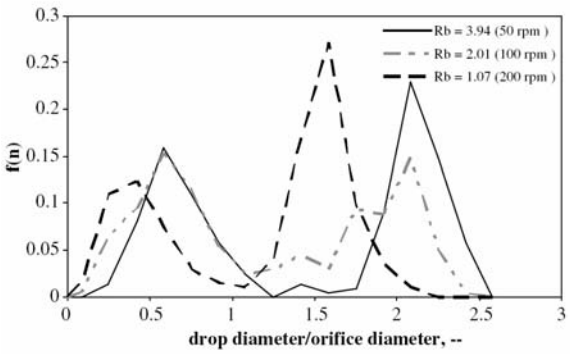

(b) Drop size distribution for three rotational rates: $\mathcal{R}b = 3.94, 2.01, 1.07(50, 100, 200$ rpm) in break-up M2 ($\mathcal{R}e > 1000; 15 < \mathcal{W}e < 20; \mathcal{O}h = 0.0029(\mu = 0.001$ Pa s, $\rho = 998.1$ kg m^3)).

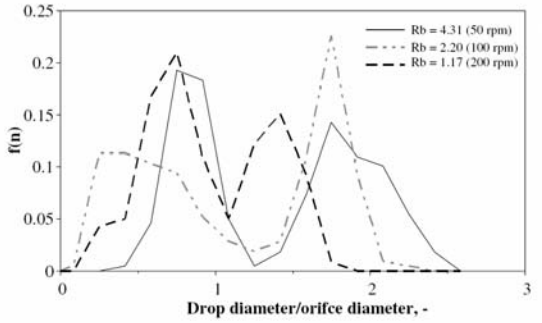

(c) Drop size distribution for three rotational rates: $\mathcal{R}b = 4.31, 2.20, 1.17(50, 100, 200$ rpm) in break-up M3 ($120 < \mathcal{R}e < 150; 20 < \mathcal{W}e < 30; \mathcal{O}h = 0.038(\mu = 0.0129$ Pa s, $\rho = 1164.6$ kg m^3)).

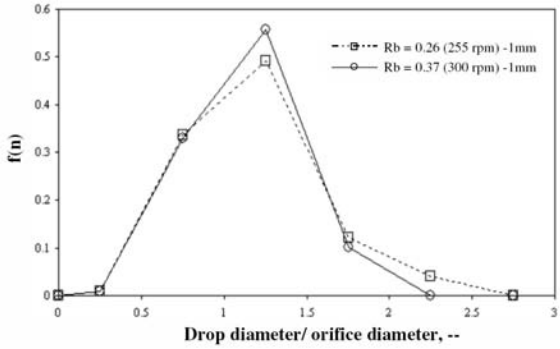

(d) Drop size distribution for two rotational rates: $\mathcal{R}b = 0.26, 0.37(255, 300$ rpm) in break-up M4 ($\mathcal{R}e < 5; \mathcal{W}e < 3; \mathcal{O}h = 0.352(\mu = 0.071$ Pa s, $\rho = 1215.5$ kg m^3)).

Figure 2.5: Drop size distributions for M1-M4 (Wong et al., 2004).

on the jet, i.e., shaking of the can due to transmission of mechanical vibrations from the drive motor and gearbox. This is an interesting factor, which will be considered in more detail later in this thesis.

M2 break-up is similar, shown in Figure 2.6, with rapidly growing varicose disturbances of short wavelength visible on the surface of the jet. However, M2 break-up is characterised by the presence of satellite drops in between the main drops leading to a bimodal distribution (see Figure 2.5(b)). Here satellite drops are formed from fragments of fluid created when the primary drop breaks off.

Typical M3 break-up is shown in Figure 2.7. M3 occurs as the velocity of high viscosity jets

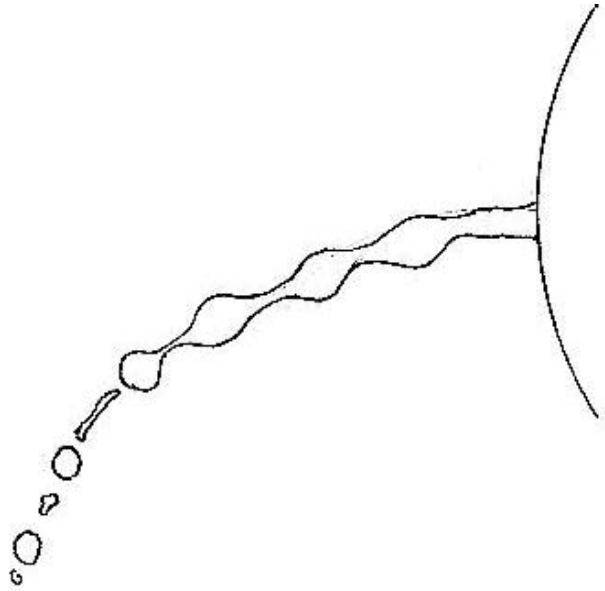

(a) Sketch showing M2 break-up.

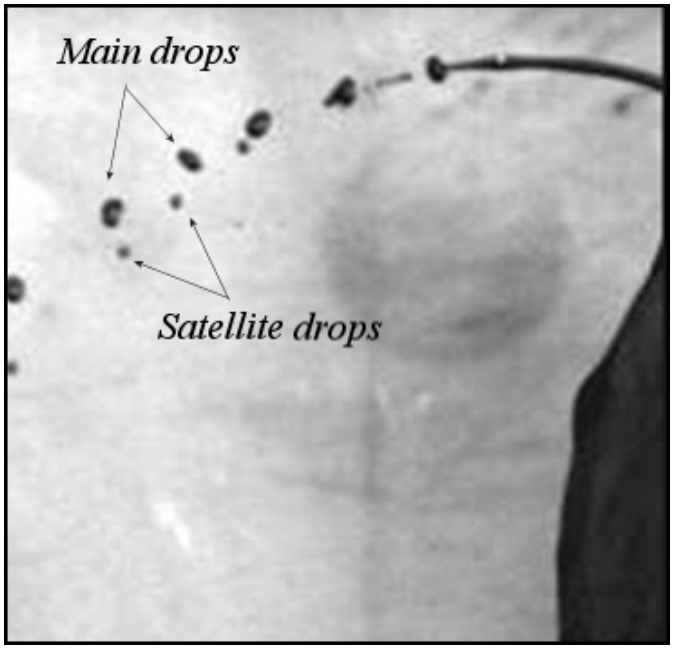

(b) Photograph showing M2 break-up.

Figure 2.6: M2 break-up (Wong et al., 2004).

is increased. The viscous forces dampen the capillary instabilities causing break-up to occur further away from the orifice. For M3 break-up, the disturbances have a longer wavelength ($2-5$ times the jet diameter) and simultaneous break-up is also observed. In between the main droplets it is also possible to observe the formation of ligaments, long thin filaments of fluid, which subsequently contract and break-up into multiple satellite droplets, again leading to a

bimodal drop size distribution (see Figure 2.5(c)).

M4 break-up, as shown in Figure 2.8, is strongly non-linear; the jet breaks up via elongation and disintegration of the jet into multiple sized fragments. M4 break-up is unique as the only mode where disturbances were observed to propagate upstream, back towards the jet orifice. Uni-modal distributions were also produced for mode M4 (see Figure 2.5(d)) due to disintegration of the entire jet into a large number of different size fragments. It is believed that there is an element of absolute instability in M4 break-up. This is currently being investigated by Rachan Bassi, a PhD student in the School of Mathematics at the University of Birmingham. Evidence for this comes from the fact that M4 occurs at very low Weber numbers.

It was found that the modes of break-up were dependent on the different influences of liquid inertia, liquid viscosity, surface tension and rotation rate acting on the jet. Using dimensional analysis, a number of dimensionless groups were identified which allowed the influence of the various parameters to be elucidated. In addition to the Weber number, the following non-dimensional parameters were identified,

$$\mathcal{R}b = \frac{U}{s_0\Omega}, \quad \mathcal{R}e = \frac{\rho U a}{\mu}, \quad \mathcal{O}h = \frac{\mu}{\sqrt{\sigma a \rho}}, \tag{2.4}$$

namely, the Rossby, Reynolds and Ohnesorge numbers.

Wong et al. (2004) developed flow maps that show regions where particular characteristics and modes occur. The mode generated was a strong function of dynamic viscosity and jet exit velocity and a dimensionless plot of Ohnesorge number, $\mathcal{O}h$, against Weber number, $\mathcal{W}e$, enabled prediction of these modes. This flow map is shown in Figure 2.9. Four distinct regions are identified, as is a region where the exit velocity is too small to generate a jet. Wong et al. (2004) also determined relationships between various non-dimensional parameters and jet break-up length and drop size. For example, it was also found that an increase in the rotational speed of the can (decreasing the Rossby number), led to a decrease in drop size for all modes of break-up.

Other significant experimental studies include the later work by Partridge et al. (2005),

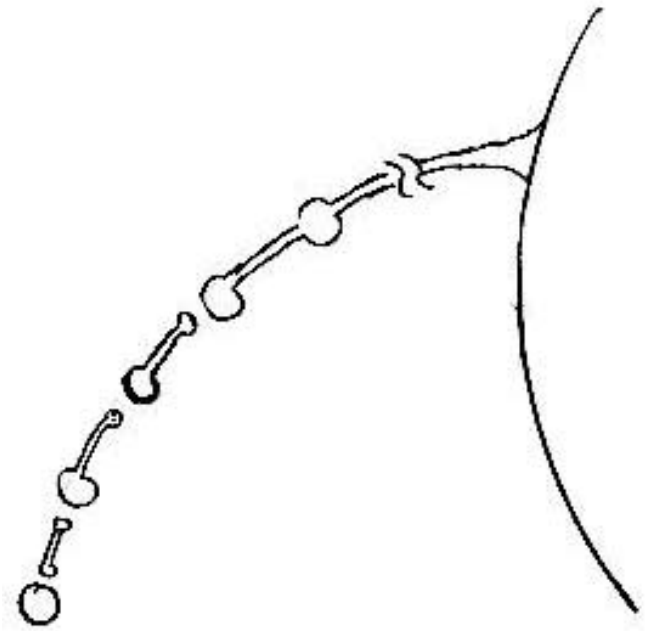

(a) Sketch showing M3 break-up.

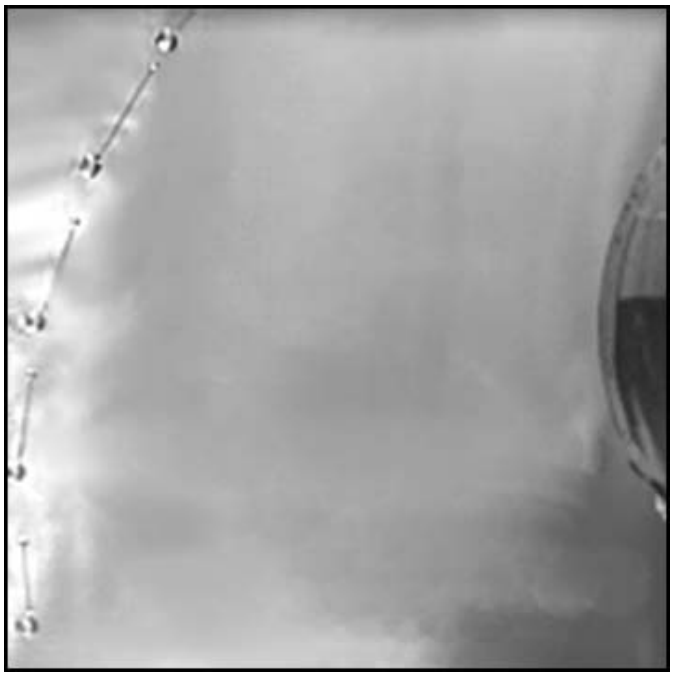

(b) Photograph showing M3 break-up.

Figure 2.7: M3 break-up (Wong et al., 2004).

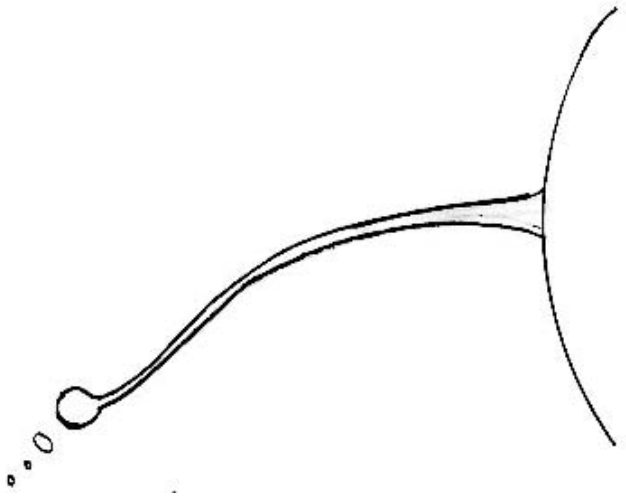

(a) Sketch showing M4 break-up.

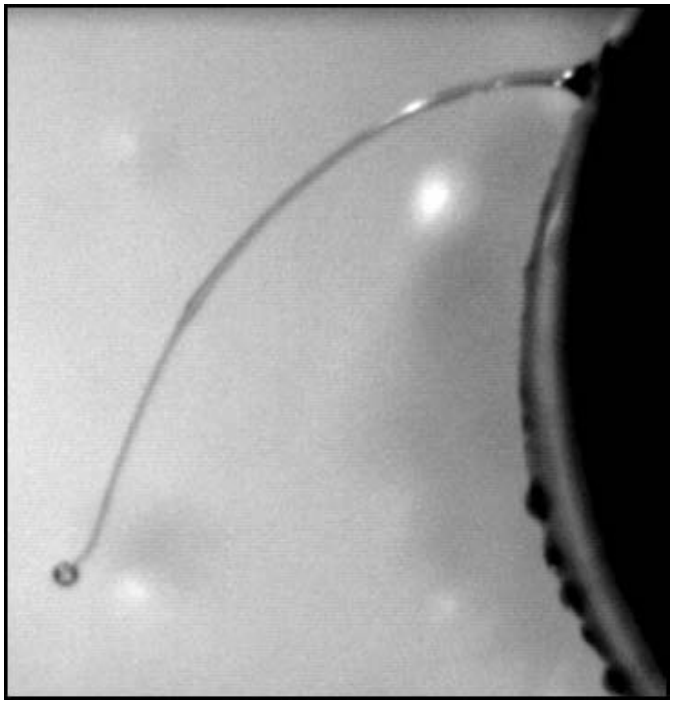

(b) Photograph showing M4 break-up.

Figure 2.8: M4 break-up (Wong et al., 2004).

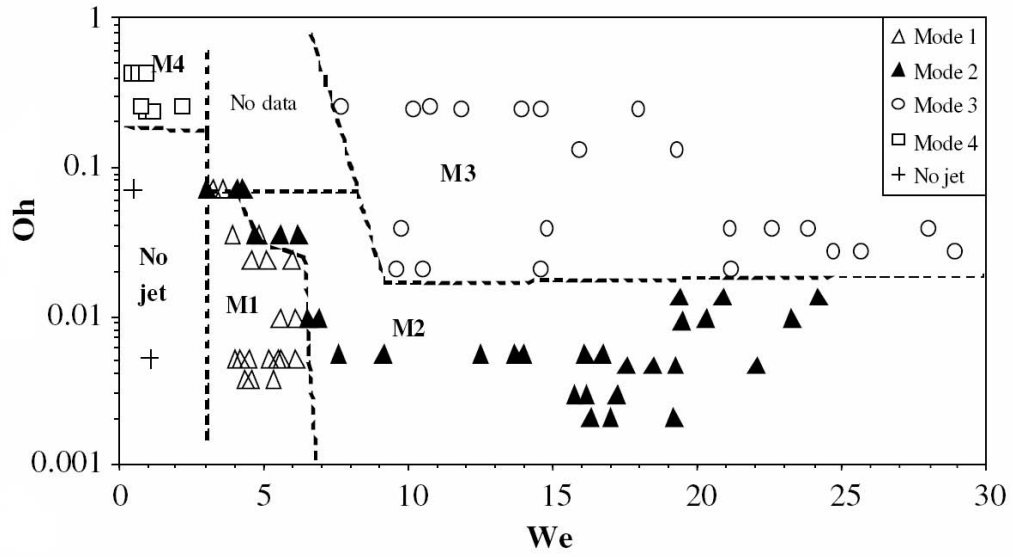

Figure 2.9: Break-up regime map on laboratory scale rig, showing $\mathcal{O}h$ versus $\mathcal{W}e$ (Wong et al., 2004).

who performed experiments on a pilot scale facility (0.285 m diameter drum). These results were compared with those of Wong et al. (2004). Partridge et al. (2005) found that there was generally good agreement on the pilot scale facility with the previously defined boundaries in Figure 2.9, although some differences were observed, notably the absence of M4 due to much higher exit Weber numbers (due to the increased scale and hence increased U) and a greater presence of satellite droplets, possibly due to vibration in the equipment; M1 was not observed on the pilot scale rig. These differences can be seen in Figure 2.10. There is a parameter region, shown in Figure 2.10, where it can be observed that both M2 and M3 break-up are encountered. The overlap is partly due to the subjective nature of classifying break-up mode and classifying break-up into the set laboratory scale regimes was not always possible. Hence a new mode of break-up, M2/M3, was identified. Briefly, jets that displayed characteristics of M2 break-up were also observed to break-up simultaneously in several places, which is typified as M3 behaviour, although no ligaments are formed. This is shown by the use of both symbols for M2/M3 in Figure 2.10. Partridge et al. (2005) suggested a possible reason for the occurrence of multiple break-up points may be increased mechanical vibration from the shaft and motor driving the rotation of the can.

Partridge et al. (2005) also noted the presence of non-axisymmetric (kink) disturbances

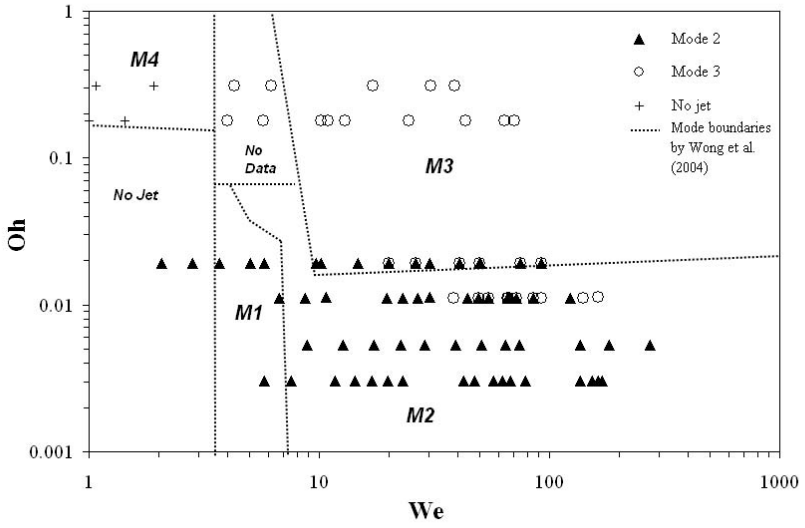

Figure 2.10: Break-up regime map for the pilot scale rig, showing $\mathcal{O}h$ versus $\mathcal{W}e$ (Partridge et al., 2005).

visible on the surface of the jet. Only axisymmetric (varicose) disturbances were observed on the laboratory scale in M1−M3. The effect of wind resistance can also be observed on the pilot scale rig, as the ligaments between the primary drops are observed to bend in a direction normal to the curved central axis of the jet. The reader is referred to Partridge et al. (2005) for a more thorough review.

A key difference between the break-up of curved jets and straight jets is the role of rotation of the can. The experimental work presented have shown that the rotation affects the exit velocity, trajectory, break-up length, drop size and the wavelength of the disturbances developing on the jet surface compared with straight jets.

2.3 Review of theoretical work on liquid jets

2.3.1 Straight liquid jets

For mathematical analysis, the most basic tool for describing liquid jets is linear stability analysis around the cylindrical base state. However, as shown by experiments, there are many important features of the break-up process which are dominated by non-linear effects.

Chandrasekhar (1961) took into account the liquid viscosity and the liquid density, which was neglected by Rayleigh, and showed mathematically that the viscosity tends to reduce the break-up rate and increase the drop size. Tomotika (1935) extended Rayleigh's original analysis to account for the presence of an outer fluid and in particular he examined the case of a very viscous fluid encased in another viscous fluid. His work highlighted the importance of viscosity and density ratios between the two fluids, as well as the importance of the ratio of viscous to surface tension forces (characterised by the Ohnesorge number) on instability.

The spatial instability of liquid jets was first considered by Keller et al. (1973). Previously, disturbances of the form, $\exp(i(kz - n\phi) + \lambda t)$, were considered, and positive values of $\mathrm{Re}(\lambda)$ caused perturbations to grow with time. The wavenumber, k, is taken to be real, and the growth rate, λ, is considered to be a complex quantity of the form $\lambda = \lambda_r + i\lambda_i$, where λ_r and λ_i/k are known as the temporal growth rate and wavespeed respectively. λ_i represents the angular frequency of the oscillation. This type of instability is a temporal instability.

This form of stability analysis assumes that disturbances grow everywhere, including at the orifice. In experimental research, where harmonic disturbances are imposed at the orifice to attempt to force jet break-up, it is suggested that disturbances are minimal close to the orifice and grow as they travel down the jet (Leib and Goldstein, 1986). Keller et al. (1973) developed a spatial instability analysis that describes the wave growing spatially rather than temporally, therefore the wave amplitude is zero at $z = 0$ and grows with z until a break-up point is reached. In spatial instability analysis there is a complex wavenumber, $k = k_r + ik_i$, where k_i is the spatial growth rate and k_r is the wavenumber, λ is considered to be purely imaginary and represents the frequency. In their analysis they found that there are infinitely many unstable modes. They found that Rayleigh's results are relevant only in the case of large Weber numbers; this explains why Rayleigh and others found such good agreement when comparing their results with experimental data for high speed jets. They also found that the spatial modes of a liquid jet are related to Rayleigh's temporal modes. Keller et al. (1973) also found, for Weber numbers less than the order of one, a new mode of faster-growing disturbances, whose wavelengths are so long that they may not be actually observable.

Leib and Goldstein (1986) showed that this new mode corresponds to absolute instability. The unstable disturbances in an absolutely unstable jet propagate in both upstream and downstream directions. Thus, the unstable disturbances expand in space over the course of time. Several authors have remarked on a singularity at $\mathcal{W}e = 1$ (Baird and Davidson, 1962; Finnicum et al., 1993; Ramos, 1996)

Non-linear dynamics of break-up

Linear stability analysis assumes that a liquid jet should break uniformly along its axis, with each droplet forming over a wavelength of the initial disturbance. However, as has been noted experimentally, this is not the case and a number of smaller satellite droplets are observed to arise through the nonlinearity of break-up. As break-up is approached the radius tends to zero locally and the description in terms of a radius function breaks down. Hence, the equations must develop a singularity at that point.

An attempt to use higher order perturbation theory (Chaudhary and Maxworthy, 1980a; Chaudhary and Redekopp, 1980) gives only a qualitative prediction of the unequal drop sizes, but is not able to describe the shape of the fluid anywhere close to pinch-off. This is not surprising as the characteristic time of the linear instability is close to the time distance from the singularity, where expansions in the radius and the velocity are bound to break down (Eggers and Dupont, 1994). Only gradually have the theoretical tools evolved that allow for a full description of the non-linear dynamics of break-up.

The three-dimensional equations describing the non-linear motion of a free surface flow are very complicated, both analytically and numerically. Becker et al. (1991) managed to produce simulations of axisymmetric drops when the flow is irrotational and inviscid. However, even with these restrictions on the flow, simulations close to the singularity become extremely costly, due to high resolutions needed in neck regions near the singularity. For this reason a reduction of the problem to a one-dimensional approximation helps save on computational time, making closeups of the singularity possible.

Lee (1974) considers the non-uniform break-up of an inviscid liquid jet. He was able to calculate the profile of the jet at break-up and estimate both the main and satellite drop sizes.

The equations of Lee (1974) were further investigated to study satellite behaviour by Pimbley and Lee (1977), who performed a systematic analysis of merging scenarios for satellite droplets. The limitations of Lee's equations is that viscosity, no matter how small, will become important in the pinch off process (Eggers, 1997). The analogous one-dimensional viscous case has been investigated by Bousfield and Denn (1987). Green (1976) derived equations that included viscosity, but he did not start from the equations of motion, but used a different method. This method involved obtaining one-dimensional approximations, based on integrating the equations of motion over a slice of the fluid. The leading-order versions of this procedure lead to the so-called Cosserat equations. Bogy (1979) investigated the linear stability of the Cosserat equations.

Schulkes (1993) used finite-element methods to compare various inviscid models, namely, the full potential-flow equations for inviscid and irrotational flow, the inviscid Cosserat equations, and the model of Lee (1974). He found considerable differences between the three cases, probably because, as shown by Eggers and Dupont (1994), inviscid models become inconsistent before break-up occurs.

Eggers and Dupont (1994) investigated the break-up of a viscous liquid jet, which included a detailed analysis of the pinch singularity and the bifurcation of a drop suspended from an orifice. Good agreement was found when simulations of drops of water suspended from an orifice were compared to the experimental results of Peregrine et al. (1990). This was the first quantitative comparison of a one-dimensional model with experiment.

The numerical code developed by Eggers and Dupont (1994) has been subsequently refined in several directions. Shi et al. (1994) used a dynamically evolving grid and Brenner et al. (1997) treated liquids with very low viscosities. Special care had to be taken, since the lack of viscous damping made the solution sensitive to perturbations. This analysis of the behavior at small viscosities was augmented by quantitative experiments.

Other contributions include those of Hilbing and Heister (1996) who developed a boundary element method to investigate the non-linear evolution and droplet formation of a straight liquid jet emerging from an orifice, in the absence of gravity, up to the point of pinch-off. They

predicted the size and formation of both main and satellite drops, taking into account the effects of velocity perturbations, wavenumbers and Weber number. They found that the break-up mode depends very sensitively on the amplitude of the initial perturbation. Encouraging agreement with the experiments of Moses et al. (1995) was found.

The main aim of Rutland and Jameson (1971) was to use the non-linear analysis of Yuen (1968) to calculate the profile of the waves on the jet at break-up and use this to predict the size of both main and satellite droplets. They found that, in general, there was good agreement between their experiments and the theory of Yuen (1968). However, their experiments also revealed satellite droplets forming through a range of wavenumbers, specifically at wavenumbers greater than 0.7, contrary to the non-linear theory.

Chaudhary and Redekopp (1980) show theoretically that satellite droplets can be reduced by introducing a secondary harmonic. This was tested by Chaudhary and Maxworthy (1980a,b), who used a piezoelectric transducer and compared the theory with experiments, both before and after break-up.

2.3.2 Curved liquid jets

Whilst there is an abundance of literature on straight jets, this work is not directly applicable to the study of more complex jet configurations where the trajectory of the jet is curved, for which there is a comparative scarcity of published material.

Keller and Weitz (1957) examined a two-dimensional steady liquid sheet curved by gravity. They found that including surface tension causes the sheet to fall more sharply than the trajectory of a sheet with no surface tension. They also found that at a Weber number of less than one, the sheets rise instead of fall. Keller and Geer (1973) analysed a curved, slender liquid sheet with both free and solid boundaries. They developed an asymptotic model using the slenderness of the stream to determine thin steady two-dimensional flows under the effect of gravity. Tuck (1976) determined the shape of a slender jet of water falling under gravity, without surface tension. He considered both a vertically falling jet and a curved jet that initially rises to a peak before falling under gravity. The trajectory of the curved liquid jet was found to be ballistic

because surface tension was neglected. This study produced results that agreed with the work of Keller and Geer (1973) for a two-dimensional sheet of water.

Dias and Vanden-Broeck (1990) considered numerically a steady two-dimensional potential free surface flow of an inviscid incompressible fluid emerging from a nozzle and falling under gravity, where the nozzle was aimed at an angle above the horizontal. Accurate results for the free surface profiles are presented. Finnicum et al. (1993) investigated, both theoretically and experimentally, the effect of applied pressure on a two-dimensional liquid curtain falling under gravity, including the effects of surface tension. They obtained an approximate equation for the location of the curtain and their theoretical predictions were in good agreement with the experimental work. More recently, Moulitsas and Georgiou (2009) numerically solved the steady two-dimensional flow of a planar Newtonian curtain issuing from a slit, taking into account gravity and surface tension effects, but only qualitative agreement was found with the experiments of Finnicum et al. (1993).

The work of Hohman et al. (2001) focuses on the process of electrospinning and analyses the mechanics of a whipping jet by examining the instability of an electrically forced fluid jet with increasing field strength. Cummings and Howell (1999) investigated nearly straight slender viscous fluid fibres. Other investigations on curved liquid jets and sheets include those of Vanden-Broeck and Keller (1982), Entov and Yarin (1984) and Yarin (1993). The investigations of Entov and Yarin allow for an arbitrary position of the centreline of the jet. In a similar vein, Dewynne et al. (1992, 1994) derived, by a systematic perturbation method, equations governing the motion of a slender viscous fibre, where no assumption was made either that the fibre is straight, or that its cross-section is of constant shape.

A mathematical formulation of the curved jet prilling problem for an inviscid fluid was introduced by Wallwork et al. (2002), who developed a linear instability analysis model to investigate a slender jet subjected to both rotational and surface tension forces. To obtain the jet curvature, a novel curved variant of the cylindrical polar co-ordinates was introduced. Details of this co-ordinate system, along with details of any models used in this thesis, can be found in the next section. Decent et al. (2002) extended this model to include the effects of gravity

and the inclusion of Newtonian viscosity was introduced by Decent et al. (2009), who used a temporal and spatial stability analysis to determine break-up lengths and drop sizes.

Detailed below is some of the current work by the Centre for Mathematical Modelling and Chemical Engineering at the University of Birmingham, on the break-up of curved liquid jets, concerning the calculation of the jet's centreline, linear stability and non-linear analysis.

Problem Formulation

To model the prilling process a large, vertical cylindrical drum of radius s_0, rotating about its axis with angular velocity Ω, is considered. A liquid jet emerges from a small circular orifice of radius a, situated on the curved surface of the drum.

The problem is examined by considering a co-ordinate system (x, y, z) rotating with the drum, having an origin on the axis of the drum and with the position of the orifice at $(0, 0, 0)$. The x-axis is in the direction normal to the surface of the drum in the initial direction of the jet and the z-axis orthogonal to the x-axis in the plane of the centreline of the jet. The positive z-axis points in the direction opposite to the motion of the drum. The positive y-axis points vertically upwards and is orientated in the direction opposite to gravitational acceleration. A graphical description of the x, y and z co-ordinates are shown in Figure 2.11.

The rotation of the drum causes the jet to curve on leaving the orifice and an analysis of the jet in (x, y, z) plane becomes cumbersome. Therefore, by introducing the co-ordinate system previously used by Wallwork et al. (2002) it is possible to work in a rotating reference frame in which the orifice is fixed. A curvilinear co-ordinate system (s, n, ϕ) is used, where s is the arclength along the centreline of the jet, measured from the orifice, and (n, ϕ) are plane polar co-ordinates in any section of the jet. The origin for the (s, n, ϕ) co-ordinate system is at the centre of the orifice on the surface of the drum. The associated unit vectors are denoted by $\mathbf{e_s}$, $\mathbf{e_n}$ and $\mathbf{e}_\phi$ respectively and are shown in Figures 2.12 and 2.13.

The centreline of the jet can be written in summation notation as $\mathbf{r}_{cl} = X_i\mathbf{e_i}$, for $i = 1..3$. Here $\mathbf{e}_1 = \mathbf{i}, \mathbf{e}_2 = \mathbf{j}$ and $\mathbf{e}_3 = \mathbf{k}$, where $\mathbf{i}, \mathbf{j}$ and $\mathbf{k}$ are unit vectors in Cartesian co-ordinates and $X_1 = X, X_2 = Y$ and $X_3 = Z$. The unit vectors in this co-ordinate system are calculated using a principal normal vector $\mathbf{p}$ and a binormal vector $\mathbf{b}$ to the centreline (shown in Figure 2.13).

Using summation notation the principal normal vector is defined as

$$\mathbf{p} = \frac{\mathbf{e_{s}}_{,s}}{|\mathbf{e_{s}}_{,s}|} \tag{2.5}$$

and the binormal vector as

$$\mathbf{b} = \mathbf{p} \times \mathbf{e_s}. \tag{2.6}$$

In the following subscripts in s are derivatives with respect to s and i, j, k and l are used for summation notation. As

$$\mathbf{e_s} = X_{i,s}\mathbf{e_i},$$

it can be seen that

$$\mathbf{p} = \frac{X_{i,ss}\mathbf{e_i}}{\sqrt{X_{j,ss}X_{j,ss}}}$$

and

$$\mathbf{b} = \frac{\varepsilon_{ijk}X_{j,ss}X_{k,s}\mathbf{e_i}}{\sqrt{X_{l,ss}X_{l,ss}}},$$

where the Levi-Civita symbol, ε_{ijk}, has its usual meaning. It is possible to describe our plane polar co-ordinates as

$$\begin{aligned}
\mathbf{e_n} &= \cos\phi\mathbf{p} + \sin\phi\mathbf{b} \\
&= = \frac{1}{\sqrt{X_{l,ss}X_{l,ss}}}\left(\cos\phi X_{i,ss} + \sin\phi\ \varepsilon_{ijk}X_{j,ss}X_{k,s}\right)\mathbf{e_i} \\
\mathbf{e_\phi} &= -\sin\phi\mathbf{p} + \cos\phi\mathbf{b} \\
&= \frac{1}{\sqrt{X_{l,ss}X_{l,ss}}}\left(-\sin\phi X_{i,ss} + \cos\phi\ \varepsilon_{ijk}X_{j,ss}X_{k,s}\right)\mathbf{e_i}
\end{aligned}$$

It is straightforward to show these form an orthogonal co-ordinate system and their derivation is explained further in Decent et al. (2002), Wallwork (2001) and Uddin (2007). The position vector of any particle, Q, relative to the orifice, O, on the free surface is given by $\mathbf{r} = \int_0^s \mathbf{e_s}ds + n\mathbf{e_n}$.

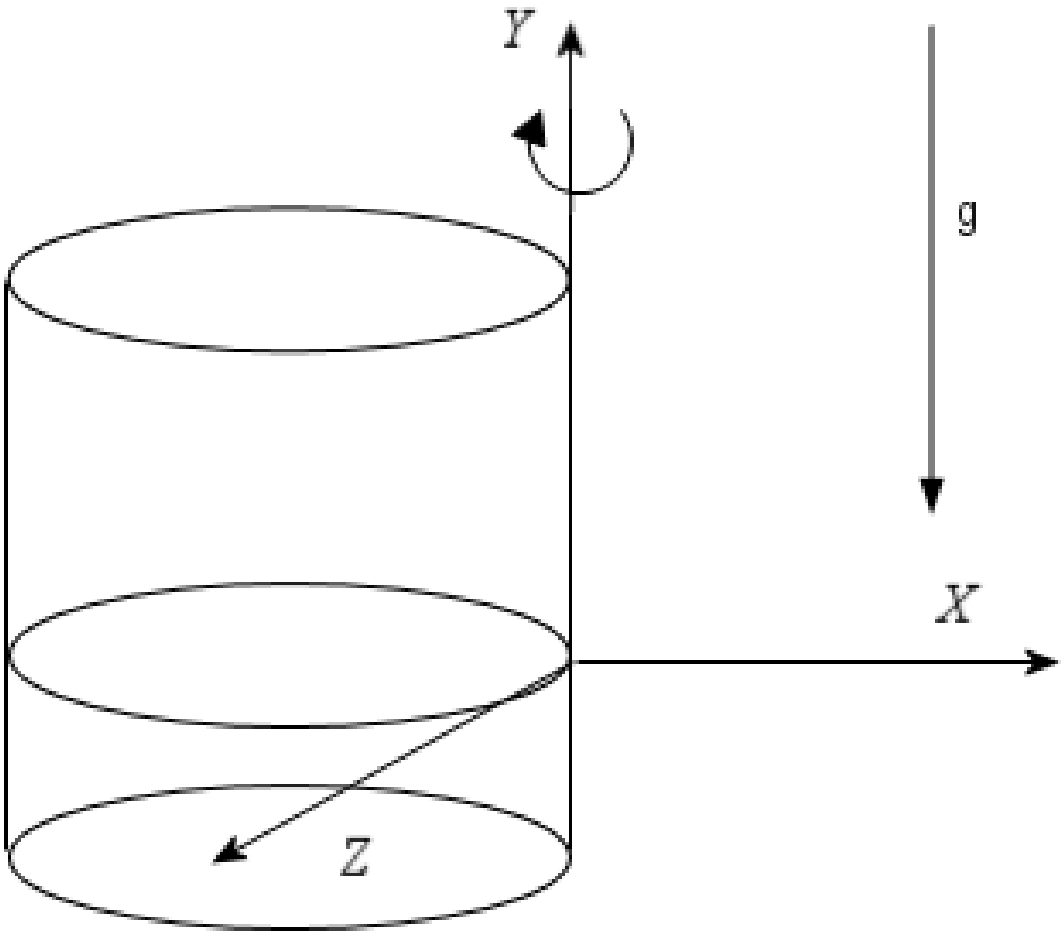

Figure 2.11: Sketch of the drum showing the fixed co-ordinate system and the directions of rotation and gravity.

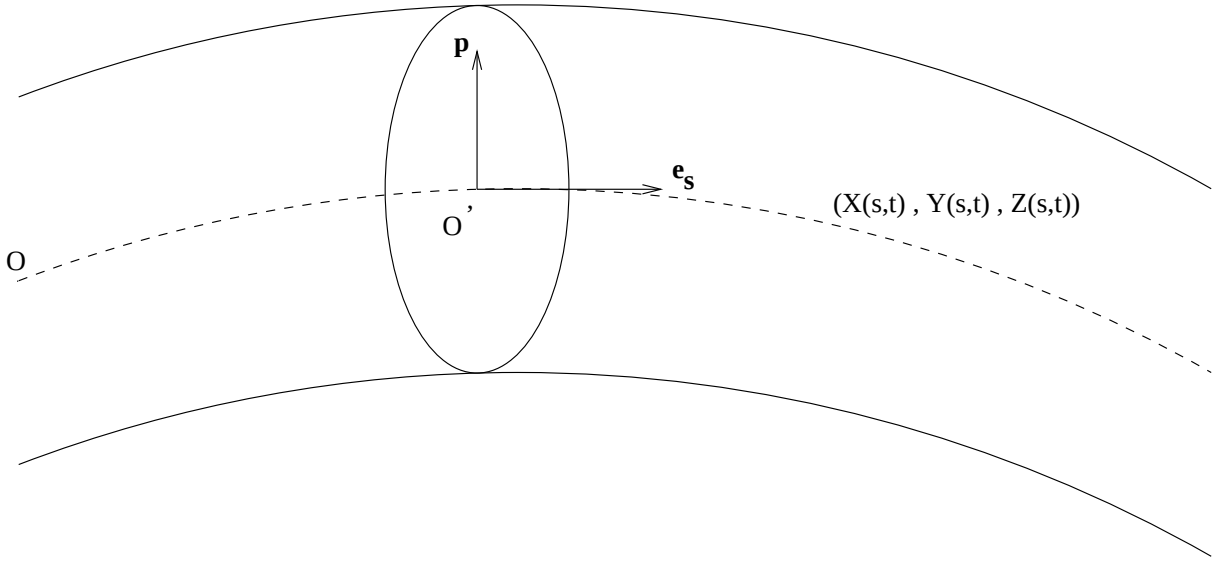

Figure 2.12: Sketch of a curved jet in the (X, Y, Z) plane.

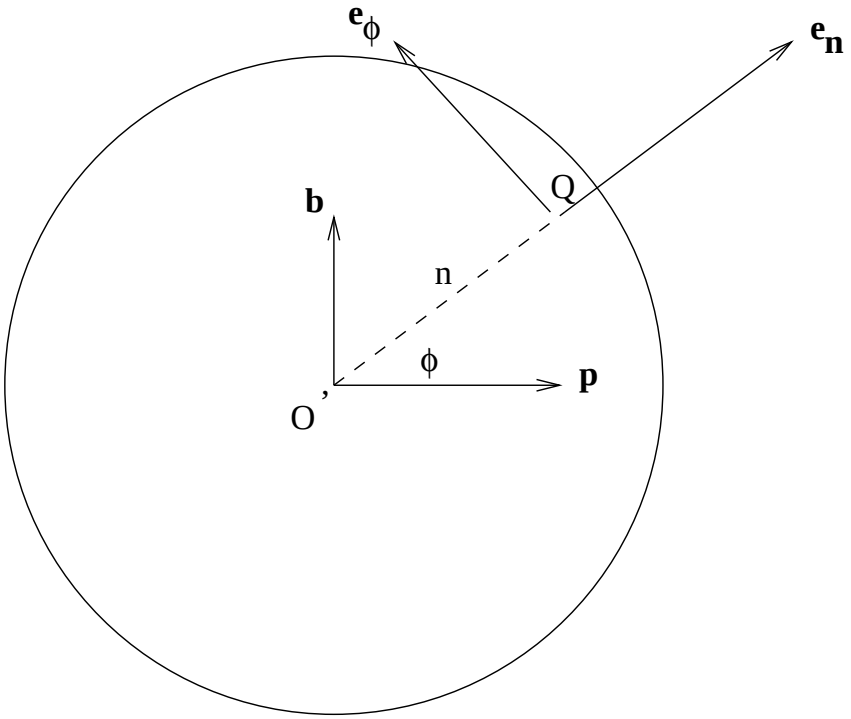

Figure 2.13: Cross-section of a curved jet

The effects of gravity on the jet can be neglected if the centripetal acceleration of the jet, $s_0\Omega^2$, where Ω is the rotation of the drum (rad s^{-1}), is much greater than the acceleration due to gravity, g, acting in the negative y direction, as is the case with industrial prilling. Thus the jet's centreline is assumed to lie solely in the $x-z$ plane and the centreline of the jet is given by $(X(s,t),0,Z(s,t))$ in Cartesian co-ordinates, where t is the time and X and Z are functions to be found. The impact of gravity has been investigated by Wallwork (2001), Decent et al. (2002) and Partridge (2006).

Equations of motion

The flow is described using the velocity vector $\mathbf{u} = u\mathbf{e}_s + v\mathbf{e}_n + w\mathbf{e}_\phi$ to arrive at the familiar equations of motion given by

$$\rho\left(\frac{\partial \mathbf{u}}{\partial t} + \mathbf{u}\cdot\nabla\right) = -\nabla p + \nabla\cdot\boldsymbol{\tau} - 2\boldsymbol{\omega}\times\mathbf{u} - \boldsymbol{\omega}\times(\boldsymbol{\omega}\times\mathbf{r}'), \tag{2.7}$$

$$\nabla\cdot\mathbf{u} = 0, \tag{2.8}$$

where ρ is the constant density of the fluid, p is the pressure within the jet, $\mathbf{r}'$ denotes the position vector in the (x,y,z) co-ordinate system, $\mathbf{r}' = \mathbf{r} + s_0\mathbf{i}$, $\boldsymbol{\tau}$ is the stress tensor, and $\boldsymbol{\omega} = \Omega\mathbf{j}$ is the angular velocity within the drum.

The free surface of the jet is described by the equation $n - R(s,t,\phi) = 0$, where $R(s,t,\phi)$ is a function giving the free surface position, and a normal vector to this surface is given by $\nabla(n - R(s,t,\phi))$. When evaluated this gives the unit normal vector as

$$\mathbf{n} = \frac{1}{E}\left(-\frac{\partial R}{\partial s}\cdot\frac{1}{h_s}\cdot\mathbf{e}_s + \mathbf{e}_n - \frac{\partial R}{\partial \phi}\cdot\frac{1}{R}\cdot\mathbf{e}_\phi\right), \tag{2.9}$$

where

$$E = \left(1 + \left(\frac{\partial R}{\partial s}\right)^2\cdot\frac{1}{h_s^2} + \left(\frac{\partial R}{\partial \phi}\right)^2\cdot\frac{1}{R^2}\right)^{\frac{1}{2}} \tag{2.10}$$

and

$$h_s = 1 + n\cos\phi(X_sZ_{ss} - Z_sX_{ss}). \tag{2.11}$$

The normal stress condition is given by

$$\mathbf{n} \cdot \Pi \cdot \mathbf{n} = \sigma\kappa,$$

where σ is the isotropic surface tension, Π is the total stress tensor defined by $-p\mathbf{I} + \tau$, with $\mathbf{I}$ being the second order identity tensor and τ the stress tensor. κ is the curvature of the free surface,

$$\kappa = \frac{1}{nh_s}\left(\frac{\partial}{\partial s}\left(\frac{-\frac{n}{h_s}\frac{\partial R}{\partial s}}{E}\right) + \frac{\partial}{\partial n}\left(\frac{nh_s}{E}\right) + \frac{\partial}{\partial \phi}\left(\frac{-\frac{h_s}{n}\frac{\partial R}{\partial \phi}}{E}\right)\right).$$

Using the two tangent vectors to the free surface, $\mathbf{t}_1 = \partial\mathbf{r}/\partial s$ and $\mathbf{t}_2 = \partial\mathbf{r}/\partial\phi$, the tangential stress conditions are given by

$$\mathbf{t}_i \cdot \Pi \cdot \mathbf{n} = 0 \quad \text{for} \quad i = 1, 2.$$

The kinematic condition is given by

$$\frac{D}{Dt}(R(s,t,\phi) - n) = 0 \quad \text{for} \quad n = R(s,\phi,t).$$

To close our system of equations an arc length condition is required

$$X_s^2 + Z_s^2 = 1.$$

The equations are non-dimensionalised using the following transformations

$$\begin{aligned} \bar{u} = \frac{u}{U}, \bar{v} = \frac{v}{U}, \bar{w} = \frac{w}{U}, \bar{p} = \frac{p}{\rho U^2}, \bar{n} = \frac{n}{a}, \epsilon = \frac{a}{s_0}, \\ \bar{R} = \frac{R}{a}, \bar{s} = \frac{s}{s_0}, \bar{t} = \frac{tU}{s_0}, \bar{X} = \frac{X}{s_0}, \bar{Z} = \frac{Z}{s_0}, \end{aligned} \tag{2.12}$$

where U is the exit speed of the jet in the rotating frame, ϵ is the small aspect ratio, R is the jet radius and u, v and w are the tangential, radial and azimuthal velocity components relative to the centreline of the jet respectively. The bars denote dimensionless quantities in the above

expressions. As $a << s_0, \epsilon << 1$ and can be considered a small parameter, providing the basis for a slender jet assumption. Substituting these scalings into our dynamical equations it is possible to obtain the full set of expressions representing the behaviour of a curved jet. These can be found in Wallwork et al. (2002) and Wallwork (2001).

The exit radius of the jet is taken to be equal to the radius of the orifice, a, so in non-dimensional variables the orifice conditions are

$$X_s = 1, X = Z = Z_s = 0, R_0 = u_0 = 1 \text{ at } s = 0. \tag{2.13}$$

Asymptotic form of the steady-state solutions

The steady jet asymptotic expansions for u, v, p, R, X, Z from Wallwork et al. (2002) are applied; w is taken to be zero, so that there is no velocity component in the azimuthal direction. The expansions are

$$\begin{aligned}
\boldsymbol{u} &= u_0(s) + \epsilon \boldsymbol{u_1}(s, n, \phi) + O(\epsilon^2), \\
p &= p_0(s, n, \phi) + \epsilon p_1(s, n, \phi) + O(\epsilon^2), \\
R &= R_0(s) + \epsilon R_1(s, \phi) + O(\epsilon^2), \\
\boldsymbol{X} &= \boldsymbol{X_0}(s) + \epsilon \boldsymbol{X_1}(s, \phi) + O(\epsilon^2),
\end{aligned}$$

where $\boldsymbol{u_i} = u_i \mathbf{e_s} + v_i \mathbf{e_n}$ and $\boldsymbol{X_i} = X_i \mathbf{i} + Z_i \mathbf{k}$ for $i = 0, 1, \ldots$. To leading order, velocity appears solely in the $\mathbf{e_s}$ direction. For simplicity of notation the leading-order components X_0 and Z_0 are rewritten as X and Z.

This resulting system of equations is as follows

$$p_0 = \frac{1}{R_0 \mathcal{W}e}, \tag{2.14}$$

$$u_0 = \left(1 + \frac{1}{\mathcal{R}b^2}\left(X^2 + 2X + Z^2\right) + \frac{2}{\mathcal{W}e}\left(1 - \frac{1}{R_0^2}\right)\right)^{1/2}, \tag{2.15}$$

$$p_1 = \frac{n}{\mathcal{W}eR_0}\cos\phi\,(X_sZ_{ss} - X_{ss}Z_s) + h_1(s), \tag{2.16}$$

$$v_1 = -\frac{n}{2}\frac{du_0}{ds}, \tag{2.17}$$

$$Z_{ss} = \frac{WeR_0X_s}{WeR_0u_0^2 - 1}\left(\frac{2u_0}{\mathcal{R}b} + \frac{ZX_s - (X+1)Z_s}{\mathcal{R}b^2}\right), \tag{2.18}$$

$$\frac{dR_0}{ds} = -\frac{WeR_0((X+1)X_s + ZZ_s)}{\mathcal{R}b^2(2WeR_0u_0^2 + 1)}, \tag{2.19}$$

$$X_s^2 + Z_s^2 = 1. \tag{2.20}$$

Equations (2.18), (2.19) and (2.20) give rise to a set of non-linear ordinary differential equations for X, Z and R_0. The system of equations can be solved numerically in MATLAB using a Runge Kutta method subject to the non-dimensional boundary conditions $X_s = 1, X = Z = Z_s = 0, u_0 = R_0 = 1$ at $s = 0$. The solutions are discussed in detail in Wallwork et al. (2002).

In Decent et al. (2009), this work was extended to include the effects of viscosity. While the steady ordinary differential equations (ODEs) found appear different to those of Wallwork et al. (2002), Decent et al. (2009) showed that at leading-order the same trajectory is found as in the inviscid case given by Wallwork et al. (2002). Viscosity does not affect the steady solution at leading-order, except in a viscous correction to p_1, which does not affect the leading-order trajectory, velocity, pressure or jet radius. This means that the slender jet approximation in the viscous case results in no shear across the jet, except at higher-order.

Linear stability analysis

Wallwork et al. (2002) performed a linear stability analysis for an inviscid rotating jet. This was extended to include the effects of gravity in Decent et al. (2002) and viscosity in the absence of gravity in Decent et al. (2009). The steady state is perturbed, using a small dimensionless parameter, δ, such that $0 < \delta \ll \epsilon \ll 1$, which measures the size of the unsteady disturbances

as in Wallwork et al. (2002).

$$\begin{aligned} \boldsymbol{u} &= \bar{\boldsymbol{u}} + \delta\tilde{\boldsymbol{u}}(s,\bar{s},t,\bar{t},n,\phi), \\ p &= \bar{p} + \delta\tilde{p}(s,\bar{s},t,\bar{t},n,\phi), \\ R &= \bar{R} + \delta\tilde{R}(s,\bar{s},t,\bar{t},\phi), \\ \boldsymbol{X} &= \bar{\boldsymbol{X}} + \delta\epsilon\tilde{\boldsymbol{X}}(s,\bar{s},t,\bar{t}), \end{aligned} \tag{2.21}$$

where $(\bar{\boldsymbol{u}},\tilde{\boldsymbol{u}}) = (\bar{u},\tilde{u})\boldsymbol{e_s} + (\bar{v},\tilde{v})\mathbf{e_n} + (\bar{w},\tilde{w})\mathbf{e}_{\boldsymbol{\phi}}$, $(\bar{\boldsymbol{X}},\tilde{\boldsymbol{X}}) = (\bar{X},\tilde{X})\mathbf{i} + (\bar{Z},\tilde{Z})\mathbf{k}$ (it should be noted that in Decent et al. (2009), the following expansion was first tried: $\boldsymbol{X} = \bar{\boldsymbol{X}} + \delta\widetilde{\boldsymbol{X}_\mathbf{0}}(s,\bar{s},t,\bar{t}) + \delta\epsilon\tilde{\boldsymbol{X}}(s,\bar{s},t,\bar{t})$, but $\widetilde{\boldsymbol{X}_\mathbf{0}}$ was found to be identically equal to zero). These linear perturbations disturb the basic steady solution (denoted by a quantity with an overbar in (2.21)), which are functions of s,n,ϕ, by unsteady quantities which are functions of $s,\bar{s},t,\bar{t},n$ and ϕ, where $\bar{s} = s/\epsilon$ is a short lengthscale and $\bar{t} = t/\epsilon$ is a small timescale associated with short wave-like disturbances (the unsteady perturbations are denoted by variables with a tilde). Therefore the small unsteady components allow motion on a short length scale which scales with the orifice a. These equations are substituted into the equations of motion and linearised in the unsteady quantities (taking terms of $O(\delta)$). The terms of $O(1)$ in δ yield the steady state equations (2.14) - (2.20). Solutions are looked for in modes of the form

$$\begin{aligned} \tilde{\boldsymbol{u}} &= \hat{\boldsymbol{u}}(s,n,\phi,t)\text{exp}(ik(s)\bar{s} + \lambda(s)\bar{t}) + c.c., \\ \tilde{p} &= \hat{p}(s,n,\phi,t)\text{exp}(ik(s)\bar{s} + \lambda(s)\bar{t}) + c.c., \\ \tilde{R} &= \hat{R}(s,\phi,t)\text{exp}(ik(s)\bar{s} + \lambda(s)\bar{t}) + c.c., \\ \tilde{\boldsymbol{X}} &= \hat{\boldsymbol{X}}(s,t)\text{exp}(ik(s)\bar{s} + \lambda(s)\bar{t}) + c.c., \end{aligned} \tag{2.22}$$

where $\hat{\boldsymbol{u}} = \hat{u}\mathbf{e_s} + \hat{v}\mathbf{e_n} + \hat{w}\mathbf{e}_{\boldsymbol{\phi}}$, $\hat{\boldsymbol{X}} = \hat{X}\mathbf{i} + \hat{Z}\mathbf{k}$, $c.c.$ denotes complex conjugate, $k(s)$ is the wavenumber and $\lambda(s)$ is the wave frequency. The wavenumber and frequency are assumed to vary along the length of the jet, which is not the case for straight jets. Looking for solutions by expanding the remaining unknowns (in the variables with 'hats') in Fourier series in ϕ, it is possible to find a countably infinite set of eigenvalue relationships, each associated with $\cos(n\phi)$

or $\sin(n\phi)$, for each integer, n. After some considerable algebra it can be determined that these are stable modes for $n \geq 1$, plus one unstable mode, corresponding to $n = 0$, which, for the viscous case (Decent et al., 2009), has the following eigenvalue relation

$$\begin{aligned}
\mathcal{W}e^{3/2}R_0^2\lambda^2\ k^2 I_0(kR_0)I_1(\tilde{k}R_0) &+ \mathcal{W}e^{3/2}R_0^2\lambda^2\ \tilde{k}^2 I_0(kR_0)I_1(\tilde{k}R_0) \\
+2i\mathcal{W}e^{3/2}R_0^2\lambda\ k^3 I_0(kR_0)I_1(\tilde{k}R_0) &+ 2i\mathcal{W}e^{3/2}u_0\lambda R_0^2\ k\tilde{k}^2 I_0(kR_0)I_1(\tilde{k}R_0) \\
-\mathcal{W}e^{3/2}R_0^2u_0^2\ k^4 I_0(kR_0)I_1(\tilde{k}R_0) &- \mathcal{W}e^{3/2}R_0^2u_0^2\ k^2\tilde{k}^2 I_0(kR_0)I_1(\tilde{k}R_0) \\
+2\mathcal{O}h\mathcal{W}eR_0^2\lambda\ k^4 I_0(kR_0)I_1(\tilde{k}R_0) &+ 2\mathcal{O}h\mathcal{W}eR_0\lambda\ k^3 I_1(kR_0)I_1(\tilde{k}R_0) \\
+2\mathcal{O}hWeR_0^2\lambda\ k^2\tilde{k}^2 I_0(kR_0)I_1(\tilde{k}R_0) &- 2\mathcal{O}h\mathcal{W}eR_0\lambda\ k\tilde{k}^2 I_1(kR_0)I_1(\tilde{k}R_0) \\
-4\mathcal{O}h\mathcal{W}e\lambda\ k^3\tilde{k} I_1(kR_0)I_0(\tilde{k}R_0) &+ 2i\mathcal{O}hWeR_0^2u_0\ k^5 I_0(kR_0)I_1(\tilde{k}R_0) \\
+2i\mathcal{O}h\mathcal{W}eR_0u_0\ k^4 I_1(kR_0)I_1(\tilde{k}R_0) &+ 2i\mathcal{O}hWeR_0^2u_0\ k^3\tilde{k}^2 I_0(kR_0)I_1(\tilde{k}R_0) \\
-2i\mathcal{O}h\mathcal{W}eR_0u_0\ k^2\tilde{k}^2 I_1(kR_0)I_1(\tilde{k}R_0) &- 4i\mathcal{O}h\mathcal{W}eR_0^2u_0\ k^4\tilde{k} I_1(kR_0)I_0(\tilde{k}R_0) \\
-\sqrt{\mathcal{W}e}\ k\tilde{k}^2 I_1(kR_0)I_1(\tilde{k}R_0) &+ \sqrt{\mathcal{W}e}\ k^3 I_1(kR_0)I_1(\tilde{k}R_0) \\
+\sqrt{\mathcal{W}e}R_0^2\ k^3\tilde{k}^2 I_1(kR_0)I_1(\tilde{k}R_0) &- \sqrt{\mathcal{W}e}R_0^2\ k^5 I_1(kR_0)I_1(\tilde{k}R_0) = 0
\end{aligned} \tag{2.23}$$

where

$$\tilde{k} = \sqrt{k^2 + \frac{\mathcal{W}e^{1/2}(\lambda + iku_0)}{\mathcal{O}h}}, \tag{2.24}$$

and I_n is the modified Bessel function of order n. Note for this mode $\tilde{w} = 0$. Here, R_0 and u_0 are functions of arclength, s, and depend upon the rotation parameter $\mathcal{R}b$. This relation is equivalent to (2.3), where $u_0 = R_0 = 1$. Wallwork et al. (2002) derived an analogous relation to (2.1) for the inviscid case.

Equation (2.23) can be interpreted both in terms of temporal and spatial stability, more detail can be found in Decent et al. (2009).

Adopting a temporal instability, k is real and λ is complex, where $\lambda = \lambda_r + i\lambda_i$. If $\lambda_r < 0$, this indicates instability. The most unstable wavenumber $k^*(s)$ is the value of k at which the growth rate λ_r is at a maximum. This can be found by examining a long wavelength approxi-

mation ($k \to 0$) of (2.23):

$$k^*(s) = \frac{1}{2^{1/4} R_0^{3/4}(s) \sqrt{\sqrt{2R_0(s)} + 3\mathcal{O}h}}. \tag{2.25}$$

If a spatial stability approach is adopted with $\lambda = -i\omega$ and $k = k_r + ik_i$, ω is a real frequency and instability occurs when $k_i < 0$. Here $k^*(s)$ is the most unstable wavenumber given by (2.23), so is the value or k_r which corresponds to a minimum in k_i. Equation (2.23) is solved numerically for $k^*(s)$ using values of $R_0(s)$ and $u_0(s)$ from the ODEs found in Decent et al. (2009).

The size of the main droplet is predicted by integrating over a wavelength at the point of break-up. The dimensional wavelength of the disturbance is given by $\lambda_\omega = 2\pi a/k^*(s)$, where $k^*(s)$ is the most unstable wavenumber given by (2.23).

Integrating over a volume of revolution

$$V_{\text{drop}} = \pi \int R_0^2 ds, \tag{2.26}$$

where R takes values of $R_0(s)$, gives the volume of the droplet. Hence the drop radius, $\hat{R}$ can be equated to a sphere so that

$$\hat{R} = \left(\frac{3V_{\text{drop}}}{4\pi} \right)^{\frac{1}{3}}. \tag{2.27}$$

It is possible to generate a drop at any point along the jet, using values of $u_0(s)$ and $R_0(s)$. If the length of break-up is given by s_b, the drop size is calculated using $u_0(s_b)$ and $R_0(s_b)$.

In summary, in Decent et al. (2009), it was found that the trajectory and steady state of a liquid jet emerging from a rotating drum is only slightly affected by viscosity, but the instability process is dominated by viscosity and surface tension. Good agreement was obtained between theoretical and experimental data.

Non-linear dynamics

Whilst linear stability theory for curved jets allowed for the prediction of the trajectory of the curved jet and the break-up length, it is only effective in describing the evolution of the jet as

pinch off is approached, and the actual break-up of liquid jets and the subsequent formation of satellite drops is again dominated by non-linear effects.

Non-linear effects have been considered for both inviscid and viscous Newtonian jets by Părău et al. (2006) and Părău et al. (2007) respectively. The results showed good qualitative agreement with the jet trajectories and disturbances present on the jet surface measured by Wong et al. (2004).

The full model equations are perturbed by the following asymptotic expansions

$$\begin{aligned} \boldsymbol{u} &= u_0(s,t) + (\epsilon n)\boldsymbol{u_1}(s,\phi,t) + O(\epsilon^2), \\ p &= p_0(s,\phi,t) + (\epsilon n)p_1(s,\phi,t) + O(\epsilon^2), \\ R &= R_0(s,t) + \epsilon R_1(s,\phi,t) + O(\epsilon^2), \\ \boldsymbol{X} &= \boldsymbol{X_0}(s) + \epsilon \boldsymbol{X_1}(s,\phi,t) + O(\epsilon^2), \end{aligned} \tag{2.28}$$

where a steady centreline at leading order has been assumed. The following equations are obtained

$$R_{0t} + u_0 R_{0s} + \frac{u_{0s} R_0}{2} = 0, \tag{2.29}$$

$$u_{0t} + u_0 u_{0s} = -\frac{1}{\mathcal{W}e}\kappa_s + \frac{(X+1)X_s + ZZ_s}{\mathcal{R}b^2} + \frac{3}{\mathcal{R}e}\frac{(R_0^2 u_{0s})_s}{R_0^2}, \tag{2.30}$$

where κ is the curvature of the free surface.

The system of equations can be solved for our leading order velocity and radius, u_0 and R_0. The initial conditions at $t = 0$ are found to satisfy the following ODEs

$$\begin{aligned} u_0 u_{0s} = -\frac{1}{2\mathcal{W}e}\frac{u_{0s}}{\sqrt{u_0}} + \frac{(X+1)X_s + ZZ_s}{\mathcal{R}b^2} + \frac{3}{\mathcal{R}e}\left(u_{0ss} - \frac{u_{0s}^2}{u_0}\right), \\ (X_s Z_{ss} - Z_s X_{ss})\left(u_0^2 - \frac{3}{\mathcal{R}e}u_{0s} - \frac{\sqrt{u_0}}{\mathcal{W}e}\right) - \frac{2u_0}{\mathcal{R}b} + \frac{((X+1)Z_s - ZX_s)}{\mathcal{R}b^2} = 0, \\ X_s^2 + Z_s^2 = 1, \end{aligned} \tag{2.31}$$

where $R_0^2 u_0^2 = 1$ and the boundary conditions are $X(0) = Z(0) = Z_s(0) = 0$ and $X_s(0) =$

$u_0(0) = 1$ at $s = 0$. This system of equations can be solved for X and Z and for u, using Newton's method (see Părău et al., 2007, for more detail).

The non-linear evolution problem is given by

$$\begin{aligned} A_t + (Au)_s &= 0 \\ u_t + \left(\frac{u^2}{2}\right)_s &= -\frac{1}{\mathcal{W}e}\frac{\partial}{\partial s}\left(\frac{4(2A + (\epsilon A_s)^2 - \epsilon^2 A A_{ss})}{(4A + (\epsilon A_s)^2)^{3/2}}\right) + \frac{(X+1)X_s + ZZ_s}{\mathcal{R}b^2} \\ &+ \frac{3}{\mathcal{R}e}\frac{(Au_s)_s}{A}, \end{aligned} \tag{2.32}$$

where $A = R_0^2$ and the full curvature has been included, else the jet is unstable to infinitesimally short waves. The initial conditions at $t = 0$ are obtained from the steady state ODEs, namely

$$A(s, t = 0) = R_0^2(s), \qquad u(s, t = 0) = u_0(s) \tag{2.33}$$

where $R_0(s)$ and $u_0(s)$ are solutions of the ODEs (2.31). Also $X(s)$ and $Z(s)$ in the above evolution PDEs are obtained from the steady state ODEs (2.31).

Wave disturbances are imposed through the boundary conditions at the orifice $s = 0$

$$A(s = 0, t) = 1, \qquad u(s = 0, t) = 1 + \delta \sin\left(\frac{\kappa t}{\epsilon}\right), \tag{2.34}$$

where δ and κ are the amplitude and frequency of the perturbation at the orifice. The introduction of ϵ shows we are searching for fast waves because of the non-dimensionalisation used. Here δ is a measure of the size of the initial perturbation, and though we have the freedom to choose the size of δ, it is usual to choose a small perturbation[1]. By setting $\kappa = k^*$ where

$$k^* = \frac{1}{2^{1/4}\sqrt{\sqrt{2} + 3\mathcal{O}h}}, \tag{2.35}$$

the most unstable mode at the orifice is imposed from (2.25), since $R_0(s = 0) = 1$.

Break-up is chosen to occur when the jet radius reaches 5% of the jet's initial radius (this

[1]Decent et al. (2009) derived this condition as $\delta << 2^{1/4}/\sqrt{3OhWe}$.

remains consistent with previous work). This value of s is the break-up length s_b that is used to generate the linear drop size prediction. Non-linear drop sizes are calculated by integrating over the wavelength of the droplet produced at break-up, substituting values of $R(s,t)$ obtained from (2.32) into (2.26) and (2.27).

Părău et al. (2007) showed that there is little deviation from the inviscid centreline as viscosity increases. It is only for very small Reynolds numbers that the centreline becomes more tightly coiled. This was verified by Decent et al. (2009) who, by considering the linear instability of the steady state, showed that viscous terms only appear at higher order. It is possible to use the inviscid steady state equations as a good approximation to the viscous steady state centreline, and this has been used by many authors (Uddin et al., 2006, 2008a).

Părău et al. (2007) also considered an unsteady centreline

$$\boldsymbol{X} = \tilde{\boldsymbol{X}}(s) + \hat{\boldsymbol{X}}(s,t) + O(\epsilon). \tag{2.36}$$

The full equations were not solved but small perturbations of the steady centreline were considered and linearised in X and Z. Părău et al. (2007) showed that the maximum deviations from the steady centreline are of order 10^{-2} and are relatively small compared to $X_0(s)$ and $Z_0(s)$ hence the trajectory is effectively steady. However, the maximum deviation increases with viscosity, so for very viscous jets the centreline could be expected to be time-dependent, as was observed in experiments (see M4 in Wong et al., 2004). In that case Părău et al. (2007) suggested that the full equations should be solved in order to calculate the trajectory, u_0 and R_0.

2.3.3 Comparison between linear and non-linear theory for curved liquid jets

In Gurney (2010), the linear theory of Decent et al. (2009) and the non-linear theory of Părău et al. (2007) were compared in detail. As the production of satellite droplets is a non-linear phenomenon of break-up, only non-linear theory predicts the impact of satellite drops, therefore the comparison between the two theories is focused on the prediction of main drop sizes.

The two models are compared for a variety of parameters, in order to investigate the degree

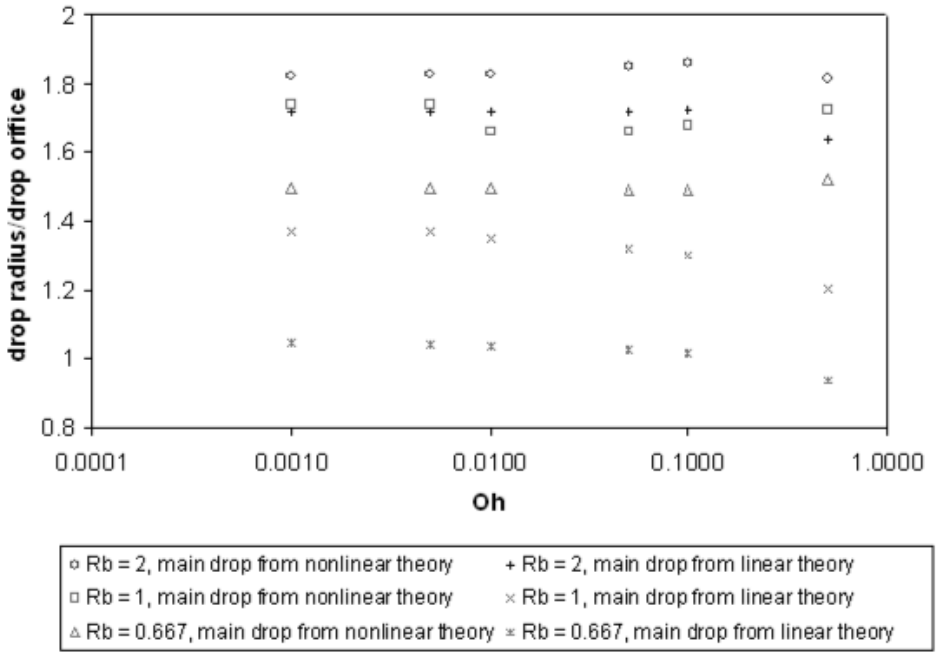

Figure 2.14: Main drop radii predictions using non-linear theory and linear theory for varying Ohnesorge number for different Rossby numbers, $\mathcal{W}e = 50, \delta = 0.01, \epsilon = 0.01$. κ varies with $\mathcal{O}h$. Figure taken from Gurney et al. (2010).

to which the two results differ. Figure 2.14, which is taken from Gurney et al. (2010), shows that both models predict similar drop sizes for low values of the Ohnesorge number, but the theories differ to their greatest extent for a larger Ohnesorge number and a smaller Rossby numbers, so in the case of a more viscous fluid at higher rotation rates. The two theories also appear to exhibit different trends for changing Ohnesorge number, although this is a weak dependence. For a more detailed comparison the reader is referred to Gurney (2010).

2.4 Comparison between theoretical and experimental work for curved liquid jets

This section outlines work done in Gurney et al. (2010), to see if the numerical simulations exhibit the same behaviour and generate droplets of a similar size to those identified experimentally.

Both Wong et al. (2004) and Partridge et al. (2005) identified a flow map of the Ohnesorge number against the Weber number, which enabled characterisation of jet break-up and M1-M4

to be predicted within the given parameter ranges. Gurney et al. (2010) used the non-linear model to predict the mode boundaries of Partridge et al. (2005). The results of this are shown in Figure 2.15

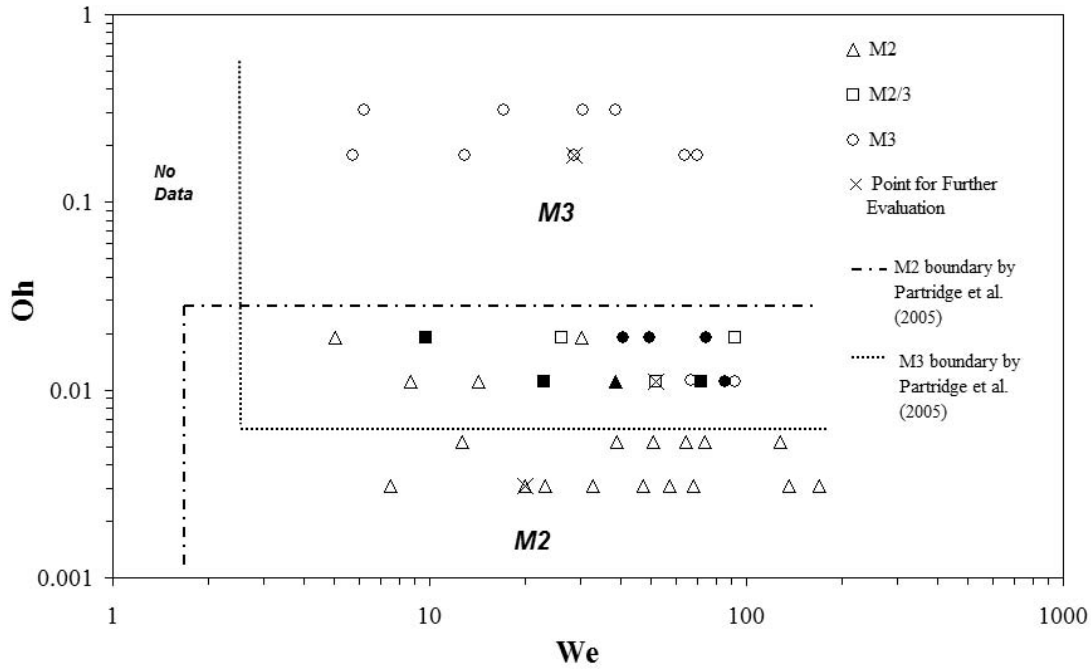

Figure 2.15: Theoretical mode predictions, overlaid onto experimental mode boundaries. Here $\delta = 0.01$, $\epsilon = 0.01$ and κ varies accordingly with $\mathcal{O}h$. $\mathcal{R}b$ is taken from the experimental data obtained from the pilot scale rig. Also plotted are the mode boundaries derived by Wong et al. (2004). (Figure taken from Gurney et al., 2010)

Each point on the flow map is a result from a numerical simulation which uses the values of dimensionless parameters obtained from the experiments. The hollow symbols denote theoretical mode break-up which matches the experimental modes of break-up, whilst the solid symbols indicate a different mode.

In both Părău et al. (2007) and Gurney (2010) it is shown that while altering δ has a significant effect on jet break-up length (when δ is smaller the jet break-up length is longer[1]), there are few qualitative differences. Therefore, in this analysis, δ was kept as constant due to the large number of break-up points and was not optimised to match the break-up length. This does not affect the nature of break-up.

[1]This is intuitive, as if the initial disturbance is larger, less time is needed for the amplitude necessary to cause break-up to develop.

All inconsistencies between modes occur at the same viscosity, $\mu = 0.00418$ Pa s, in the transition period between M2 and M3 break-up. This is thought to be due to the subjective nature of classifying modes of break-up, which makes comparing experimental and theoretical break-up difficult in this transitionary sector found between modes. Discrepancies tend to occur at higher Weber numbers, indicating that the non-linear model is more sensitive to rotation rate.

In Gurney et al. (2010), the three data points marked by crosses in Figure 2.15 are evaluated in more detail. The theoretical simulations, using the model of Părău et al. (2007), for these data points were compared to experimental images, with δ optimised to match the experimental break-up length. Drop size distributions were also compared.

It was found that excellent agreement could be achieved when the numerical simulations, were compared to experimental images for less viscous jets. Figure 2.16 shows the numerical simulation for a jet of water superimposed over an experimental photograph. The theoretical drop size predictions of drop sizes from both linear (Decent et al., 2009) and non-linear theory (Părău et al., 2007) were also examined for the experimental jet. Very little difference was found for the predictions of primary drop size using linear and non-linear theory and this was also found to correspond very well with the experimental mean drop size.

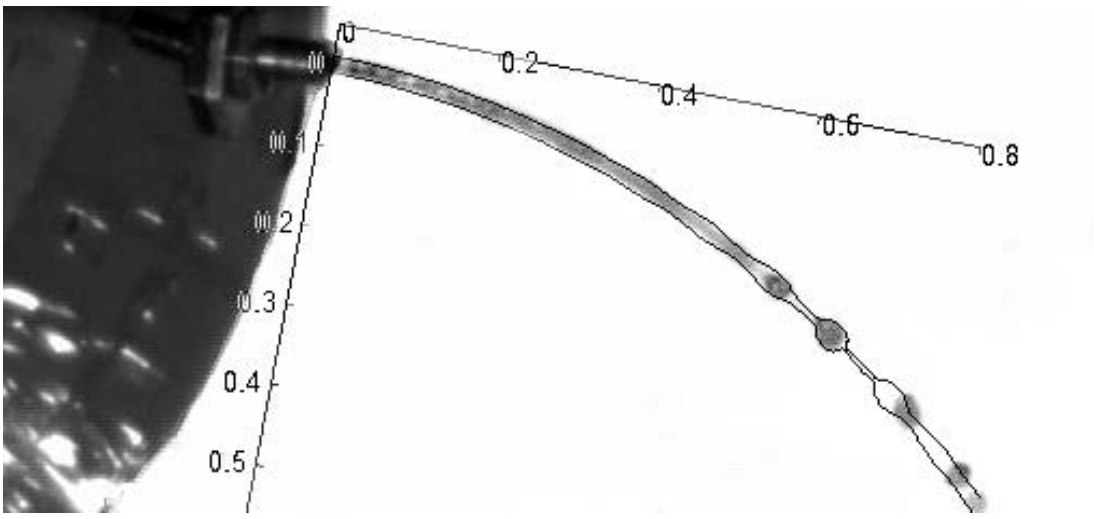

Figure 2.16: Numerical simulation imposed onto the experimental image for a jet of water. Here $\mathcal{W}e = 20.03, \mathcal{R}b = 2.189, \mathcal{O}h = 0.003051, \kappa = 0.7048$ and $\delta = 0.00199$.

However, as the jet becomes more viscous it was found that the model was less accurate

(Gurney et al., 2010). It was found that, as the viscosity increases, the non-linear model generates droplets that are too large in size, while linear theory predicts smaller drops and is towards the lower end of the experimental drop size distribution.

These results, together with those in Section 2.3.3 indicate that the two theories differ more for high rotation rates and viscosities, and that the non-linear theory predicts droplets much larger than those obtained experimentally.

2.5 Non-Newtonian liquid jets

2.5.1 Non-Newtonian fluids

Newton's law of viscosity for an incompressible fluid states that the shear stress, τ, experienced by a fluid is directly proportional to the shear rate, $\dot{\gamma}$, so

$$\tau = \mu\dot{\gamma}, \tag{2.37}$$

where the constant of proportionality is the dynamic viscosity, μ (Pa s).

For non-Newtonian fluids this law is not obeyed. Non-Newtonian fluids do not generally have constant viscosity and the internal structure of these fluids is such that the viscosity depends on the rate at which the fluid is sheared and may also depend on the duration of shearing. However, the shear stress is still a function of the shear rate and if these two quantities are graphed a 'flow curve' can be obtained and the apparent viscosity, which changes with both time and shear rate can be defined as

$$\eta = \frac{\tau}{\dot{\gamma}}. \tag{2.38}$$

There are many different non-Newtonian fluids and the constitutive equations that model them are numerous. Non-Newtonian fluids generally fall into two groups, time independent and time dependent fluids.

The simplest time independent materials are those in which the behaviour is completely independent of the previous deformation history of the material. The most common type of time

independent non-Newtonian fluid behaviour is shear thinning or pseudoplastic behaviour, this is characterised by a material having a viscosity which is a monotonically decreasing function of shear rate. At rest the fluid has a microstructure, which, as the fluid is sheared, is gradually broken down. Since the rheological behaviour is independent of time, the process must be reversible. As the shear rate increases the equilibrium number of interactions or entanglements decreases, resulting in a lower apparent viscosity. When the rate of strain is decreased a higher apparent viscosity is obtained as the structure is recovered.

Shear thickening or dilatant materials have a viscosity which is a monotonically increasing function of shear rate. A deformation of this type causes rearrangement of the microstructure, leading to an increase in viscosity as the shear rate is increased. These are less common than shear thinning fluids, but most concentrated suspensions of non-aggregating solid particles show some shear thickening behaviour in the correct conditions. It is also important to note that typically, the flow curve of a shear thickening suspension of particles can exhibit some shear thinning behaviour at low shear rates.

Visco-plastic materials are fluids that exhibit a yield stress; below a certain critical shear stress there is no deformation of the fluid and it behaves like a solid, but when that yield value is exceeded, the material disintegrates and the fluid flows.

Time dependent materials can be considered to have a memory, or a relaxation time which is long compared to the experiment. As materials are sheared they experience changes in their structure which cause the effective viscosity to change with time. Thixotropic materials shear thin over long timescales and the material suffers a reduction in apparent viscosity. It is typical for a hysteresis loop to be formed in a test in which the shear rate is steadily ramped up and then ramped down over the same period of time. Rheopectic materials do the opposite to thixotropic ones and shear thicken over long timescales. The flow curve again displays a hysteresis loop but, compared to a thixotropic material, the results are inverted.

Complex, structured fluids that simultaneously show both viscous and elastic behaviour are known as viscoelastic fluids. A critical property of viscoelastic fluids is that they are able to support a small amount of internal stress without deforming. The time for these shear stresses

to relax as the internal structures break down and return to the rest state is referred to as the relaxation time.

This thesis is primarily concerned with time independent shear thinning and shear thickening non-Newtonian fluids and will focus on these.

Power law fluids

Both shear thickening and shear thinning materials can be fitted by a power law model. For power law fluids

$$\boldsymbol{\tau} = \eta(\boldsymbol{\nabla u} + (\boldsymbol{\nabla u})^T) = \eta\boldsymbol{\gamma}, \tag{2.39}$$

where $\boldsymbol{\nabla u}$ is the velocity gradient tensor, the transpose of which is $(\boldsymbol{\nabla u})^T$, $\boldsymbol{\tau}$ is the stress tensor, $\boldsymbol{\gamma}$ is the rate of strain tensor and η is the apparent (effective) viscosity and is a function of shear rate, $\dot{\gamma}$, such that

$$\eta = k\dot{\gamma}^{\alpha-1}. \tag{2.40}$$

The shear rate is given by the second invariant of the rate of strain tensor,

$$\dot{\gamma} = \sqrt{\frac{\boldsymbol{\gamma} : \boldsymbol{\gamma}}{2}}. \tag{2.41}$$

In the above expressions, α is the flow index number and is dimensionless and k is the fluid consistency index, which has dimensions of Pa s^{α}. Fluids which follow a power law model are deemed shear thickening or shear thinning depending on whether α is greater than, or less than unity. In the special case when $\alpha = 1, k = \eta$ and the Newtonian fluid is recovered. The fluid consistency index, k measures the relative viscosity of the fluid and α determines how non-Newtonian the fluid is. In the industrial context, the processing of non-Newtonian fluids is common. In a non-Newtonian fluid, the relationship between the shear stress and the strain rate is non-linear, and can also be time-dependent. The addition of polymers or immiscible phases creates liquid mixtures with non-Newtonian flow properties. Paints, slurries and polymer solutions are all examples which are ubiquitous in the industrial environment.

Despite obvious industrial interest, studies of the break-up of non-Newtonian jets are com-

paratively sparse when compared to the myriad of literature available on Newtonian jets. The focus of the majority of studies are on straight liquid jets, that being an axially symmetric flow with the jet having a circular cross-section at every point along its length, and both time-dependent (viscoelastic) and time-independent fluids have been considered. Work on viscoelastic materials (mostly polymer solutions), have elucidated some interesting features, notably the more rapid growth of non-linear surface tension driven deformations, yet a retardation of the break-up of viscoelastic filaments due to extensional stresses (Bousfield et al., 1986). This leads to the classic 'beads on a string' jet shape which was first noted by Goldin et al. (1969) and has been studied in depth by e.g. Li and Fontelos (2003) and Clasen et al. (2006). In this case, small droplets are connected by thin cylindrical ligaments several orders of magnitude smaller than the drops. It was found that capillary pressure drives the thinning process while viscous and elastic forces oppose it. A review of this area is given by McKinley (2003).

A number of straight jet studies have investigated the behaviour of time-independent shear thinning or shear-thickening fluids, models have been developed assuming a power or Carreau constitutive law. Doshi et al. (2003) performed asymptotic solutions of the governing equations and showed that the effects of inertia become increasingly dominant as the point of pinch-off is reached, as found for Newtonian fluids by Eggers (1993). Dravid et al. (2008) found good agreement between these models and experiments at low Reynolds numbers.

A number of authors have investigated the instability of non-Newtonian fluids with power law rheology for classical problems, including flow down an inclined plane (Balmforth et al., 2003; Hwang et al., 1994), between concentric cylinders (Coronado-Matutti et al., 2004), as well as gravity driven shear flows (Berezin et al., 1998).

Uddin et al. (2006) investigated the break-up of curved non-Newtonian liquid jets using a linear asymptotic analysis assuming a power law (Ostwald de Wale) shear dependence of the fluid viscosity. Both shear thinning and shear thickening dependencies were examined. Later work by the same group developed a non-linear model (Uddin et al., 2008a) which enabled prediction of drop size and jet shape as well as the break-up length, which could also be obtained from the earlier linear analysis. A summary of the model of Uddin et al. (2008a) is given here,

as this work is used later in this thesis to enable a comparison between the numerical scheme and experimental results.

2.5.2 Curved power law liquid jets

Formulation of problem

The prilling process is again modelled using the co-ordinate system of Wallwork et al. (2002), where one co-ordinate is lying along the centreline of the jet, corresponding to the arclength, s, with the remaining co-ordinates, the plane polar co-ordinates, n, ϕ (radial and azimuthal), in any cross section of the jet. The associated unit vectors are represented by $\mathbf{e_s}$, $\mathbf{e_n}$ and $\mathbf{e}_\phi$ respectively.

The effects of gravity are neglected as $s_0\Omega^2 << g$. The centreline of the jet in Cartesian co-ordinates is $(X_0(s), 0, Z_0(s))$, with the X-axis in the direction normal to the surface of the container in the initial direction of the jet as it emerges from the orifice, and the Z-axis orthogonal to the X-axis in the plane of the centreline of the jet. The positive Z-axis points in the direction opposite to the motion of the container. The orifice of radius, a, which the liquid jet emerges from, has its centre at position $(0, 0, 0)$.

Non-dimensional equations are derived as in Uddin et al. (2006), using the transformations

$$\begin{aligned} &\bar{u} = \frac{u}{U}, \bar{v} = \frac{v}{U}, \bar{w} = \frac{w}{U}, \bar{p} = \frac{p}{\rho U^2}, \bar{n} = \frac{n}{a}, \epsilon = \frac{a}{s_0}, \\ &\bar{R} = \frac{R}{a}, \bar{s} = \frac{s}{s_0}, \bar{t} = \frac{tU}{s_0}, \bar{X} = \frac{X}{s_0}, \bar{Z} = \frac{Z}{s_0}, \bar{\eta} = \frac{\eta}{k}, \end{aligned} \tag{2.42}$$

where U is the exit speed of the jet in the rotating frame, ρ is the liquid density, ϵ is a small aspect ratio, p is the pressure, R is the jet radius, α is the flow index number and is dimensionless, k (Pa s$^\alpha$) is the fluid consistency index, and u, v and w are the tangential, radial and azimuthal velocity components relative to the centreline of the jet respectively. The bars denote dimensionless quantities in the above expressions.

From (2.39), $\tau_{ij} = \eta\gamma_{ij}$. It is possible to evaluate the nine stress components and an expres-

sion for η can be obtained by using the expressions for γ_{ij}, such that

$$\eta = k \sum_{ij} \frac{\gamma_{ij}\gamma_{ij}}{2}^{\frac{\alpha-1}{2}}. \tag{2.43}$$

The flow is described using the velocity vector $\mathbf{u} = u\mathbf{e_s} + v\mathbf{e_n} + w\mathbf{e_\phi}$. The overbars are dropped and we arrive at the equations of motion describing the dynamics of the jet as in Uddin et al. (2008a). These include the continuity equation, Navier-Stokes equations, and the kinematic condition, tangential and normal stress conditions on the jet's surface $n = R(s, \phi, t)$ in this co-ordinate system. The resulting non-dimensional equations of motion differ to those found in Decent et al. (2009) through the dynamic viscosity being replaced by η and the inclusion of derivatives of η. These equations are given in full in Chapter 6.

We also have an arclength condition which is

$$X_s^2 + Z_s^2 = 1 \tag{2.44}$$

and

$$v = w = 0 \quad \text{on} \quad n = 0, \tag{2.45}$$

since on the centreline of the jet there is purely tangential flow. The orifice conditions are as given in Equation (2.13).

Assuming that the leading order axial component of the velocity is independent of ϕ, variables u, v, w, p are expanded in asymptotic series in ϵr (see Eggers, 1997; Hohman et al., 2001),

and R, X, Z in asymptotic series in ϵ. Dropping overbars, this gives

$$\begin{aligned}
u(s,n,\phi,t) &= u_0(s,t) + (\epsilon n)u_1 + (\epsilon n)^2 u_2 + ... \\
v(s,n,\phi,t) &= (\epsilon n)v_1 + (\epsilon n)^2 v_2 + ... \\
w(s,n,\phi,t) &= (\epsilon n)^2 w_2 + ... \\
p(s,n,\phi,t) &= p_0(s,n,\phi,t) + (\epsilon n)p_1 + ... \\
R(s,n,\phi,t) &= R_0(s,t) + \epsilon R_1 + ... \\
[X,Z](s,n,\phi,t) &= [X_0,Z_0](s) + \epsilon[X_1,Z_1](s,t) + ...,
\end{aligned}$$

where $u_1, u_2, v_1, v_2, w_2, p_1$ and R_1 are in general functions of s, ϕ and t. It was shown in Părău et al. (2006) and Părău et al. (2007) that the assumption that the centreline remains for all time at its steady configuration (as long as the Weber number is not very small) is a good one and hence, at leading order X and Z are taken to be functions of s only. The resulting power law model is given in Uddin et al. (2006).

Steady state solution

The initial conditions ($R_0(0) = u_0(0) = 1$) are used to evaluate the kinematic condition, thus yielding $R_0^2 u_0 = 1$. A system of three ODEs in three unknowns, (2.46) - (2.48), is obtained as in Uddin et al. (2008a), namely

$$\left(\frac{dX_0}{ds}\right)^2 + \left(\frac{dZ_0}{ds}\right)^2 = 1, \quad (2.46)$$

$$\begin{aligned}
u_0\frac{du_0}{ds} = \frac{\frac{du_0}{ds}}{2\mathcal{W}e\sqrt{u_0}} + \frac{(X_0+1)\frac{dX_0}{ds} + Z_0\frac{dZ_0}{ds}}{\mathcal{R}b^2} \\
+\frac{3\left|\sqrt{3}\frac{du_0}{ds}\right|^{\alpha-1}}{\mathcal{R}e_\alpha}\cdot\left(\alpha\frac{d^2u_0}{ds^2} - \frac{\left(\frac{du_0}{ds}\right)^2}{u_0}\right), \quad (2.47)
\end{aligned}$$

$$\begin{aligned}
(\frac{dX_0}{ds}\frac{d^2Z_0}{ds^2} - \frac{dZ_0}{ds}\frac{d^2X_0}{ds^2})\left(\frac{(7-\alpha)\left|\sqrt{3}\frac{du_0}{ds}\right|^{\alpha-1}\frac{du_0}{ds}}{2\mathcal{R}e_\alpha} + \frac{\sqrt{u_0}}{\mathcal{W}e} - u_0^2\right) + \frac{2}{\mathcal{R}b}u_0 \\
-\frac{(X_0+1)\frac{dZ_0}{ds} - Z_0\frac{dX_0}{ds}}{\mathcal{R}b^2} - \frac{(\alpha-1)\left|\sqrt{3}\frac{du_0}{ds}\right|^{\alpha-1}}{\mathcal{R}e_\alpha}\cdot u_0\left(\frac{dX_0}{ds}\frac{d^3Z_0}{ds^3} - \frac{dZ_0}{ds}\frac{d^3X_0}{ds^3}\right) = 0. \quad (2.48)
\end{aligned}$$

where $\mathcal{R}e_\alpha$ is the Reynolds number based on the radius of the can, s_0, so $\mathcal{R}e_\alpha = (\rho/k)\, s_0^n U^{2-\alpha}$.

This system of equations can be solved for X_0 and Z_0, for the steady trajectory, and for u_0, using a finite difference scheme as in Părău et al. (2006), Părău et al. (2007) and Uddin et al. (2008a), with the boundary conditions at the nozzle as $X_0(0) = Z_0(0) = Z_s(0) = 0$ and $u_0(0) = X_s(0) = 1$. The resulting steady state solution is then used as the initial state for the finite difference scheme.

Temporal instability

The non-linear temporal solutions are obtained from solving the following non-linear system in Uddin et al. (2008a),

$$\frac{\partial A}{\partial t} = -\frac{\partial}{\partial s}(Au_0), \tag{2.49}$$

$$\begin{aligned}\frac{\partial u_0}{\partial t} + u_0\frac{\partial u_0}{\partial s} &= -\frac{1}{\mathcal{W}e}\frac{4\left(2A + \left(\epsilon\frac{\partial A}{\partial s}\right)^2 - \epsilon^2 A\frac{\partial^2 A}{\partial s^2}\right)}{(4A + \left(\epsilon\frac{\partial A}{\partial s}\right)^2)^{\frac{3}{2}}} \\ &+ \frac{(X_0+1)\frac{\partial X_0}{\partial s} + Z_0\frac{\partial Z_0}{\partial s}}{\mathcal{R}b^2} + \frac{3}{\mathcal{R}e_\alpha}\frac{\partial}{\partial s}\left(\left|\sqrt{3}\frac{\partial u_0}{\partial s}\right|^{\alpha-1}\frac{\partial u_0}{\partial s}A\right),\end{aligned} \tag{2.50}$$

where $A = R_0^2$. These equations include the expression for the full curvature, following the method of Eggers (1997), as in Părău et al. (2007). This set of equations is solved using the second order space centered explicit scheme of *Richtmyer* which is based on the Lax-Wendroff finite difference schemes. The equations are discretised by using a second order method for first derivatives, but first order for second derivatives. The initial values for $u_0(s,t)$ and $A(s,t)$ are the solution to the steady state equations, (2.46) - (2.48). The instability is introduced through upstream boundary conditions, corresponding to conditions at the nozzle,

$$A(0,t) = 1, \quad u_0(0,t) = 1 + \delta\sin\left(\frac{\kappa t}{\epsilon}\right), \tag{2.51}$$

where κ is a non-dimensional frequency and δ is the magnitude of the initial non-dimensional velocity disturbance.

Numerical simulations using this model, allow the effects of changing, not only the sys-

tem parameters, but the frequency, κ, and the amplitude, δ, of initial disturbances on break-up lengths and the size of main or satellite droplets to be examined. Briefly, it was found in Uddin et al. (2008a) that both break-up lengths and satellite drop sizes decrease as the shear thinning properties of the fluid is increased. The effect of altering other parameters is explored in much more detail in Uddin (2007) and Uddin et al. (2008a) for both shear-thinning and shear-thickening liquids. The behaviour of non-Newtonian liquid jets is examined in more detail in Chapter 5.

2.6 Surfactants

The addition of a surfactant[1] to an aqueous solution lowers the equilibrium surface tension of the solution, due to adsorption of the surfactant at the air-water interface.

A molecule of surfactant is amphiphilic, meaning it contains two distinct parts, a hydrophilic 'head' and a hydrophobic 'tail.' A surfactant molecule will position itself on the free surface so that the head points towards the liquid and the tail points away from the liquid into the free surface. Surfactants can also assemble in the bulk solution into aggregates, examples of which are micelles. The concentration at which surfactants begin to form micelles is known as the critical micelle concentration, or cmc. When micelles form in water, their tails form a core, and their heads form an outer shell that maintains favorable contact with water.

By investigating the linear instability of a liquid thread with a viscous surrounding fluid, Hansen et al. (1999) found that surfactants slow the growth of disturbances. Timmermans and Lister (2002) also used linear stability theory, as well as a one-dimensional non-linear model to investigate the surface tension driven motion of a surfactant covered liquid thread in inviscid surroundings. Scaling close to break-up shows that surfactant is swept away from the pinching region and then has little effect. Non-linear models based on one-dimensional approximations to the exact two-dimensional (three-dimensional axisymmetric) governing equations have also been examined by Kwak and Pozrikidis (2001) and Craster et al. (2002).

The effect of surfactants on the deformation of droplets has also been considered exten-

[1] from the term surface active agent

sively by Stone and Leal (1990), who determined the degree of deformation is influenced by accumulation of surfactant at the ends and the dilution of the overall surfactant concentration.

Theoretical analysis of the necking of a viscous Newtonian thread in the presence of an insoluble surfactant was investigated by Craster et al. (2002), who found that the presence of surfactants at the air liquid interface gives rise to surface tension gradients and Maragoni stresses that dramatically affect the dynamics leading to jet break-up and satellite formation. It was found that the size of the satellite formed during break-up decreases with increasing initial surfactant concentration.

Uddin et al. (2008b) studied the effects of an insoluble surfactant on the break-up of a rotating liquid jet. Using a long wavelength approximation the governing equations are reduced to a set of one-dimensional equations and asymptotic theory is used to find steady solutions. A linear instability analysis is then performed on these solutions. It was found that the most unstable wavenumber and growth rate of disturbances decrease as the effectiveness of surfactants is increased. The equations are also solved numerically to investigate the effects of changing the initial surfactant concentration and other fluid parameters. It was found that as the initial surfactant concentration increases the break-up length increases. A greater initial surfactant concentration also leads to reduced curving of the jet. The differences in break-up lengths between rotating surfactant-laden jets and surfactant-free jets also increases with the rate of rotation and satellite droplet size decreases as the rate of rotation is increased, with the effect of surfactants amplifying the reduction in sizes. The presence of surfactants at fixed rotation rates is also shown to produce larger main droplets at low disturbance wavenumbers whilst satellite droplets are smaller for moderate disturbance wavenumbers. Uddin and Decent (2009) extended the work of Uddin et al. (2008b) by investigating the instability of a rotating liquid jet, having a power law rheology, with a layer of surfactants along its free surface. Surfactants were found to impede the growth of disturbances and thus produce longer jets. Surfactant free jets were found to produce larger droplets for large rotation rates, as compared to jets with surfactants, however, for smaller rotation rates, this result is reversed. Droplets become smaller as the Weber number is increased.

Experimental studies have also been performed. Davies and Makepeace (1978) observed that surfactants reduce the surface velocity by up to 24% compared to a laminar jet of water. At the critical micelle concentration (and below) of sodium dodecyl sulphate a reduction in surface velocity was observed (Jobert and Leblond, 1979). Battal et al. (2003) measured hydrodynamic flow profiles and surfactant adsorption simultaneously in an axisymmetric liquid jet. They designed a Doppler velocimeter that can measure both the surface velocity and detect Maragoni flows at the surface of the jet and detected significant Maragoni effects in surfactant solutions. Liao et al. (2004) performed linear stretching experiments with a soluble surfactant. They found that, depending on the viscosity of the bridge, the presence of surfactant can either increase the length to break-up (if $\mathcal{O}h >> 1$) or decrease it (if $\mathcal{O}h << 1$). More details on the effects of surfactants on liquid jets can be found in Chapter 5.3.

CHAPTER 3

MATERIALS AND METHODS

This Chapter describes the materials and methods used to carry out experiments on both a pilot and laboratory scale rig. Previous work on Newtonian fluids on both the pilot and laboratory scale rig are described in Chapter 2. In the industrial context, the processing of non-Newtonian fluids is common and experiments have been performed using both non-Newtonian fluids and fluids containing surfactants. All fluids used were aqueous solutions, so experiments were also repeated on both the pilot and laboratory scale using distilled water, to ensure that a systematic comparison can be made and to allow for a clear understanding of the role of both apparent viscosity and dynamic surface tension on the dynamics of jet break-up and drop formation.

3.1 Fluids used

3.1.1 Shear thinning fluids

The fluids chosen for the experiments were dilute aqueous solutions of carboxymethylcellulose, CMC (Blanose Aqualon, France), which has a molecular weight of 240.2 g/mol. CMC is a cellulose derivative with time independent shear-thinning rheological properties at low concentrations, which can be approximately fitted using the power-law model (Schowalter, 1978). Three different concentrations of CMC (0.1%, 0.2% and 0.3% by weight) were used, with physical properties shown in Table 3.1.

The solutions were dyed black with Nigrosine (BD Chemicals, UK Suppliers), a water-soluble black dye, to ensure photographic clarity. Tests were conducted to confirm that the

Table 3.1: Properties of shear thinning fluids examined.

Liquid	Density (ρ) [kg m^{-3}]	Surface tension (σ) [N m^{-1}]	Consistency index (k) [Pa s$^{\alpha}$]	Power law exponent (α)
0.1% CMC	1025.05	0.0700	0.012	0.920
0.2% CMC	1025.55	0.0712	0.061	0.748
0.3% CMC	1026.99	0.0717	0.199	0.654

addition of the dye did not significantly alter the liquids' physical properties. The desired liquid was prepared as to the requirements of each experiment. Nigrosine was added to the required amount of distilled water and following this, concentrations of 0.1% w/v, 0.2% w/v and 0.3% w/v of CMC were added very slowly to the vortex of vigorously agitated water and nigrosine at a rate that allowed for reasonable dispersion without allowing the solution viscosity to build up before all the CMC was added. The solution was left to mix overnight, using a 10 cm, 45° 4 pitched blade turbine, to ensure any remaining segregation was removed by molecular diffusion.

The rheological behaviour was characterised using a controlled stress rheometer (TA AR 1000, TA Instruments, USA) equipped with a 4 cm diameter, 1° cone and plate geometry. Flow curves of shear stress versus shear rate, obtained by performing a steady-state shear ramp from $0.1 < \dot{\gamma} < 1000$ s^{-1}, were fitted approximately between $1 < \dot{\gamma} < 100$ s^{-1} using the power law model:

$$\tau = k\dot{\gamma}^{\alpha}, \tag{3.1}$$

where τ is the shear stress (Pa), $\dot{\gamma}$ is the shear rate (s^{-1}), k is the consistency index (Pa s$^{\alpha}$) and α is the power law exponent. The apparent viscosity, η, is given by

$$\eta = \frac{\tau}{\dot{\gamma}} = k\dot{\gamma}^{\alpha-1}.$$

Rheological parameters for each fluid are given in Table 3.1. Measurements of these properties were made over a range of temperatures, enabling the correct values to be used given the temperature of the fluids used within the facility. Due to ambient laboratory conditions, fluid temperatures varied from 21 to 24°C, however, the temperature of the fluids used remained constant over the duration of a single experiment.

Several previous studies have used dilute polymer solutions to successfully mimic power-law behaviour (Kitamura and Takahashi, 1982; Dravid et al., 2008), and the data obtained in Table 3.1 is comparable with that in Kitamura and Takahashi (1982). However, as an extra check, oscillatory tests were also performed. No regime was found where the storage modulus became a significant parameter and hence the flow behaviour appears to be viscous dominated under all observed experimental conditions.

Surface tension was measured using a Du Nouy ring tensiometer and density was measured using a density bottle. All measurements were repeated at least three times, both prior to and after each set of experiments, and the absolute errors were less than 5%.

3.1.2 Shear thickening fluids

Experiments were also performed using aqueous suspensions of Thermflo starch, 51-1458 (National Starch Food Innovation, Bridgewater, NJ), a modified food starch derived from waxy maize.

Starch granules are known to be insoluble in cold water at room temperature. A simple shear thickening fluid can be created using a suspension of solid particles in a liquid matrix. This allows solidification of the fluid by congregation of the particles under stress. As stress increases, the particle solute reacts to the shear by strengthening bonds to adjacent particles in reaction to the stress.

Two different concentrations of Thermflo starch were used in experiments 35% w/w and 40% w/w, with approximate physical properties as shown in Table 3.2. Nigrosine was again added to the required amount of distilled water. Following this, Thermflo starch at concentrations of 35% w/w and 40% w/w was slurried in this solution at room temperature under mechanical stirring to avoid settling. The suspension was kept continuously agitated.

There are several difficulties associated with measuring the rheometry of the starch slurry created. The solution would settle quickly, so in transferring the solution to the rheometer it is likely that the particles would already begin to settle, meaning that the rheology of the solution measured in all likelihood differs to that which is being experimented on. It is also very difficult

Table 3.2: Properties of shear thickening fluids examined.

Liquid	Density (ρ) [kg m^{-3}]	Surface tension (σ) [N m^{-1}]	Consistency index (k) [Pa s$^{\alpha}$]	Power law exponent (α)
0.35% starch	1159.97	0.049	0.016	1.131
0.40% starch	1185.4	0.0485	0.095	1.215

to find a shear thickening fluid which is not elastic. Hence, the experimental results presented here are not those of strictly non elastic shear thickening fluids, but merely a representation of the varying concentrations of starch, mixed with water.

Nonetheless, an attempt to measure flow behaviour was made, using a 4 cm diameter parallel steel plate geometry in the controlled stress rheometer, and a steady-state shear ramp was performed from $0.02 < \dot{\gamma} < 200$ s^{-1}. The flow curves were approximately fitted between $1 < \dot{\gamma} < 100$ s^{-1} using the power law model to obtain approximate values for k and α in Table 3.2. Density and surface tension were measured in the same way as previously.

3.1.3 Dimensionless parameters

From dimensional analysis, two characteristic length scales are present in the apparatus, the drum radius, s_0, and the jet radius, a. The Reynolds number, $\mathcal{R}e$, of the flow can be based on either scale. For consistency with previous experiments (Partridge et al., 2005), $\mathcal{R}e$ is based on the characteristic dimension of the jet flow, a, so the generalised Reynolds number is $\mathcal{R}e = (\rho/k)\,(a^{\alpha}U^{2-\alpha})$. A Reynolds number, $\mathcal{R}e_{\alpha}$, based on the radius of the drum, s_0, is used when comparing experimental results with the numerical scheme, to remain consistent with the definition used in the model of Uddin et al. (2008a). In addition, as the Ohnesorge number is defined as $\mathcal{O}h = \sqrt{\mathcal{W}e}/\mathcal{R}e$, this becomes velocity dependent with the use of the non-Newtonian Reynolds number.

It should also be noted that the Rossby number, $\mathcal{R}b = U/s_0\Omega$, takes into account not only the rotation rate of the jet but also the jet exit velocity which is affected by the centrifugal forces due to the rotation of the drum (as well as the orifice size). To identify the influence of rotation rate alone upon jet break-up without considering exit velocity, the parameter $\mathcal{F}r/\mathcal{R}b$ is used (Wong et al., 2004), where $\mathcal{F}r$ is the Froude number and is defined as $\mathcal{F}r = U/\sqrt{gH}$, where

H is the height of the liquid in the drum above the nozzle. Hence, this dimensionless number is a ratio of the exit velocity to the velocity which would be expected due to the hydrostatic head in the drum (ignoring losses due to the orifice). Therefore,

$$\mathcal{F}r/\mathcal{R}b = \frac{\Omega s_0}{\sqrt{gH}},$$

which is independent of exit velocity.

3.1.4 Surfactants

To examine the influence of surface tension, surfactant was introduced into the water at increasing concentrations (0.05%, 0.1% and 0.3% by weight). The surfactant used was Sodium Dodecyl Sulphate (SDS) (which has a molecular weight of 288.38 g/mol) for its ability to significantly reduce the surface tension of aqueous solutions using low concentrations. Studies were restricted to low concentrations of surfactant so that bulk non-Newtonian properties can be neglected (Aytouna et al., 2010; Cooper-White et al., 2002; Rafaï et al., 2004). Measurement of the surface tension properties of surfactant in the aqueous solutions at the concentrations used were measured using a T60 bubble pressure tensiometer (SITA Messtechnik GmbH, Germany). Before each experiment, the tensiometer was calibrated with respect to purified water. The critical micelle concentration (cmc) of SDS in pure water at 25°C is 8.1×10^{-3} M, which equates to approximately 0.24%.

Plots of surface tension against surface age for this fluid are shown in Figure 3.1 for $0.05 - 0.3\%$ SDS. As the effective surface age of the fluid increases, surface tension reduces. In Figure 3.1(c) there is less change, as the concentration of surfactant in the aqueous solution is above the cmc level, so the surface should be already be saturated. Approximate values of surface tension can be extracted by reading off the graph at bubble lifetimes corresponding to jet break-up times. The properties for the fluids use in this study are given in Table 3.3.

[1]The surface tensions stated are for the solutions with SDS (with concentrations from 0.05 - 0.3% by weight), are the values measured in water (from Figure 3.1); $t_1 = 0.03$ s, $t_1 = 1$ s, $t_3 = 10$ s.

[2]The surface tensions measured here are the range of surface tensions at the point of jet break-up for that solution (again taken from Figure 3.1)

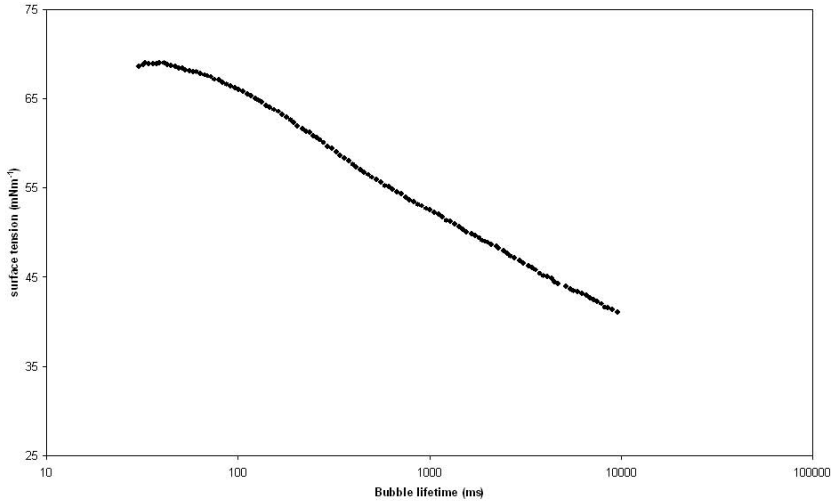

(a) 0.05% SDS

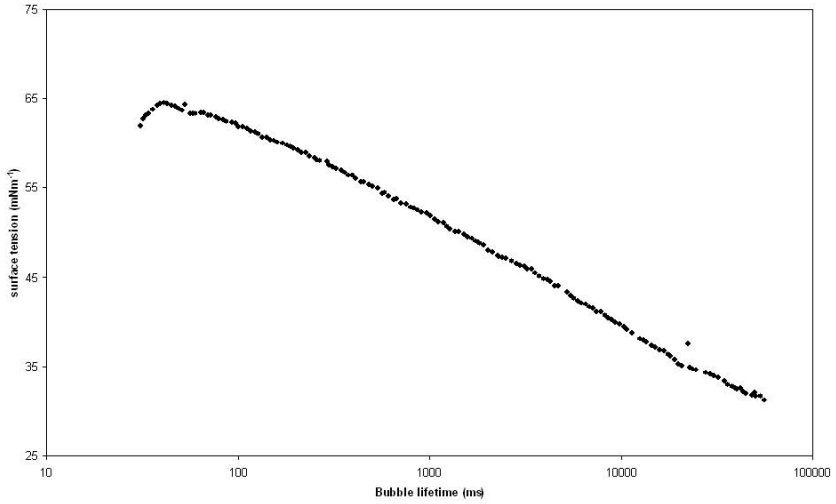

(b) 0.1% SDS

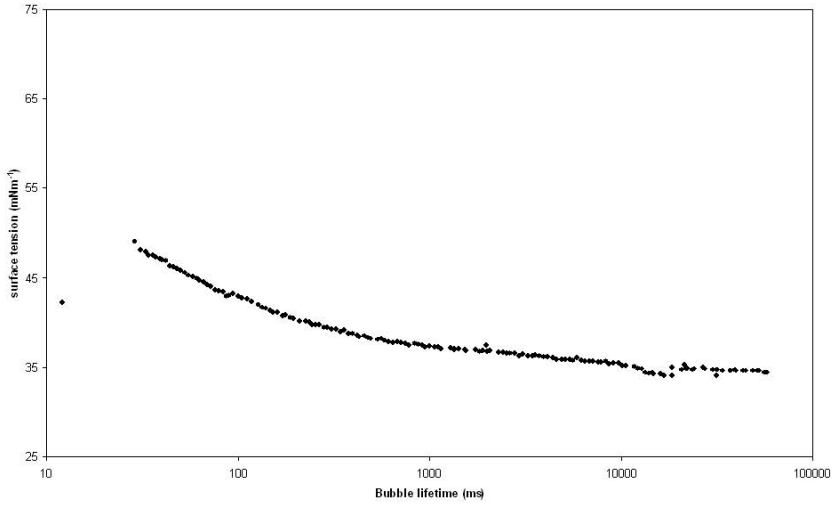

(c) 0.3% SDS

Figure 3.1: Plot of surface tension against bubble lifetime (effective surface age) for (a) 0.05% SDS, (b) 0.1% SDS and (c) 0.3% SDS in water ($\mu = 10$ mPa s).

Table 3.3: Properties of surfactants examined.

Liquid	Density (ρ) [kg m^{-3}]	Viscosity (μ) [Pa s]	σ_{t_1} / σ_{t_2} / σ_{t_3} [1] [N m^{-1}]	σ_{bu} [2] [N m^{-1}]	σ_s [N m^{-1}]
0.05% SDS	997.5	0.001	0.069 / 0.053 / 0.041	0.065 - 0.068	0.027
0.1% SDS	997.5	0.001	0.062 / 0.047 / 0.037	0.057 - 0.061	0.029
0.3% SDS	997.5	0.001	0.049/ 0.037 / 0.035	0.041 - 0.43	0.034

After the addition of surfactant, the rheology of the fluids was tested and non-Newtonian behaviour was not observed. The viscosity was also found to be independent of surfactant concentration.

3.2 Experimental setup

3.2.1 Laboratory scale rig

Experiments were performed using the laboratory scale rig, briefly described in Section 2.2.2. The apparatus consists of a cylindrical can with a diameter, D, of 0.85 m and a height of 0.115 m, that contains two diametrically opposed orifices of radius, a, of 0.0005 m and 0.0015 m respectively. A schematic is shown in Figure 3.2. The can was partially filled with liquid to a height, H, to give liquid aspect ratios, H/D, ranging from $2/3 - 5/4$. The can was attached by means of a long thin shaft to an electronic stirrer (Heidolph Stirrer - Model RZR2021) with a digitally controlled rotation rate, which was varied from $50 - 300$ rpm ($\Omega = 5.24 - 3.14$ rad s^{-1}). The average exit velocity of the jet, U (ms^{-1}), was calculated from the volume change in the drum over a measured time interval. The change in volume was sufficiently small that the velocity may be taken as constant (Wong et al., 2004). A summary of experimental conditions for each liquid system is given in Table 3.4.

3.2.2 Pilot scale rig

Experiments have also been performed using a pilot scale facility as shown in Figure 3.3(a). A schematic diagram of the experimental set up is shown in Figure 3.3(b). The majority of the experiments on the laboratory scale were repeated on the pilot scale[1]; this enabled a larger

[1]The exception to this is the experiments with starch. This would have proved impractical due to the potential difficulty faced in cleaning the rig after each experiment.

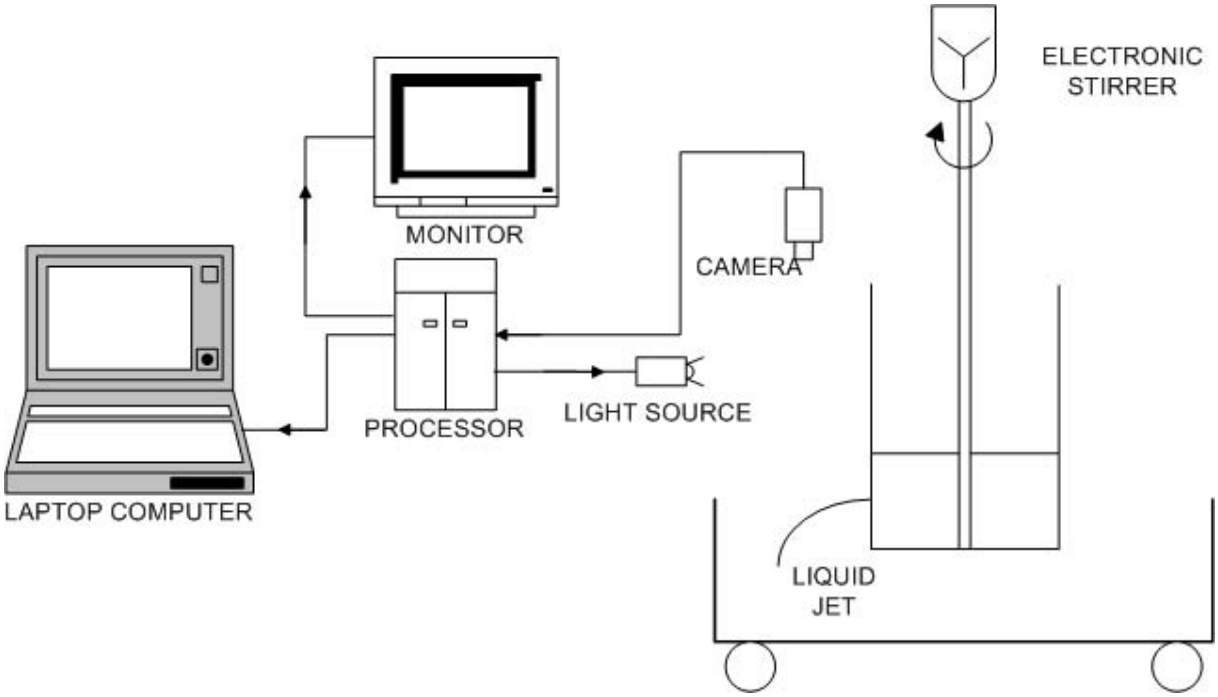

Figure 3.2: Schematic diagram of laboratory scale experimental set-up.

Table 3.4: Properties of liquid systems examined on laboratory scale rig.

	Liquid				
	0.1% w/v CMC	0.2% w/v CMC	0.3% w/v CMC	35% w/w Starch	40% w/w Starch
U [ms^{-1}]	0.468 - 0.970	0.622 - 0.930	0.641 - 0.771	0.81 - 0.94	0.82 - 1.04
$\mathcal{W}e$	1.60 - 16.50	5.57 - 18.68	5.89 - 12.77	23.27 - 31.47	24.43 - 39.93
$\mathcal{R}b$	0.50 - 4.65	0.56 - 2.05	0.50 - 1.10	0.12 - 0.30	0.13 - 0.31
$\mathcal{O}h$	0.02193 - 0.03654	0.03659 - 0.04477	0.06877 - 0.07800	0.12762 - 0.13001	1.25707 - 1.32533
$\mathcal{R}e$	34.65 - 185.20	52.70 - 118.13	31.11 - 51.96	37.80 - 42.88	3.93 - 4.77

Table 3.5: Properties of liquid systems examined on pilot scale rig.

	Liquid					
	0.1% CMC	0.2% CMC	0.3% CMC	0.05% SDS	0.1% SDS	0.3% SDS
U [ms^{-1}]	0.494 - 3.565	0.364 - 2.466	0.100 - 2.944	0.95 - 2.63	0.50 - 2.46	0.69 - 2.51
$\mathcal{W}e$	5.37 - 118.45	2.91 - 89.37	0.22 - 124.68	19.49 - 148.19	5.39 - 130.21	10.18 - 135.17
$\mathcal{R}b$	0.52 - 1.99	0.39 - 1.21	0.22 - 1.08	0.52 - 1.90	0.55 - 2.55	0.56 - 0.77
$\mathcal{O}h$	0.02026 - 0.03546	0.03038 - 0.04648	0.04603 - 0.08839	0.00301 - 0.00369	0.00301 - 0.00369	0.00301
$\mathcal{R}e$	73.34 - 536.86	36.59 - 299.93	3.36 - 242.54	1460.50 - 4035.61	707.94 - 3778.48	1059.92 - 3861.97

range of parameters to be studied since a larger exit velocity can be obtained. It was shown in Wong et al. (2004) that, for Newtonian fluids, exit velocity had a large influence on break-up on the laboratory scale, so experiments on the pilot scale would provide a more realistic insight to break-up behaviour on the industrial scale. The apparatus used consists of a cylindrical drum of diameter, D, of 0.285 m and height 0.5 m. The drum was partially filled to a height, H, to give a liquid aspect ratio (H/D) ranging from $1/2$ to $1/4$. The drum contains one orifice of variable radius, $a = 0.0005, 0.001$ or 0.0015 m. The drum was attached by a shaft to a motor drive controlled by a speed controller (Eurotherm 690+), which has a top speed of 600 rpm. The rotational speed of the drum was varied from 30 to 300 rpm ($\Omega = 3.14 - 31.4$ rad s^{-1})

The desired orifice size was selected and fitted to the can and a bung was used to prevent liquid escaping from the can before the experiment. At the start of each experiment, an axisymmetric vortex developed inside the drum and this was allowed to reach a steady state before any images were taken. The spin up time of the vortex varied between 30 and 180 seconds, depending upon the rotation rate chosen. The drop in the level of liquid within the drum, dH, was measured over the time, t, in seconds, taken to complete the experiment. This was then used to calculate the average exit velocity of the jet, U (ms^{-1}), leaving the orifice, using the following formula

$$U = \frac{s_0 dH}{a^2 t},$$

where s_0 is the radius (m) of the drum. The drop in the level of the liquid was sufficiently small that the velocity can be assumed as constant during each experiment. A summary of experimental conditions for each liquid system is given in Table 3.5.

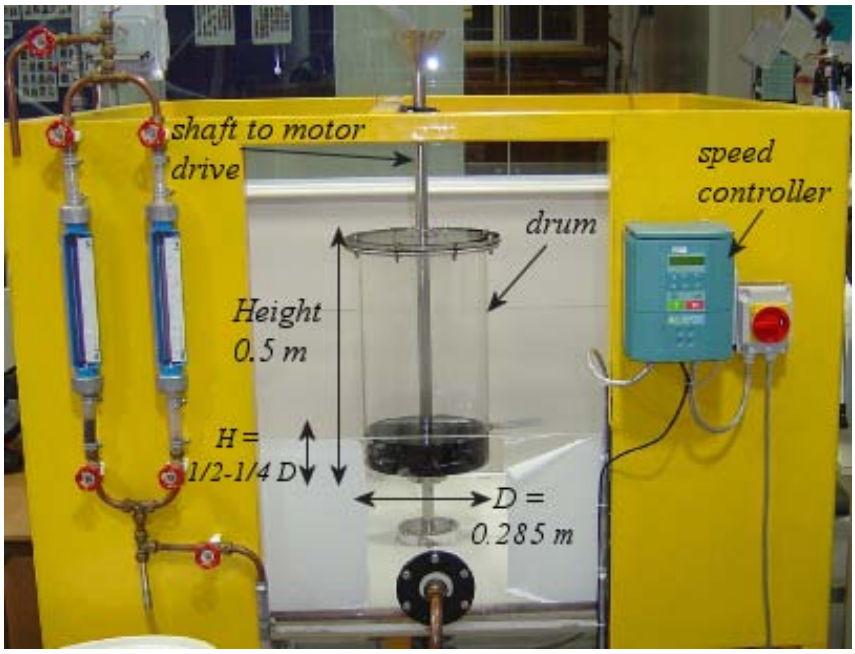

(a) Photograph of the pilot facility.

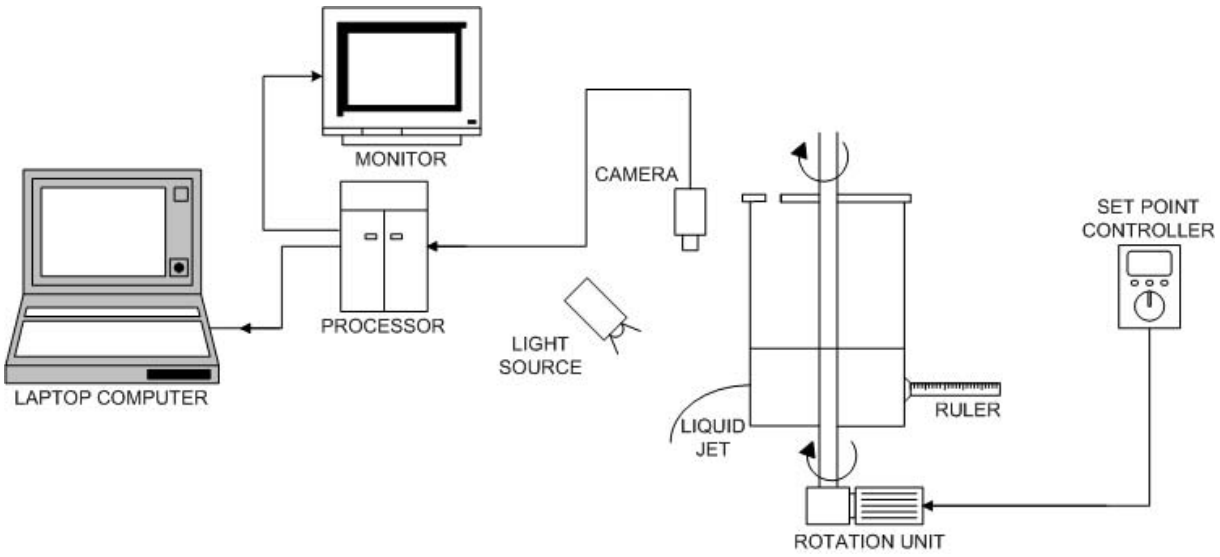

(b) Schematic diagram of the pilot scale experimental set-up.

Figure 3.3: The pilot scale rig

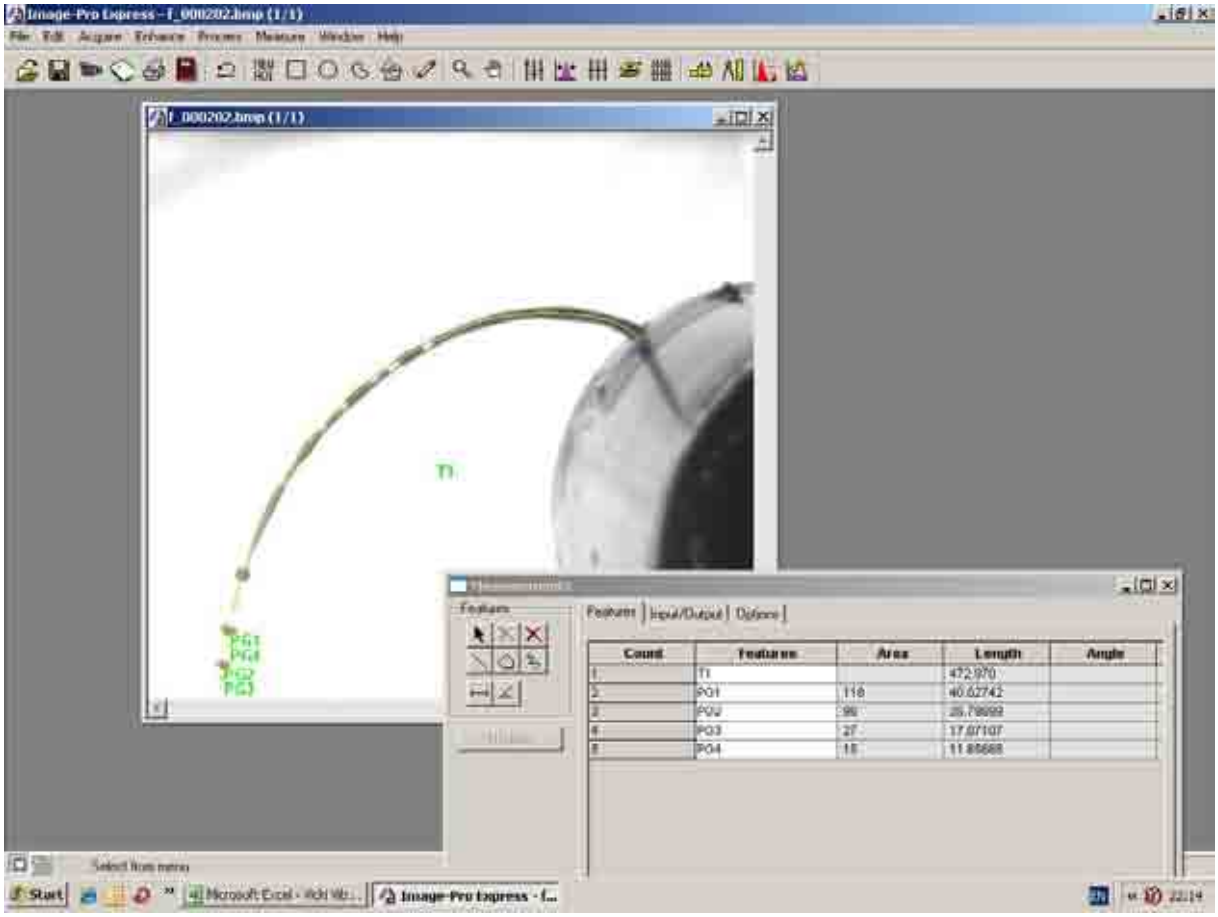

Figure 3.4: Image analysis using Image-Pro Express software (Datacell Ltd., U.K).

The trajectory of the jet was captured by means of a high speed digital camera (Photron Fastcam Super 10K), which is capable of capturing up to $10,000$ frames per second. A 12 mm lens was used to take images of the whole jet and a 25 mm lens was used to elucidate features close to the break-up point. A high powered light (Photron Beard Blond) was used to illuminate the jet.

A rule was attached to the opposite side of the drum to the orifice at the same height for calibration purposes. An image of the rule was taken and saved to the personal computer. This image was used for calibrating the image analysis software for drop size and break-up length measurements. A typical measurement made using the software is shown in Figure 3.4.

Next the solution was added to the can to the required height, dependent upon the aspect ratio selected, and the desired rotation rate was selected.

To start the experiment the bung was removed and the motor to drive the can and the timer

were switched on simultaneously. Images of the jet were taken when the liquid in the can was observed to have reached a steady state. When the experiment had run for the required amount of time[1], the drum was stopped and the bung was replaced. The drop in liquid level in the can was measured and recorded so that the exit velocity could be calculated and the images of break-up length and drop size were downloaded from the camera onto a personal computer for analysis using Image-Pro Express software (Datacell Ltd., U.K) and MATLAB. At each condition, to ensure reproducibility, the experiment was repeated three times. One of the parameters was then altered and the above process repeated.

Image Pro Express software was used to measure break-up length. The software program was calibrated using the calibration image recorded before each experiment. The break-up length was measured as shown in Figure 3.4. At least 35 images were examined to ascertain the break-up length from origin to detachment.

3.2.3 Mean drop size and size distributions

In order to minimise the time required for analysis of one population of drop sizes it is desirable to measure as few drops as possible to give a representative sample. Wu et al. (1995) reported using $40 - 200$ droplets from experimental studies, since their analysis was limited by the relatively small number of droplets formed. Yet in McCreery and Stoots (1996) each drop diameter distribution was based on as many as $10,000$ individual drop measurements. Wong et al. (2004) provides justification for the use of 200 individual drop measurements. In this study, a preliminary drop size analysis was performed by assessing 50, 100, 200 and 500 droplets based on plots of drop diameter normalised against the orifice diameter and $f(d)$, the relative frequency. It should be noted that rather than measuring the actual diameter of the droplet, to increase accuracy, the 2-dimensional area of the particle was instead measured, as shown in Figure 3.4, and this was then equated to the *projected area diameter*, d_{A} ; the diameter of the sphere with

[1]The amount of time the experiment ran for was dependent upon the nozzle size, rotation rate and aspect ratio. It had to run for such a time that there is a significant drop in the level of the liquid in the drum, but not so much that this drop in liquid level could sufficiently alter the exit velocity of the jet (up to a maximum of 10%).

Table 3.6: Effect of sample size on the mean drop diameter.

Mean Diameter (cm)	Liquid			
	50	100	200	500
d_{10}	0.3719	0.3670	0.3569	0.3597
d_{32}	0.3986	0.3994	0.3922	0.3950

the same projected area as the particle, as described by Clift et al. (1978),

$$d_{\mathrm{A}} = \sqrt{\frac{4A_{\mathrm{p}}}{\pi}}$$

where A_{p} is the projected area.

Two image settings were used i.e., 512×480 pixels and 265×480 pixels for respective frame rates of 500 and 250 frames per second. The accuracy of the measurements depended on the minimum drop size which could be measured by the software. This was between 5 and 7 pixels which translates as approximately 1×10^{-4} m in absolute length.

To define $f(d)$, drops within a sample are considered to have a normalised diameter of d. The range of drop sizes were sub-divided into a finite number of distinct intervals. The number, d, then corresponds to the centre of each interval. To find $f(d)$ corresponding to the diameter d the following formula is used

$$f(d) = \frac{\text{The number of drops with normalised diameter } d}{\text{Total number of drops measured}}.$$

Figure 3.5 shows that the relative frequency distribution plots for different sample sizes virtually overlap. It should be noted that in order to obtain the largest population between 400-500 frames are required.

No significant variation was seen from the four sample sizes as the difference in mean diameters calculated from two consecutive samples was, for all comparisons, smaller than 5%, as shown in Table 3.6.

To remain consistent with previous work (Wong et al., 2004; Partridge et al., 2005), the drop size distribution plots shown here were obtained by assessing at least 200 individual droplets.

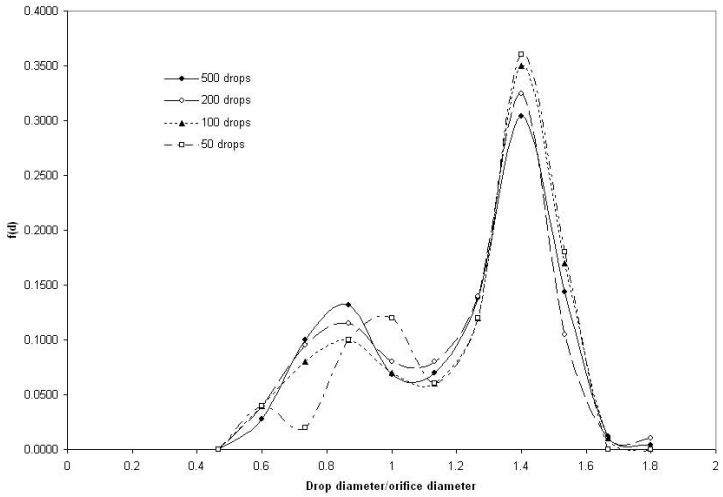

Figure 3.5: Effect of the sample size on the relative frequency distribution. $\mathcal{R}b = 0.6876(60 \text{ rpm}); \mathcal{O}h = 0.0407(k = 0.0610 \text{ Pa s}, \alpha = 0.748, \rho = 1026 \text{ kg m}^{-3})$

3.2.4 Image analysis algorithm for in-plane drop recognition

Rather than measure 200 drops using Image Pro Express, as shown in Figure 3.4, it is possible to use MATLAB to expedite this analysis.

The captured raw images of droplet size were processed with a set of image analysis routines written in MATLAB release 2006b, equipped with the image analysis toolbox (Mathworks Inc., USA). The image algorithms used are similar to those in Chung et al. (2009), which were developed for recognising gas bubbles and measuring the average local gas bubble velocities, as well as the local velocities of the liquid phase, within small stirred vessel reactors. A flowchart summarising the major steps followed in the analysis algorithm is shown in Figure 3.6.

Detection of the drop from the raw image relies on the contrast in grayscale between the drop and the background. Thus, the analysis process was based on recognising the localised variation in grayscale. A uniform background is difficult to achieve due to shadows from the drum and the camera and small defects on the base of the tank. In several images the drum and the length of jet before break-up is also present. A typical raw image of droplet sizes, obtained from experiments which illustrate this is shown in Figure 3.7. The dark areas represent an inconsistency in the background grayscale levels which downgrade the quality of drop recognition. For this reason,

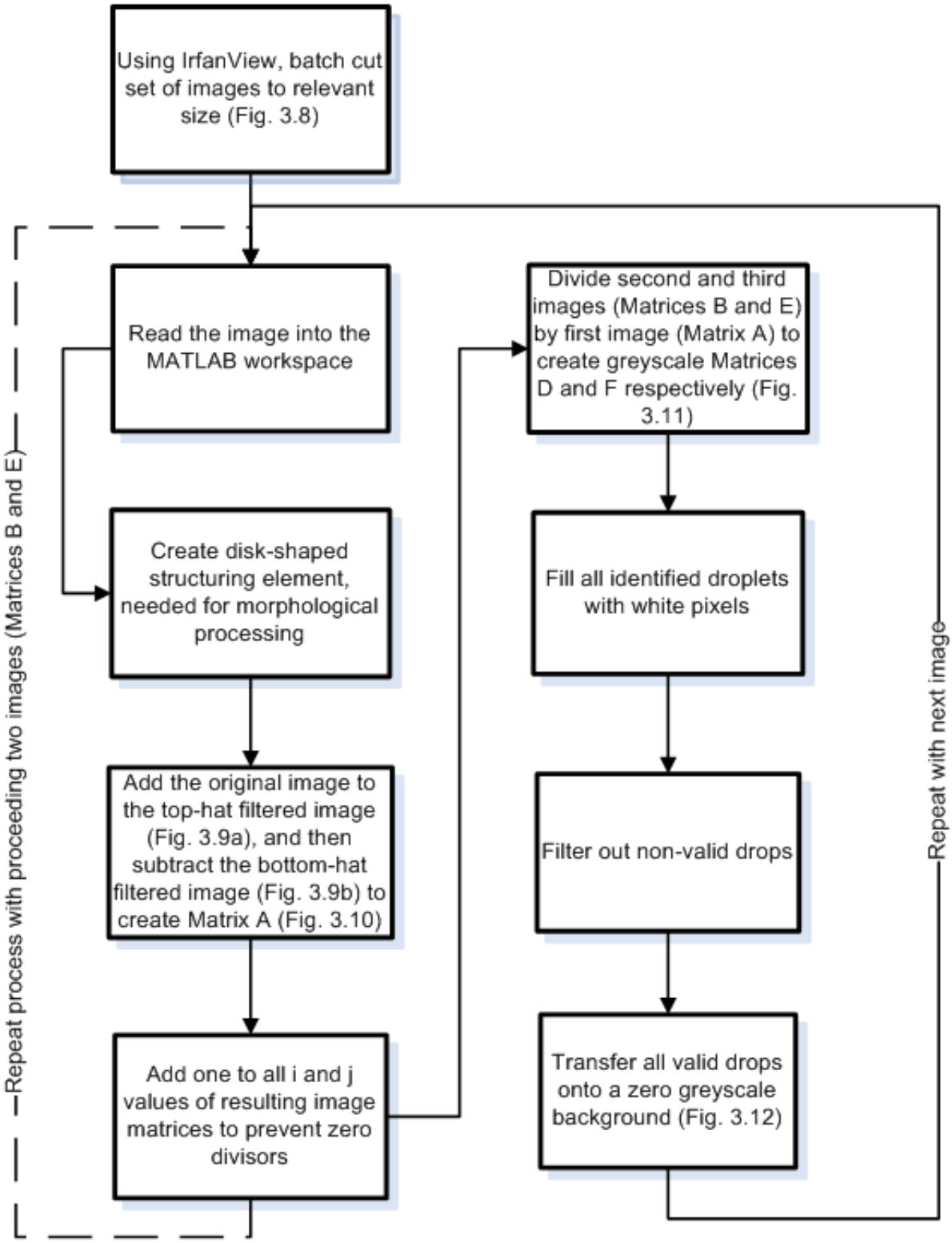

Figure 3.6: Flowchart of droplet image analysis algorithm.

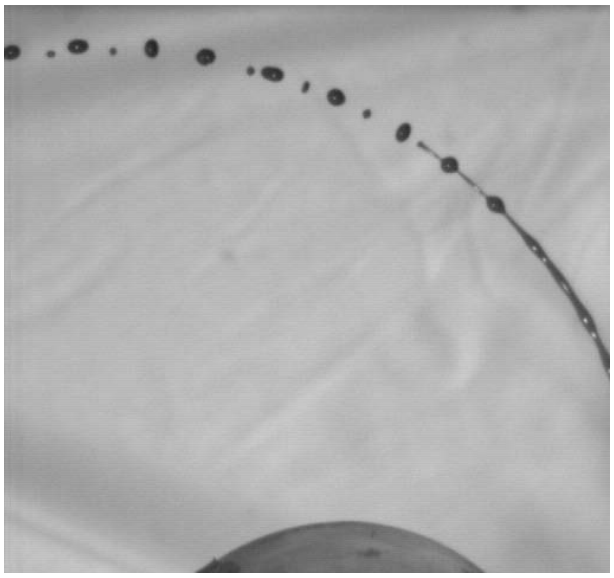

Figure 3.7: A typical raw image obtained from the experiments.

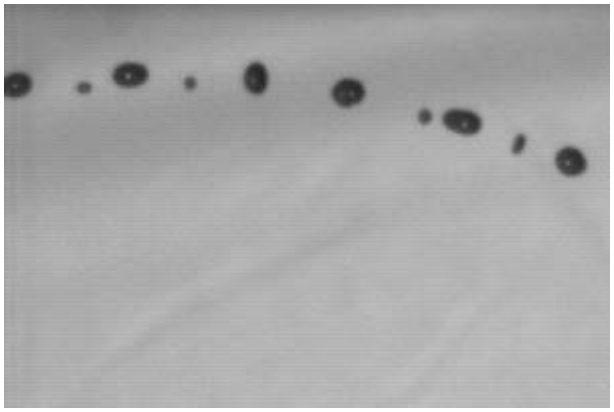

Figure 3.8: Experimental image after batch cutting in IrfanView.

it is first necessary to cut the image to a more convenient size, so that only the drops are present in the image. The cut image is shown in Figure 3.8. The image was cut using IrfanView and stored in a temporary folder. The edited images can then be called into MATLAB from this folder.

In order to help identify the droplets from the background area, morphological top hat and bottom hat filtering was used. Top-hat filtering computes the morphological opening of the image and then subtracts the result from the original image. Bottom-hat filtering is the equivalent of subtracting the input image from the result of performing a morphological closing operation on the input image. Top-hat filtering and bottom-hat filtering can be used together to enhance contrast in an image. Both top and bottom hat filtering require the use of a structuring element.

(a) Top hat filtered image.

(b) Bottom hat filtered image

Figure 3.9: Experimental image following image editing.

In this algorithm a disk shaped structure was used. The top hat and bottom hat filtered images can be seen in Figure 3.9.

The cut image was added to the top-hat filtered cut image and then subtracted from the bottom hat filtered cut image as illustrated in Figure 3.10. This process is repeated for the next two subsequent images to give grayscale matrices A, B and E, where the i and j values take the place of pixels and are valued between 0 (black) and 255 (white).

To filter out any noise and identify where droplets occur, it is necessary to divide matrices B and E by Matrix A, resulting in matrices D and F respectively. Matrix D is shown in Figure 3.11. It should be noted that before matrices are divided, it is necessary to add 1 to all the i and j values of the resulting image matrices, so that when the matrices are divided the denominator

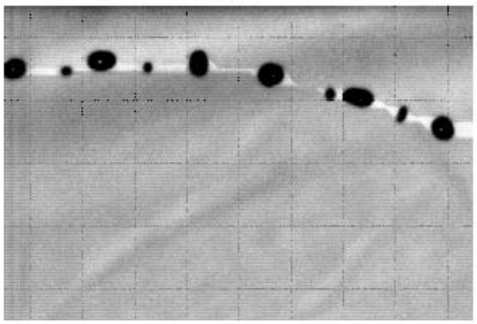

Figure 3.10: Grayscale image representing Matrix A.

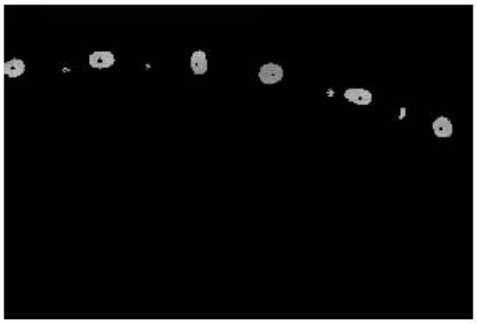

Figure 3.11: Grayscale image representing Matrix D.

Figure 3.12: Black and white image representing Matrix C following filtering of partial droplets and noise.

is never equal to zero.

Following this it is possible to form Matrix C, which identifies the position of the droplets in the first image, by allowing the condition that if the i and j values of Matrix D and Matrix F are greater than or equal to 1, the i and j values of Matrix C are set to 1, otherwise they are set to 0. This creates a binary Matrix C, where the values of 1 correspond to the white droplets and the values of 0 correspond to the black background. Incomplete droplets are filtered out and also filled with white pixels, by eliminating any partial droplets that touch the borders of the image. Hence, once the full droplets have been identified, they are transferred onto a zero grayscale (i.e., black) background, as shown in Figure 3.12.

It is now possible to use MATLAB to measure properties of the image regions. Using the 'area' command the actual number of pixels in the region are measured. It is also possible to measure the area equivalent diameter, perimeter or various other quantities.

This process is repeated for all the images that have been batch cut. It is also possible to create a video showing the areas of droplets that have been measured as a second visual check to check that the drops are approximated reasonably well. A screenshot from the video, compared to the original image is shown in Figure 3.13.

This algorithm was tested extensively against experiments for which 200 manual measurements of drops existed. All the manual measurements for experiments using water were redone and the drop size distributions and mean drop sizes compared, as shown in Figure 3.14. Only

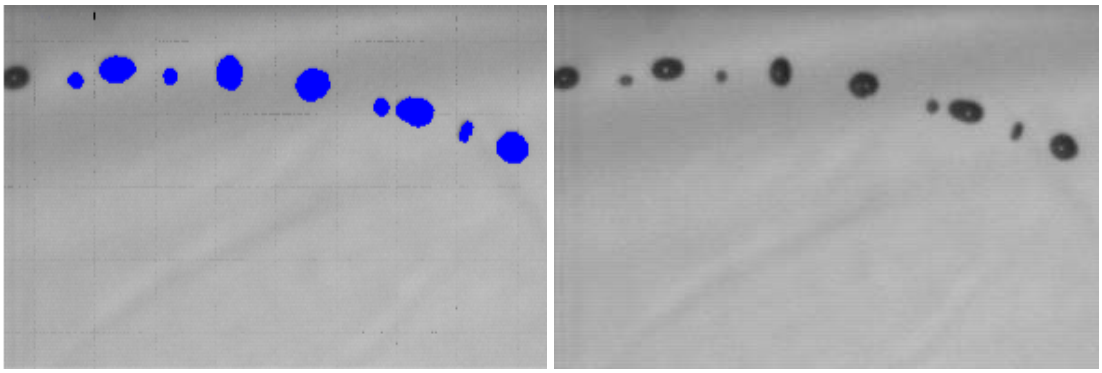

(a) (b)

Figure 3.13: (a) Screenshot from the video resulting from the image analysis process compared to (b) the original batch cut image.

small variations were seen in any of the samples. The difference in mean diameters between the manual measurement and using the image algorithm was, for all comparisons, smaller than 5%.

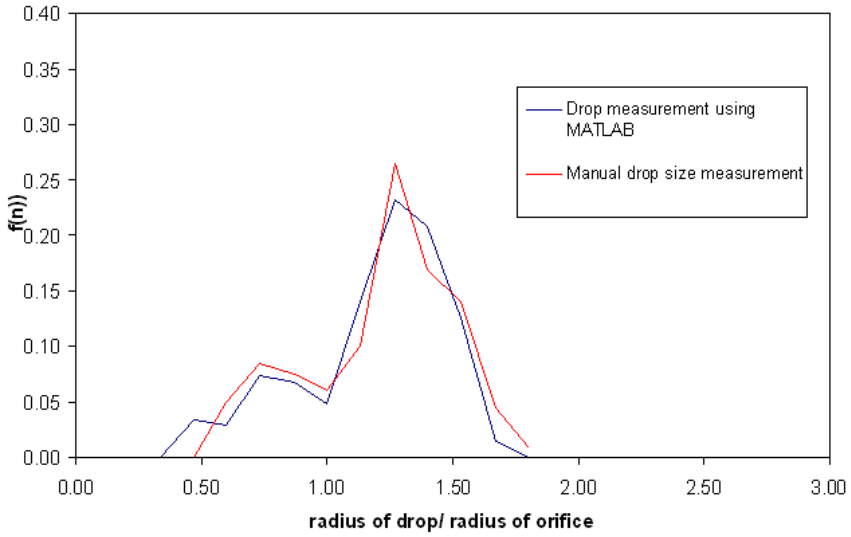

Figure 3.14: Effect of the method of drop size analysis on the relative frequency distribution ($\mathcal{W}e = 47.414, \mathcal{R}b = 0.549(180 \text{ rpm}), \mathcal{O}h = 0.003059, \mathcal{R}e = 2253.45$).

Whilst this thesis has maintained the use of 200 droplet sizes to produce drop size distributions, which maintain consistency with earlier work (Partridge et al., 2005; Wong et al., 2004), in future work, this algorithm would enable the measurements of many more drops to be taken quickly and accurately.

CHAPTER 4

LABORATORY SCALE STUDY OF CURVED JET BREAK-UP USING NON-NEWTONIAN FLUIDS

Experiments were performed on the laboratory scale rig to determine whether the non-Newtonian fluids exhibit any new features of break-up. This is to build a basis for further examination, both experimentally on the larger pilot scale rig and theoretically using mathematical models developed in this thesis and those developed by Uddin et al. (2008a). This section discusses the results of these experiments and also makes comparisons with the laboratory scale work of Wong et al. (2004), which was performed for Newtonian fluids.

4.1 Shear thinning fluids

4.1.1 Features of break-up

Using shear thinning fluids, over the parameter ranges studied in these experiments (given in Table 3.4), the shapes of the jets upon break-up did not resemble the modes observed by either Wong et al. (2004) or Partridge et al. (2005). Since the only change between these experiments and the experiments by Wong et al. (2004) is the use of dilute polymer solutions, the differences can be attributed to the shear thinning rheology of these fluids. Images of the break-up of the jets are shown in Figures 4.1 - 4.5. Considerable elongation of the jet was observed. At low values of Ω, axisymmetric (*varicose*) disturbances are observed (Figure 4.1(a)), but these become non-axisymmetric (*kink*) as the rotational speed of the drum, Ω, is increased (Figure 4.1(b)).

Primary droplets are formed from the growth of long wavelength instabilities ($\lambda >> a$) with

(a)

(b)

Figure 4.1: Experimental images showing (a) varicose disturbances along the jet ($\mathcal{W}e = 4.62, \mathcal{R}b = 1.260, \mathcal{O}h = 0.0269, \mathcal{R}e = 79.70 \rho = 1025$ kg m^{-3}, $k = 0.012$ Pa s, $\alpha = 0.092$), (b) kink disturbances along the jet ($\mathcal{W}e = 12.77, \mathcal{R}b = 0.525, \mathcal{O}h = 0.0687, \mathcal{R}e = 51.96 \rho = 1027$ kg m^{-3}, $k = 0.199$ Pa s, $\alpha = 0.654$)

long ligaments being formed in-between the droplets. These ligaments pinch off from primary droplets at both, or either, ends and either contract to form satellite droplets, as can be seen in Figure 4.2(a), or will merge with the main droplet, as in Figure 4.2(b). These mechanisms apply to both kink and varicose disturbances. Multiple satellite droplets were frequently formed simultaneously from the fragmentation of liquid threads connecting the primary droplets. In addition, the ligaments appear to stretch between the main droplets with a curvature normal to the curved central axis of the jet (Figure 4.1(b)). This curvature becomes more dramatic with increasing apparent viscosity, η and rotation rate, Ω. Blaisot and Adeline (2003) suggested that the formation of kink instabilities is due to the increasing influence of aerodynamic resistance. Partridge et al. (2005) observed a slight curvature of the ligaments between drops using Newtonian fluids but the effect was much less.

While the break-up mechanism of shear thinning liquid jets appears to be entirely different to that observed for Newtonian jets, there are some features of break-up that are common to both.

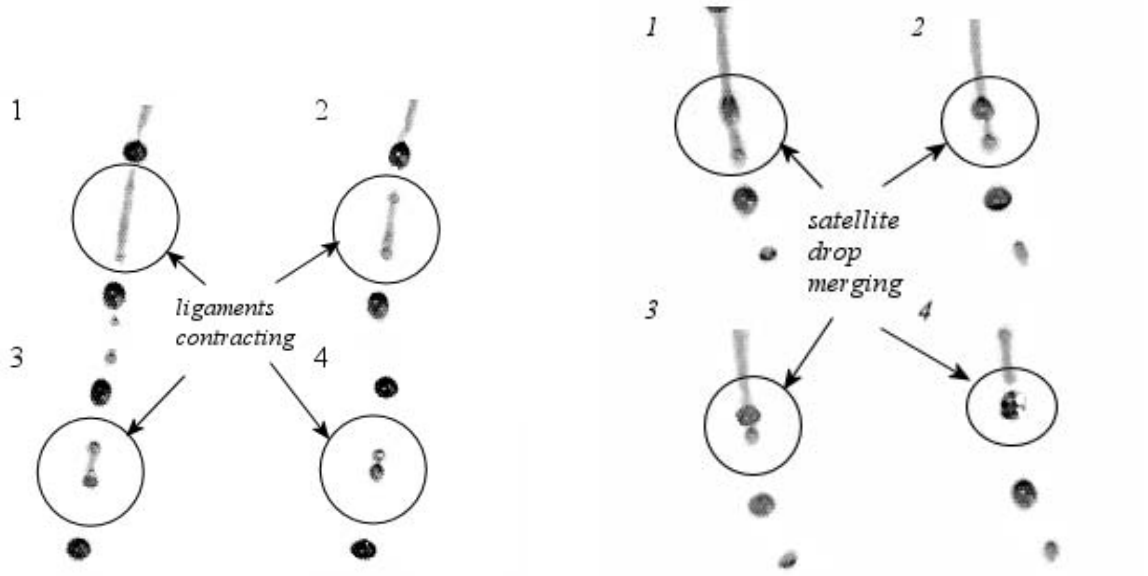

(a) (b)

Figure 4.2: Experimental images showing (a) satellite droplets being formed by contraction of the ligament between primary droplets, (b) satellite droplets recoiling to merge with the main droplets ($\mathcal{W}e = 13.20, \mathcal{R}b = 0.70, \mathcal{O}h = 0.0221, \mathcal{R}e = 164.11\rho = 1025$ kg m^{-3}, $k = 0.012$ Pa s, $\alpha = 0.920$)

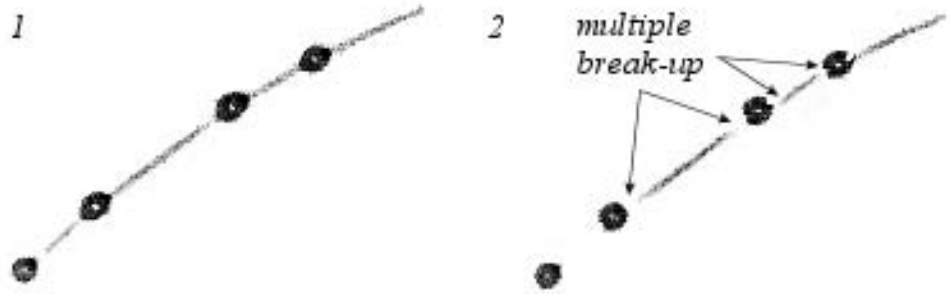

Figure 4.3: Experimental image, where the jet can be seen breaking up at multiple points along the jet. $\mathcal{W}e = 9.62, \mathcal{R}b = 0.834, \mathcal{O}h = 0.0418, \mathcal{R}e = 87.65$, ($\rho = 1026$ kg m^{-3}, $k = 0.060$ Pa s, $\alpha = 0.748$).

This includes occurrences of multiple break-up, coalescence and the formation of doublets.

Break-up of the jet at multiple points occurs on the pilot scale rig for Newtonian jets (Partridge et al., 2005) and is also observed to occur throughout all parameter ranges the experiments were performed at for shear thinning fluids (Figure 4.3). Multiple break-up occurs for both high and low rotation rates, although it appears to occur more frequently at higher rotation rates, possibly due to increased mechanical vibration from the shaft and motor driving the rotation of the can. As the rotation rate increases and multiple break-up occurs, longer chains of fluid break-up. Secondary break-up can then occur where the chains go on to break-up again (Figure

Figure 4.4: Experimental image, where the jet can be seen breaking into chains, consisting of multiple ligaments and drops. Secondary break-up will occur in theses chains. $\mathcal{W}e = 15.43, \mathcal{R}b = 0.633, \mathcal{O}h = 0.0375, \mathcal{R}e = 104.78$, ($\rho = 1025$ kg m^{-3}, $k = 0.012$ Pa s, $\alpha = 0.920$)

4.4). At high rotation rates this multiple break-up of chains dominates and it is unusual to have separate primary and satellite drops formed by pinch off.

The occurrence of doublets has also been observed. Rather than the fluid breaking into a primary and satellite droplet, instead two smaller primary droplets are formed, as shown in Figure 4.5. This occurs more frequently for increasing rotation rates.

4.1.2 Incoherent jets and absolute stability

It was not possible to obtain coherent results for all experimental parameters. As the apparent viscosity increased, the jet had increasing difficulty in emanating from the can orifice which brings into question the 'absolute stability' of the jet (Lin and Lian, 1990). In some parameter regimes, a coherent jet is not formed at the orifice and the jet breaks up or drips almost immediately as it leaves the orifice. By reducing the jet exit rotation rate (and hence the jet exit velocity) it was possible to observe this phenomena of the jet dripping or not jetting correctly at values of $\mathcal{W}e \sim 1$. (This is shown in Wong et al., 2004). This is likely to correspond with the

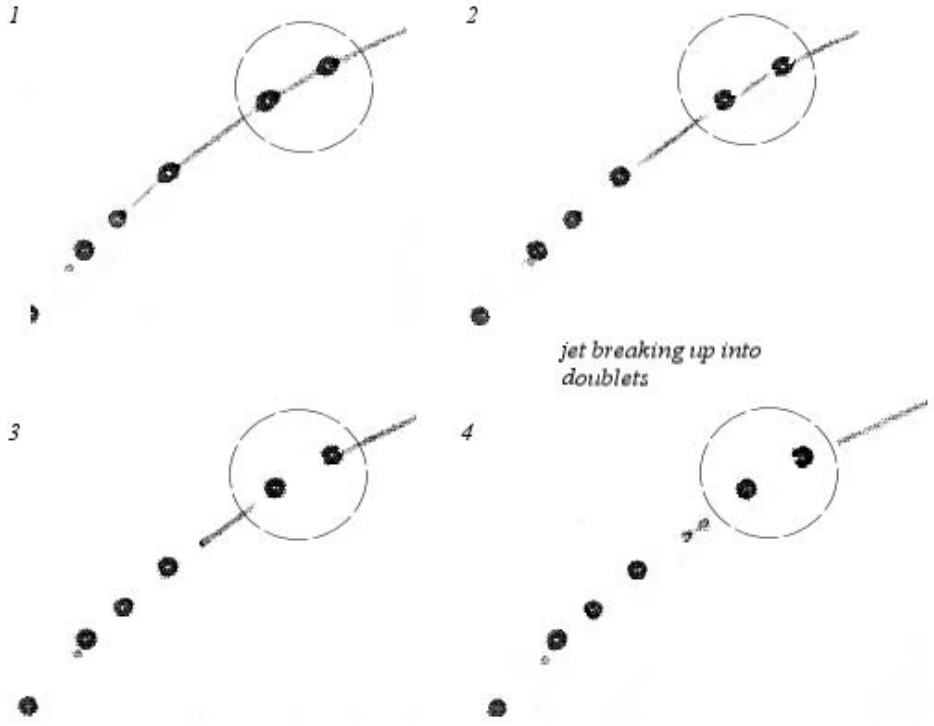

Figure 4.5: Experimental image, where the jet can be seen breaking into doublets. $\mathcal{W}e = 9.62, \mathcal{R}b = 0.834, \mathcal{O}h = 0.0418, \mathcal{R}e = 87.65$, ($\rho = 1026$ kg m^{-3}, $k = 0.060$ Pa s, $\alpha = 0.748$).

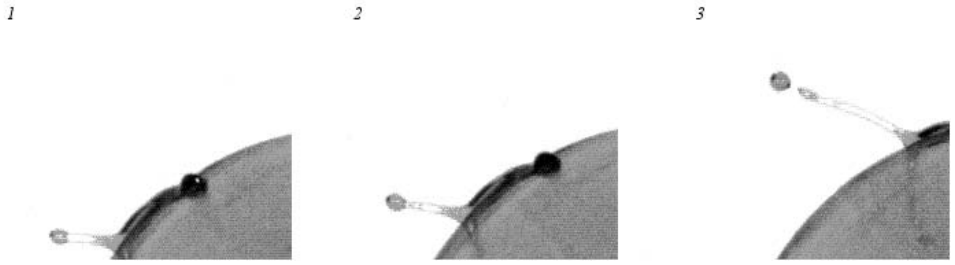

Figure 4.6: Absence of coherent jet when a = 0.0005 m . $\mathcal{W}e = 2.31, \mathcal{R}b = 0.50, \mathcal{O}h = 0.0360, \mathcal{R}e = 41.98$($\rho = 1025$ Kg m^{-3}, $k = 0.012$ Pa s, $\alpha = 0.92$)

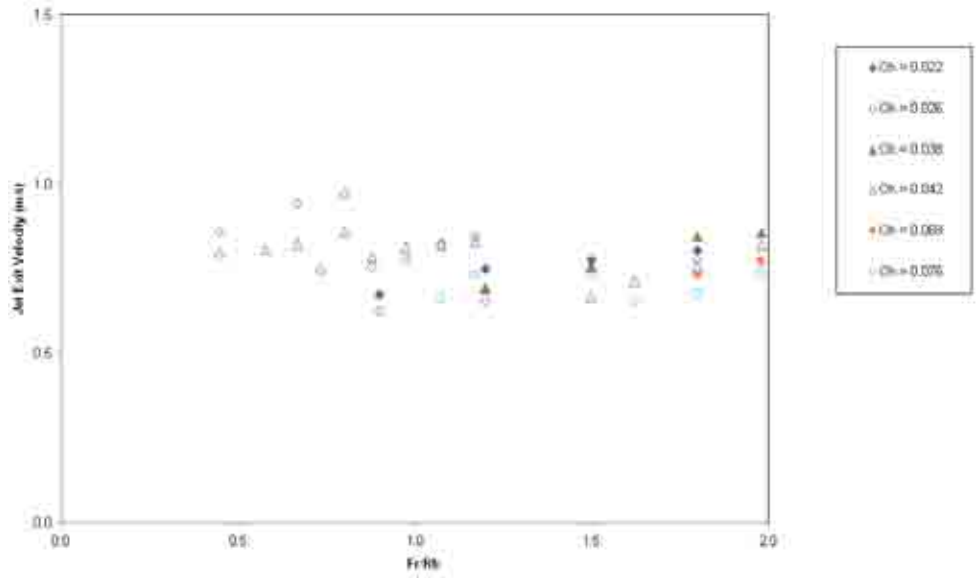

Figure 4.7: Influence of the rotation rate ($\mathcal{F}r/\mathcal{R}b$) on jet exit velocity for different viscosity fluids ($0.022 < \mathcal{O}h < 0.076$).

occurrence of a singularity at $\mathcal{W}e = 1$ as found in the work of Wallwork et al. (2002), Finnicum et al. (1993) and Baird and Davidson (1962).

In some cases, when a is small, it is also possible that the wall of the can poses significant resistance to flow, so that the drag force on the jet prevents flow through the orifice. When a was set to 0.0005 m, the jet had difficulty exiting from the can, even for fluids with low apparent viscosity. This is shown in Figure 4.6.

4.1.3 Effect of rotation rate and other parameters on exit velocity and break-up length

Figure 4.7 shows the influence of the rotation rate ($\mathcal{F}r/\mathcal{R}b$) on jet exit velocity. As Ω increases above zero, a centrifugal acceleration component, $s_0\Omega^2$, augments the gravitational force and hence the exit velocity increases. The increase is a weak function of $\mathcal{O}h$, showing similar behaviour to the Newtonian fluids used by Wong et al. (2004).

A plot of the exit velocity against Weber number can be seen in Figure 4.8. This shows that the jet exit velocity increases with respect to the Weber number with respect to $\mathcal{O}h$. The data can be grouped into two different sets, where the orifice size is $a = 0.0001$ and 0.00015. For a given exit velocity, it can be seen that the calculated Weber number is greater for the larger

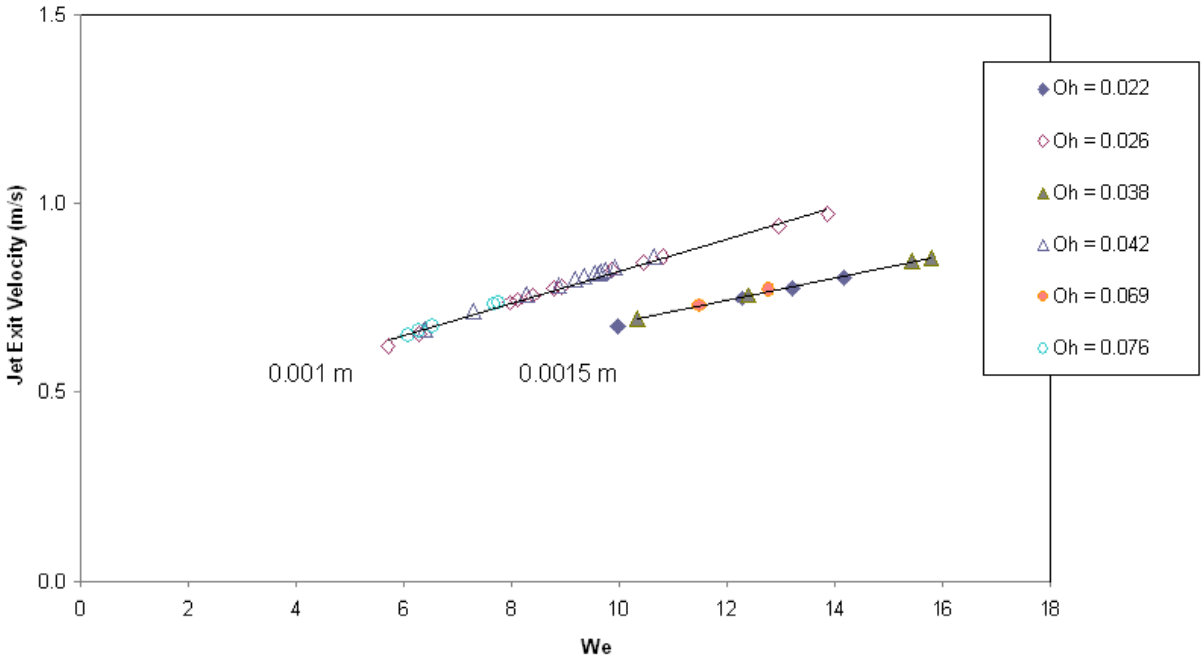

Figure 4.8: Influence of Weber number on jet exit velocity for different viscosity fluids ($0.022 < \mathcal{O}h < 0.076$).

orifice size.

The stability diagram for a straight jet usually consists of a plot of break-up length against jet exit velocity (i.e., break-up length against either $\mathcal{R}e$ or $\mathcal{W}e$), as this allows for different regimes to be elucidated (Wong et al., 2004). The laboratory scale experiments by Wong et al. (2004) showed no conclusive trends on this plot and for different viscosity fluids, the break-up length can either increase or decrease over the same range of $\mathcal{R}e$ or $\mathcal{W}e$. However, for shear thinning non-Newtonian fluids, Figure 4.9 indicates break-up length increases with Weber number with the rate of increase being a function of the value of $\mathcal{O}h$. Similarly, in Figure 4.10 it can be seen that while liquid properties dominate the break-up length, for each liquid system the break-up length does increase with increasing Reynolds number.

If a plot of the dimensionless break-up versus $\mathcal{F}r/\mathcal{R}b$ is considered a general trend emerges (see Figure 4.11). The data indicates that the break-up length increases with $\mathcal{F}r/\mathcal{R}b$, which is to be expected as increasing the rotation rate causes the trajectory of the jet to become more curved and the jet breaks up further away to the orifice.

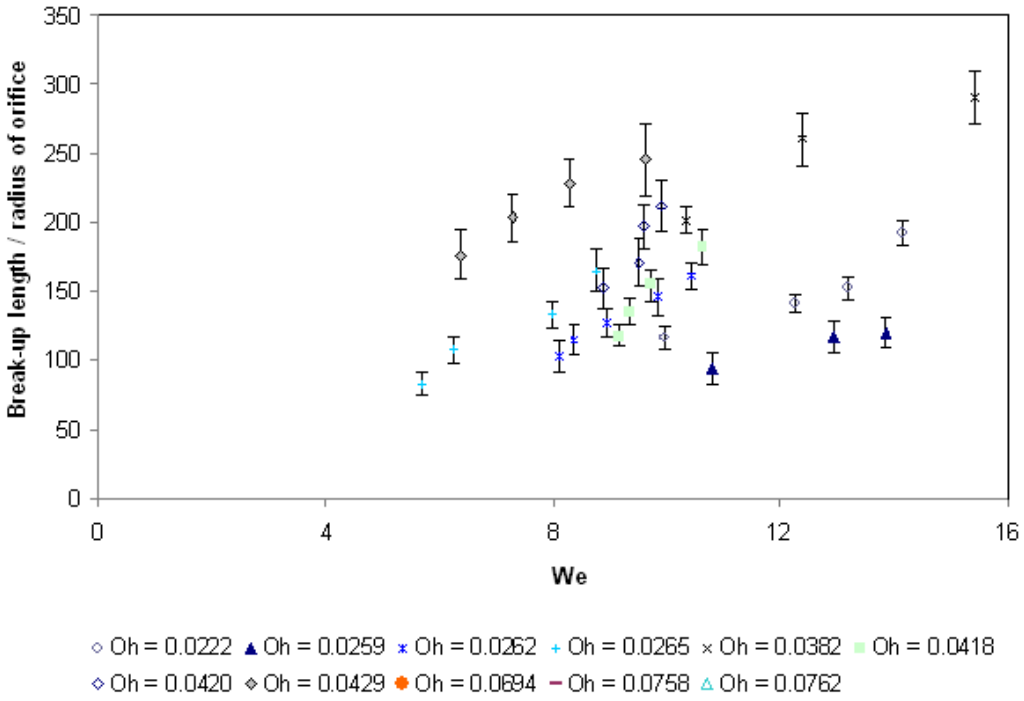

Figure 4.9: Influence of $\mathcal{W}e$ on break-up length of the spiralling jet for different viscosity fluids ($0.022 < \mathcal{O}h < 0.076$).

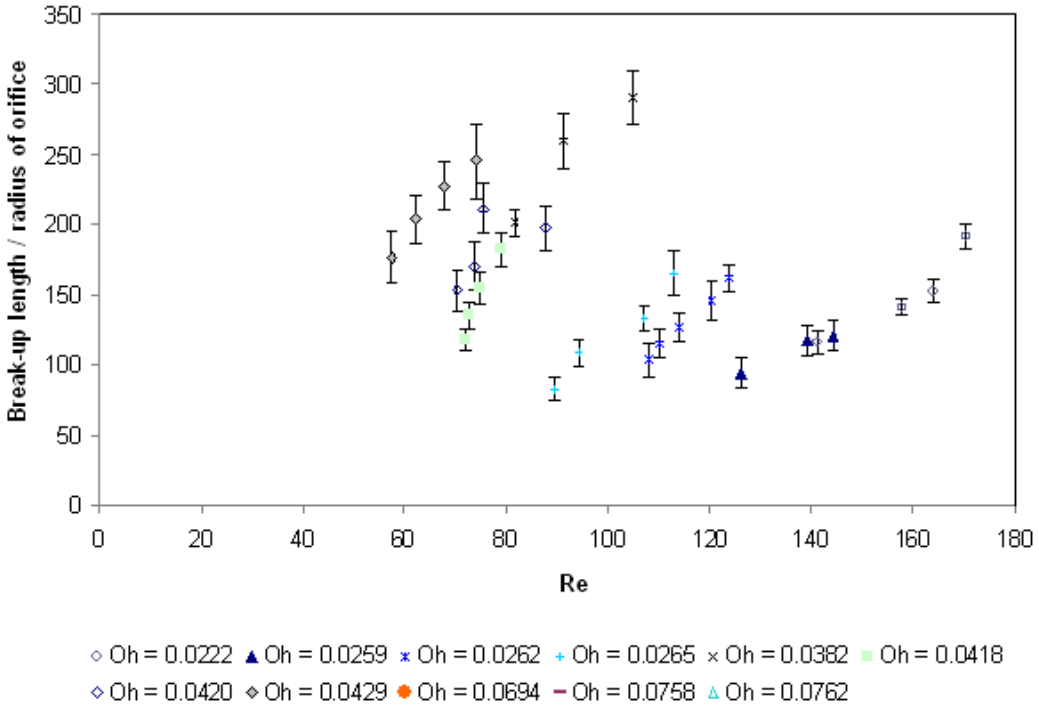

Figure 4.10: Influence of $\mathcal{R}e$ on break-up length of the spiralling jet for different viscosity fluids ($0.022 < \mathcal{O}h < 0.076$).

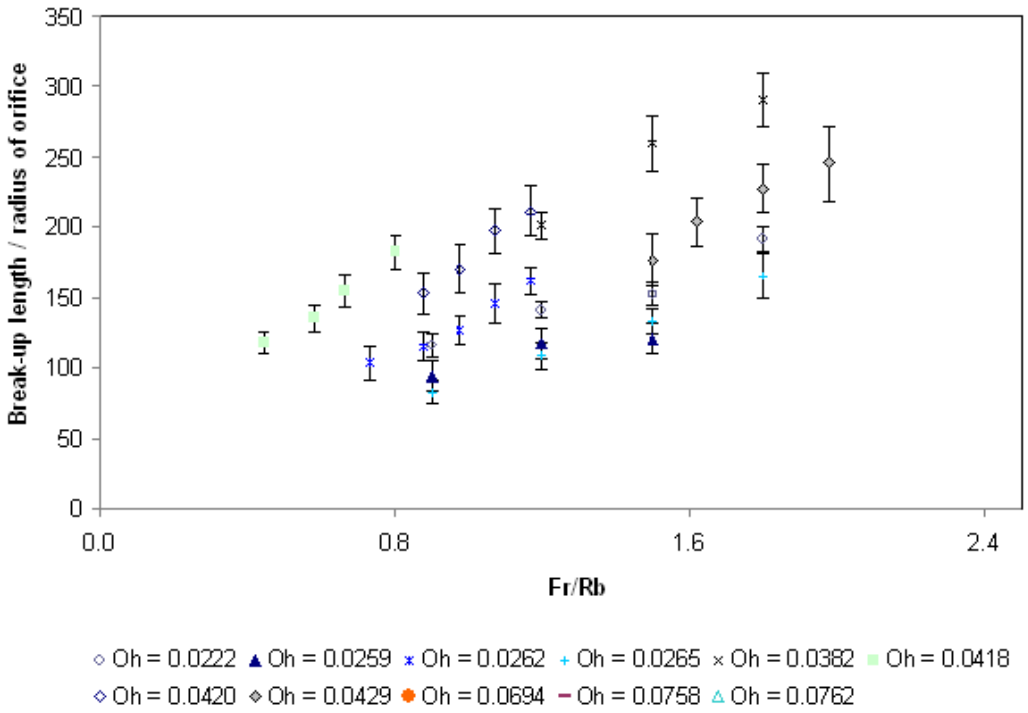

Figure 4.11: Influence of rotation rate upon break-up length of the spiralling jet for different viscosity fluids ($0.022 < \mathcal{O}h < 0.076$).

4.1.4 Drop size as a function of system parameters

Wong et al. (2004) and Partridge et al. (2005) carried out studies on the drop size distributions obtained for each break-up mode at the laboratory scale and pilot scale respectively. It was found that viscosity, rotation rate and exit velocity were all important in determining the drop size distributions. The key findings are given here, while some of the remaining measured drop size distributions can be found in Appendix A.1.

An example of drop size distributions for a shear thinning fluid is shown in Figure 4.12. Generally the drop size distributions for shear thinning fluids can be seen to progressively change from bimodal to unimodal as the apparent viscosity and rotation rate increases. As can be seen in Figure 4.12(a), at low rotational rates the distribution is unsurprisingly bimodal, with the smallest peak indicating the size of the satellite droplets and larger peak indicating the size of the main droplets. Increasing the rotation rate, and hence the exit velocity, causes the drop size distribution to become progressively more unimodal, with one broad peak, as seen in Figure 4.12(b) with the number of satellites further reducing, but the size of the satellites

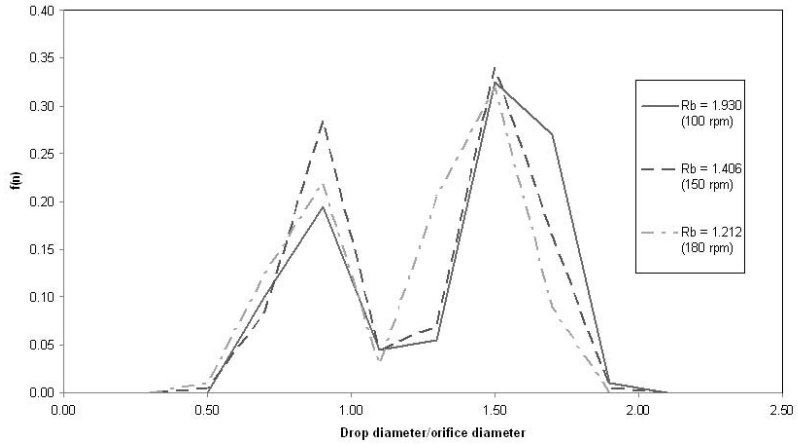

(a)

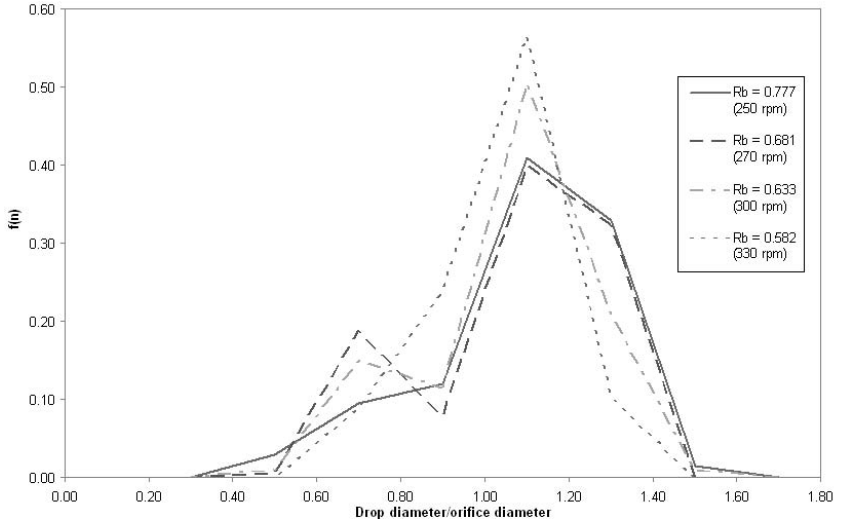

(b)

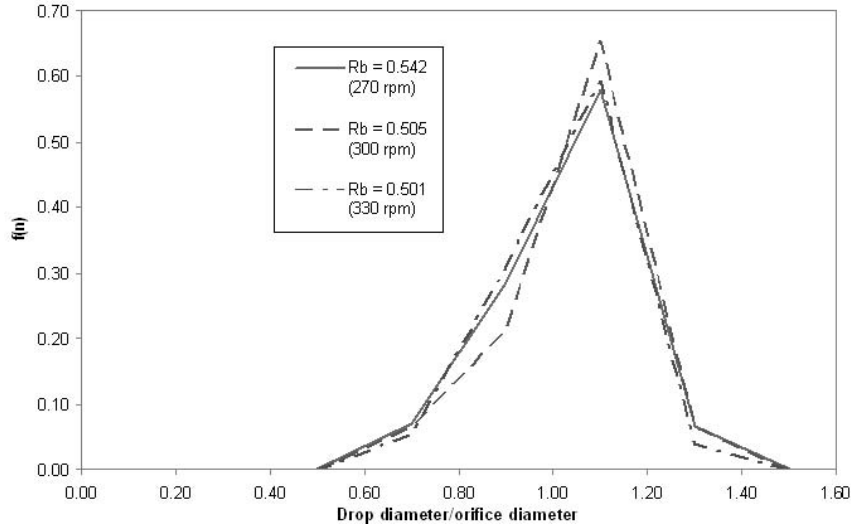

(c)

Figure 4.12: Drop size distributions for a solution of (a) 0.1% CMC with a liquid aspect ratio of $5/4$, flowing through a nozzle of diameter 0.002 m, (b) 0.2% CMC with a liquid aspect ratio of $2/3$, flowing through a nozzle of diameter 0.002 m, (c) 0.3% CMC with a liquid aspect ratio of $2/3$, flowing through a nozzle of diameter 0.002 m.

apparently increasing as Ω increases. For solutions with high apparent viscosity, indicated by Figure 4.12(c) it can be seen that the drop size distributions become more strongly unimodal.

The effect of the Ohnesorge number on drop sizes (and velocity[1]) can be seen in Figure 4.13(a). The lines shown on this graph and in Figures 4.13(b) - 4.13(c) are shown to guide the eye. With increasing Ohnesorge number (increasing apparent viscosity) the size of the primary and satellite droplets decreases slightly. This is the same trend as for Newtonian fluids as reported by Wong et al. (2004). Viscous forces act as a damping mechanism on the wave growth by impeding surface perturbations on the jet. So more viscous jets tend to remain intact for longer, increasing break-up length and eventually breaking into droplets that are smaller in size.

Figure 4.13(b) shows the effect of altering the rotation rate on the drop size. The Rossby number is inversely proportional to the rotation rate of the can and increasing the can rotation rate corresponds to a decrease in $\mathcal{R}b$ and an increase in exit velocity, which can be seen to reduce both the primary and satellite drop sizes, although the decrease is more significant for the primary drops. Wong et al. (2004) showed that in Newtonian fluids, increasing the rate of rotation (decreasing $\mathcal{R}b$) reduced the primary drop sizes although the satellite drop sizes were only marginally affected.

The effect of jet exit velocity upon average primary and satellite drop size is shown in Figure 4.13(c). For the data presented for the 3 mm diameter nozzle, the size of both primary and satellite droplets can be seen to slightly decrease with increasing U, however for the 2 mm diameter nozzle there is no conclusive trend. For low exit velocities the growth rate of capillary waves is determined by a balance of surface tension and viscous forces alone, while inertial forces are insignificant. As the exit velocity increases, inertial forces become increasingly important and increase the growth rate of the disturbance (Eggers, 1997).

[1]The Ohnesorge number is defined as $\mathcal{O}h = \sqrt{\mathcal{W}e}/\mathcal{R}e$ and so as the Reynolds number for non-Newtonian fluids is defined as $\mathcal{R}e = (\rho/k)\,(a^{\alpha}U^{2-\alpha})$ the Ohnesorge number becomes velocity dependent

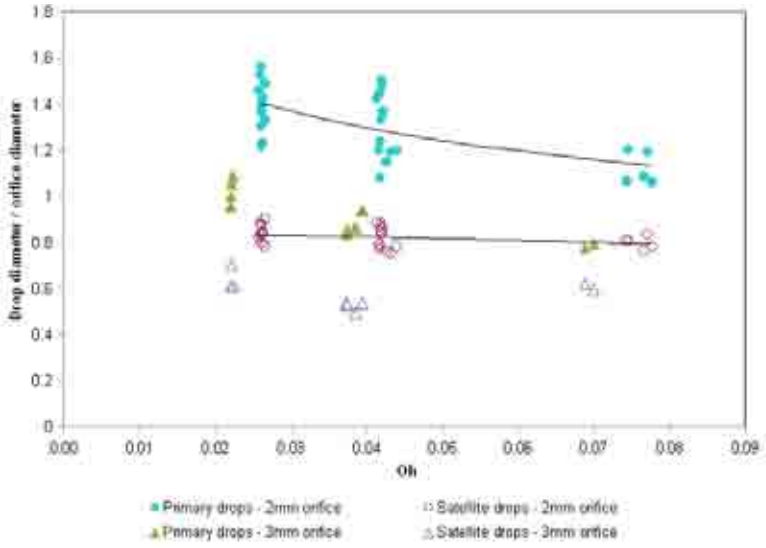

(a) Effect of Ohnesorge number on primary and corresponding satellite drop sizes.

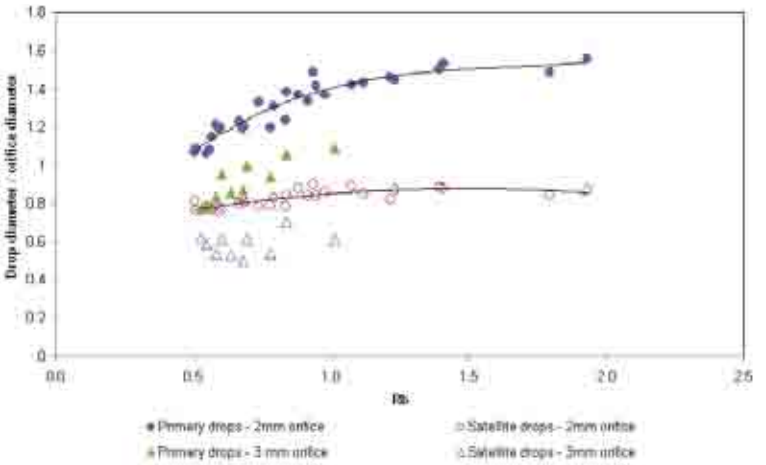

(b) Effect of Rossby number on primary and corresponding satellite drop sizes.

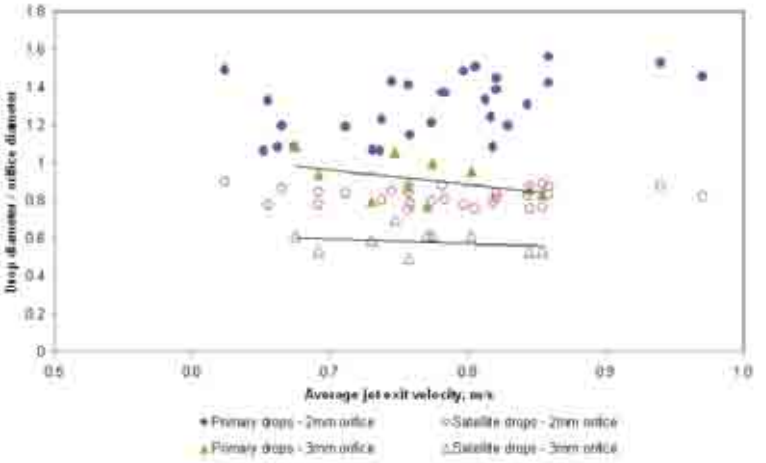

(c) Effect of average jet exit velocity on primary and corresponding satellite drop sizes.

Figure 4.13: Effect of various parameters on primary and corresponding satellite drop sizes.

4.2 Shear thickening fluids

Yarin (1993) investigated power law liquid jets numerically to reveal the so called 'sausage' shaped droplets for shear thinning liquids and large spherical droplets resembling the 'beads-on-string' setup for shear thickening liquids.

It was not possible to perform the same number of experiments for shear thickening liquids that fitted the power law model as for shear thinning liquids. For small orifice radius, a, considerable problems were experienced both with liquid exiting from the can and with forming coherent jets. Consequently it was only possible to examine shear thickening liquid jets at $a = 0.0015$. The parameter ranges examined are given in Table 3.4.

While the break-up mechanism appeared different to that seen for shear thinning liquid jets, very little variation was seen for the parameter ranges examined and break-up appears to be qualitatively similar to M3 break-up for Newtonian liquid jets as seen in Wong et al. (2004).

It was observed in Uddin (2007), when non-linear jet simulations were performed, that for shear thickening liquids the drops were particularly well formed and the ligaments between them were clear. This is also true experimentally (Figure 4.14). For shear thickening jets, the disturbances have a long wavelength and simultaneous break-up points are observed, with long thin ligaments forming in between the main droplets. These subsequently contract and break-up into satellite droplets, leading to a bimodal drop size distribution (Figures 4.15 and 4.16). All these features can be observed in Figure 4.14. It can also be seen that the break-up resembles the 'beads-on-string' phenomena where the jet assumes the geometry of spherical droplets connected by long slender ligaments.

The drop size distributions obtained were all bimodal and similar to those displayed in Figure 4.15. Droplets were observed to become increasingly well formed and more like the beads on string shape for increasing rotation rate and apparent viscosity. This corresponds with an increasing number of satellite droplets (for 40% starch an almost symmetrical distribution is obtained as in Figure 4.16) as they are individually formed from the ligaments contracting. For lower rotation rates there is a tendency for the ligaments to contract whilst still attached to the

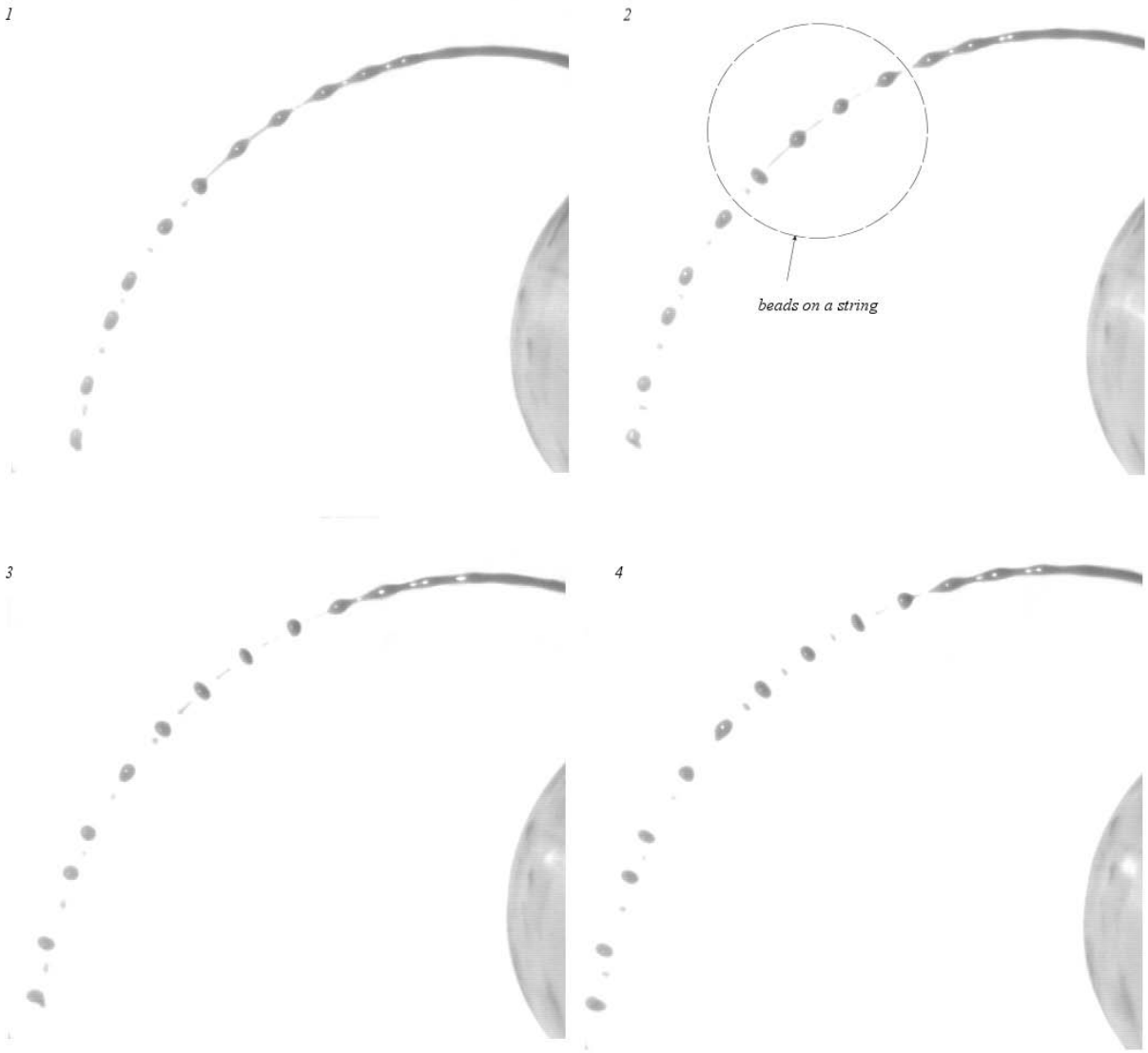

Figure 4.14: Break-up can be seen to resemble the 'beads-on-string' phenomena.

main droplet, forming larger primary droplets.

In Uddin (2007) non-linear simulations suggest that when the cylindrical drum rotates with a high rotation rate, the break-up length of shear thickening liquid jets increases significantly (as the apparent viscosity begins to increase) and at the same time larger droplets are produced once break-up takes place, in comparison with shear thinning liquid jets.

As can be seen in Figure 4.17, the break-up obtained for shear thickening jets is shorter than for shear thinning jets on the laboratory scale, which is contrast to the work of Uddin (2007). Figure 4.18, which compares the sizes of primary and satellite droplet sizes for shear thinning and shear thickening jets, shows that while shear thickening jets do indeed produce

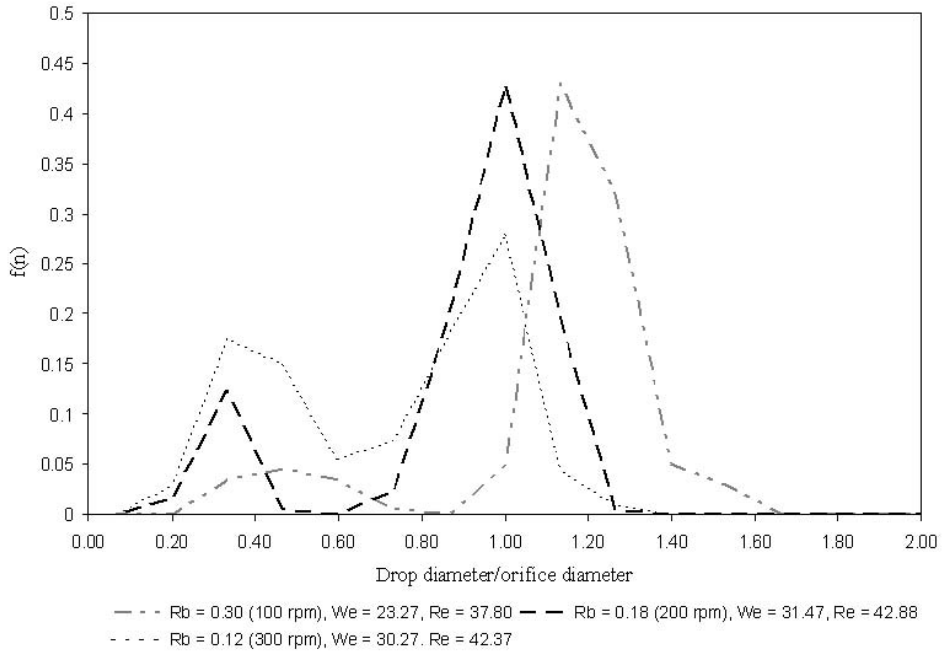

Figure 4.15: Drop size distributions for a solution of 35% Starch with a liquid aspect ratio of $2/3$, flowing through a nozzle of diameter 0.003 m.

slightly larger primary droplets in most cases, when compared to shear thinning jets, there is more variation with the satellite droplets produced, which, in some cases, are smaller.

However, as can be seen from Figures 4.17 and 4.18 the shear thickening and shear thinning jets are operating in very different parameter ranges, with $\mathcal{F}r/\mathcal{R}b$ being significantly higher for shear thickening jets. Due to the limited number of experiments possible to perform for shear thickening jets, it was not possible to obtain shear thickening jets in the same dimensionless parameters ranges as shear thinning jets. This difference in ranges makes a comparison difficult and could explain why there are discrepancies with the behaviour predicted by Uddin (2007).

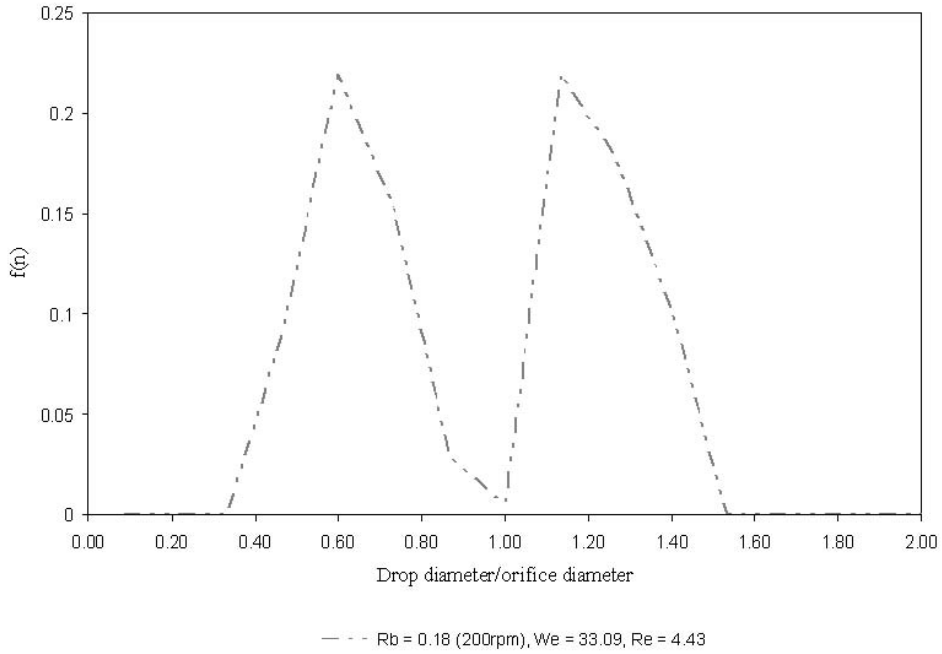

Figure 4.16: Drop size distribution for a solution of 40% Starch with a liquid aspect ratio of $2/3$, flowing through a nozzle of diameter 0.003 m.

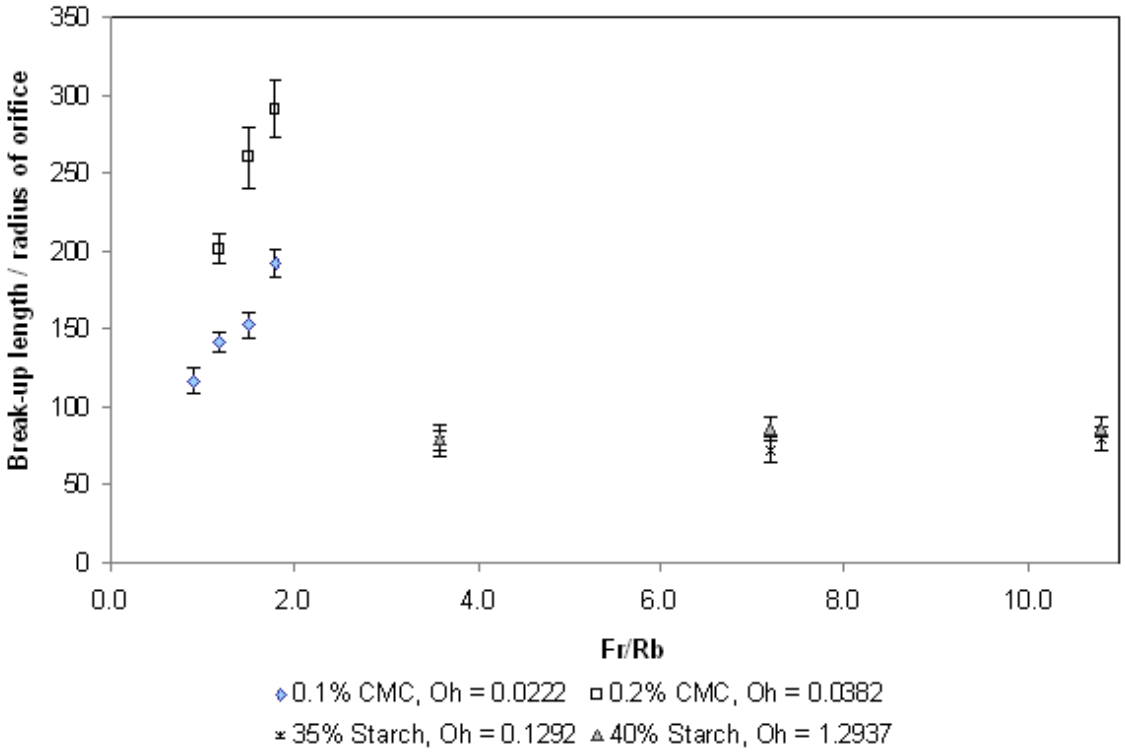

Figure 4.17: The effect of rotation rate on the break-up length for shear thickening and shear thinning jets flowing through a nozzle of diameter 0.003 m, with an aspect ratio of $2/3$.

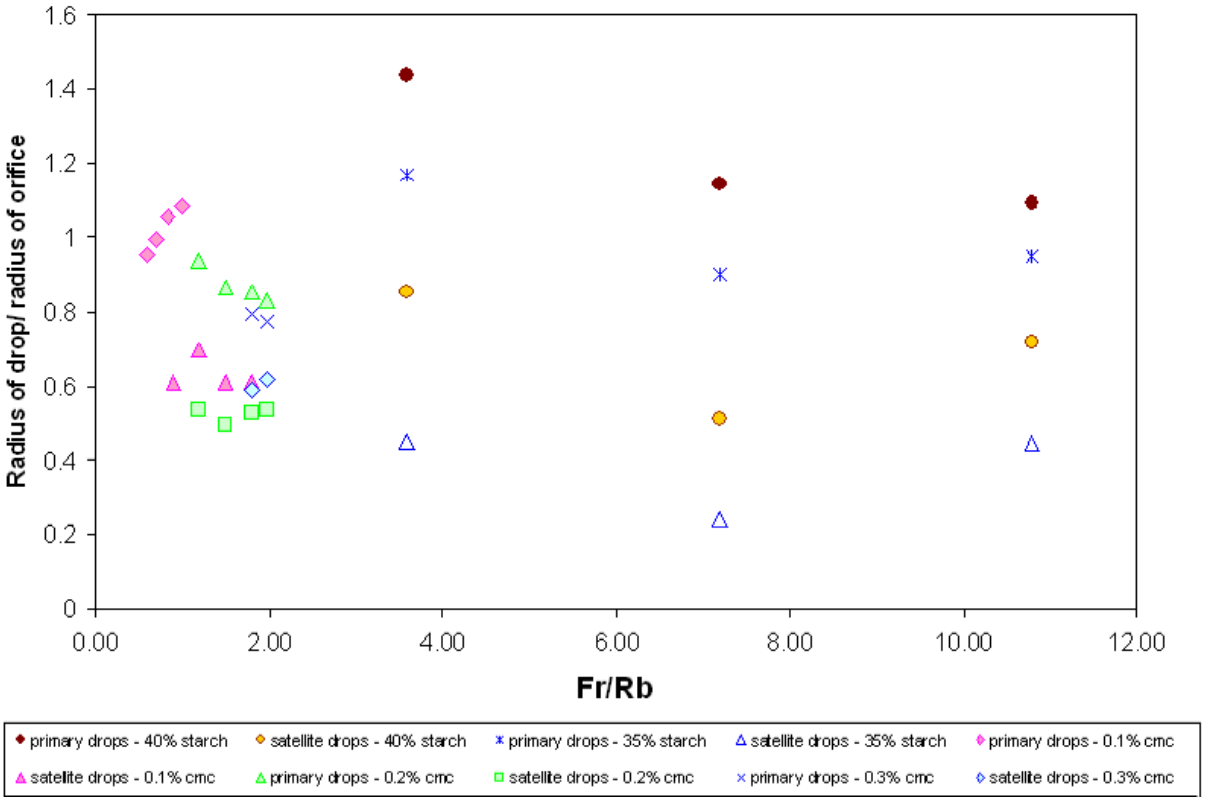

Figure 4.18: The effect of rotation rate on the primary and satellite drop size for shear thickening and shear thinning jets flowing through a nozzle of diameter 0.003 m, with an aspect ratio of $2/3$.

4.3 Conclusions

Analysis was performed on the break-up mechanisms and droplet formation of both shear thinning and shear thickening liquid jets emerging from the side of a perforated can rotating about its vertical axis at the laboratory scale. These results were compared to experiments performed by Wong et al. (2004) for Newtonian fluids on the laboratory scale.

The shear thinning fluids examined were observed to display unique characteristics of break-up that differ to those found for Newtonian fluids with two different mechanisms of satellite droplet formation being found. The ligaments were observed to stretch between the main droplets with a curvature normal to the curved central axis of the jet. This curvature was found to become more dramatic with increasing apparent viscosity and rotation rate.

Break-up length was found to increase with increasing apparent viscosity and rotation rate of the fluid. The drop size distributions obtained were found to differ from those achieved for Newtonian fluids. Drop size distributions appear to progressively change from bimodal to unimodal, as the apparent viscosity and rotation rate increase, with increasing numbers of primary droplets than satellite droplets found. The size of primary droplets decreased with increasing rotation rate, but satellite droplets were found to be only marginally affected.

The break-up mechanism of shear thickening liquid jets was found to be different to that obtained for shear thinning liquid jets, with very little variation for the parameter ranges examined. Break-up appeared to be qualitatively similar to M3 break-up for Newtonian liquid jets, with droplets being particularly well formed. The 'beads-on-string' phenomena was also commonly observed for increasing rotation rate and apparent viscosity. The drop size distributions for shear thickening fluids obtained were all bimodal, with larger primary droplets found for lower rotation rates due to the tendency for the ligaments to contract whilst still attached to the main droplet.

Comparisons between shear thinning and shear thickening liquid jets were difficult to make due to the large difference in dimensionless parameter ranges between the fluids used.

CHAPTER 5

PILOT SCALE STUDY OF CURVED JET BREAK-UP USING PSEUDOPLASTIC FLUIDS AND FLUIDS CONTAINING SURFACTANTS

Following the initial experiments detailed in Chapter 4, the dynamics of the break-up of curved jets of pseudoplastic (shear thinning) liquids is examined in more detail using experimental and numerical methods in this Chapter.

A pilot scale experimental facility is used, where the jet emanates from an orifice near the base of a cylindrical drum of 0.285 m diameter, rotating about its vertical axis. Images of the jet trajectory, break-up and of the drops formed are captured using a high speed camera. As a larger exit velocity can be attained on the pilot scale rig, a larger range of parameters can be studied. On the laboratory scale it was found that exit velocity had a significant influence on the break-up mechanisms of a non-Newtonian jet. Experiments on the pilot scale rig should provide more realistic insights into break-up on an industrial scale.

The liquid rheology is again fitted using a power law model, with the power law index, α, and consistency index ranging between $0.654 - 0.920$ and $0.012 - 0.199$ Pa s$^{\alpha}$ respectively. The influence of these parameters, along with the rotation rate ($30 - 300$ rpm) and the orifice size (radius 0.001 and 0.0015 m) upon the jet break-up and drop size distributions produced is examined. Significant features of the break-up dynamics are shown to be attributed to the shear-thinning effects of the fluid.

Experiments performed on the pilot scale are compared with simulations of the shape of the

jet's free surface, generated from a non-linear finite difference model (Uddin et al., 2008a). It is shown that the model can be used with reasonable accuracy to predict primary drop size, but that it is less accurate when used to predict the size of satellite droplets.

Section 5.3 also details the results of a brief study examining the influence of varying surface tension along the jet, using surfactants.

5.1 Shear thinning fluids

5.1.1 Prediction and features of break-up

Similarly to the results found in Chapter 4, over the parameter ranges studied (given in Table 3.5), the shapes of the jets upon break-up did not resemble the modes observed for Newtonian jets by either Wong et al. (2004) or Partridge et al. (2005). However, marked differences were observed as shown in images of the break-up of the jets (Figures 5.1 and 5.2). Similarly to experiments on the laboratory scale, at low values of Ω, axisymmetric disturbances are observed, but these rapidly become non-axisymmetric as the rotational speed of the drum is increased. A typical example of non-axisymmetric break-up is shown in Figure 5.1(a). Typically, the primary droplets are formed from the growth of long wavelength instabilities ($\lambda >> a$) with long ligaments being formed in-between the main droplets. The ligaments will sometimes break from one end and contract to form a satellite droplet which merges with the main droplet, or forms a separate satellite droplet (both shown in Figure 5.1(b)). In addition, on the pilot scale the ligament was also observed to shatter to form several satellite droplets which are approximately an order of magnitude smaller than the primary droplets (Figure 5.1(c)). These mechanisms apply to both kink and varicose disturbances. This was not observed on the laboratory scale.

As observed on the laboratory scale, the ligaments appear to stretch between the main droplets with a curvature normal to the curved central axis of the jet (Figure 5.1(a)). This curvature again increases with apparent viscosity, η and Ω. While curvature of the ligaments was observed on the laboratory scale it can be seen that the effects are far more dramatic on the pilot scale. Figure 5.1(a) shows that the curvature of the ligaments can be so severe that the centre-line of the jet can be completely displaced. Since the ligaments in between droplets for

(a)

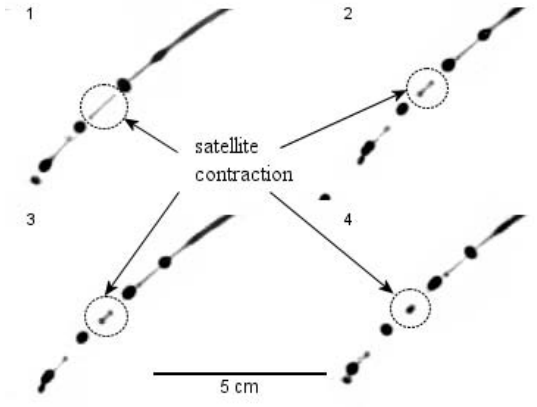

(b)

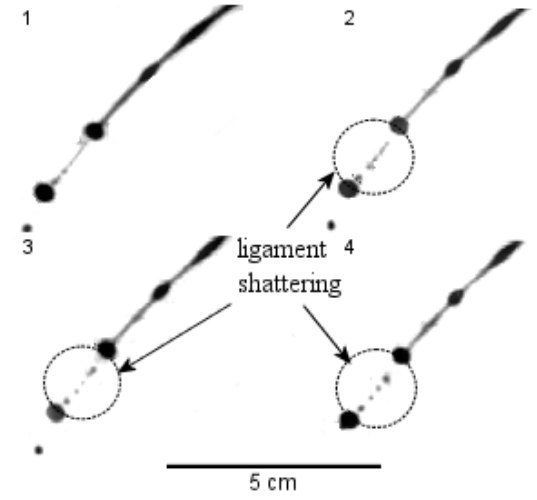

(c)

Figure 5.1: Experimental images showing (a) non-axisymmetric disturbances along the jet ($\mathcal{W}e = 65.99, \mathcal{R}b = 0.473, \mathcal{O}h = 0.0519, \mathcal{R}e = 156.31, \rho = 1027$ kg m^{-3}, $k = 0.199$ Pa s, $\alpha = 0.654$), (b) satellite droplets being formed by contraction of the ligaments between the primary droplets and (c) the ligament shattering ($\mathcal{W}e = 5.37, \mathcal{R}b = 0.552, \mathcal{O}h = 0.0229, \mathcal{R}e = 101.00, \rho = 1025$ kg m^{-3}, $k = 0.0120$ Pa s, $\alpha = 0.920$)

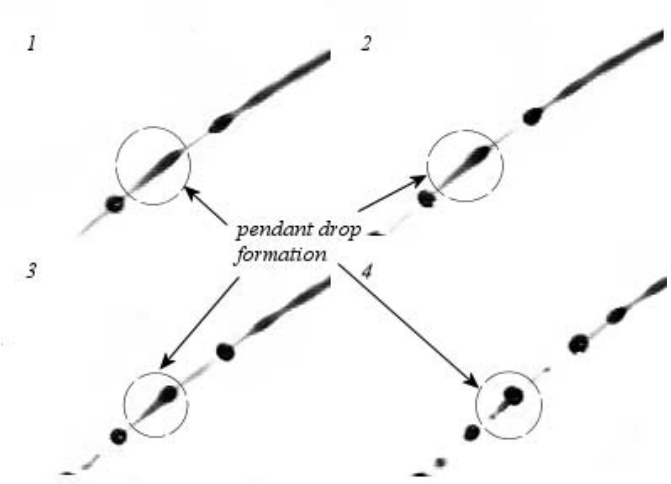

Figure 5.2: Experimental images showing pendant drop formation

shear thinning fluids are much longer and thinner than those observed for Newtonian fluids, a likely explanation is that their much reduced mass makes them more susceptible to the effects of air resistance.

The formation of pendant-shaped drops, shown in Figure 5.2, is another observed feature, described as 'torpedo-like' (Davidson and Cooper-White, 2006). This typically occurs at low rotation rates and low apparent viscosity and was not detected on the laboratory scale. As the jet thins and the droplet begins to form, the neck of the pendant remains notably thicker, of the order of a, than the usual connecting ligaments while the tail thins in the usual way. Pinch-off occurs at the thick neck and the thin tail, leaving a tear-shaped droplet which then contracts under the action of surface tension to form a sphere. This mode of break-up was not observed in the previous experimental studies (Wong et al., 2004; Partridge et al., 2005), although Davidson and Cooper-White (2006) refer to the evolution of pendant drops in the break-up of straight jets using both Newtonian and non-Newtonian fluids. Observed mechanisms of formation of satellite drops in the presence of pendant drops are: contraction of the ligament, or shattering of the ligament, as shown in Figure 5.1.

The formation of pendant drops and axisymmetric disturbances can be roughly grouped on the $\mathcal{O}h - \mathcal{W}e$ flow regime map as shown in Figure 5.3, with pendant drop formation more readily observed at lower values of $\mathcal{W}e$ (lower Ω) and $\mathcal{O}h$ (lower η).

The introduction of the rotation rate into the prediction of features complicates the analysis;

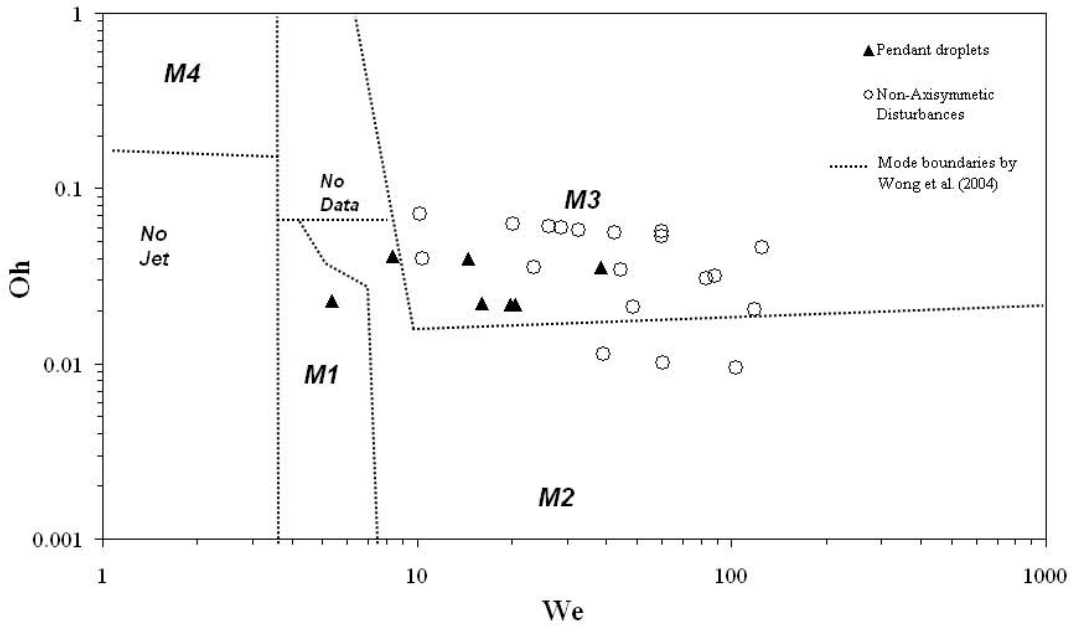

Figure 5.3: A flow map showing features of break-up observed for shear thinning fluids.

since the jet exit velocity is affected by the centrifugal forces generated due to the rotation of the can, these two variables are coupled.

A plot of the Ohnesorge number against the Rossby number (Figure 5.4(a)) illustrates that while regions corresponding to Newtonian break-up modes can be identified (see (Wong et al., 2004) for more details), there is some overlap in the prediction of pendant droplets and non-axisymmetric disturbances. In this overlap, it would not be possible to predict features of jet break-up.

A plot of the Ohnesorge number against $\mathcal{F}r/\mathcal{R}b$ (Figure 5.4(b)) shows less of an overlap between the two features detailed and suggests that as the rotation rate is increased the features observed are likely to move from that of pendant droplets to that of non-axisymmetric disturbances. Pendant drops appear to be associated with low exit speeds, this would explain why they disappear as Ω, and $\mathcal{F}r/\mathcal{R}b$, increases. Similarly to the experiments performed on the laboratory scale, features such as multiple break-up, coalescence and doublets can be observed throughout, however, there appears to be an increase in the number of multiple break-up points observed and an increasing rate of drop collisions at higher rotation rates.

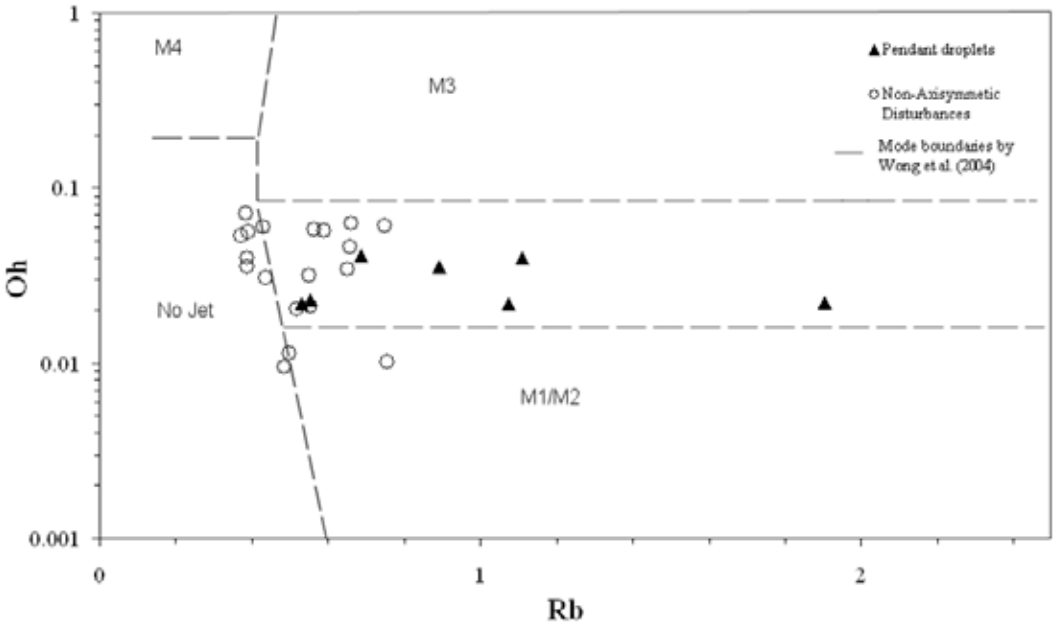

(a) $\mathcal{O}h$ versus $\mathcal{R}b$

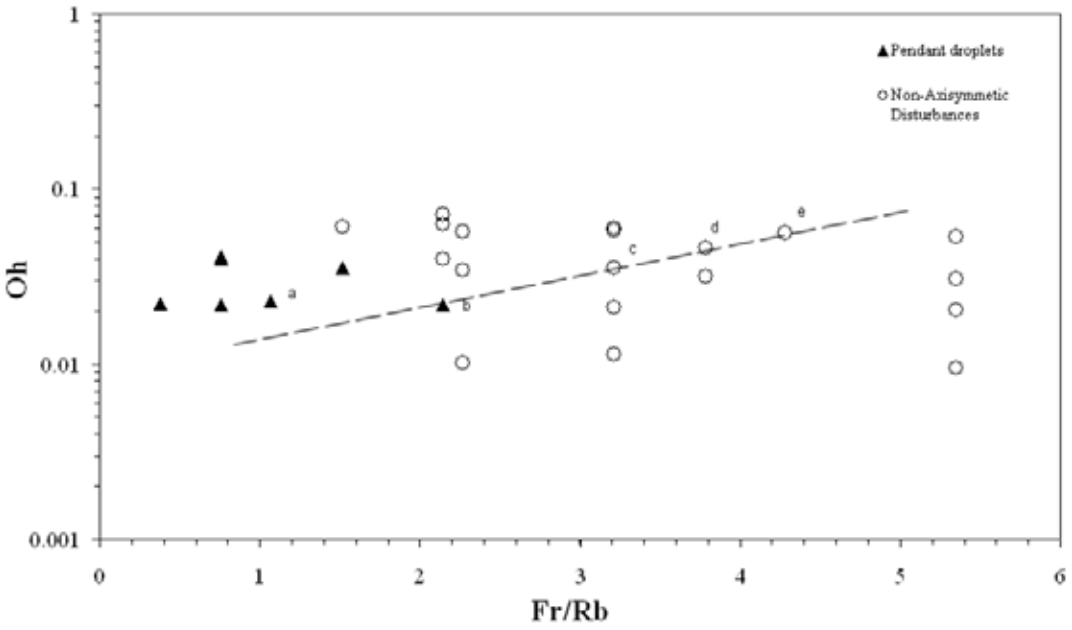

(b) $\mathcal{O}h$ versus $\mathcal{F}r/\mathcal{R}b$

Figure 5.4: Flow maps showing features of break-up for shear thinning fluids.

If we are to take parameter values along the diagonal line shown in Figure 5.4(b) we can examine how the features observed change with increasing rotation rate and Ohnesorge number, images corresponding to points (a) - (e) are shown in Figure 5.5. Figure 5.5(a) shows that the jet is still axisymmetric. The same is true in Figure 5.5(b). In Figure 5.5(c) the jet is now non-axisymmetric and becomes more so in Figures 5.5(d) and 5.5(e), with the centreline being displaced and the ligaments becoming increasingly frail and elongated.

Incoherent jets

There were some limitations in running the experiments and it was not possible to obtain coherent results for all parameter ranges. Occurrences of incoherent jets, as seen on the laboratory scale, were common for low rotation rates when the Weber number was close to 1.

At high rotation rates, for increasing apparent viscosity, there were also cases where, due to the extreme length of the jet before break-up, the jet would spiral around the can making it increasingly difficult to capture the break-up length.

At low rotation rates, at high apparent viscosity, there were also occurrences where the jet hit the bottom of the rig before break-up.

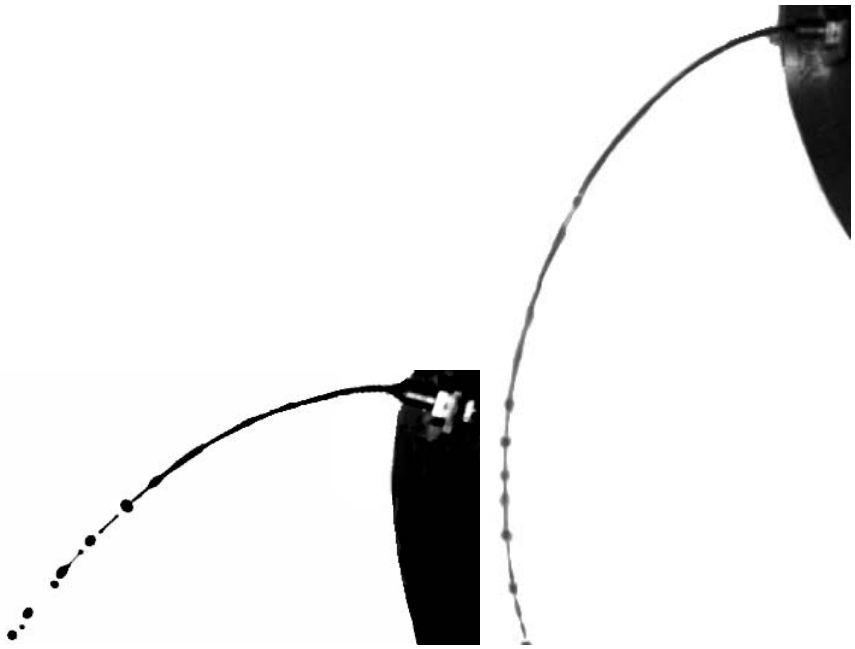

(a) $\mathcal{W}e = 5.37, \mathcal{R}b = 0.5523, \mathcal{O}h = 0.0220, \mathcal{R}e = 100.99, \rho = 1025$ kg m^{-3}, $k = 0.012$ Pa s, $\alpha = 0.920$

(b) $\mathcal{W}e = 19.76, \mathcal{R}b = 0.5295, \mathcal{O}h = 0.0218, \mathcal{R}e = 203.99, \rho = 1025$ kg m^{-3}, $k = 0.012$ Pa s, $\alpha = 0.920$

(c) $\mathcal{W}e = 23.50, \mathcal{R}b = 0.5875, \mathcal{O}h = 0.0356, \mathcal{R}e = 136.11, \rho = 1026$ kg m^{-3}, $k = 0.061$ Pa s, $\alpha = 0.748$

(d) $\mathcal{W}e = 124.68, \mathcal{R}b = 0.6580, \mathcal{O}h = 0.0460, \mathcal{R}e = 242.54, \rho = 1027$ kg m^{-3}, $k = 0.199$ Pa s, $\alpha = 0.654$

(e) $\mathcal{W}e = 46.23, \mathcal{R}b = 0.4885, \mathcal{O}h = 0.0558, \mathcal{R}e = 121.68, \rho = 1027$ kg m^{-3}, $k = 0.199$ Pa s, $\alpha = 0.654$

Figure 5.5: Features of break-up illustrated at different points along the flow map (a) - (e).

5.1.2 Lengths of ligaments and wavelengths

It has been noted that for all shear thinning liquids examined, that one of the most obvious features of break-up which differs to that of Newtonian break-up is non-axisymmetric distur-

bances down the jet and extreme curvature of the ligaments. It has also been noted that the lengths of these ligaments do not appear to be of a constant length. Instead there appears to be a huge variation between the lengths of the ligaments even in a single experiment. Similarly, it also appears that the wavelengths of the waves travelling down the jet are not as uniform as for Newtonian fluids. It is these observations that has led to the following attempt to quantify the lengths of ligaments and the wavelengths for different liquid systems and rotation rates.

For each liquid system at varying rotation rates at least 50 ligament lengths and wavelengths were measured, to try and establish if there was any correlation in the ligament length. Figure 5.6 shows a typical ligament distribution diagram for a shear thinning non-Newtonian liquid. Similar frequency distributions were obtained for all liquid systems examined. Figure 5.7 shows

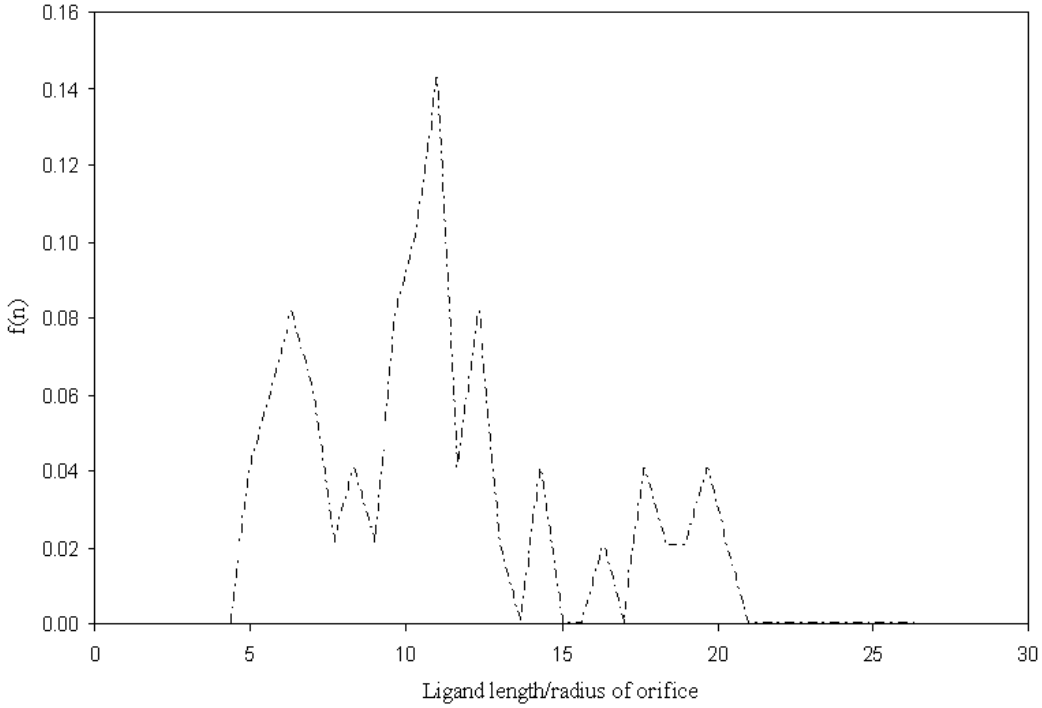

Figure 5.6: Ligament distribution diagram for a solution of 0.3% CMC. $\mathcal{W}e = 28.78, \mathcal{R}b = 0.429, \mathcal{O}h = 0.0559, \mathcal{R}e = 89.4307, \rho = 1027$ kg m^{-3}, $k = 0.199$ Pa s, $\alpha = 0.654$

the average lengths of ligaments measured for various liquid systems, where the error bars represent the standard deviation which in some cases is as high as 50%. The lines on Figure 5.7 and on Figure 5.8 are shown to guide the eye. As can be seen from Figure 5.7 for increasing

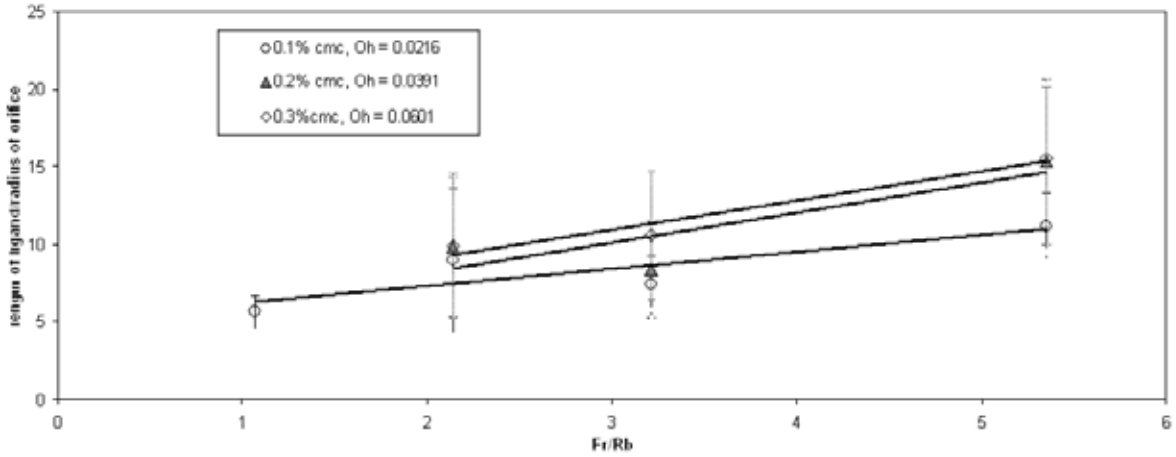

Figure 5.7: Length of ligaments against $\mathcal{F}r/\mathcal{R}b$ for 0.1%, 0.2% and 0.3% CMC solutions.

rotation rate (increasing $\mathcal{F}r/\mathcal{R}b$), as well as increasing apparent viscosity (represented by the different liquid systems), there is a general increase in the lengths of ligaments observed. However, the standard deviation is very large, as a wide sample of ligament lengths was found for each rotation rate and liquid system. Hence, the distributions obtained are likely to be too wide for any differences to be statistically valid.

Figure 5.8 shows the average wavelengths measured for various liquid systems, with the error bars representing the standard deviation. Figure 5.8 shows that the same trends occur for wavelengths as ligaments and that the average wavelength can be seen to increase for increasing rotation rate and increasing apparent viscosity. The standard deviations obtained here are slightly smaller than for the ligament lengths, suggesting there will be a smaller distribution of values.

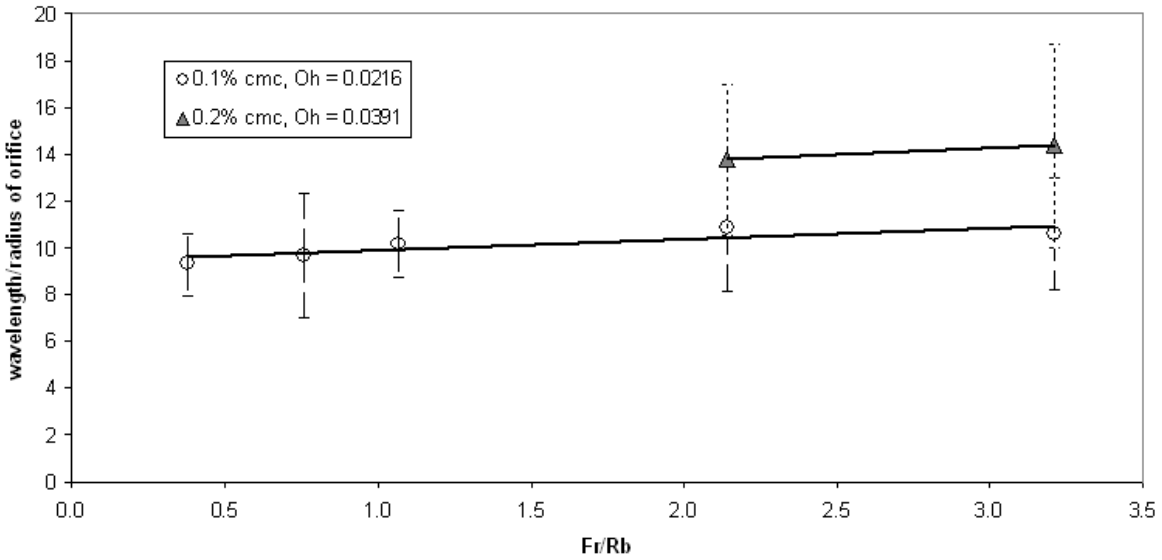

Figure 5.8: Wavelengths against $\mathcal{F}r/\mathcal{R}b$ for 0.1% and 0.2% CMC solutions.

5.1.3 Influence of system parameters on exit velocity and break-up length

The effect of Rossby number on jet exit velocity is shown in Figure 5.9. The data from the laboratory scale is also shown and it can be seen that the jet exit velocity achieved on the pilot scale, as expected, is much higher than that obtained on the laboratory scale.

The influence of rotation rate, $\mathcal{F}r/\mathcal{R}b$, on exit velocity is examined in Figure 5.10. A similar trend to that determined on the laboratory scale is observed, where the exit velocity, as a weak function of $\mathcal{O}h$, increases with respect to $\mathcal{F}r/\mathcal{R}b$.

For shear thinning fluids, unlike the Newtonian fluids examined by Wong et al. (2004), where no conclusive trends were found, it is indicated by Figure 5.11(a) and 5.11(b) that break-up length increases with both increasing Weber number and Reynolds number, with the rate of increase being a strong function of the liquid properties (the Ohnesorge number associated with that fluid). This is analogous with results of the laboratory scale experiments.

A general trend is apparent if a plot of the dimensionless break-up length versus $\mathcal{F}r/\mathcal{R}b$ is considered (see Figure 5.11(c)). The data indicates that the break-up length increases with $\mathcal{F}r/\mathcal{R}b$, which is consistent with findings in Chapter 4.1.3. Increasing the rotation rate causes the trajectory of the jet to become more curved and the jet breaks up further away to the orifice.

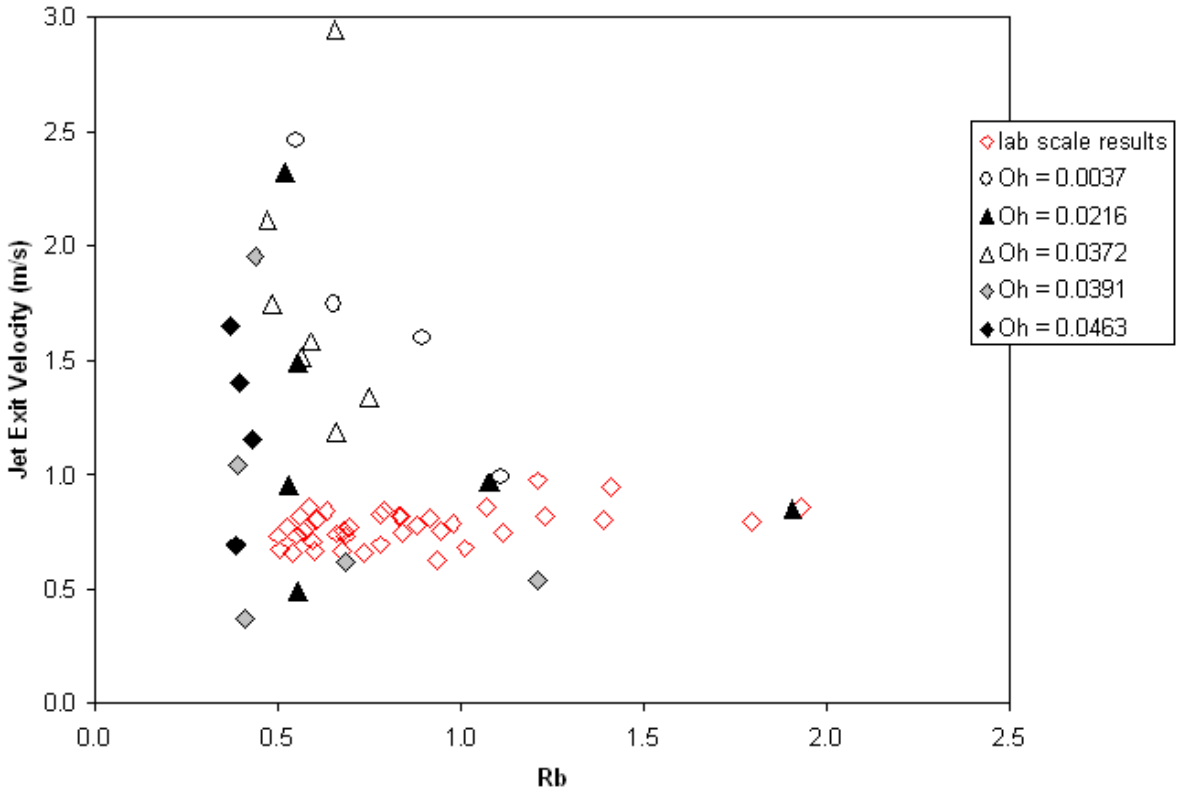

Figure 5.9: Influence of Rossby number on jet exit velocity for different viscosity fluids (0.0037 < $\mathcal{O}h$ < 0.0463). Data from the laboratory scale experiments is also shown (0.0222 < $\mathcal{O}h$ < 0.0762)

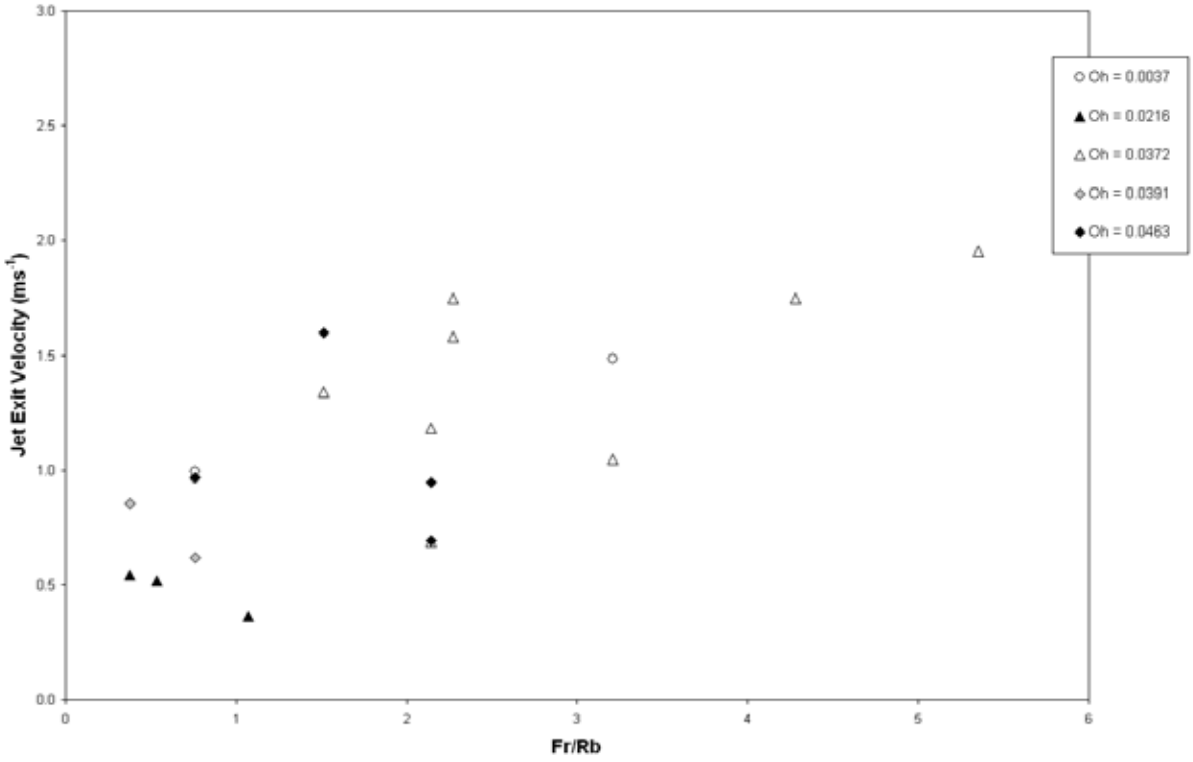

Figure 5.10: Influence of $\mathcal{F}r/\mathcal{R}b$ on exit velocity for different viscosity fluids ($0.0037 < \mathcal{O}h < 0.0463$).

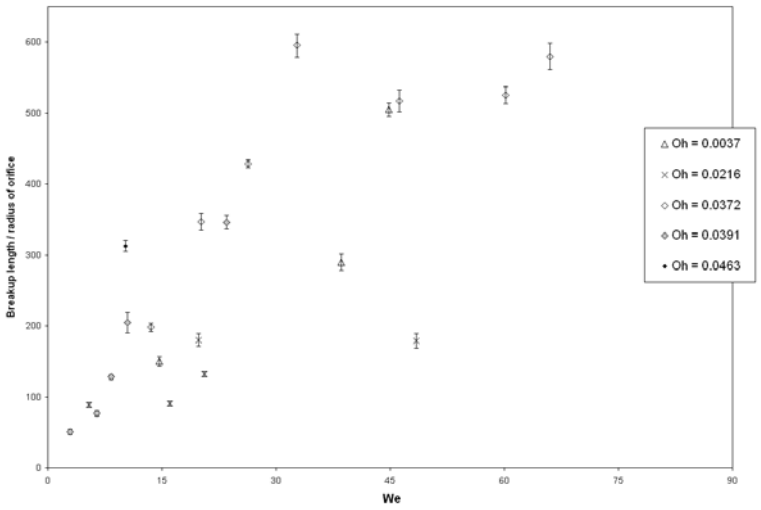

(a) Influence of $\mathcal{W}e$ on the break-up length for different viscosity fluids

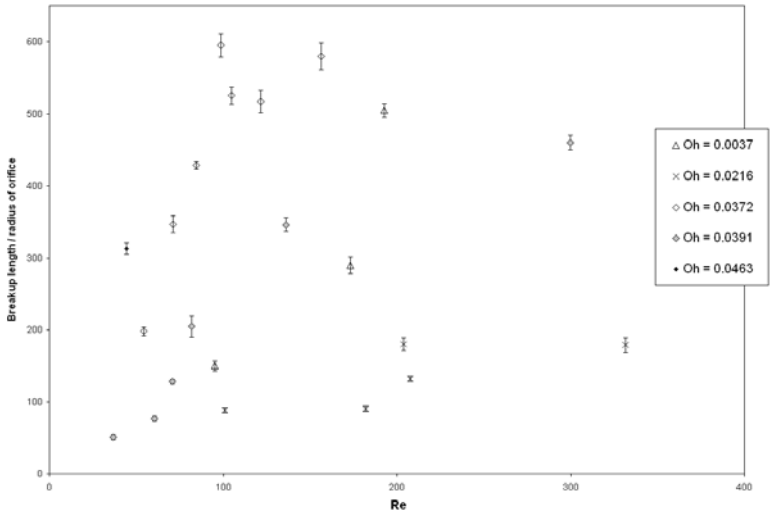

(b) Influence of $\mathcal{R}e$ on the break-up length for different viscosity fluids

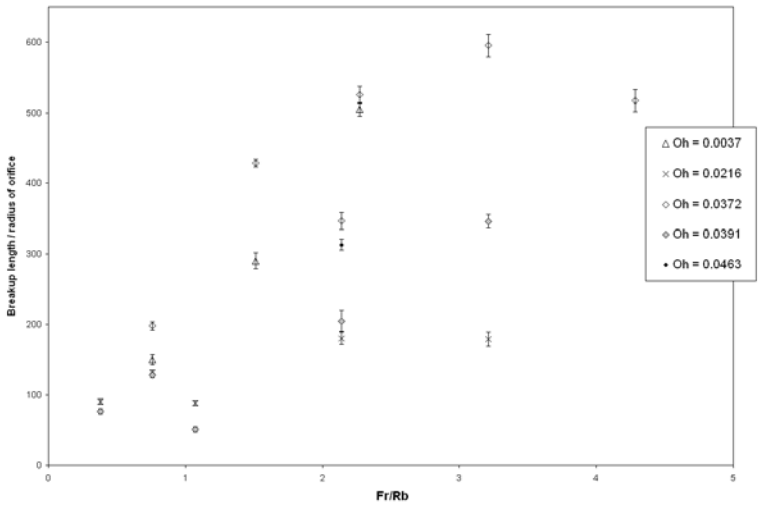

(c) Influence of $\mathcal{F}r/\mathcal{R}b$ on the break-up length for different viscosity fluids

Figure 5.11: Influence of (a) Weber number, (b) Reynolds number and (c) rotation rate upon the non-dimensional break-up length of the spiralling jet for different viscosity fluids ($0.0037 < \mathcal{O}h < 0.0463$).

5.1.4 Drop size as a function of system parameters

It is not possible to compare drop size distributions from the laboratory scale directly to those obtained from the pilot scale, as it is not possible to achieve the same values of $\mathcal{R}e, \mathcal{W}e, \mathcal{R}b$ and $\mathcal{F}r$ simultaneously on both scales. Hence it is only possible to achieve a qualitative comparison.

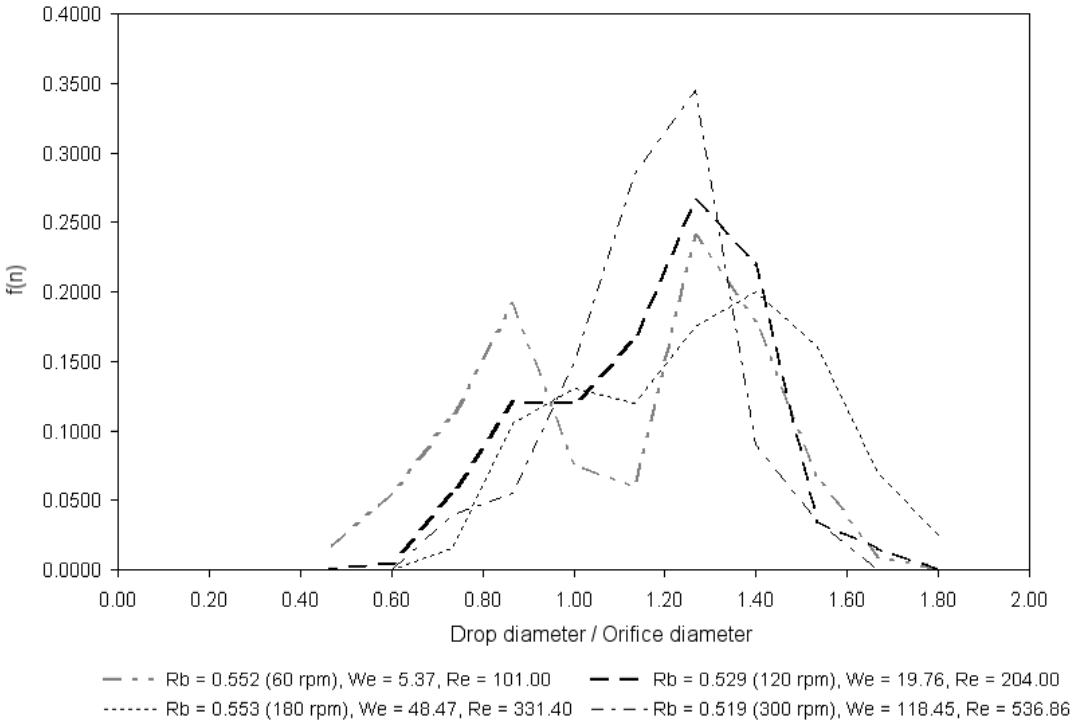

Figure 5.12: Drop size distribution for a solution of 0.1% CMC with a liquid aspect ratio of $1/4$ flowing through a nozzle of diameter 0.003 m.

The key findings are given here and the remainder of the measured drop size distributions can be found in Appendix A.2. An example of a drop size distribution for a shear thinning fluid is shown in Figure 5.12. Increasing the rotation rate, and hence the exit velocity, causes the drop size distribution to become progressively more unimodal, with one broad peak. The size of the satellite drops increases, and their numbers drop as Ω increases. A more extensive study of drop size distributions for non-Newtonian shear thinning fluids on the pilot scale can be found in Appendix A.2.

The effect of jet exit velocity upon average primary and satellite drop size is shown in Figure 5.13(a). For the data presented for the 2 mm nozzle, the drop size is shown to decrease with

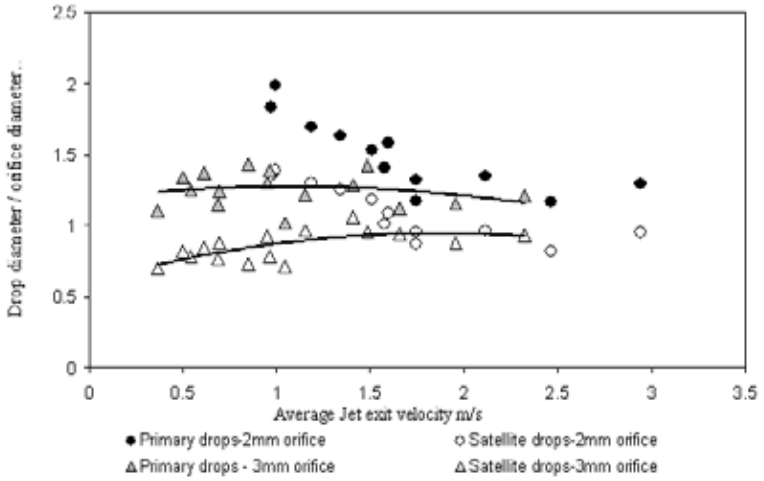

(a) Effect of U on primary and corresponding satellite drop sizes.

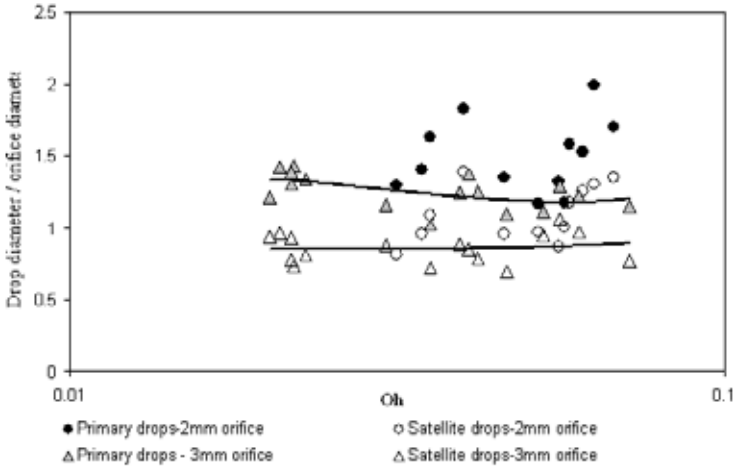

(b) Effect of $\mathcal{O}h$ on primary and corresponding satellite drop sizes.

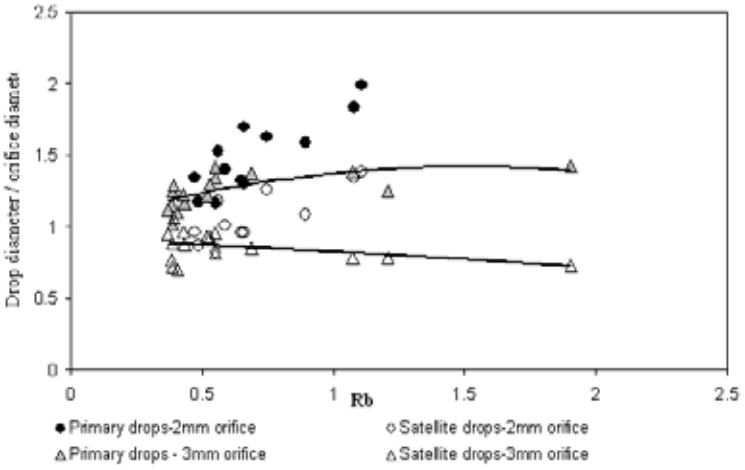

(c) Effect of $\mathcal{R}b$ on primary and corresponding satellite drop sizes.

Figure 5.13: Influence of (a) average jet exit velocity, (b) Ohnesorge number and (c) Rossby number upon primary and corresponding satellite drop sizes.

increasing U, however for the 3 mm nozzle there is no conclusive trend. Similar results were obtained for Newtonian fluids by Wong et al. (2004). On the laboratory scale a slight decrease was found for the 3 mm nozzle, however there were no significant effects for the 2 mm nozzle.

In Wong et al. (2004), the drop size was also plotted versus $\mathcal{O}h$ and $\mathcal{R}b$ and shown to be weakly dependent, but no monotonic relationship could be established. Repeating the same analysis for the data on the pilot scale produced no conclusive trends for the Ohnesorge number as shown in Figure 5.13(b). This differs to the results found on the laboratory scale rig, where increasing the Ohnesorge number led to a decrease in drop size for both primary and satellite droplets.

For increasing rotation rate (decreasing $\mathcal{R}b$), as seen in Figure 5.13(c), a decrease in the main drop sizes is observed, however, the satellite drop sizes from the 3 mm orifice appear to be slightly increasing. This can also be confirmed from the drop size distribution plots found in Appendix A.2. This differs to the results found on the laboratory scale, where a decrease in Rossby number led to a reduction in size for both primary and satellite drops.

This analysis shows that it is not possible to develop a predictive capability for drop size and features of break-up for non-Newtonian fluids based solely on a dimensional approach; more sophisticated modelling of the non linear behaviour is required. This is not surprising since this has also been observed previously for Newtonian fluids at both laboratory (Wong et al., 2004) and pilot scale (Partridge et al., 2005). Nevertheless, from an engineering perspective, observing how the jet break-up is affected by process parameters gives a useful feel for how the system behaves. In the following section, comparisons of the experimental results are made with the numerical models developed.

5.2 Numerical results and comparison with experiments

Simulations of the shape of the jet free surface generated from a non-linear finite difference model (Uddin et al., 2008a) are compared with the experiments, with some agreement.

In Uddin et al. (2008a), when the theoretical model is examined in detail it is possible to consider each dimensionless parameter separately, to elucidate the specific influence of Rossby

number, Weber number and Reynolds number. Experimentally, it is not possible to hold one parameter and vary the others, as they are all coupled together. Therefore a detailed comparison is made between the experiments and the numerical simulations, by using specific parameters obtained experimentally. The theoretical break-up length is matched to that obtained experimentally to allow the trajectory and shape of the jets to be compared. A more general comparison is performed for the whole data set, with both primary and satellite drop sizes examined to ascertain the accuracy of the model in predicting drop size.

5.2.1 Numerical scheme

The mathematical model of Uddin et al. (2008a) is used in this thesis to enable a comparison between previous theoretical work and experimental data. More detail about the model can be found in Chapter 2, along with Uddin et al. (2008a) and Uddin (2007). For ease of reference a brief summary and the key equations are repeated here.

A non-linear steady state of the governing continuum equations was identified giving a system of three ODEs in three unknowns, (5.1) - (5.3), in Uddin et al. (2008a), namely

$$\left(\frac{dX_0}{ds}\right)^2 + \left(\frac{dZ_0}{ds}\right)^2 = 1, \tag{5.1}$$

$$u_0\frac{du_0}{ds} = \frac{\frac{du_0}{ds}}{2\mathcal{W}e\sqrt{u_0}} + \frac{(X_0+1)\frac{dX_0}{ds} + Z_0\frac{dZ_0}{ds}}{\mathcal{R}b^2} + \frac{3\left|\sqrt{3}\frac{du_0}{ds}\right|^{\alpha-1}}{\mathcal{R}e_\alpha}\cdot\left(\alpha\frac{d^2u_0}{ds^2} - \frac{\left(\frac{du_0}{ds}\right)^2}{u_0}\right), \tag{5.2}$$

$$\left(\frac{dX_0}{ds}\frac{d^2Z_0}{ds^2} - \frac{dZ_0}{ds}\frac{d^2X_0}{ds^2}\right)\left(\frac{(7-\alpha)\left|\sqrt{3}\frac{du_0}{ds}\right|^{\alpha-1}\frac{du_0}{ds}}{2\mathcal{R}e_\alpha} + \frac{\sqrt{u_0}}{\mathcal{W}e} - u_0^2\right) + \frac{2}{\mathcal{R}b}u_0 - \frac{(X_0+1)\frac{dZ_0}{ds} - Z_0\frac{dX_0}{ds}}{\mathcal{R}b^2} - \frac{(\alpha-1)\left|\sqrt{3}\frac{du_0}{ds}\right|^{\alpha-1}}{\mathcal{R}e_\alpha}\cdot u_0\left(\frac{dX_0}{ds}\frac{d^3Z_0}{ds^3} - \frac{dZ_0}{ds}\frac{d^3X_0}{ds^3}\right) = 0, \tag{5.3}$$

where u_0 is the non-dimensionalised jet velocity along its centreline, s is the arclength along the centreline of the jet, and X_0 and Z_0 are orthogonal co-ordinates which describe the centreline of the jet trajectory. Here $\mathcal{R}e_\alpha$ is the Reynolds number based on the radius of the drum, s_0, so $\mathcal{R}e_\alpha = (s_0/a)^\alpha\,\mathcal{R}e$. The centreline of the jet in Cartesian co-ordinates is $(X_0(s), 0, Z_0(s))$,

with the X-axis in the direction normal to the surface of the drum in the initial direction of the jet as it emerges from the orifice, with the Z-axis orthogonal to the X-axis in the plane of the centreline of the jet. The positive Z-axis points in the direction opposite to the motion of the drum. There is no motion of the jet centreline in the vertical Y-axis direction since gravity is neglected, which is justified since the rotation rate is high and hence $s_0\Omega^2 << g$; where g is the acceleration due to gravity. The orifice of radius a, from which the liquid jet emerges, has its centre at position $(0, 0, 0)$. Here X_0, Z_0 and s are non-dimensionalised with respect to s_0, and u_0 is non-dimensionalised with respect to U.

This system of equations is solved for X_0 and Z_0, for the steady trajectory, and for u_0, using a Runge-Kutta method (for more detail see Uddin et al., 2008a; Uddin, 2007), with the boundary conditions at the nozzle as $X_0(0) = Z_0(0) = Z_s(0) = 0$ and $u_0(0) = X_s(0) = 1$. The resulting steady state solution is then used as the initial state for the following time-dependent finite difference scheme.

The non-linear temporal solution is obtained by solving the following non-linear equations

$$\frac{\partial A}{\partial t} = -\frac{\partial}{\partial s}(Au_0), \tag{5.4}$$

$$\begin{aligned}\frac{\partial u_0}{\partial t} + u_0\frac{\partial u_0}{\partial s} &= -\frac{1}{\mathcal{W}e}\frac{4\left(2A + \left(\epsilon\frac{\partial A}{\partial s}\right)^2 - \epsilon^2 A\frac{\partial^2 A}{\partial s^2}\right)}{(4A + \left(\epsilon\frac{\partial A}{\partial s}\right)^2)^{\frac{3}{2}}} \\ &+ \frac{(X_0+1)\frac{\partial X_0}{\partial s} + Z_0\frac{\partial Z_0}{\partial s}}{\mathcal{R}b^2} + \frac{3}{\mathcal{R}e_\alpha}\frac{\partial}{\partial s}\left(\left|\sqrt{3}\frac{\partial u_0}{\partial s}\right|^{\alpha-1}\frac{\partial u_0}{\partial s}A\right),\end{aligned} \tag{5.5}$$

where $A = R_0^2$ and $R_0(s,t)$ is the non-dimensionalised radius of the jet (with respect to the orifice radius a). In (5.4)-(5.5), $u_0(s,t)$ is non-dimensionalised with respect to U and time, t, is non-dimensionalised with respect to s_0/U.

These equations are solved using the second order space centered explicit scheme of *Richtmyer* which is based on the Lax-Wendroff finite difference scheme and is similar to that used in the work of Părău et al. (2006, 2007). The equations are discretised using a second order method for first derivatives, but first order for second derivatives. The initial value at $t = 0$ for $u_0(s,t)$ is the solution to the steady state equations, (5.1) - (5.3). The initial value at $t = 0$ for

$A(s,t) = R_0^2$ is found from the steady kinematic condition $R_0^2 u_0 = 1$, while X_0 and Z_0 are fixed at all times using the solutions from (5.1) - (5.3), as given in Părău et al. (2006), Părău et al. (2007) and Uddin et al. (2008a). The instability is introduced through upstream boundary conditions, corresponding to conditions at the nozzle,

$$A(0,t) = 1, \quad u_0(0,t) = 1 + \delta \sin\left(\frac{\kappa t}{\epsilon}\right), \tag{5.6}$$

where κ is a non-dimensional frequency and δ is the magnitude of the initial non-dimensional velocity disturbance. Apart from changing the system parameters ($\mathcal{W}e, \mathcal{R}b, \mathcal{R}e$), both the frequency, κ, and the amplitude, δ, of the orifice perturbation can be altered in the numerical scheme (Uddin et al., 2008a). Uddin et al. (2008a) derived the most unstable frequency, κ^*, corresponding to the fastest growing linear wave, as

$$\kappa^* = \frac{1}{2^{1/4}} \cdot \frac{1}{\sqrt{\mathcal{O}hf + \sqrt{2}}}, \tag{5.7}$$

where

$$f(\alpha) = 3\alpha \left|\sqrt{3}\frac{\partial u_0}{\partial s}\right|^{\alpha-1} \quad \text{at } s = 0. \tag{5.8}$$

κ is set equal to κ^* in (5.6) to generate jets where break-up is caused by the fastest growing wave in order to match theory with experiments.

Break-up is chosen to occur when the non-dimensional jet radius has reached an arbitrarily small value which, for consistency with earlier works (Uddin et al., 2008a; Părău et al., 2006, 2007), is taken as five percent of the initial jet radius. For all the simulations, a non-dimensional spatial step size, ds, of 5×10^{-4} is used. The time step was chosen to be less than half the square of the space set to ensure the Courant condition was observed; hence dt was set equal to 1×10^{-7}. This is found to be sufficient for convergence of the code. For more detail on the accuracy of the numerical scheme the reader is referred to Uddin et al. (2008a) and Uddin (2007). Drop volume was obtained by numerical integration of the jet profile at the break-up time using the trapezoidal rule, given in Equation (2.26). Hence the drop radius is calculated using Equation

(2.27).

5.2.2 Numerical results

To perform a meaningful comparison with the experimental data, it is necessary to assign values to the amplitude and frequency of the disturbance, δ and κ, respectively. As break-up should be dominated by the fastest growing, or most unstable, wave this criteria can be met by setting $\kappa = \kappa^*$ using (5.7). Setting a value of δ is more problematic, since it cannot be measured experimentally. Uddin (2007) examined the effect of changing the value of δ in the simulations, and found that increasing δ led to shorter break-up times according to an exponential relationship, in agreement with linear theory. Hence increasing δ also leads to shorter break-up lengths, although this had only a weak effect on the calculated size of the primary drops.

To corroborate this, tests on two different liquid systems with different system parameters, taken from the experiments performed, were run to verify these results. The values of the parameters these results are run for are experiments 1 and 5, given in Table 5.1.

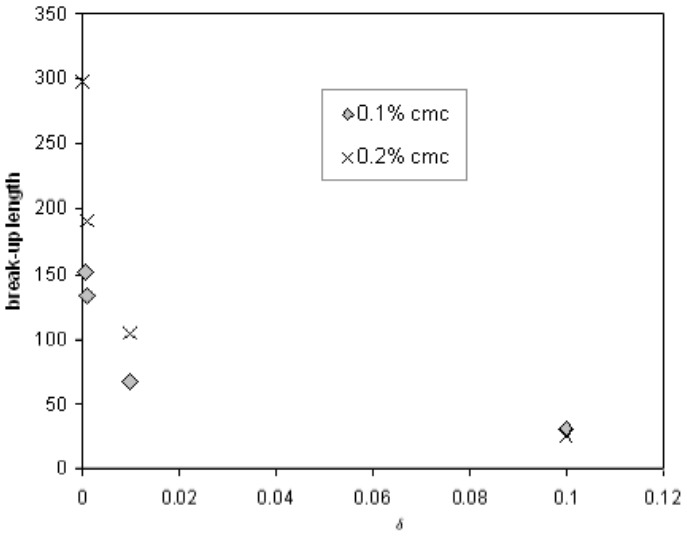

Figure 5.14: Effect of altering the amplitude of the initial disturbance, δ, on the break up length for 0.1% CMC and 0.2% CMC. Here $\kappa = 0.69$ and $\kappa = 0.70$ respectively. If the amplitude of the initial disturbance is increasing there is an approximate exponential decay in break-up length shown for both regimes.

As can be seen from Figure 5.14, increasing the amplitude of the disturbance at the orifice has a dramatic effect on break-up length for both experiments. The effect of altering the ampli-

Table 5.1: Experimental parameters utilised in optimisation of the amplitude of the initial perturbation.

Exp.	Liquid	Aspect ratio	a (m)	Rotation (Ω)	$\mathcal{W}e$	$\mathcal{R}b$	$\mathcal{O}h$	$\mathcal{R}e_\alpha$	κ^*	Break-up/a	Optimal δ
1	0.1% CMC	1/2	0.0015	6.28	20.58	1.0757	0.0218	13696.51	0.693	131.96	0.001
2	0.1% CMC	1/4	0.0015	12.56	19.76	0.5295	0.0218	13460.11	0.694	180.20	0.0075
3	0.2% CMC	1/4	0.0015	3.14	6.46	1.2102	0.0420	1820.54	0.684	76.63	0.002
4	0.2% CMC	1/2	0.001	6.28	14.60	1.1093	0.0400	3894.87	0.705	150.13	0.0001
5	0.2% CMC	1/2	0.001	12.56	38.37	0.8929	0.0356	7085.76	0.705	289.96	0.0001
6	0.3% CMC	1/4	0.001	12.56	13.55	1.0805	0.0678	1386.99	0.679	197.97	0.00006

tude of the disturbance is also shown in Figure 5.15 where the profile of the jet for varying δ is shown.

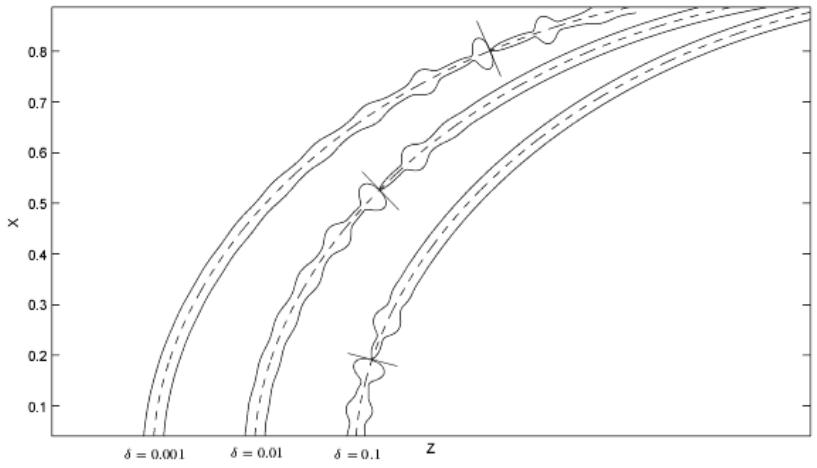

Figure 5.15: The profile of a shear thinning jet for different amplitudes of the initial disturbance. Here $\mathcal{W}e = 20.58, \mathcal{R}b = 1.0757, \mathcal{R}e_\alpha = 13696.51$ and $\kappa = 0.84$. For increasing initial disturbance amplitude there is a dramatic decay in break-up length.

It was also investigated whether varying δ had any effect on altering the size of the primary or satellite drop size produced by the model. Figure 5.16 confirms the results of Uddin (2007), that changing δ has little effect on either the primary or satellite drop size.

Therefore, the approach taken in this work is to optimise the value of δ to match the break-up lengths obtained experimentally in each case. This was performed for six selected experiments as shown in Table 5.1, which also gives the values of δ and κ^* used in the simulations.

Comparison between the drop sizes obtained from the simulations and experiments is shown in Figure 5.17 as a function of the Weber number. The error bars represent the standard deviation of the drop size distributions obtained from each experiment. Reasonable agreement is obtained

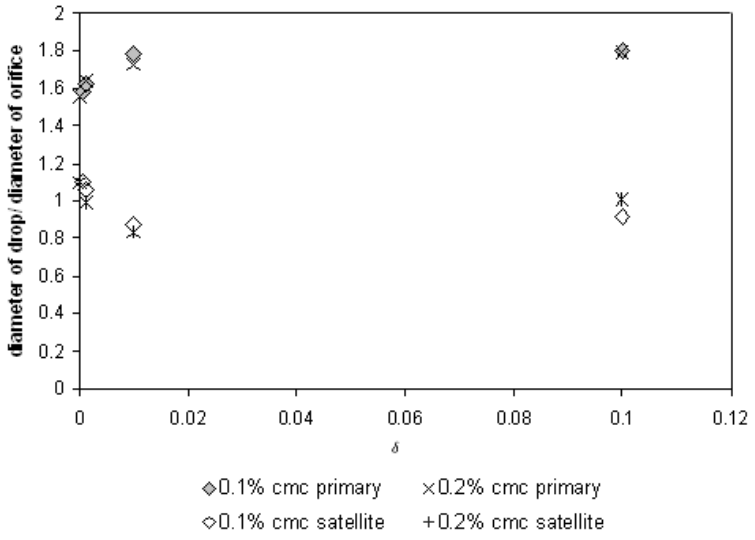

Figure 5.16: Effect of altering the amplitude of the initial disturbance, δ, on the primary and satellite drop sizes for 0.1% CMC and 0.2% CMC. Here $\kappa = 0.69$ and $\kappa = 0.70$ respectively. There appears to be no real correlation between altering δ and predicted primary or satellite drop size.

apart from Experiment 3, where a 25% larger theoretical drop size is predicted. Possible reasons for this are examined later.

The prediction of the creation of satellite drops from the simulations is somewhat subjective, since several different mechanisms have been observed in the experiments by which the ligaments may or may not form satellites (Figure 5.1). These are contraction into the primary drop (and hence no satellite), contraction to form a single satellite, or shattering to form several much smaller satellites. This issue is illustrated in Figure 5.18, which gives examples of the shapes of the jets at the point of break-up for Experiments 1 and 3. To aid illustration, the curvature of the jet has been removed so that it appears straight. In both Figures 5.18(a) and 5.18(b), the primary droplet can be clearly identified from the pinch off point upstream of the drop break-up (marked as point A) and the pinch off point further downstream (point B). From the experiments, it is known that the satellite drops form from the ligaments, so a droplet size could be calculated on the basis of the ligament formed between point A and point C. However, whilst in Figure 5.18(b) the ligament is thin and point C has a well defined minimum, this is not the case in Figure 5.18(a). It is not clear therefore, whether the ligament in Experiment 1 would break off to form a satellite, remain attached to the next primary drop and contract into it, or

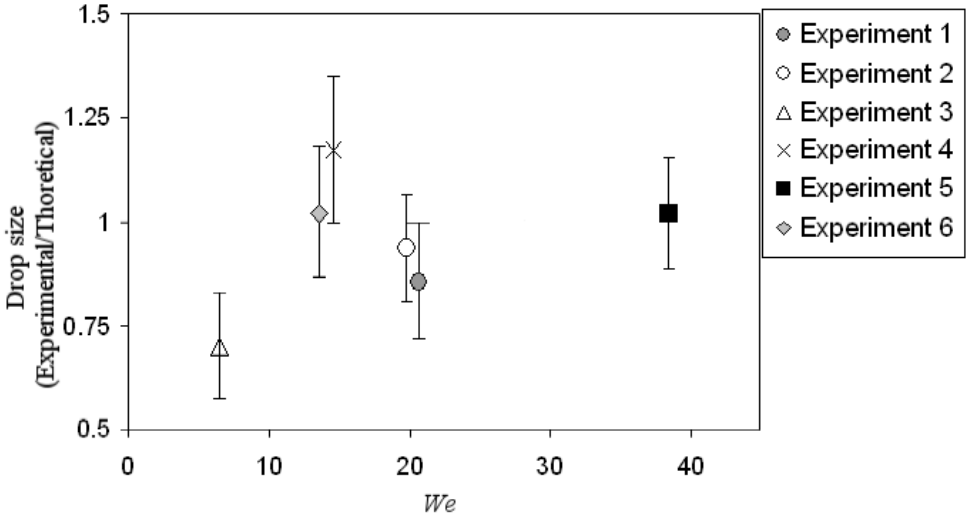

Figure 5.17: Experimental primary drop sizes/Theoretical drop size predictions for Experiments 1 - 6, as detailed in Table 5.1, plotted against the Weber number. The error bars represent the standard deviation of the primary drop sizes obtained from the drop size distributions.

shatter to form many satellite droplets. If the spherical equivalent drop sizes of both these ligaments are calculated, the non-dimensional satellite drop size for Experiment 1 is found as 1.059, compared with an experimental value of 0.785. Agreement is much improved for experiment 3 with a theoretical value of 0.780 comparing reasonably with an experimental value of 0.702. Consequently, in examination of the jet shapes, the assumption of satellite drop formation is only made when a clearly defined minimum is observed at point C, although this approach does not take into account shattering of the ligaments to produce multiple satellite droplets.

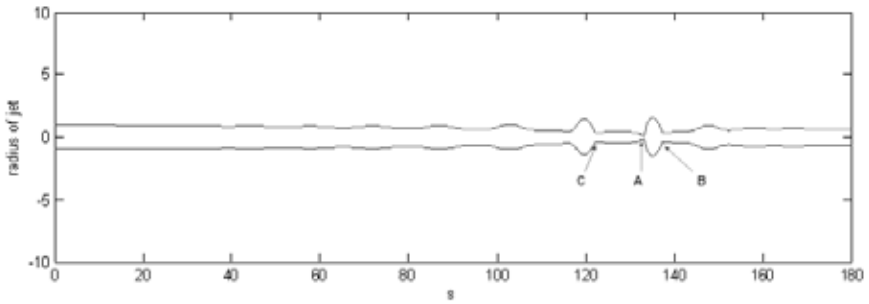

(a)

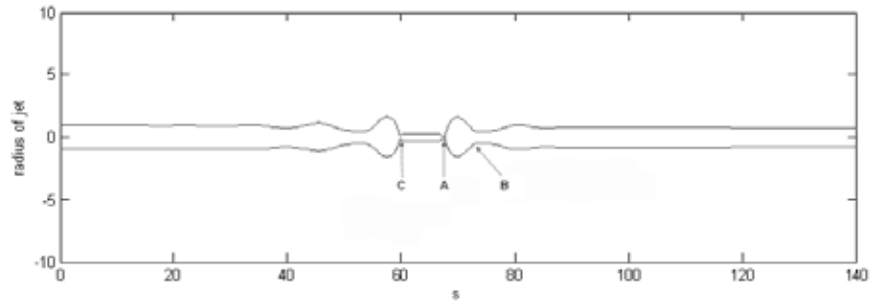

(b)

Figure 5.18: Numerical simulations of Experiments (a) 1 and (b) 3

Figures 5.19-5.22, show selected numerical solutions of experiments 1-6 respectively, superimposed over experimental images obtained for the same parameters where δ has been fitted in each case to give a theoretical break-up length matching that measured experimentally.

There is good agreement of the curvature of the jet between the numerical solution and the experimental image shown in Figure 5.19(a). The amplitude of perturbations on the surface of the jet is seen to be growing down the jet in both the numerical solution and the experimental image. This occurs for all of the six experiments. It is also noted that some experimental features, such as the thinning and lengthening of the ligaments between droplets, are missing from the numerical simulations.

The primary drop sizes produced by the numerical simulation in Figure 5.19(a) are bigger than those obtained experimentally. In Figure 5.19(b), however, while there is good agreement between the experimental and numerical primary drop size for Experiment 2 (as shown in Figure 5.17), there is less good agreement of jet curvature, with the numerical solution appearing to be slightly more curved than the experimental jet. A close-up of both experimental and theoretical break-up is also shown where it appears that disturbances on the surface of the jet do not appear to be growing quickly enough.

In Figure 5.20(a) there appears to be particularly poor agreement between the numerical solution and the experiment. The numerical solution curves significantly more than the experimental jet and the droplet produced by the numerical simulation also appears to be much bigger than any of the droplets produced in the experiment. As noted previously, Figure 5.17 also shows that there is poor agreement between the primary drop size predicted by the numerical solution and the average experimental primary drop size. However, it should be noted that the Rossby number for this experiment is comparatively high, indicating a low rotation rate (30 rpm), so there is a possibility that gravity is causing the jet to fall significantly out of the $X-Z$ plane. In order to verify this, the 3-d centreline, which includes the effects of gravity (taken from Decent et al., 2002), is plotted for the same experimental parameters. The centreline can then be compared to the 2-d inviscid centreline obtained, which neglects the effects of gravity. The results of this are shown in Figure 5.20(b) and in the $X-Z$ plane by the dashed line in

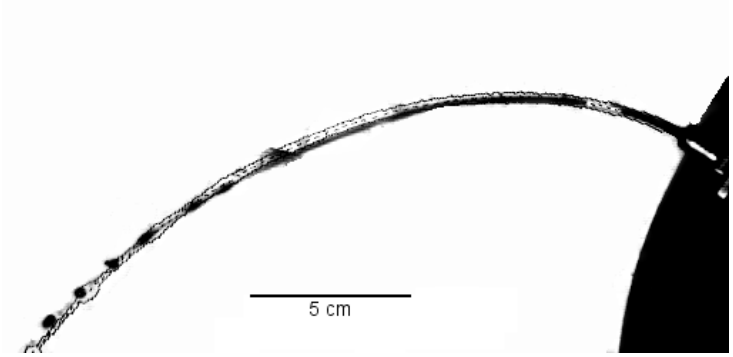

(a) Comparison of numerical solutions with experimental image for Experiment 1 ($\rho = 1025$ kg m^{-3}, $k = 0.012$ Pa s, $\alpha = 0.920$).

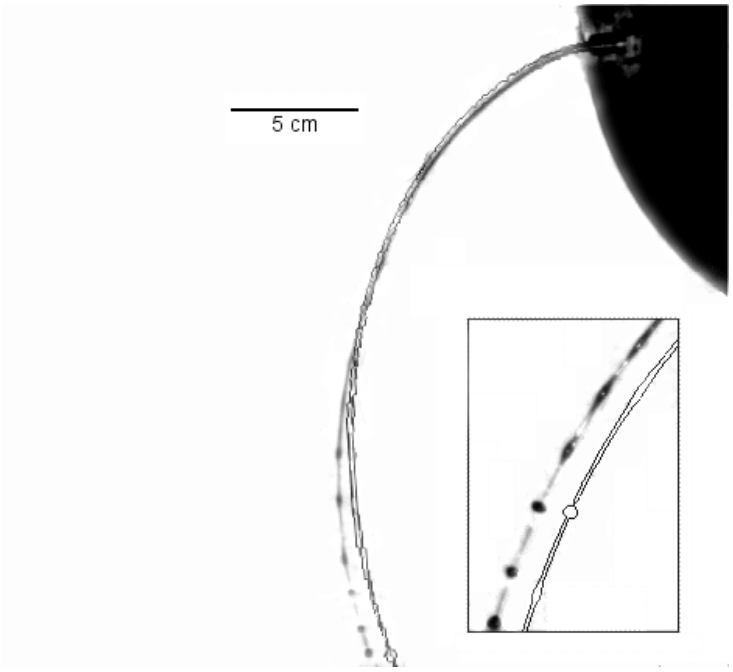

(b) Comparison of numerical solution with experimental image for Experiment 2 ($\rho = 1025$ kg m^{-3}, $k = 0.012$ Pa s, $\alpha = 0.920$).

Figure 5.19: Comparison of numerical solutions with experimental images for Experiments 1-2

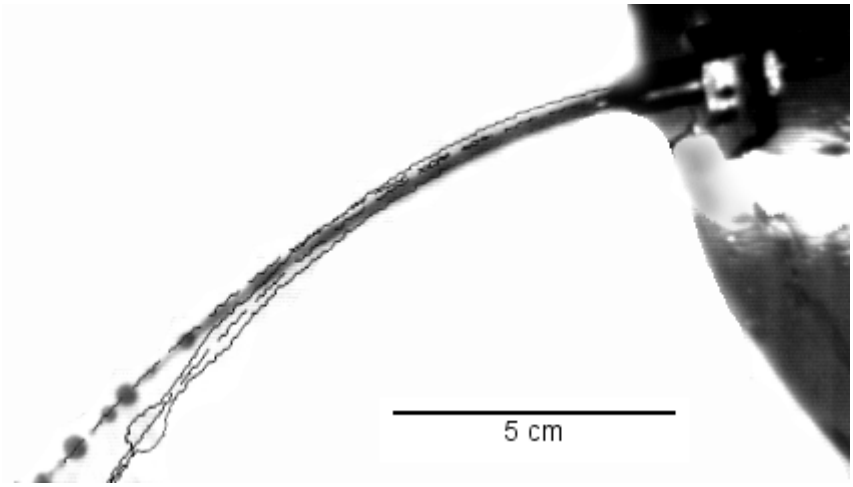

(a) Comparison of numerical solution with experimental image for Experiment 3 ($\rho = 1026$ kg m^{-3}, $k = 0.060$ Pa s, $\alpha = 0.748$).

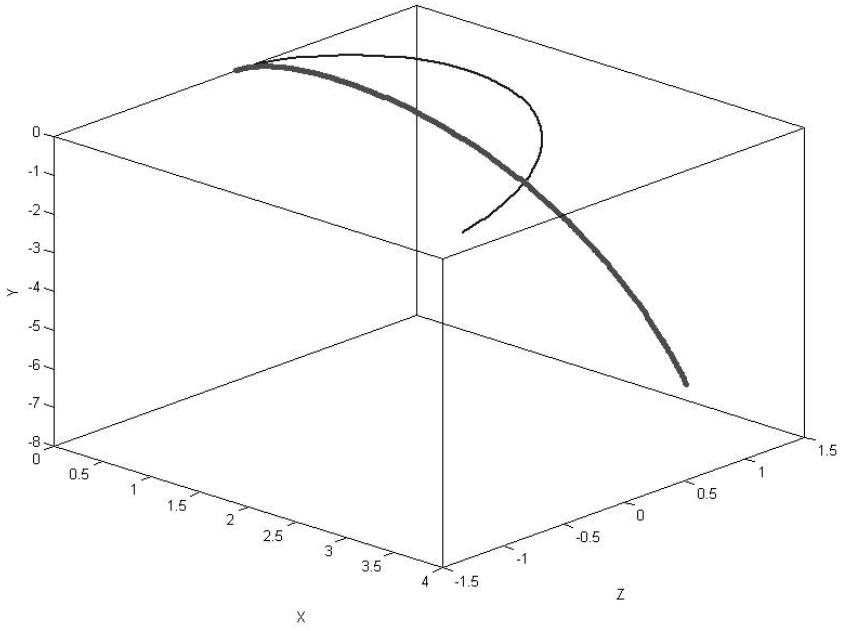

(b) Comparison of 2-d and 3-d linear inviscid centrelines for Experiment 3. $\mathcal{F}r = 0.458$ ($\rho = 1026$ kg m^{-3}, $k = 0.060$ Pa s, $\alpha = 0.748$).

Figure 5.20: (a) Comparison of numerical solution with experimental image for Experiment 3 and (b) comparison of 2-d and 3-d linear inviscid centrelines for Experiment 3. $\mathcal{F}r = 0.458$ ($\rho = 1026$ kg m^{-3}, $k = 0.060$ Pa s, $\alpha = 0.748$).The thinner line represents the linear inviscid 2-d centreline of the jet and the thicker line represents the linear inviscid 3-d centreline which includes the effects of gravity. It can be seen that this centreline falls out of the $X - Z$ plane.

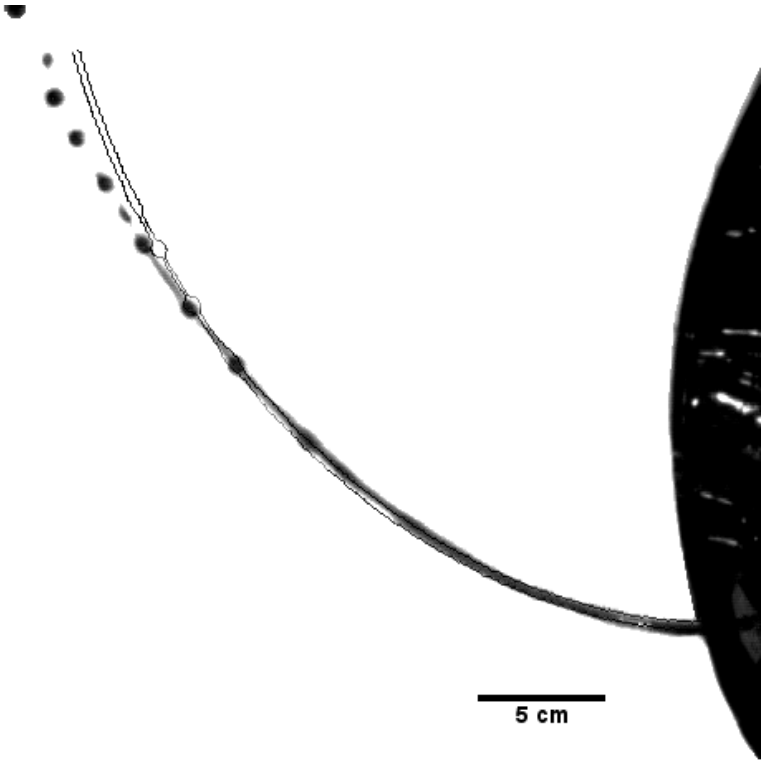

(a) Comparison of numerical solution with experimental image for Experiment 4 ($\rho = 1026$ kg m^{-3}, $k = 0.060$ Pa s, $\alpha = 0.748$).

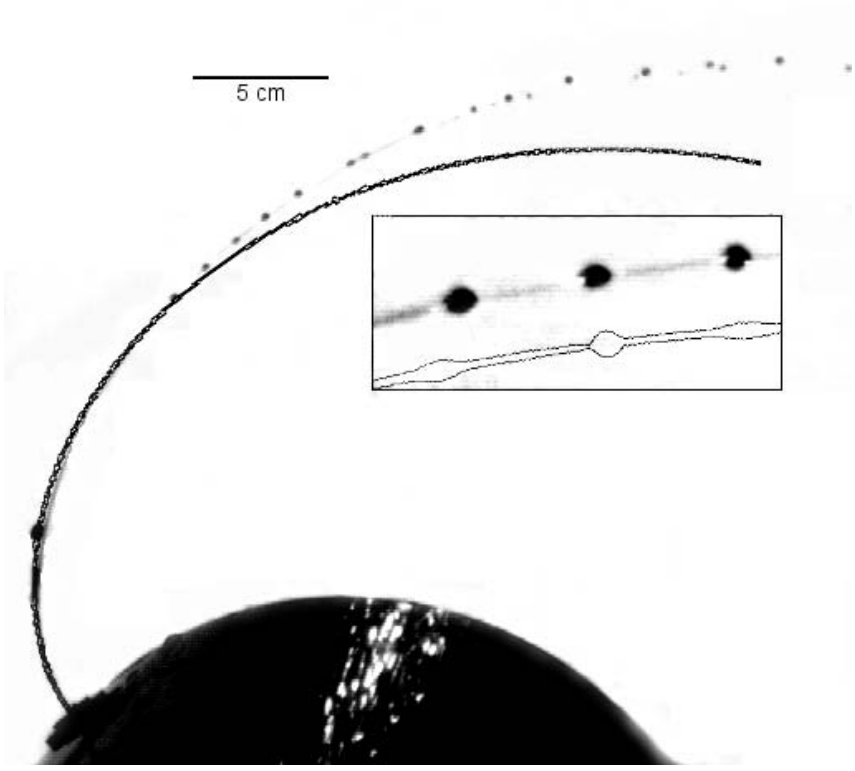

(b) Comparison of numerical solution with experimental image for Experiment 5 ($\rho = 1026$ kg m^{-3}, $k = 0.060$ Pa s, $\alpha = 0.748$).

Figure 5.21: Comparison of numerical solutions with experimental images for Experiments 4-5.

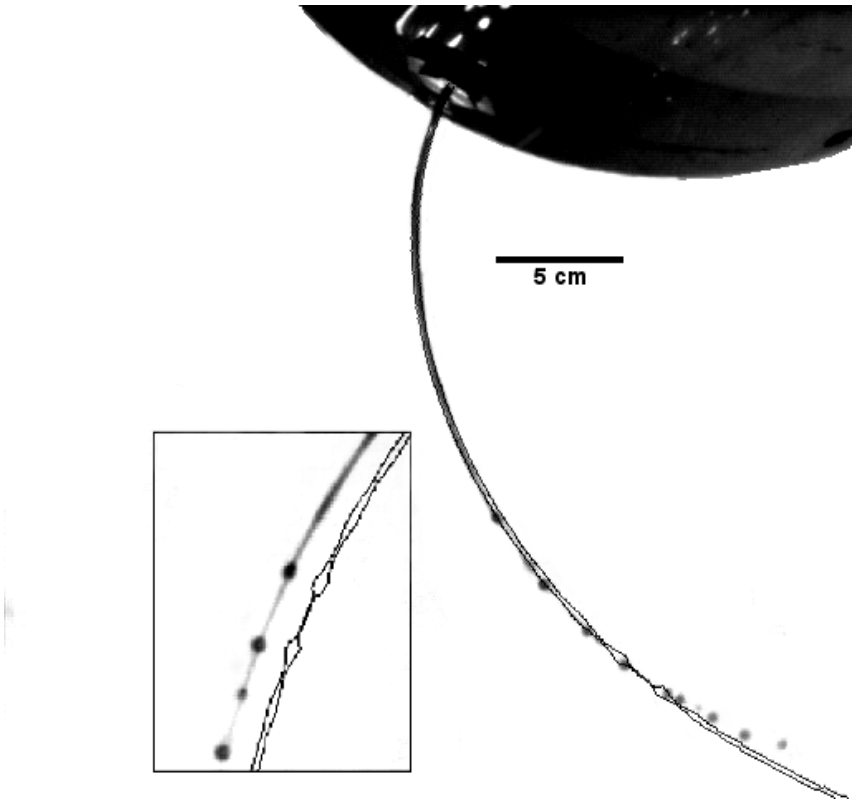

Figure 5.22: Comparison of a numerical solution and experiment for Experiment 6 ($\rho = 1027$ kg m^{-3}, $k = 0.120$ Pa s, $\alpha = 0.654$).

Figure 5.20(a) which shows much improved agreement with the experiments.

The theoretical prediction in Figure 5.21(a) shows reasonable agreement with the experimental jet in terms of both jet shape and experimental drop size, while better agreement is found in Figures 5.21(b) and 5.22, where the numerical solution was also relatively accurate in predicting primary drop size. The numerical solution appears to be slightly more curved than the experimental image in Figure 5.21(b), although it should be emphasised that we would only expect the curvature to agree up to the point of break-up and not beyond it. In Figure 5.22 it should be noted that while experimentally it appears that two smaller droplets are forming after the main primary droplet, the numerical solution fails to capture these intricate features of break-up.

5.2.3 Drop size predictions for whole data set

Uddin (2007) showed that while changing δ had a dramatic effect on break-up times, there was little effect on the primary or satellite drop sizes. It was observed that main drop sizes varied

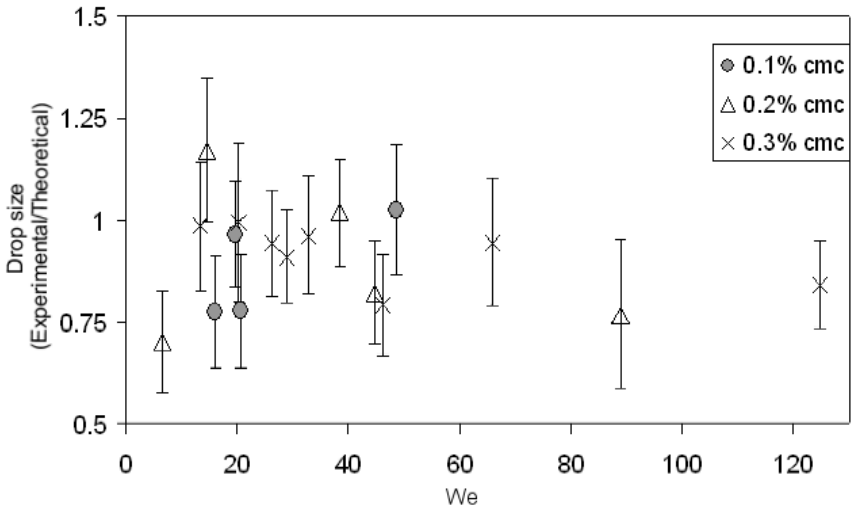

(a)

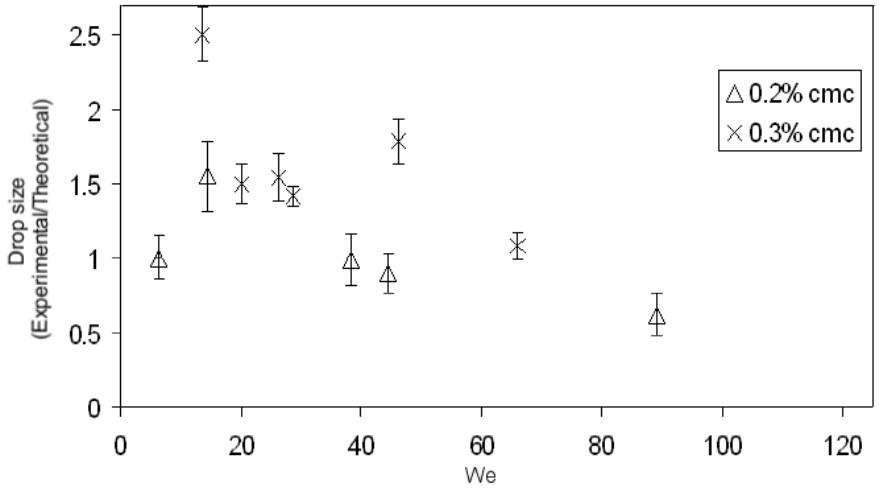

(b)

Figure 5.23: (a) Primary and (b) satellite droplets/theoretical drop size predictions for experiments, as shown in Table 5.2, plotted against the Weber number. Drop sizes are grouped by liquid system and the error bars represent the standard deviations given by the distribution of primary and satellite drop sizes obtained

Table 5.2: Table of normalised drop sizes for experiments and predictions using numerical model.

Exp.	k [Pa s$^{\alpha}$]	α	$\mathcal{W}e$	$\mathcal{R}b$	$\mathcal{O}h$	$\mathcal{R}e$	Primary drop radius/radius of orifice Exp. value $\pm$ s.d.	Num. model	Sat. drop radius/radius of orifice Exp. value $\pm$ s.d.	Num. model
-	0.0120	0.92	16.06	1.90	0.0220	181.98	1.434 ± 0.138	1.845	0.735 ± 0.123	-
1	0.0120	0.92	20.58	1.08	0.0218	207.58	1.389 ± 0.142	1.784	0.785 ± 0.127	-
2	0.0120	0.92	19.76	0.53	0.0218	203.99	1.305 ± 0.129	1.425	0.924 ± 0.122	-
-	0.0120	0.92	48.47	0.55	0.0210	331.44	1.423 ± 0.161	1.388	0.958 ± 0.111	-
3	0.060	0.748	6.46	1.21	0.0420	60.25	1.252 ± 0.126	1.784	0.786 ± 0.146	0.780
4	0.060	0.748	14.60	1.10	0.040	95.16	1.993 ± 0.178	1.700	1.391 ± 0.232	0.869
5	0.060	0.748	38.37	0.89	0.035	173.11	1.584 ± 0.133	1.554	1.089 ± 0.171	1.094
-	0.060	0.748	44.63	0.65	0.034	192.85	1.325 ± 0.123	1.608	0.956 ± 0.135	1.0681
-	0.060	0.748	88.95	0.55	0.032	296.80	1.164 ± 0.185	1.514	0.820 ± 0.137	1.308
-	0.199	0.654	28.78	0.43	0.060	89.43	1.220 ± 0.115	1.341	0.968 ± 0.068	0.681
6	0.199	0.654	13.54	1.08	0.068	54.25	1.833 ± 0.156	1.860	1.346 ± 0.178	0.537
-	0.199	0.654	26.32	0.75	0.061	84.38	1.632 ± 0.129	1.732	1.256 ± 0.162	0.813
-	0.199	0.654	124.68	0.66	0.046	242.54	1.299 ± 0.108	1.547	0.954 ± 0.128	-
-	0.199	0.654	20.17	0.66	0.063	71.17	1.699 ± 0.194	1.707	1.305 ± 0.146	0.867
-	0.199	0.654	32.74	0.56	0.058	98.60	1.529 ± 0.145	1.590	1.181 ± 0.093	-
-	0.199	0.654	46.23	0.49	0.056	121.68	1.173 ± 0.126	1.480	0.871 ± 0.133	0.487
-	0.199	0.654	66.00	0.47	0.0252	156.31	1.345 ± 0.158	1.424	0.967 ± 0.150	0.891

very slowly (less than 2%) as the disturbance amplitude was increased from $0.01 < \delta < 0.1$. The implications of this are that it is not necessary to optimise δ on break-up length to obtain a prediction of drop size for each experiment. This was also shown by Partridge (2006) who found that provided δ is of the correct order, reasonable agreement between theoretical predictions and experimental results is possible.

The theoretical drop sizes estimated by the non-linear evolution equations are given in Table 5.2 (subject to limitations in the analysis as illustrated in Figure 5.18), along with the experimental results and parameters examined. The numerical simulations are run with $\delta = 0.01$ and $\kappa = \kappa^*$ (5.7). The values of ds and dt quoted are sufficient for all parameter ranges where results are given. For some parameter ranges, no matter how small ds and dt were made, the code appeared not to converge at all. The theory assumes convective instability, and it is possible that in some of the parameter ranges examined, break-up is due to absolute instability. It can be seen from Figure 5.23(a), where the theoretical value is again compared to the experimental mean of the primary drop sizes, that for all Weber numbers, reasonable agreement between drop sizes acquired experimentally and theoretically is obtained. The majority of the drop sizes predicted are too large when compared to the experimental values, yet the majority are within 25%. No

obvious trends were found when the accuracy of the theoretical drop predictions was plotted against other dimensionless parameters.

The quality of the satellite droplet predictions are illustrated in Figure 5.23(b). Again the mean experimental satellite droplet is used for direct comparison. It can be seen that, for all Weber numbers, the satellite drop sizes predicted by the numerical solution compare less well than for the primary drops, as indicated by the much greater spread of values. On occasion the theoretical drop size is almost twice as big as the experimental value for some parameters and less than half as small for another, however for the majority the agreement is within 50%. In cases of high rotation rate and high viscosity, Newtonian fluids show similar discrepancies between experiments and simulations (Gurney et al., 2010). As with primary drop size predictions there appears to be no conclusive trends between the accuracy of the numerical solution and varying Weber number, or indeed any other dimensionless parameter; although there does appear to be some weak correlation between the accuracy of the satellite drop sizes and the liquid system tested.

While primary drop sizes can be predicted with reasonable agreement with the experiments ($\sim 25\%$) for fixed δ, more work is needed to improve the accuracy of satellite drop prediction. These inaccuracies in measuring satellite droplets could be due to the complex behaviour of ligaments. The numerical simulation runs until the jet is assumed to break up. Ligament break-up occurs after jet break-up and the behaviour of the ligaments and hence, satellite drop formation cannot be fully ascertained using this non-linear analysis.

5.3 Surfactants

As it is well known that, in many cases, the addition of even small amounts of surfactants markedly reduces the surface tension, this work is of relevance to industrial prilling, where surfactants could be used without drastically altering the constitution of the material to be prilled.

The effect of adding surfactant into aqueous solutions at increasing concentrations (0.05, 0.1 and 0.3% w/v) was compared qualitatively and quantitatively to Newtonian jets of water ($\mu = 0.001$ Pa s). The break-up mode of water was found to be M2 for all rotation rates

examined on the pilot scale and increasing the rotation rate causes the trajectory of the jet to become more curved. Break-up of the jet at multiple points also occurs on the pilot-scale for increasing rotation rate. A comprehensive study on the break-up of Newtonian liquid jets was performed in Partridge (2006) and further information can be found there.

Figure 5.24 shows qualitatively, for a 0.1% SDS aqueous solution, how the trajectory of the jets and break-up length are affected by increasing rotation rate. It can be seen in Figure 5.24(a) that the curvature of the trajectory of the jet only increases slightly with increasing rotation rate. The same is shown in Figure 5.24(b).

Qualitative differences between a jet containing 0.1% SDS and a jet of water are shown in Figure 5.25 and 5.26. All other experimental conditions (aspect ratio, nozzle radius, rotation rate) remain constant, although there are obviously differences in the dimensionless parameters. It is obvious that a decrease in surface tension has a marked effect and disturbances are visible immediately on exit of the liquid from the nozzle, with the droplets themselves seeming more unstable.

As is observed in Figure 5.25(a), initially there is no difference in the trajectory between the water jet and the jet containing the SDS although as can be seen the jet containing the SDS has a longer break-up length. This is to be expected, as the surface tension for the surfactant jet should be lower at break-up than the jet of water, hence disturbances due to surface tension grow more slowly.

As the rotation rate increases to 60 rpm in Figure 5.25(b) it can be seen that the surfactant jet again has longer break-up length and that there is a difference in the trajectories of the jet. The jet containing the surfactant is less curved than the water jet.

As the rate of rotation increases again to 120 rpm (Figure 5.26(a)) the differences in the break-up length and trajectory can once again be seen. However as the rate of rotation increases again up to 180 rpm, in Figure 5.26(b), it can be seen that the jet containing surfactant actually breaks up sooner than the jet of water. This also occurs at 300 rpm, in Figure 5.26(c). A possible explanation for this is that the jet is breaking up due to vibrations in the rig and that the surface tension forces are not strong enough to hold the jet together.

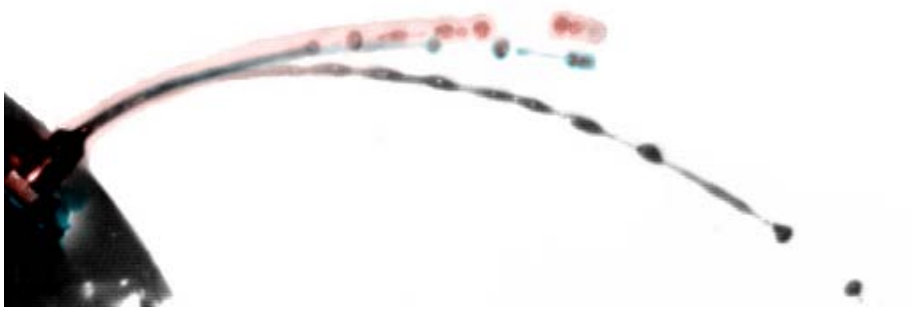

(a)

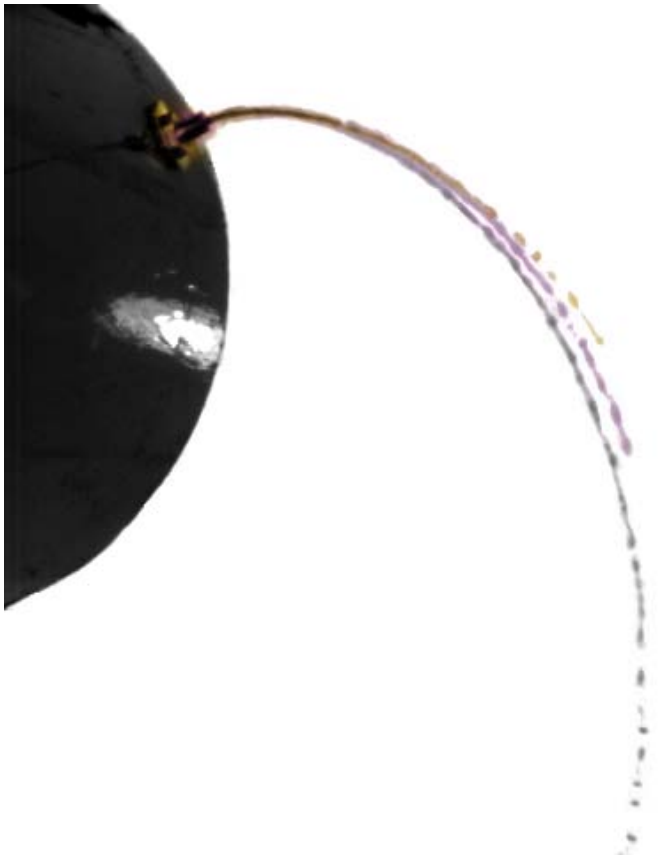

(b)

Figure 5.24: 0.1% SDS jet at increasing rotation rates (a) Red jet - $\mathcal{R}b = 1.12$ (30 rpm), Blue jet - $\mathcal{R}b = 0.76$ (60 rpm) and Grey jet - $\mathcal{R}b = 0.62$ (120 rpm) (b) Orange jet - $\mathcal{R}b = 0.59$ (180 rpm), Purple jet - $\mathcal{R}b = 0.58$ (240 rpm) and Grey jet - $\mathcal{R}b = 0.56$ (300 rpm). The curvature of the trajectory of the jet can be seen to increase with increasing rotation rate.

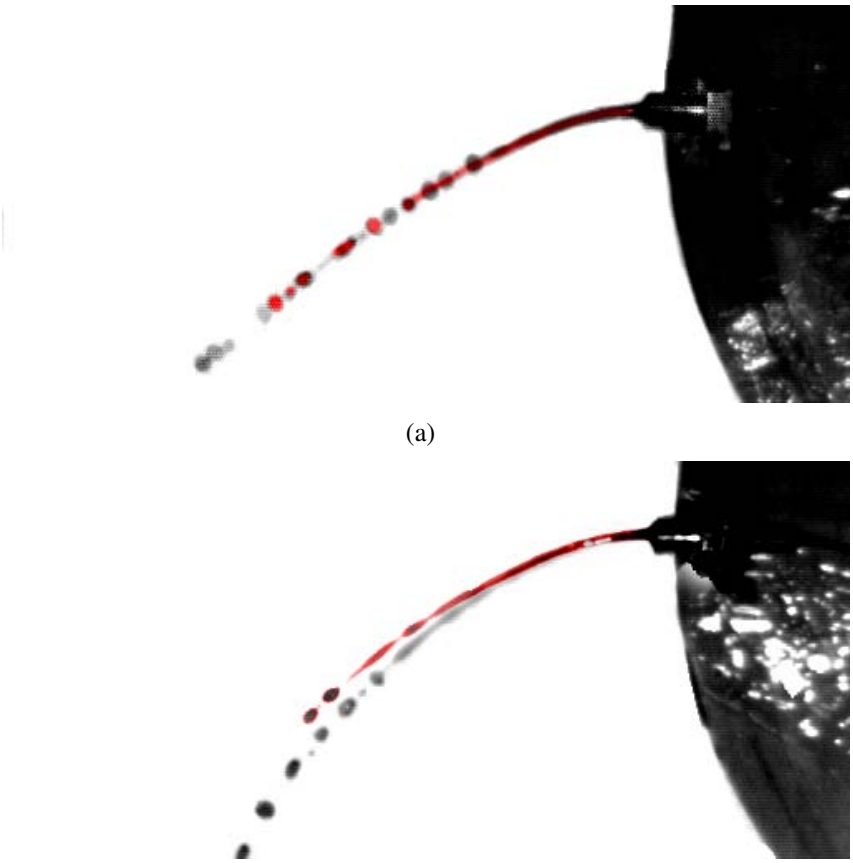

(a)

(b)

Figure 5.25: Images showing differences in break-up between a solution of 0.1% SDS (shown in red) and a jet of water (grey) with a liquid aspect ratio of $1/2$ flowing through a 3 mm nozzle at (a) 30 rpm ($\mathcal{R}b = 1.96, \mathcal{W}e = 16.43, \mathcal{R}e = 1343$), (b) 60 rpm ($\mathcal{R}b = 1.01, \mathcal{W}e = 17.37, \mathcal{R}e = 1382$)

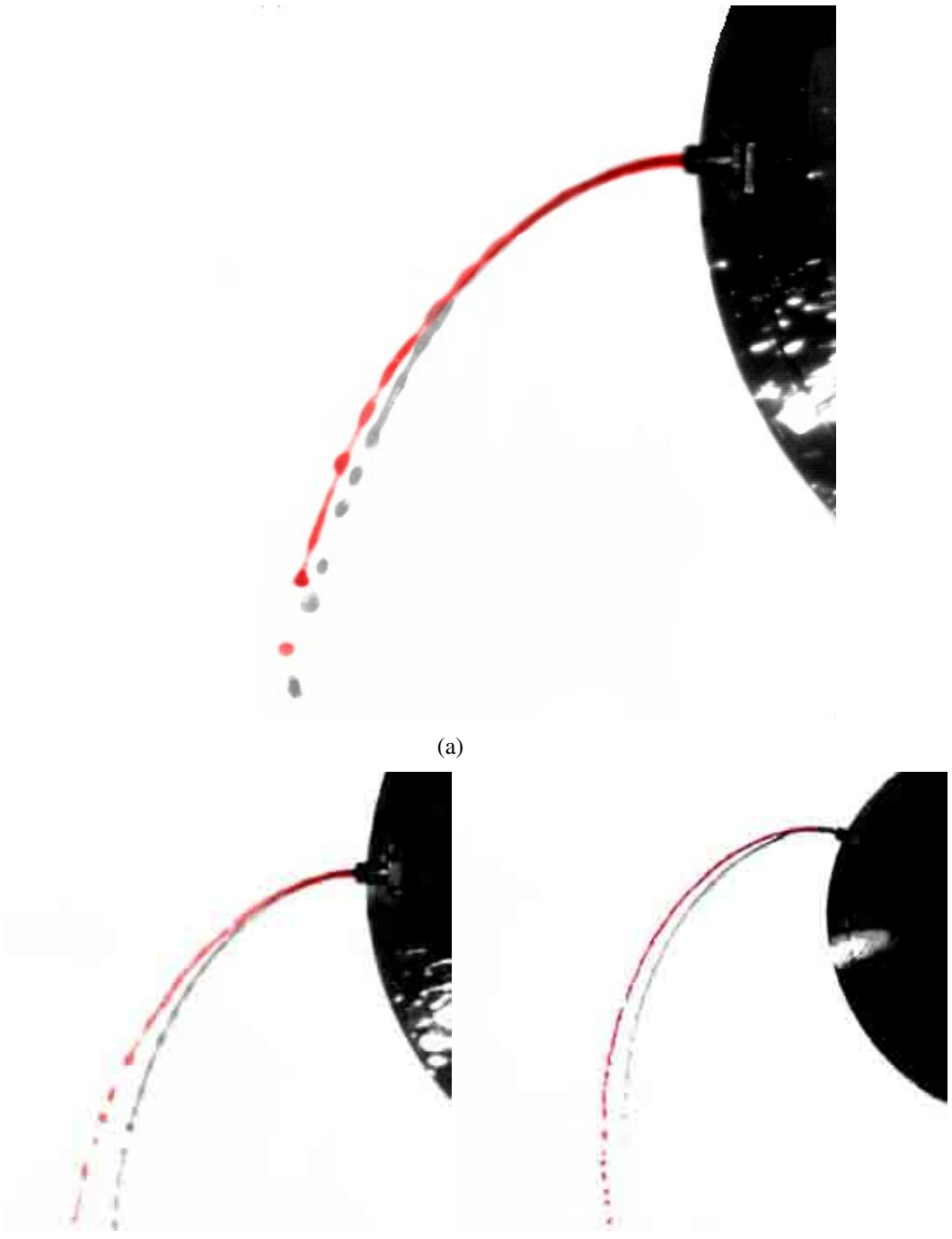

(a)

(b) (c)

Figure 5.26: Images showing differences in break-up between a solution of 0.1% SDS (shown in red) and a jet of water (grey) with a liquid aspect ratio of $1/4$ flowing through a 3 mm nozzle at (a) 120 rpm ($\mathcal{R}b = 0.60, \mathcal{W}e = 54.51, \mathcal{R}e = 2447$), (b) 180 rpm ($\mathcal{R}b = 0.58, \mathcal{W}e = 93.09, \mathcal{R}e = 3196$), (c) 300 rpm ($\mathcal{R}b = 0.56, \mathcal{W}e = 135.02, \mathcal{R}e = 3847$).

It is obvious from all the images of surfactant jets examined so far that the droplets produced from break-up are less well formed and appear less spherical than those obtained from both Newtonian and non-Newtonian jets examined. This is due to weakened surface tension effects, which acts to contract a droplet to a sphere, such that its surface area is minimised.

5.3.1 Influence of system parameters on exit velocity and break-up length

The effect of the Rossby number on jet exit velocity is shown in Figure 5.27. The data obtained from experiments on shear thinning liquid jets and Newtonian water jets on the pilot scale is also shown. It can be seen that the data is comparable and that the exit velocity of surfactant laden jets is similar both to that of water and shear thinning liquid jets on the pilot scale, although no obvious trends are apparent.

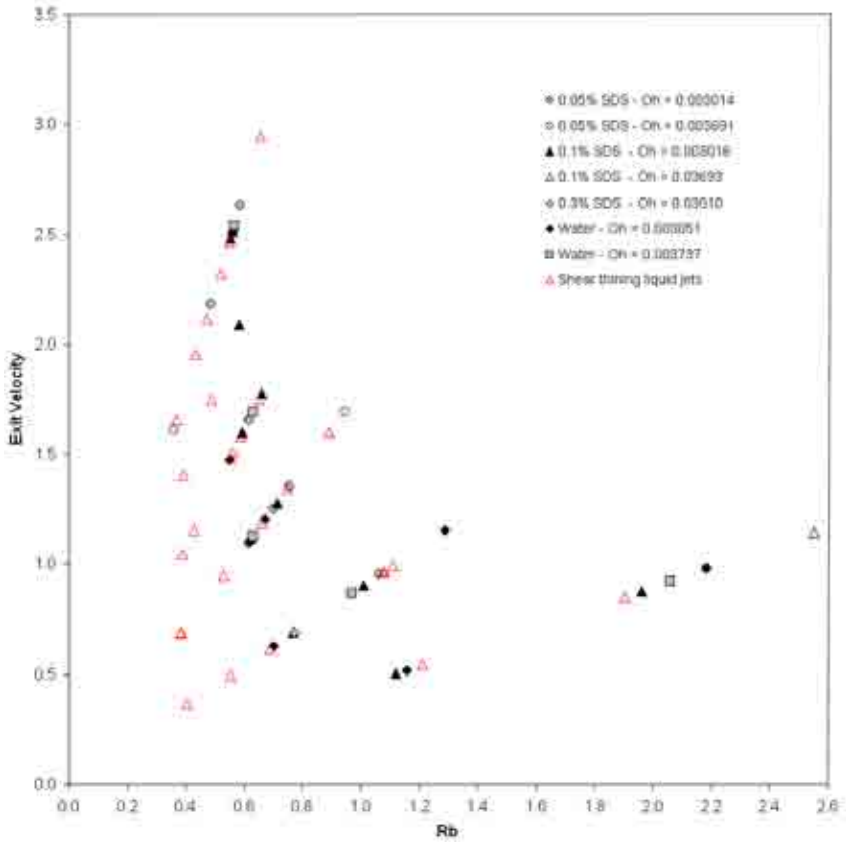

Figure 5.27: Influence of Rossby number on jet exit velocity for solutions with varying concentration of surfactant (0.05 - 0.3% SDS).

The influence of rotation rate, $\mathcal{F}r/\mathcal{R}b$ on jet exit velocity is shown in Figure 5.28 and it can be observed that the exit velocity increases with increasing rotation rate, as expected. The data

is again compared to water, and it can be seen that there are no obvious differences due to the addition of surfactant and decreasing surface tension on the exit velocity of the jet.

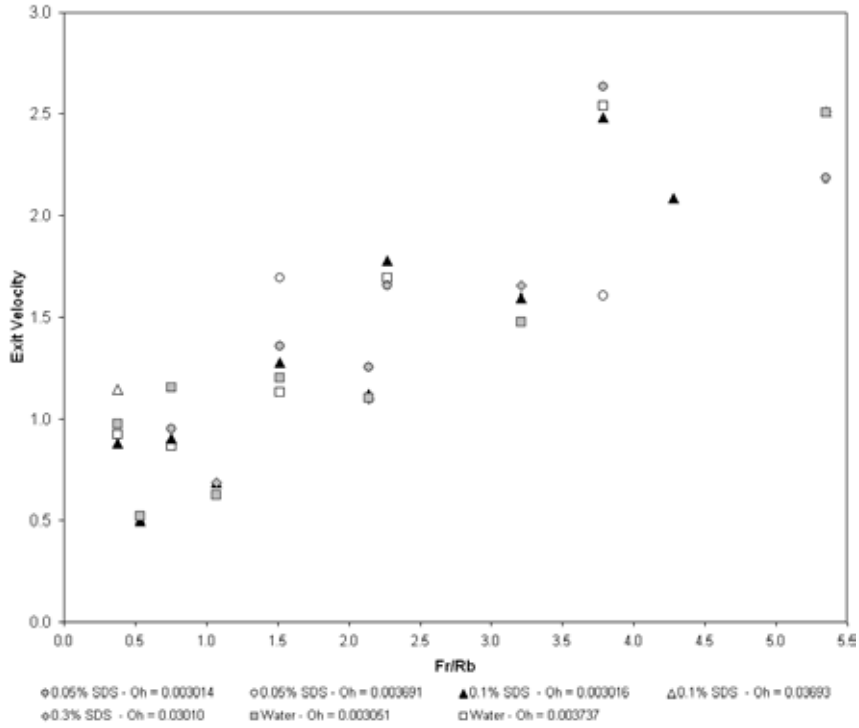

Figure 5.28: Influence of $\mathcal{F}r/\mathcal{R}b$ on jet exit velocity for solutions with varying concentration of surfactant (0.05 - 0.3% SDS).

For surfactants, Figure 5.29(a) illustrates that break-up length increases with Weber number and is not dissimilar to break-up lengths obtained for water for dimensionless parameters in the same range. Break-up length was also found to increase with increasing Reynolds number, as shown in Figure 5.29(b) and is again comparable with the break-up length of water. Break-up length can also be seen to increase with rotation rate, which would be expected, as demonstrated by Figure 5.29(c). In Figures 5.29(a) - 5.29(c) the concentration of surfactant present (0 - 0.3%) appears to have little effect on the trends found in each case and the data collapses quite well, within the statistical spread observed, regardless of the liquid system.

5.3.2 Drop size as a function of system parameters

As shown in previous figures, qualitatively the droplets themselves seem more unstable and less well formed when surfactants are added. In this section the quantitative effects of surfactant on

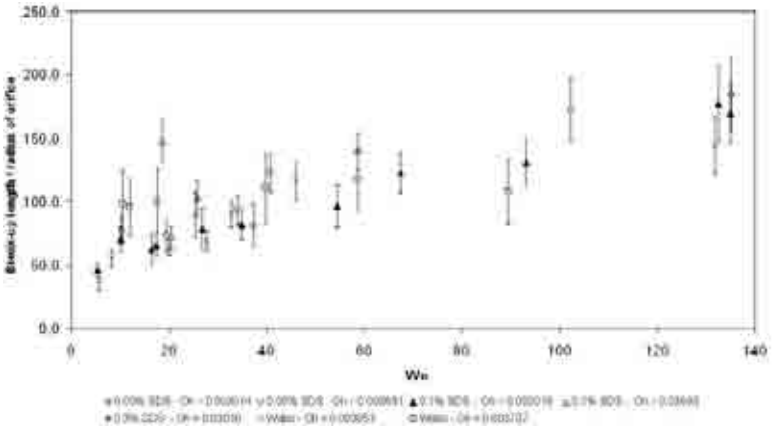

(a) Influence of $\mathcal{W}e$ on the break-up length for solutions with varying concentration of surfactant.

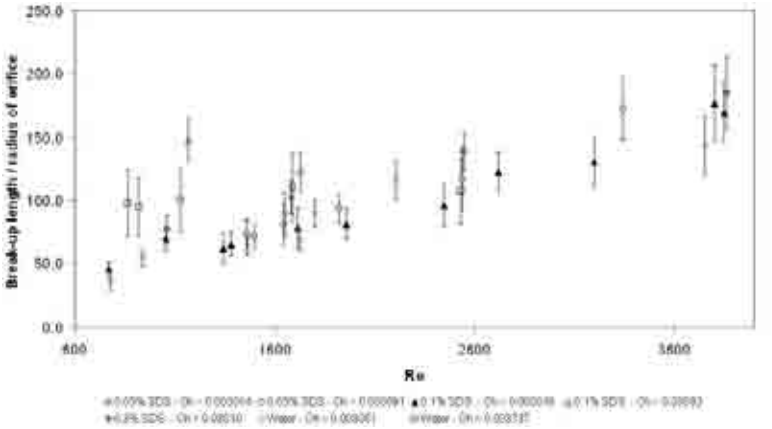

(b) Influence of $\mathcal{R}e$ on the break-up length for solutions with varying concentration of surfactant.

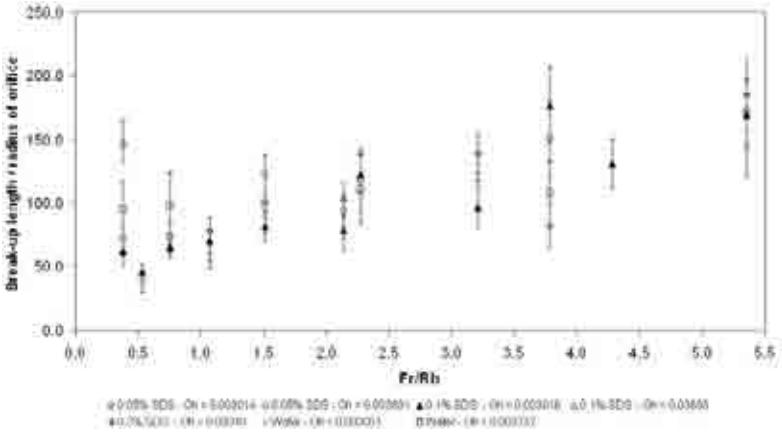

(c) Influence of $\mathcal{F}r/\mathcal{R}b$ on the break-up length for solutions with varying concentration of surfactant.

Figure 5.29: Influence of (a) Weber number, (b) Reynolds number and (c) rotation rate upon the non-dimensional break-up length of the spiralling jet solutions with varying concentration of surfactant (0.05 - 0.3% SDS).

drop size are examined.

The effect of jet exit velocity on primary and satellite droplets is shown in Figure 5.30(a). Primary droplets emanating from the 3 mm nozzle can be seen to decrease with increasing exit velocity. However, for satellite droplets and droplets occurring from the 2 mm nozzle there appears to be no monotonic relationship between exit velocity and droplet size. Satellite droplets appear mostly unaffected by changes in U. The trendlines marked on the graph are shown to guide the eye.

When the effect of Rossby number on drop size is examined, in Figure 5.30(b), it can be seen that the drop sizes appear to generally increase with increasing Rossby number. This occurs for both primary and satellite droplets.

As the addition of SDS to an aqueous solution has minimal effect on the viscosity of the fluid, a plot of drop size against Ohnesorge number is largely redundant.

An example of a drop size distribution for a 0.1% SDS solution can be seen in Figure 5.31. As the rotation rate increases both the size of the primary and satellite droplets appear to reduce in size. Increasing rotation rate also causes the main droplet peak to decrease and the satellite droplet peak to increase, hence a greater spread of droplets is obtained. The drop size distribution becomes more distinctly bimodal as Ω increases.

A more extensive study of drop size distributions for surfactants on the pilot scale can be found in Appendix A.3.

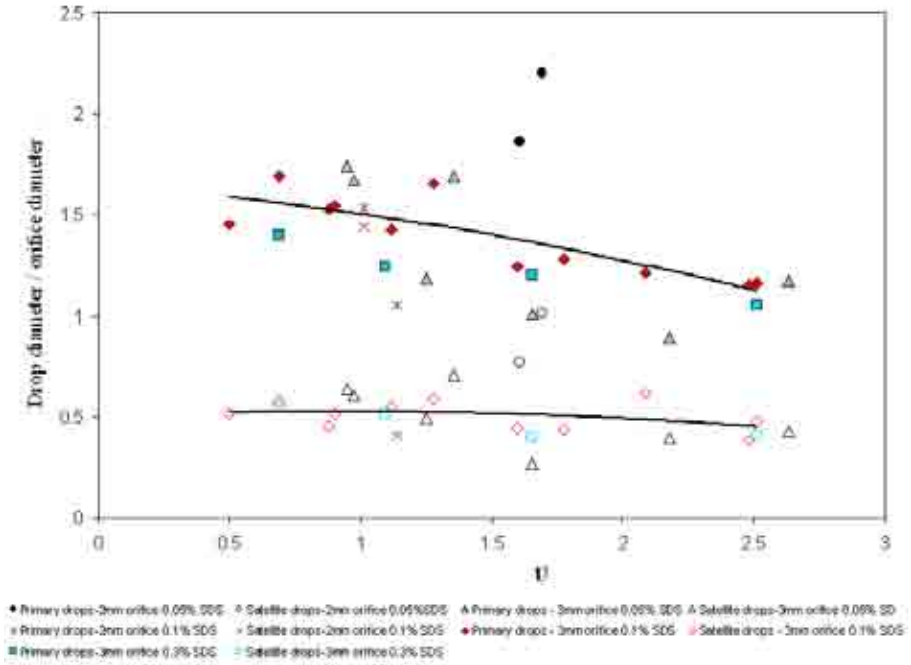

(a) Effect of U on primary and corresponding satellite drop sizes.

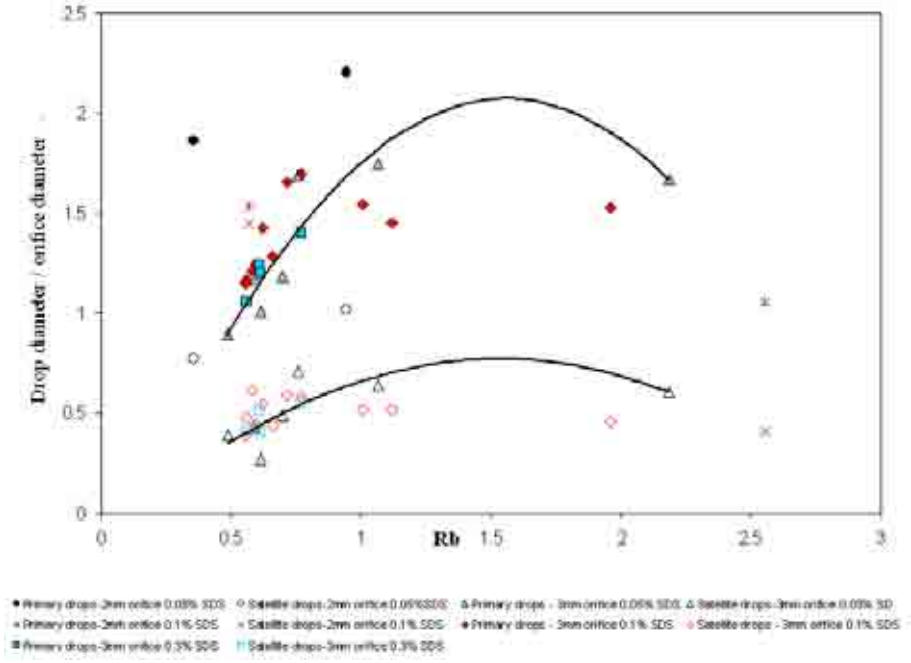

(b) Effect of $\mathcal{R}b$ on primary and corresponding satellite drop sizes.

Figure 5.30: Influence of (a) average jet exit velocity and (b) Rossby number upon primary and corresponding satellite drop sizes for varying concentrations of surfactant.

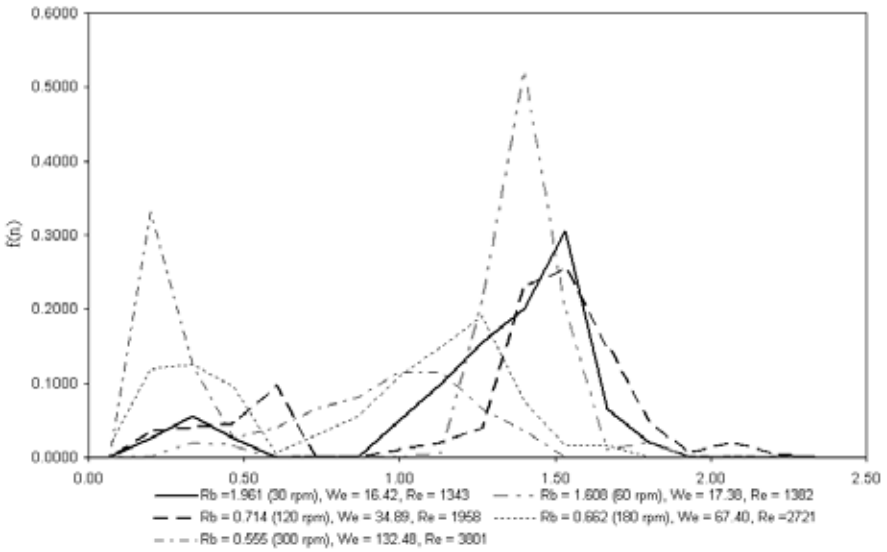

Figure 5.31: Drop size distribution for a solution of 0.1% SDS with a liquid aspect ratio of $1/2$ flowing through a nozzle of diameter 0.003 m.

5.4 Conclusions

An investigation of the break-up mechanisms and drop formation of curved shear-thinning liquid jets emerging from the side of a perforated drum rotating about its vertical axis was carried out on the pilot scale.

Comparison with previous experiments with Newtonian fluids performed at the pilot scale (Partridge et al., 2005) showed that the jet shapes at break-up were markedly different, with none of the previously observed break-up modes being detected. Extreme curvature of the ligaments between the primary drops, resulting from the growth of long wavelength disturbances, were attributed to the effects of air resistance. This phenomena, together with the formation of pendant droplets, could be predicted on a flow regime map of Ohnesorge number versus Weber number.

Mechanisms of satellite formation from the ligaments are either contraction to form a single droplet, or by the ligament shattering to form several droplets. In some cases the ligament contracts into the primary droplet and no satellite is formed. This creates difficulties in the prediction of satellite droplet formation from the theoretical simulations; satellite droplets are only calculated if a clear minimum in the drop radius is observed either side of the ligament.

Predictions of both primary and satellite drop size give reasonable agreement over the parameter ranges of the experiments, with agreement within 25% for the primary drops and mostly within 50% for the satellite drops, if formed. For six selected experiments, where the theoretical and experimental break-up lengths are matched, good qualitative agreement of jet shape and trajectory is found, provided that the assumption of the negligible effect of gravity holds.

A study of the influence of varying surface tension along the jet through the addition of a soluble surfactant was also performed. It was found that, due to weakened surface tension effects, which acts to contract a droplet, such that its surface area is minimised, the droplets produced from break-up are less well formed and appear less spherical than those obtained from both Newtonian and non-Newtonian jets examined.

The break-up length of the jet was also examined and compared to that found for Newtonian fluids. At lower rotation rates, the surfactant jets were found to have a longer break-up length, which is to be expected, as the surface tension for the surfactant jet should be lower at break-up than the jet of water, hence disturbances due to surface tension are damped. The curvature of the jets was also found to be less, which agrees with the work of Uddin et al. (2008b). However, as the rate of rotation increased, it was found that the surfactant jets actually breaks up sooner than the jet of water. This may be due to increased mechanical vibration in the rig as the rotation rate increases, with the surface tension forces present in the surfactant jet not being strong enough to hold the jet together.

CHAPTER 6

LINEAR ANALYSIS OF PSEUDOPLASTIC CURVED JETS[1]

In this Chapter, the effects of the non-Newtonian rheology on the trajectory of curved liquid jets are examined theoretically and, by applying the methods of Rayleigh (1879a,b) and Weber (1931), their linear instability is determined using a mixture of computational and asymptotic methods. The stability of the jet is analysed using spatial (Keller et al., 1973) and temporal stability methods.

While the non-linear model provides a simulation of the jet, the drop sizes predicted are generally too large. It was found in the Newtonian case, in Gurney et al. (2010), that the linear model actually gives a more accurate prediction of drop size in cases of high viscosity. By developing a linear model for power law fluids, it is possible to see if this is the same. Additionally we can obtain more information about the jets, by enabling us to examine growth rates and wavenumbers.

Uddin (2007) found the most unstable wave by taking a long wavelength approximation of his equations and then perturbed by δ to find a long wavelength dispersion relation. The calculations presented here extend those of Uddin (2007) by making no assumption as to whether the waves are in any sense, long or short, which gives rise to a more general dispersion relation. This will enable a linear prediction of primary drop sizes. Additionally, the computational time of the linear model is less expensive than that of the non-linear model and, as can be seen in

[1]This Chapter has been largely published in Hawkins et al. (2010).

Chapter 5.2.2 and 5.2.3 it is not possible to predict satellite droplets for all cases anyway using the non-linear model. This suggests that having a linear model available could be advantageous, particularly in the prediction of primary drop sizes.

The sizes of the droplets produced by this instability are determined by considering the most unstable wave mode. This enables a quantitative comparison between theoretical and experimental results to be made, by comparing droplet sizes predicted from the theory with experimental measurements.

6.1 Jet co-ordinate system

6.2 Problem formulation

To model the prilling process, as described in Chapter 2.3.2, a large circular cylindrical drum of radius s_0, rotating about its vertical axis of symmetry with angular velocity, Ω, is considered. A liquid jet emerges from a small circular orifice of radius a, situated on the curved surface of the drum.

A co-ordinate system, (x, y, z) which rotates with the drum, is used. This is shown in Figure 2.11 and more detail can be found in Chapter 2.3.2. The curvilinear co-ordinate system, (s, n, ϕ), introduced by Wallwork et al. (2002) is used to describe the curved jet, where s is the arclength along the centreline of the jet, measured from the orifice, and (n, ϕ) are the plane polar co-ordinates in the radial and azimuthal directions in any cross section of the jet. The origin of the co-ordinate system is at the centre of the circular cross section of the jet. The associated unit vectors are denoted by $\mathbf{e_s}$, $\mathbf{e_n}$ and $\mathbf{e}_\phi$ respectively and are shown in Figure 6.1 and Figure 2.13 in Chapter 2.

The effects of gravity on the jet can be neglected if the centripetal acceleration of the jet, $s_0\Omega^2$, where Ω is the rotation of the drum (rad s^{-1}), is much greater than the acceleration due to gravity, g, acting in the negative y direction, as is the case with industrial prilling. Thus the jet's centreline is assumed to lie solely in the $x - z$ plane and the centreline of the jet is given by $(X(s,t), 0, Z(s,t))$ in Cartesian co-ordinates, where t is the time and X and Z are functions

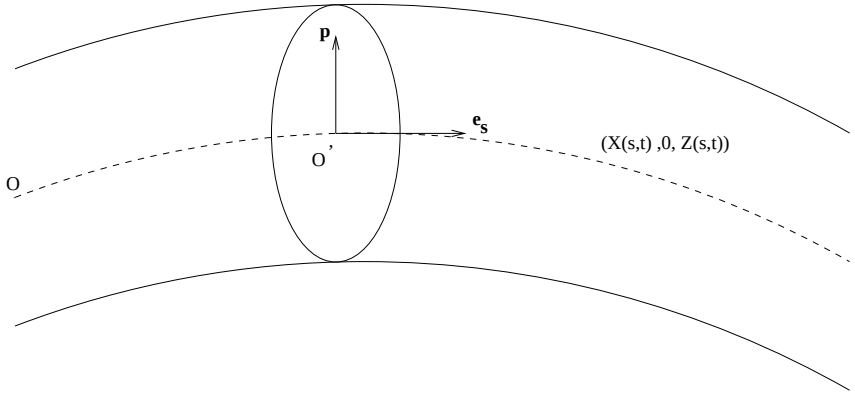

Figure 6.1: Sketch of a curved jet in the (X, Z) plane.

to be found.

The unit vectors in this co-ordinate system are calculated using a principal normal vector, **p**, and a binormal vector, **b**, to the centreline (shown in Figure 2.13 in Chapter 2) and are as defined in Equations (2.5) and (2.6) in Chapter 2.

These form an orthogonal co-ordinate system (Uddin, 2007) and once again, the position vector of any particle, Q, relative to the centre of the orifice, O, on the free surface is given by $\mathbf{r} = \int_0^s \mathbf{e_s} ds + n\mathbf{e_n}$.

The flow is described using the velocity vector $\mathbf{u} = u\mathbf{e_s} + v\mathbf{e_n} + w\mathbf{e}_\phi$, to arrive at the equations of motion describing the dynamics of the jet. These include Euler's equations and the continuity equation

$$\rho\left(\frac{\partial \mathbf{u}}{\partial t} + \mathbf{u}\cdot\nabla\mathbf{u}\right) = -\nabla p + \nabla\cdot\boldsymbol{\tau} - 2\boldsymbol{\omega}\times\mathbf{u} - \boldsymbol{\omega}\times(\boldsymbol{\omega}\times\mathbf{r'}), \tag{6.1}$$

$$\nabla\cdot\mathbf{u} = 0, \tag{6.2}$$

where ρ is the constant density of the fluid, p is the pressure within the jet, $\boldsymbol{\tau}$ is the stress tensor, $\boldsymbol{\omega} = \Omega\mathbf{j}$ is the angular velocity vector of the container and $\mathbf{r'} = \mathbf{r} + s_0\mathbf{i}$.

The surface of the jet is described by the equation $n - R(s,t,\phi) = 0$, where $R(s,t,\phi)$ is a function giving the free surface position. A normal vector to this surface is given by $\nabla(n - R(s,t,\phi))$. When evaluated this gives the unit normal vector as

$$\mathbf{n} = \frac{1}{E}\left(-\frac{\partial R}{\partial s}\cdot\frac{1}{h_s}\cdot\mathbf{e}_s + \mathbf{e}_n - \frac{\partial R}{\partial \phi}\cdot\frac{1}{R}\cdot\mathbf{e}_\phi\right), \tag{6.3}$$

where

$$E = \left(1 + \left(\frac{\partial R}{\partial s}\right)^2 \cdot \frac{1}{h_s^2} + \left(\frac{\partial R}{\partial \phi}\right)^2 \cdot \frac{1}{R^2}\right)^{\frac{1}{2}} \tag{6.4}$$

and

$$h_s = 1 + n\cos\phi(X_s Z_{ss} - Z_s X_{ss}). \tag{6.5}$$

The normal stress condition is given by $\mathbf{n} \cdot \Pi \cdot \mathbf{n} = \sigma\kappa$, where Π is the total stress tensor, σ is the isotropic surface tension and κ is the curvature of the free surface,

$$\kappa = \frac{1}{nh_s}\left(\frac{\partial}{\partial s}\left(\frac{-\frac{n}{h_s}\frac{\partial R}{\partial s}}{E}\right) + \frac{\partial}{\partial n}\left(\frac{nh_s}{E}\right) + \frac{\partial}{\partial \phi}\left(\frac{-\frac{h_s}{n}\frac{\partial R}{\partial \phi}}{E}\right)\right).$$

Using the two tangent vectors to our free surface, $\mathbf{t}_1 = \partial\mathbf{r}/\partial s$ and $\mathbf{t}_2 = \partial\mathbf{r}/\partial\phi$, it is possible to form tangential stress conditions $\mathbf{t}_i \cdot \Pi \cdot \mathbf{n} = 0$, for $i = 1, 2$. The kinematic condition is given by

$$\frac{D}{Dt}(R(s,t,\phi) - n) = 0, \qquad \text{for} \quad n = R(s,\phi,t).$$

Non-dimensional equations are derived as in Uddin et al. (2006), using the transformations

$$\begin{aligned} &\bar{u} = \frac{u}{U}, \bar{v} = \frac{v}{U}, \bar{w} = \frac{w}{U}, \bar{p} = \frac{p}{\rho U^2}, \bar{n} = \frac{n}{a}, \epsilon = \frac{a}{s_0}, \\ &\bar{R} = \frac{R}{a}, \bar{s} = \frac{s}{s_0}, \bar{t} = \frac{tU}{s_0}, \bar{X} = \frac{X}{s_0}, \bar{Z} = \frac{Z}{s_0}, \bar{\eta} = \frac{\eta}{k}, \end{aligned} \tag{6.6}$$

where U is the exit speed of the jet in the rotating frame, ρ is the liquid density, ϵ is a small aspect ratio, p is the pressure, R is the jet radius, k (Pa s$^\alpha$) is the fluid consistency index, and u, v and w are the tangential, radial and azimuthal velocity components relative to the centreline of the jet respectively. The bars denote dimensionless quantities in the above expressions.

For power-law fluids

$$\boldsymbol{\tau} = \eta(\boldsymbol{\nabla u} + (\boldsymbol{\nabla u})^T) = \eta\boldsymbol{\gamma}, \tag{6.7}$$

where $\boldsymbol{\nabla u}$ is the velocity gradient tensor, the transpose of which is $(\boldsymbol{\nabla u})^T$, $\boldsymbol{\tau}$ is the stress tensor, $\boldsymbol{\gamma}$ is the rate of strain tensor and η is the apparent (effective) viscosity and is a function

of shear rate, $\dot{\gamma}$, such that

$$\eta = k\dot{\gamma}^{\alpha-1}, \tag{6.8}$$

where α is the flow index number and is dimensionless. The shear rate is given by the second invariant of the rate of strain tensor,

$$\dot{\gamma} = \sqrt{\frac{\boldsymbol{\gamma} : \boldsymbol{\gamma}}{2}}. \tag{6.9}$$

For power law fluids the viscosity is not constant and we know (from Uddin, 2007) that

$$\begin{aligned}
(\boldsymbol{\nabla} \cdot \boldsymbol{\tau})_j &= (\boldsymbol{\nabla} \cdot (\eta\gamma))_j \\
&= \eta(\boldsymbol{\nabla} \cdot (\boldsymbol{\nabla}\boldsymbol{u} + \boldsymbol{\nabla}\boldsymbol{u}^T))_j + \frac{\gamma_{ij}}{h_i}\partial_i\eta \\
&= (\eta\boldsymbol{\nabla}^2\boldsymbol{u})_j + \frac{\gamma_{ij}}{h_i}\partial_i\eta
\end{aligned} \tag{6.10}$$

where the free indices go through s, n and ϕ and h_i are the structure functions given by

$$h_s = 1 + n\cos\phi(X_s Z_{ss} - Z_s X_{ss}),\ h_n = 1,\ h_\phi = n.$$

Using (6.8) and (6.9), the apparent viscosity η has the form

$$\eta = k\left(\frac{\boldsymbol{\gamma} : \boldsymbol{\gamma}}{2}\right)^{\frac{\alpha-1}{2}}.$$

To evaluate the components of the stress tensor, $\boldsymbol{\tau}$, it is necessary to determine the gradient of a vector field as in Uddin (2007)

$$\nabla\boldsymbol{u} = \left(\sum_i \frac{\boldsymbol{e_i}}{h_i}\frac{\partial}{\partial x_i}\right)\left(\sum_j \frac{\boldsymbol{e_j}}{h_j}u_j\right).$$

The orthogonal set of vectors $\boldsymbol{e}_s, \boldsymbol{e}_n$ and $\boldsymbol{e}_\phi$ are not constant and their derivatives can be expressed as

$$\frac{\partial \boldsymbol{e_\alpha}}{\partial b} = \frac{\boldsymbol{e_\beta}}{h_\alpha}\frac{\partial h_\beta}{\partial\alpha} - \delta_{\alpha\beta}\sum_\gamma \frac{\boldsymbol{e_\gamma}}{h_\gamma}\frac{\partial h_\alpha}{\partial\gamma}.$$

Here, the variables α, β and γ go through s, n and ϕ and the Kroneker delta has its usual interpretations. Recalling (6.7), we have that $\tau_{ij} = \eta\gamma_{ij}$, and the nine stress components (from Uddin, 2007), are written as

$$\begin{aligned}
\tau_{ss} &= \frac{2\eta}{h_s}\left(\frac{\partial u}{\partial s} + (v\cos\phi - w\sin\phi)(X_s Z_{ss} - X_{ss} Z_s)\right) && (6.11)\\
\tau_{nn} &= 2\eta\left(\frac{\partial v}{\partial n}\right) && (6.12)\\
\tau_{\phi\phi} &= \frac{2\eta}{n}\left(\frac{\partial w}{\partial \phi} + v\right) && (6.13)\\
\tau_{sn} = \tau_{ns} &= \eta\left(\frac{1}{h_s}\frac{\partial v}{\partial s} + \frac{\partial u}{\partial n} - \frac{u}{h_s}\cos\phi(X_s Z_{ss} - X_{ss} Z_s)\right) && (6.14)\\
\tau_{n\phi} = \tau_{\phi n} &+ \eta\left(\frac{\partial w}{\partial n} = \frac{w}{n} + \frac{1}{n}\frac{\partial v}{\partial \phi}\right) && (6.15)\\
\tau_{s\phi} = \tau_{\phi s} &= \eta\left(\frac{1}{n}\frac{\partial n}{\partial \phi} + \frac{u}{h_s}\sin\phi(X_s Z_{ss} - X_{ss} Z_s) + \frac{1}{h_s}\frac{\partial w}{\partial s}\right). && (6.16)
\end{aligned}$$

An expression for η can be obtained by using the expressions for γ_{ij} such that

$$\eta = k\sum_{ij}\frac{\gamma_{ij}\gamma_{ij}}{2}^{\frac{\alpha-1}{2}}. \tag{6.17}$$

6.3 The equations of motion

The resulting non-dimensional equations of motion differ to those found in Decent et al. (2009) in the Newtonian case, through the dynamic viscosity being replaced by η and by the inclusion of the derivatives of η.

Dropping overbars for simplicity the continuity equation is

$$\begin{aligned}
\epsilon n\frac{\partial u}{\partial s} + (1 + \epsilon n\cos\phi\,(X_s Z_{ss} - X_{ss} Z_s))\left(v + n\frac{\partial v}{\partial n} + \frac{\partial w}{\partial \phi}\right)\\
+\epsilon n\,(X_s Z_{ss} - X_{ss} Z_s)\,(v\cos\phi - w\sin\phi) = 0, \qquad (6.18)
\end{aligned}$$

and the Navier-Stokes equations are

$$
\begin{aligned}
&(1+\epsilon n\cos\phi\,(X_sZ_{ss}-X_{ss}Z_s))\left(\epsilon\frac{\partial u}{\partial t}\right.\\
&\left.+\epsilon v\cos\phi\,(Z_{st}X_s-X_{st}Z_s)+\epsilon w\sin\phi\,(X_{st}Z_s-Z_{st}X_s)+v\frac{\partial u}{\partial n}+\frac{w}{n}\frac{\partial u}{\partial\phi}\right)\\
&+\epsilon u\frac{\partial u}{\partial s}+\epsilon u\,(X_sZ_{ss}-X_{ss}Z_s)\,(v\cos\phi-w\sin\phi)\\
&=-\epsilon\frac{\partial p}{\partial s}+\left(\frac{2\epsilon}{\mathcal{R}b}\,(v\cos\phi-w\sin\phi)\right.\\
&\left.+\frac{\epsilon}{\mathcal{R}b^2}\,((X+1)X_s+ZZ_s)\right)(1+\epsilon n\cos\phi\,(X_sZ_{ss}-X_{ss}Z_s))\\
&+\frac{\eta}{\epsilon\mathcal{R}e_\alpha}\left(\frac{-\epsilon^3 n\cos\phi\,(X_sZ_{sss}-X_{sss}Z_s)}{(1+\epsilon n\cos\phi\,(X_sZ_{ss}-X_{ss}Z_s))^2}\left(\frac{\partial u}{\partial s}\right.\right.\\
&\left.+v\cos\phi\,(X_sZ_{ss}-X_{ss}Z_s)-w\sin\phi\,(X_sZ_{ss}-X_{ss}Z_s)\right)\\
&+\frac{\epsilon^2}{(1+\epsilon n\cos\phi\,(X_sZ_{ss}-X_{ss}Z_s))}\left(-u\,(X_sZ_{ss}-X_{ss}Z_s)^2+\frac{\partial^2 u}{\partial s^2}\right.\\
&+2\frac{\partial v}{\partial s}\cos\phi\,(X_sZ_{ss}-X_{ss}Z_s)+v\cos\phi\,(X_sZ_{sss}-X_{sss}Z_s)\\
&\left.-2\frac{\partial w}{\partial s}\sin\phi\,(X_sZ_{ss}-X_{ss}Z_s)-w\sin\phi\,(X_sZ_{sss}-X_{sss}Z_s)\right)\\
&+(1+2\epsilon n\cos\phi\,(X_sZ_{ss}-X_{ss}Z_s))\frac{\partial u}{\partial n}+n\,(1+\epsilon n\cos\phi\,(X_sZ_{ss}-X_{ss}Z_s))\frac{\partial^2 u}{\partial n^2}\\
&\left.-\epsilon\frac{\partial u}{\partial\phi}\sin\phi\,(X_sZ_{ss}-X_{ss}Z_s)+(1+\epsilon n\cos\phi\,(X_sZ_{ss}-X_{ss}Z_s))\frac{1}{n}\frac{\partial^2 u}{\partial\phi^2}\right)\\
&+\frac{1}{\epsilon\mathcal{R}e_\alpha}\left\{\frac{2\epsilon^2}{1+\epsilon n\cos\phi(X_sZ_{ss}-X_{ss}Z_s)}\frac{\partial\eta}{\partial s}\left(\frac{\partial u}{\partial s}+(v\cos\phi-w\sin\phi)(X_sZ_{ss}-X_{ss}Z_s)\right)\right.\\
&+\frac{1}{n}\frac{\partial\eta}{\partial\phi}\left(\epsilon u\sin\phi(X_sZ_{ss}-X_{ss}Z_s)+\frac{1+\epsilon n\cos\phi(X_sZ_{ss}-X_{ss}Z_s)}{n}\frac{\partial u}{\partial\phi}+\epsilon\frac{\partial w}{\partial s}\right)\\
&\left.+\frac{\partial\eta}{\partial n}\left(\epsilon\frac{\partial v}{\partial s}-\epsilon u\cos\phi(X_sZ_{ss}-X_{ss}Z_s)+1+\epsilon n\cos\phi(X_sZ_{ss}-X_{ss}Z_s)\frac{\partial u}{\partial n}\right)\right\},
\end{aligned}
\tag{6.19}
$$

$$
\begin{aligned}
&(1+\epsilon n\cos\phi\,(X_sZ_{ss}-X_{ss}Z_s))\left(\epsilon\frac{\partial v}{\partial t}+\epsilon u\cos\phi\,(X_{st}Z_s-Z_{st}X_s)+v\frac{\partial v}{\partial n}+\frac{w}{n}\frac{\partial v}{\partial\phi}-\frac{w^2}{n}\right)\\
&\qquad+\epsilon u\frac{\partial v}{\partial s}-\epsilon\cos\phi\,(X_sZ_{ss}-X_{ss}Z_s)\,u^2\\
&\qquad=\left(-\frac{\partial p}{\partial n}-\frac{2\epsilon}{\mathcal{R}b}u\cos\phi\right.\\
&\left.+\frac{\epsilon\cos\phi}{\mathcal{R}b^2}\left((X+1)Z_s-ZX_s+\epsilon n\cos\phi\right)\right)(1+\epsilon n\cos\phi\,(X_sZ_{ss}-X_{ss}Z_s))\\
&\qquad+\frac{1}{\epsilon\mathcal{R}e_\alpha}\frac{\eta}{n}\left(\frac{-\epsilon^3n^2\cos\phi\,(X_sZ_{sss}-X_{sss}Z_s)}{(1+\epsilon n\cos\phi\,(X_sZ_{ss}-X_{ss}Z_s))^2}\left(\frac{\partial v}{\partial s}\right.\right.\\
&\qquad\left.-u\cos\phi\,(X_sZ_{ss}-X_{ss}Z_s)\right)\\
&\qquad+\frac{\epsilon^2n}{(1+n\cos\phi\,(X_sZ_{ss}-X_{ss}Z_s))}\left(-v\cos^2\phi\,(X_sZ_{ss}-X_{ss}Z_s)^2+\frac{\partial^2v}{\partial s^2}\right.\\
&\qquad-2\frac{\partial u}{\partial s}\cos\phi\,(X_sZ_{ss}-X_{ss}Z_s)-u\cos\phi\,(X_sZ_{sss}-X_{sss}Z_s)\\
&\qquad\left.+w\sin\phi\cos\phi\,(X_sZ_{ss}-X_{ss}Z_s)^2\right)+(1+2\epsilon n\cos\phi\,(X_sZ_{ss}-X_{ss}Z_s))\frac{\partial v}{\partial n}\\
&\qquad+n\,(1+\epsilon n\cos\phi\,(X_sZ_{ss}-X_{ss}Z_s))\frac{\partial^2v}{\partial n^2}-\epsilon\left(\frac{\partial v}{\partial\phi}-w\right)\sin\phi\,(X_sZ_{ss}-X_{ss}Z_s)\\
&\qquad\left.+(1+\epsilon n\cos\phi\,(X_sZ_{ss}-X_{ss}Z_s))\frac{1}{n}\left(\frac{\partial^2v}{\partial\phi^2}-v-2\frac{\partial w}{\partial\phi}\right)\right)\\
&\qquad+\frac{1}{\epsilon\mathcal{R}e_\alpha}\left\{\frac{\epsilon}{1+\epsilon n\cos\phi(X_sZ_{ss}-X_{ss}Z_s)}\frac{\partial\eta}{\partial s}\left(\epsilon\frac{\partial v}{\partial s}-\epsilon u\cos\phi(X_sZ_{ss}-X_{ss}Z_s)\right.\right.\\
&\qquad\left.+(1+\epsilon n\cos\phi(X_sZ_{ss}-X_{ss}Z_s))\frac{\partial u}{\partial n}\right)\\
&\qquad+\frac{\partial\eta}{\partial n}\left(2(1+\epsilon n\cos\phi(X_sZ_{ss}-X_{ss}Z_s))\frac{\partial v}{\partial n}\right)\\
&\qquad\left.+\frac{1+\epsilon n\cos\phi(X_sZ_{ss}-X_{ss}Z_s)}{n}\frac{\partial\eta}{\partial\phi}\left(\frac{\partial w}{\partial n}-\frac{w}{n}+\frac{1}{n}\frac{\partial v}{\partial\phi}\right)\right\}
\end{aligned}
\tag{6.20}
$$

and

$$
\begin{aligned}
&(1+\epsilon n\cos\phi\,(X_sZ_{ss}-X_{ss}Z_s))\left(\epsilon\frac{\partial w}{\partial t}+\epsilon u\sin\phi\,(Z_{st}X_s-X_{st}Z_s)+v\frac{\partial w}{\partial n}+\frac{w}{n}\frac{\partial w}{\partial\phi}+\frac{vw}{n}\right)\\
&\qquad+\epsilon u\frac{\partial w}{\partial s}+\epsilon\sin\phi\,(X_sZ_{ss}-X_{ss}Z_s)\,u^2\\
&\qquad=\left(-\frac{1}{n}\frac{\partial p}{\partial\phi}+\frac{2\epsilon}{\mathcal{R}b}u\sin\phi\right.\\
&\left.+\frac{\epsilon\sin\phi}{\mathcal{R}b^2}\,(ZX_s-(X+1)Z_s-\epsilon n\cos\phi)\right)(1+\epsilon n\cos\phi\,(X_sZ_{ss}-X_{ss}Z_s))\\
&\qquad+\frac{1}{\epsilon\mathcal{R}e_\alpha}\frac{\eta}{n}\left(\frac{-\epsilon^3\cos\phi\,(X_sZ_{sss}-X_{sss}Z_s)}{(1+\epsilon n\cos\phi\,(X_sZ_{ss}-X_{ss}Z_s))^2}\left(\frac{\partial w}{\partial s}\right.\right.\\
&\qquad\left.+u\sin\phi\,(X_sZ_{ss}-X_{ss}Z_s)\right)\\
&+\frac{\epsilon^2 n}{(1+\epsilon n\cos\phi\,(X_sZ_{ss}-X_{ss}Z_s))}\left(-w\sin^2\phi\,(X_sZ_{ss}-X_{ss}Z_s)^2+\frac{\partial^2 w}{\partial s^2}\right.\\
&\qquad+2\frac{\partial u}{\partial s}\sin\phi\,(X_sZ_{ss}-X_{ss}Z_s)+u\sin\phi\,(X_sZ_{sss}-X_{sss}Z_s)\\
&\left.+v\sin\phi\cos\phi\,(X_sZ_{ss}-X_{ss}Z_s)^2\right)+(1+2\epsilon n\cos\phi\,(X_sZ_{ss}-X_{ss}Z_s))\frac{\partial w}{\partial n}\\
&+n\,(1+\epsilon n\cos\phi\,(X_sZ_{ss}-X_{ss}Z_s))\frac{\partial^2 w}{\partial n^2}-\epsilon\left(\frac{\partial w}{\partial\phi}+v\right)\sin\phi\,(X_sZ_{ss}-X_{ss}Z_s)\\
&\qquad\left.+(1+\epsilon n\cos\phi\,(X_sZ_{ss}-X_{ss}Z_s))\frac{1}{n}\left(\frac{\partial^2 w}{\partial\phi^2}-w+2\frac{\partial v}{\partial\phi}\right)\right)\\
&+\frac{1}{\epsilon\mathcal{R}e_\alpha}\left\{\frac{\epsilon}{1+\epsilon n\cos\phi(X_sZ_{ss}-X_{ss}Z_s)}\frac{\partial\eta}{\partial s}\left(\epsilon\frac{\partial w}{\partial s}+\epsilon u\sin\phi(X_sZ_{ss}-X_{ss}Z_s)\right.\right.\\
&\qquad\left.+\frac{1+\epsilon n\cos\phi(X_sZ_{ss}-X_{ss}Z_s)}{n}\frac{\partial u}{\partial\phi}\right)\\
&\qquad+\frac{1+\epsilon n\cos\phi(X_sZ_{ss}-X_{ss}Z_s)}{n}\frac{\partial\eta}{\partial n}\left(\frac{\partial v}{\partial\phi}-w+n\frac{\partial w}{\partial n}\right)\\
&\qquad\left.+\frac{2(1+\epsilon n\cos\phi(X_sZ_{ss}-X_{ss}Z_s))}{n^2}\frac{\partial\eta}{\partial\phi}\left(\frac{\partial w}{\partial\phi}+v\right)\right\}. \qquad (6.21)
\end{aligned}
$$

6.4 The boundary conditions

The kinematic condition is

$$(1+\epsilon n\cos\phi\,(X_sZ_{ss}-X_{ss}Z_s))\left(\epsilon\frac{\partial R}{\partial t}+(Z_sX_t-X_sZ_t)\cos\phi+\frac{w}{n}\frac{\partial R}{\partial\phi}-v\right.$$
$$\left.+\frac{\partial R}{\partial\phi}\frac{\sin\phi}{n}\,(X_tZ_s-X_sZ_t)\right)+\epsilon u\frac{\partial R}{\partial s}$$
$$-\epsilon\frac{\partial R}{\partial s}\,(X_tX_s+Z_tZ_s+\epsilon n\cos\phi\,(X_sZ_{ss}-X_{ss}Z_s))=0\quad\text{on}\quad n=R, \tag{6.22}$$

the tangential stress conditions on $n=R$ are

$$\left(1-\frac{\epsilon^2}{h_s^2}\left(\frac{\partial R}{\partial s}\right)^2\right)\left(\epsilon\frac{\partial v}{\partial s}+h_s\frac{\partial u}{\partial n}-\epsilon u\cos\phi\,(X_sZ_{ss}-X_{ss}Z_s)\right)$$
$$+2\epsilon\frac{\partial R}{\partial s}\left(\frac{\partial v}{\partial n}-\frac{\epsilon}{h_s}\frac{\partial u}{\partial s}-\frac{\epsilon\,(X_sZ_{ss}-X_{ss}Z_s)}{h_s}\,(v\cos\phi-w\sin\phi)\right)=0 \tag{6.23}$$

and

$$\left(\frac{\partial w}{\partial n}-\frac{w}{R}+\frac{1}{R}\frac{\partial v}{\partial\phi}\right)\left(1-\frac{1}{R^2}\left(\frac{\partial R}{\partial\phi}\right)^2\right)+\frac{2}{R}\frac{\partial R}{\partial\phi}\left(\frac{\partial v}{\partial n}-\frac{1}{R}\left(v+\frac{\partial w}{\partial\phi}\right)\right)=0, \tag{6.24}$$

the normal stress condition is

$$p-\frac{2\eta}{\mathcal{R}e_\alpha E^2}\left(\frac{\epsilon^2}{h_s^3}\left(\frac{\partial R}{\partial s}\right)^2\left(\frac{\partial u}{\partial s}+(v\cos\phi-w\sin\phi)\,(X_sZ_{ss}-X_{ss}Z_s)\right)\right.$$
$$+\frac{1}{\epsilon}\frac{\partial v}{\partial n}+\frac{1}{\epsilon R^3}\left(\frac{\partial R}{\partial\phi}\right)^2\left(v+\frac{\partial w}{\partial\phi}\right)-\frac{\epsilon}{h_s}\frac{\partial R}{\partial s}\left(\frac{1}{h_s}\frac{\partial v}{\partial s}+\frac{1}{\epsilon}\frac{\partial u}{\partial n}-\frac{u}{h_s}\cos\phi\,(X_sZ_{ss}-X_{ss}Z_s)\right)$$
$$\left.-\frac{1}{\epsilon R}\frac{\partial R}{\partial\phi}\left(\frac{\partial w}{\partial n}-\frac{w}{R}+\frac{1}{R}\frac{\partial v}{\partial\phi}\right)+\frac{\epsilon}{Rh_s}\frac{\partial R}{\partial s}\frac{\partial R}{\partial\phi}\left(\frac{1}{\epsilon R}\frac{\partial u}{\partial\phi}+\frac{u\sin\phi\,(X_sZ_{ss}-X_{ss}Z_s)}{h_s}+\frac{1}{h_s}\frac{\partial u}{\partial s}\right)\right)$$
$$=\frac{\kappa}{\mathcal{W}e}\quad\text{on}\quad n=R, \tag{6.25}$$

where

$$\kappa=\frac{1}{h_s}\left(\epsilon^2\frac{\partial}{\partial s}\left(-\frac{1}{h_sE}\frac{\partial R}{\partial s}\right)+\frac{1}{n}\frac{\partial}{\partial n}\left(\frac{nh_s}{E}\right)+\frac{\partial}{\partial\phi}\left(-\frac{h_s}{n^2E}\frac{\partial R}{\partial\phi}\right)\right) \tag{6.26}$$

is the curvature of the free surface,

$$h_s = 1 + \epsilon n \cos\phi \left(X_s Z_{ss} - X_{ss} Z_s \right), \tag{6.27}$$

$$E = \left(1 + \frac{\epsilon^2}{h_s^2} \left(\frac{\partial R}{\partial s} \right)^2 + \frac{1}{n^2} \left(\frac{\partial R}{\partial \phi} \right)^2 \right)^{1/2}, \tag{6.28}$$

the arclength condition is

$$X_s^2 + Z_s^2 = 1 \tag{6.29}$$

$$\text{and} \quad v = w = 0, \quad \text{on} \quad n = 0, \tag{6.30}$$

since on the centreline of the jet there is purely tangential flow. The initial conditions at the orifice are $X = Z = Z_s = 0, X_s = 1, R = 1$ and $u = 1$ at $s = 0$.

The dimensionless parameters in these equations are the Weber number, $\mathcal{W}e = \rho U^2 a/\sigma$, the Rossby number, $\mathcal{R}b = U/\left(s_0 \Omega\right)$, the aspect ratio, $\epsilon = a/s_0$ (which is small as the asymptotics are based on this; this also corresponds to a slender jet) and the generalised Reynolds number based on the radius of the drum $\mathcal{R}e_\alpha = (\rho/k) s_0^\alpha U^{2-a}$. The Reynolds number is based on the radius of the can, s_0, rather than the characteristic radius of the jet, a, to remain consistent with earlier work (Părău et al., 2006, 2007; Uddin et al., 2006). A modified Reynolds number which scales with a is introduced in the next Section.

Equations (6.18)-(6.30) are the full set of equations that represent the behaviour of a curved jet. In Section 6.5 a steady asymptotic solution, based on a small ϵ, is presented.

6.5 Asymptotic form of the steady-state solutions

In Wallwork et al. (2002), an inviscid steady jet trajectory and steady expressions for the velocity, pressure and jet radius, based on a regular slender jet asymptotic expansion, using $0 < \epsilon << 1$, were obtained. This calculation was extended in Decent et al. (2009) to include Newtonian viscosity and is adapted here to include non-Newtonian power-law rheology.

The steady jet asymptotic expansions for u, v, p, R, X, Z from Wallwork et al. (2002) are applied, along with a steady jet expansion for η, the apparent viscosity; w is taken to be zero, so that there is no velocity component in the azimuthal direction. The expansions are

$$\begin{aligned}
\boldsymbol{u} &= u_0(s) + \epsilon \boldsymbol{u_1}(s,n,\phi) + O(\epsilon^2),\\
p &= p_0(s,n,\phi) + \epsilon p_1(s,n,\phi) + O(\epsilon^2),\\
R &= R_0(s) + \epsilon R_1(s,\phi) + O(\epsilon^2),\\
\boldsymbol{X} &= \boldsymbol{X_0}(s) + \epsilon \boldsymbol{X_1}(s,\phi) + O(\epsilon^2),\\
\eta &= \eta_0(s) + \epsilon \eta_1(s,n,\phi) + O(\epsilon^2),
\end{aligned}$$

where $\boldsymbol{u_i} = u_i \boldsymbol{e_s} + v_i \boldsymbol{e_n}$, $v_0 = 0$ and $\boldsymbol{X_i} = X_i \mathbf{i} + Z_i \mathbf{k}$ for $i = 0, 1, \ldots$. For simplicity of notation the leading-order components X_0 and Z_0 are rewritten as X and Z.

When this asymptotic expansion is considered, the expression for η, in Equation (6.17), can be simplified and expressed as

$$\begin{aligned}
\eta = \quad & k|\sqrt{3}u_{0s}|^{\alpha-1}\left(1 + (\epsilon n)\tfrac{\alpha-1}{u_{0s}}\left(\left(u_0\left(X_s Z_{ss} - Z_s X_{ss}\right)\right.\right.\right. \\
& \left.\left.\left. -\tfrac{u_{0s}}{2}\left(X_s Z_{ss} - Z_s X_{ss}\right)\right)\cos\phi\right) + O(\epsilon)^2\right).
\end{aligned} \tag{6.31}$$

The leading order equations are obtained for the steady flow as

$$n\frac{\mathrm{d}u_0}{\mathrm{d}s} + v_1 + n\frac{\partial v_1}{\partial n} = 0, \tag{6.32}$$

$$\begin{aligned}
u_0\frac{\mathrm{d}u_0}{\mathrm{d}s} &= -\frac{\partial p_0}{\partial s} + \frac{1}{\mathcal{R}b^2}\left((X+1)X_s + ZZ_s\right)\\
&+ \frac{\eta_0}{\widetilde{\mathcal{R}e_\alpha}}\left(\frac{1}{n}\frac{\partial u_1}{\partial n} + \frac{\partial^2 u_1}{\partial n^2} + \frac{1}{n^2}\frac{\partial^2 u_1}{\partial \phi^2}\right),
\end{aligned} \tag{6.33}$$

$$\frac{\partial p_0}{\partial n} = 0, \tag{6.34}$$

$$\begin{aligned}
-\cos\phi(X_s Z_{ss} - Z_s X_{ss})u_0^2 &= -\frac{\partial p_1}{\partial n} - \frac{2u_0\cos\phi}{\mathcal{R}b} + \frac{\cos\phi}{\mathcal{R}b^2}\left((X+1)Z_s - ZX_s\right)\\
&+ \frac{\eta_0}{\widetilde{\mathcal{R}e_\alpha}}\left(\frac{1}{n}\frac{\partial v_1}{\partial n} + \frac{\partial^2 v_1}{\partial n^2} + \frac{1}{n^2}\left(-v_1 + \frac{\partial^2 v_1}{\partial \phi^2}\right)\right),
\end{aligned} \tag{6.35}$$

$$\frac{\partial p_0}{\partial \phi} = 0, \tag{6.36}$$

$$\begin{aligned}
\sin\phi(X_sZ_{ss}-Z_sX_{ss})u_0^2 &= -\frac{1}{n}\frac{\partial p_1}{\partial\phi}+\frac{2u_0\sin\phi}{\mathcal{R}b}+\frac{\sin\phi}{\mathcal{R}b^2}\left(ZX_s-(X+1)Z_s\right)\\
&+ \frac{\eta_0}{\widetilde{\mathcal{R}e_\alpha}}\left(\frac{2}{n^2}\frac{\partial v_1}{\partial\phi}\right), \qquad (6.37)\\
u_0\frac{\mathrm{d}R_0}{\mathrm{d}s} &= v_1 \text{ on } n=R_0, \qquad (6.38)\\
\frac{\partial u_1}{\partial n} &= u_0\cos\phi(X_sZ_{ss}-Z_sX_{ss}) \text{ on } n=R_0, \qquad (6.39)\\
p_0 &= \frac{1}{nWe} \text{ on } n=R_0, \qquad (6.40)
\end{aligned}$$

$$p_1-\frac{2\eta_0}{\widetilde{\mathcal{R}e_\alpha}}\frac{\partial v_1}{\partial n}=\frac{1}{\mathcal{W}e}\left(-\frac{1}{R_0^2}\left(R_1+\frac{\partial^2R_1}{\partial\phi^2}\right)+\cos\phi(X_sZ_{ss}-Z_sX_{ss})\right) \text{ on } n=R_0, \quad (6.41)$$

$$v_1=0 \text{ on } n=0 \qquad (6.42)$$

and

$$X_s^2+Z_s^2=1. \qquad (6.43)$$

A new scaling for the Reynolds number based on the initial jet radius, namely $\widetilde{\mathcal{R}e}_\alpha = \epsilon\mathcal{R}e_\alpha = O(1)$ is used here to give a reduced Reynolds number. This scaling is necessary so that in Section 6.6 it is possible to obtain a distinguished limit in the resulting unstable equations.

On first inspection the above equations appear different to the leading order equations for the inviscid case stated in Wallwork et al. (2002). However, at leading-order these equations actually produce the same leading order trajectory as in the inviscid case. Guided by Wallwork et al. (2002) and Decent et al. (2009), (6.32) - (6.43) are solved as follows. Equations (6.34) and (6.36) imply that $p_0 = p_0(s)$. From the continuity equation, (6.32)

$$v_1=-\frac{n}{2}\frac{du_0}{ds}+\frac{k}{n}. \qquad (6.44)$$

Using (6.30), $k = 0$. Hence, $v_1 = -n/2\ du_0/ds$. Substituting this expression for v_1 into equations (6.35) and (6.37), it can be seen that the non-Newtonian terms on the right hand sides of these equations become identically equal to zero. Therefore apparent viscosity now only

appears in (6.33) and in (6.41). Equation (6.33) can be rewritten as

$$f(s) = \nabla^2_{n,\phi} u_1, \tag{6.45}$$

$$\text{where} \qquad \nabla^2_{n,\phi} = \frac{1}{n}\frac{\partial}{\partial n} + \frac{\partial^2}{\partial n^2} + \frac{1}{n^2}\frac{\partial^2}{\partial \phi^2}$$

is the in-plane Laplacian operator, and

$$f(s) = \frac{\widetilde{\mathcal{R}e_\alpha}}{\eta_0}\left(u_0\frac{\mathrm{d}u_0}{\mathrm{d}s} + \frac{\mathrm{d}p_0}{\mathrm{d}s} - \frac{1}{\mathcal{R}b^2}\left(\left(X+1\right)X_s + ZZ_s\right)\right).$$

Therefore (6.45) has to be solved subject to (6.39). This is a Neumann problem on a circular domain, where s is a parameter. The method of Nayfeh (1970) can be followed closely and a solvability argument can be used to analyse the problem. To determine a solvability condition, (6.45) is multiplied by $u(s,n,\phi)$ and the result is integrated over the domain of interest S ($0 \le n \le R_0$, $0 \le \phi \le 2\pi$), giving

$$\iint\limits_S u\nabla^2_{n,\phi}u_1 \; dS = \iint\limits_S uf(s) \; dS. \tag{6.46}$$

Now from Green's identity

$$\iint\limits_S \left(u\nabla^2_{n,\phi}u_1 - u_1\nabla^2_{n,\phi}u\right) \; dS = \int\limits_B \left(u\frac{\partial u_1}{\partial n} - u_1\frac{\partial u}{\partial n}\right) \; dB, \tag{6.47}$$

where B is the boundary of S (so that $n = R_0$ on B). Let u satisfy the homogeneous Neumann problem, so that

$$\nabla^2_{n,\phi}u = 0 \quad \text{with} \quad \frac{\partial u}{\partial n} = 0 \quad \text{on} \quad n = R_0, \tag{6.48}$$

while u_1 satisfies (6.45) subject to

$$\frac{\partial u_1}{\partial n} = g(s)\cos\phi \quad \text{on} \quad n = R_0, \tag{6.49}$$

where $g(s) = u_0\left(X_s Z_{ss} - X_{ss} Z_s\right)$. Therefore

$$\iint\limits_S u\nabla^2_{n,\phi} u_1 \, dS = \int\limits_B u\frac{\partial u_1}{\partial n} \, dB. \tag{6.50}$$

From (6.46), (6.49) and (6.50) we obtain

$$\int\limits_0^{2\pi}\int\limits_0^{R_0} unf(s)\, dn\, d\phi = \int\limits_0^{2\pi}\left[u\frac{\partial u_1}{\partial n}\right]_{n=R_0} R_0\, d\phi = \int\limits_0^{2\pi}[u]_{n=R_0} R_0 g(s)\cos\phi\, d\phi. \tag{6.51}$$

The general solution to

$$\nabla^2_{n,\phi} u = 0$$

is given by

$$u = \beta(s)\phi + \sigma(s)ln(n) + \gamma(s) + \sum_{\lambda=1}^{\infty} n^\lambda \left(C_\lambda \cos(\lambda\phi) + D_\lambda \sin(\lambda\phi)\right). \tag{6.52}$$

The term $\beta(s)\phi$ is not periodic with 2π and $\sigma(s)ln(n)$ is singular at $n = 0$. Therefore $\beta(s) = \sigma(s) = 0$ for all s. Consequently,

$$\left[\frac{\partial u}{\partial n}\right]_{n=R_0} = \sum_{\lambda=1}^{\infty} \lambda R_0^{\lambda-1}\left(C_\lambda \cos(\lambda\phi) + D_\lambda \sin(\lambda\phi)\right). \tag{6.53}$$

For u to satisfy the homogeneous problem (6.48), $C_\lambda = D_\lambda = 0$ for all λ. Therefore the general solution to (6.45) which is bounded in $0 \le n \le R_0$ and also periodic in ϕ with period

2π is $u = \gamma(s)$ for some $\gamma(s)$. The left hand side of (6.51) becomes

$$\gamma(s)f(s)\int_0^{2\pi}\int_0^{R_0} n\,dn\,d\phi = \gamma(s)f(s)\pi R_0^2, \tag{6.54}$$

and the right hand side of (6.51) gives

$$\gamma(s)R_0 g(s)\int_0^{2\pi}\cos\phi\;d\phi = 0. \tag{6.55}$$

Therefore, $\gamma(s)f(s)R_0^2 = 0$. Here, R_0 cannot be zero and since $u = \gamma(s)$ is the general solution to the homogeneous problem, we must have $f(s) = 0$ for all s (see Nayfeh, 1970). Therefore (6.33) and (6.39) give rise to two equations; namely $f(s) = 0$ and $\nabla^2_{n,\phi}u_1 = 0$. Neither of these expressions contain apparent viscosity.

Finally if we perform the calculation $\sin\phi$(6.35) + $\cos\phi$(6.37) we obtain

$$\sin\phi\frac{\partial p_1}{\partial n} + \cos\phi\frac{1}{n}\frac{\partial p_1}{\partial \phi} = 0,$$

which has the solution $p_1 = n\cos\phi g_1(s) + h_1(s) + k_1(s)$, where $k_1(s)$ is the viscous part of p_1. Substituting this solution into equation (6.41) we obtain

$$R_0\cos\phi g_1(s) + h_1(s) + k_1(s) + \frac{\eta_0}{\widetilde{\mathcal{R}e_\alpha}}\frac{\mathrm{d}u_0}{\mathrm{d}s} = \frac{1}{\mathcal{W}e}\left(-\frac{1}{R_0}\left(R_1 + \frac{\partial^2 R_1}{\partial\phi^2}\right) + \cos\phi\left(X_s Z_{ss} - X_{ss}Z_s\right)\right),$$

which has the solution $R_1 = g_2(s)\cos\phi + g_3(s)\sin\phi - h_1(s)WeR_0^2$ and $k_1(s) = -\frac{\eta_0}{\widetilde{\mathcal{R}e_\alpha}}\frac{\mathrm{d}u_0}{\mathrm{d}s}$. Since R_1 must be periodic in ϕ with period 2π, it can not have a particular solution of the form $\phi\sin\phi$. Therefore

$$g_1 = \frac{1}{\mathcal{W}e}R_0\left(X_s Z_{ss} - X_{ss}Z_s\right)$$

and

$$p_1 = \frac{n}{\mathcal{W}eR_0}\cos\phi\,(X_sZ_{ss} - X_{ss}Z_s) + h_1(s) - \frac{\eta_0}{\widetilde{\mathcal{R}e_\alpha}}\frac{\mathrm{d}u_0}{\mathrm{d}s}, \tag{6.56}$$

where $h_1(s)$ could be found at next order in the asymptotic expansion. It should be noted that p_1 only appears as derivatives with respect to n and ϕ in equations (6.35) and (6.37). By substituting (6.56) into (6.35) and (6.37) no viscous contribution from p_1 is obtained since the viscous term in (6.56) in η_0 is dependent on s only. Therefore, the non-Newtonian terms vanish and the same leading order problem for the trajectory is found here as in the inviscid case in Wallwork et al. (2002), along with the following leading order equation for η_0:

$$\eta_0 = \left|\sqrt{3}\,\frac{\mathrm{d}u_0}{\mathrm{d}s}\right|^{\alpha-1}, \tag{6.57}$$

which gives the non-Newtonian component of the system. Hence the apparent viscosity does not affect the steady solution at leading order, except in (6.57) and in a correction to p_1 in (6.56) which does not affect the trajectory, velocity, pressure or jet radius at leading order. This confirms the approach adopted in Uddin et al. (2006, 2008a) and Părău et al. (2006) also showed numerically that viscosity is not important to the trajectory except in very high viscosity liquids. The slender jet approximation in this case results in no shear across the jet at leading order.

The set of equations (6.32) - (6.43) are reduced to a set of ODEs that can be solved numerically.

$$p_0 = \frac{1}{R_0\mathcal{W}e}, \tag{6.58}$$

$$u_0 = \left(1 + \frac{1}{\mathcal{R}b^2}\left(X^2 + 2X + Z^2\right) + \frac{2}{\mathcal{W}e}\left(1 - \frac{1}{R_0^2}\right)\right)^{1/2}, \tag{6.59}$$

$$p_1 = \frac{n}{\mathcal{W}eR_0}\cos\phi\,(X_sZ_{ss} - X_{ss}Z_s) + h_1(s) - \frac{\eta_0}{\widetilde{\mathcal{R}e_\alpha}}\frac{du_0}{ds}, \tag{6.60}$$

$$v_1 = -\frac{n}{2}\frac{du_0}{ds}, \tag{6.61}$$

$$Z_{ss} = \frac{WeR_0X_s}{WeR_0u_0^2 - 1}\left(\frac{2u_0}{\mathcal{R}b} + \frac{ZX_s - (X+1)Z_s}{\mathcal{R}b^2}\right), \tag{6.62}$$

$$\frac{dR_0}{ds} = -\frac{WeR_0((X+1)X_s + ZZ_s)}{\mathcal{R}b^2(2WeR_0u_0^2 + 1)}, \tag{6.63}$$

$$\frac{du_0}{ds} = -\frac{2u_0}{R_0}\frac{dR_0}{ds}, \tag{6.64}$$

$$X_s^2 + Z_s^2 = 1. \tag{6.65}$$

Equations (6.62), (6.63) and (6.65) give rise to a set of non-linear ordinary differential equations for X, Z and R_0. The system of equations is solved numerically in MATLAB using a Runge Kutta method subject to the initial conditions $X_s = 1, X = Z = Z_s = 0, u_0 = R_0 = 1$ at $s = 0$. To leading order, apparent viscosity does not affect the centreline position, although Equation (6.57) is solved for η_0.

Figures 6.2(a) and 6.2(b) show the trajectory of the centreline of a steady jet for various parameter values. The graphs in Figure 6.2(a) show the trajectory for various values of the Rossby number for fixed Weber number. Smaller Rossby number correspond to more tightly coiled loops. Figure 6.2(b) shows the centreline for varying values of the Weber number, for fixed Rossby number. The loops with smaller values of the Weber number are more tightly coiled.

Figures 6.3(a) and 6.3(b) present how the radius of the jet, R_0, varies with arclength, s, for various Weber and Rossby numbers respectively. The graphs show that the jet thins as it leaves the orifice as expected. Figure 6.3(b) shows that the jets thins more dramatically for decreasing Rossby number.

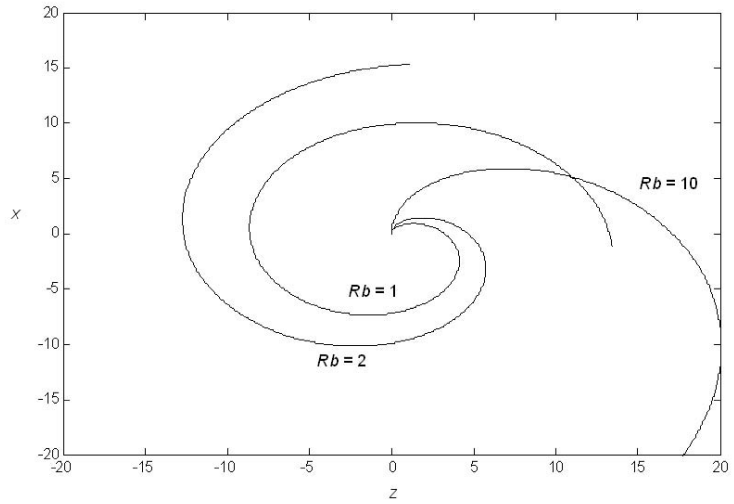

(a) The effects of the variations in rotation on the centreline of the jet in the (X-Z) plane for various values of the Rossby number $\mathcal{R}b = 1, 210$ with $\mathcal{W}e = 18000$. The origin has been translated to the centre of the container.

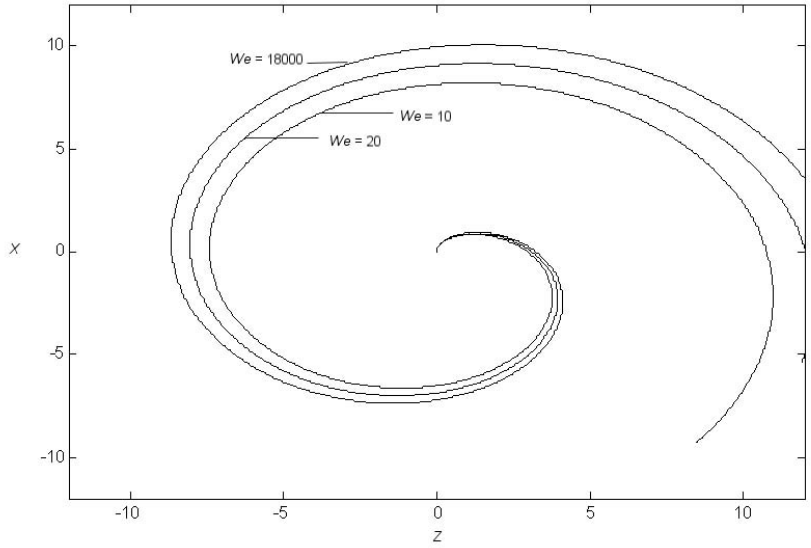

(b) The centreline of a jet in the (X-Z) plane for various Weber numbers $\mathcal{W}e = 10, 20, 18000$ with $\mathcal{R}b = 1$. The loops with a smaller value of Weber number are more tightly coiled. The origin has been translated to the centre of the container.

Figure 6.2: The centreline of the steady jet for various parameter values.

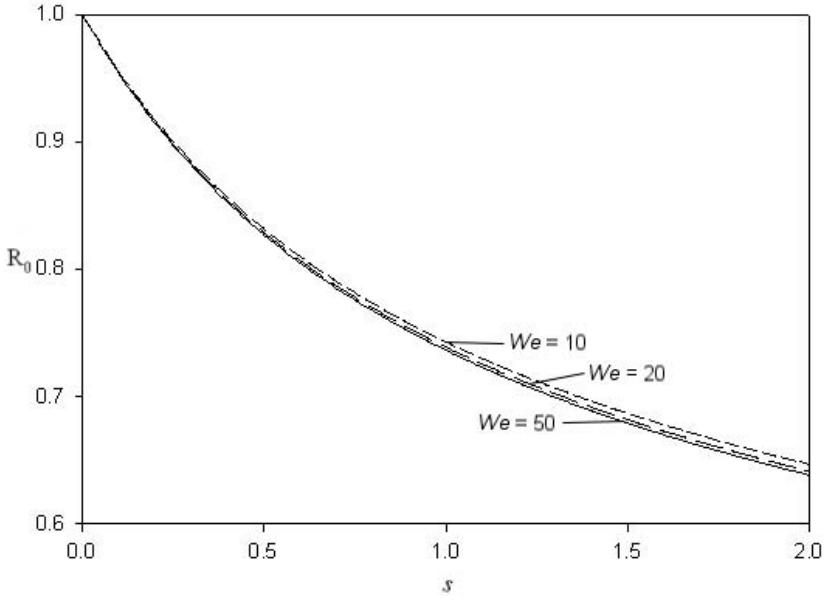

(a) The behaviour of arclength, s, against the radius of the jet for various Weber numbers ($\mathcal{R}b = 1$).

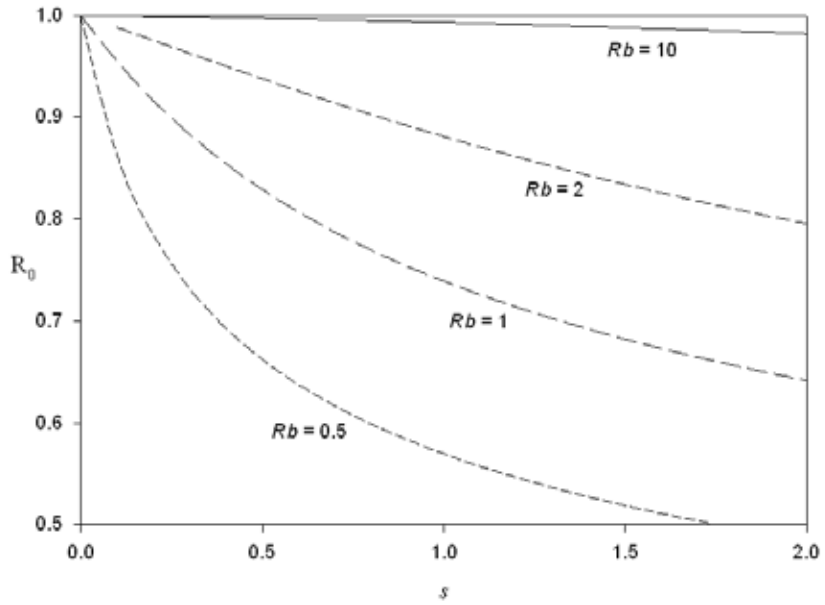

(b) The behaviour of arclength, s, against the radius of the jet for various Rossby numbers ($\mathcal{W}e = 20$).

Figure 6.3: The behaviour of the arclength, s, against the radius of the jet for various parameter values.

6.6 Linear instability of the steady state solutions

A linear stability analysis of the steady state solutions is now performed using

$$\begin{aligned}
\boldsymbol{u} &= \bar{\boldsymbol{u}} + \delta\tilde{\boldsymbol{u}}(s,\bar{s},t,\bar{t},n,\phi),\\
p &= \bar{p} + \delta\tilde{p}(s,\bar{s},t,\bar{t},n,\phi),\\
R &= \bar{R} + \delta\tilde{R}(s,\bar{s},t,\bar{t},\phi),\\
\boldsymbol{X} &= \bar{\boldsymbol{X}} + \delta\epsilon\tilde{\boldsymbol{X}}(s,\bar{s},t,\bar{t}),\\
\eta &= \bar{\eta} + \delta\tilde{\eta}(s,\bar{s},t,\bar{t},n,\phi).
\end{aligned} \tag{6.66}$$

where $(\bar{\boldsymbol{u}},\tilde{\boldsymbol{u}}) = (\bar{u},\tilde{u})\boldsymbol{e_s} + (\bar{v},\tilde{v})\boldsymbol{e_n} + (\bar{w},\tilde{w})\boldsymbol{e_\phi}$, $(\bar{\boldsymbol{X}},\tilde{\boldsymbol{X}}) = (\bar{X},\tilde{X})\mathbf{i} + (\bar{Z},\tilde{Z})\mathbf{k}$ and δ is a small dimensionless parameter, such that $0 < \delta \ll \epsilon \ll 1$, which generates small unsteady disturbances as in Wallwork et al. (2002) (we note that we first tried $\boldsymbol{X} = \bar{\boldsymbol{X}} + \delta\widetilde{\boldsymbol{X}_\mathbf{0}}(s,\bar{s},t,\bar{t}) + \delta\epsilon\tilde{\boldsymbol{X}}(s,\bar{s},t,\bar{t})$, but $\widetilde{\boldsymbol{X}_\mathbf{0}}$ was found to be identically equal to zero). These linear perturbations disturb the basic steady solution (denoted by a quantity with an overbar in (6.66)), which are functions of s,n,ϕ, by unsteady quantities which are functions of $s,\bar{s},t,\bar{t},n$ and ϕ, where $\bar{s} = s/\epsilon$ is a short lengthscale and $\bar{t} = t/\epsilon$ is a small timescale associated with short wave-like disturbances. The unsteady perturbations are denoted by variables with a tilde, so that $\tilde{u}$ is the unsteady viscous linear perturbation to the streamwise velocity component u. Therefore the small unsteady components allow motion on a short length scale which scales with the orifice a.

These equations are substituted into the non-Newtonian equations of motion and linearised in the unsteady quantities (taking terms of $O(\delta)$). The leading order equations in ϵ are:

$$n\frac{\partial\tilde{u}}{\partial\bar{s}} + \tilde{v} + n\frac{\partial\tilde{v}}{\partial n} + \frac{\partial\tilde{w}}{\partial\phi} = 0, \tag{6.67}$$

$$\frac{\partial\tilde{u}}{\partial\bar{t}} + u_0(s)\frac{\partial\tilde{u}}{\partial\bar{s}} = -\frac{\partial\tilde{p}}{\partial\bar{s}} + \frac{\eta_0(s)}{\widetilde{\mathcal{R}e_\alpha}}\left(\frac{\partial^2\tilde{u}}{\partial\bar{s}^2} + \frac{1}{n}\frac{\partial\tilde{u}}{\partial n} + \frac{\partial^2\tilde{u}}{\partial n^2} + \frac{1}{n^2}\frac{\partial^2\tilde{u}}{\partial\phi^2}\right), \tag{6.68}$$

$$
\begin{aligned}
&\frac{\partial \tilde{v}}{\partial \bar{t}} + u_0(s)\frac{\partial \tilde{v}}{\partial \bar{s}} + u_0(s)\cos\phi\left(Z_s\frac{\partial^2 \tilde{X}}{\partial \bar{s}\partial \bar{t}} - X_s\frac{\partial^2 \tilde{Z}}{\partial \bar{s}\partial \bar{t}}\right)\\
-\quad &\cos\phi\left(X_s\frac{\partial^2 \tilde{Z}}{\partial \bar{s}^2} - Z_s\frac{\partial^2 \tilde{X}}{\partial \bar{s}^2}\right)u_0^2(s) = -\frac{\partial \tilde{p}}{\partial n}\\
+\quad &\frac{\eta_0(s)}{\widetilde{\mathcal{R}e_\alpha}}\left(-u_0(s)\cos\phi\left(X_s\frac{\partial^3 \tilde{Z}}{\partial \bar{s}^3} - Z_s\frac{\partial^3 \tilde{X}}{\partial \bar{s}^3}\right) + \frac{\partial^2 \tilde{v}}{\partial \bar{s}^2}\right.\\
+\quad &\left.\frac{1}{n}\frac{\partial \tilde{v}}{\partial n} + \frac{\partial^2 \tilde{v}}{\partial n^2} + \frac{1}{n^2}\left(-\tilde{v} + \frac{\partial^2 \tilde{v}}{\partial \phi^2} - 2\frac{\partial \tilde{w}}{\partial \phi}\right)\right),
\end{aligned}
\tag{6.69}
$$

$$
\begin{aligned}
&\frac{\partial \tilde{w}}{\partial \bar{t}} + u_0(s)\frac{\partial \tilde{w}}{\partial \bar{s}} + u_0(s)\sin\phi\left(X_s\frac{\partial^2 \tilde{Z}}{\partial \bar{s}\partial \bar{t}} - Z_s\frac{\partial^2 \tilde{X}}{\partial \bar{s}\partial \bar{t}}\right)\\
+\quad &\sin\phi\left(X_s\frac{\partial^2 \tilde{Z}}{\partial \bar{s}^2} - Z_s\frac{\partial^2 \tilde{X}}{\partial \bar{s}^2}\right)u_0^2(s) = -\frac{1}{n}\frac{\partial \tilde{p}}{\partial \phi}\\
+\quad &\frac{\eta_0(s)}{\widetilde{\mathcal{R}e_\alpha}}\left(u_0(s)\sin\phi\left(X_s\frac{\partial^3 \tilde{Z}}{\partial \bar{s}^3} - Z_s\frac{\partial^3 \tilde{X}}{\partial \bar{s}^3}\right) + \frac{\partial^2 \tilde{w}}{\partial \bar{s}^2}\right.\\
+\quad &\left.\frac{1}{n}\frac{\partial \tilde{w}}{\partial n} + \frac{\partial^2 \tilde{w}}{\partial n^2} + \frac{1}{n^2}\left(-\tilde{w} + \frac{\partial^2 \tilde{w}}{\partial \phi^2} - 2\frac{\partial \tilde{v}}{\partial \phi}\right)\right),
\end{aligned}
\tag{6.70}
$$

$$
\frac{\partial \tilde{R}}{\partial \bar{t}} + \left(Z_s\frac{\partial \tilde{X}}{\partial \bar{t}} - X_s\frac{\partial \tilde{Z}}{\partial \bar{t}}\right)\cos\phi - \tilde{v} + u_0(s)\frac{\partial \tilde{R}}{\partial \bar{s}} = 0 \text{ on } n = R_0, \tag{6.71}
$$

$$
\frac{\partial \tilde{v}}{\partial \bar{s}} + \frac{\partial \tilde{u}}{\partial n} - u_0(s)\cos\phi\left(X_s\frac{\partial^2 \tilde{Z}}{\partial \bar{s}^2} - Z_s\frac{\partial^2 \tilde{X}}{\partial \bar{s}^2}\right) = 0 \text{ on } n = R_0, \tag{6.72}
$$

$$
\tilde{p} - \frac{2\eta_0(s)}{\widetilde{\mathcal{R}e_\alpha}}\frac{\partial \tilde{v}}{\partial n} = \frac{1}{\mathcal{W}e}\left(-\frac{1}{R_0^2}\left(\tilde{R} + \frac{\partial^2 \tilde{R}}{\partial \phi^2}\right) + \cos\phi\left(X_s\frac{\partial^2 \tilde{Z}}{\partial \bar{s}^2} - Z_s\frac{\partial^2 \tilde{X}}{\partial \bar{s}^2}\right) - \frac{\partial^2 \tilde{R}}{\partial \bar{s}^2}\right) = 0 \text{ on } n = R_0, \tag{6.73}
$$

$$
\tilde{v} = \tilde{w} = 0 \quad \text{on} \quad n = 0, \tag{6.74}
$$

$$
X_s\frac{\partial \tilde{X}}{\partial \bar{s}} + Z_s\frac{\partial \tilde{Z}}{\partial \bar{s}} = 0 \tag{6.75}
$$

where

$$u_0 = \left(1 + \frac{(X^2 + 2X + Z^2)}{\mathcal{R}b^2} + \frac{2}{\mathcal{W}e}\left(1 - \frac{1}{R_0}\right)\right)^{\frac{1}{2}} \tag{6.76}$$

is the steady leading-order steady jet speed that results from Section 6.5. Note that the chosen scaling for the Reynolds number, $\widetilde{\mathcal{R}e_\alpha}$ is such that viscosity appears in the solution to the linear perturbations.

Having taken the leading order equations in ϵ, we then look for solutions in modes of the form

$$\begin{aligned}
\tilde{\boldsymbol{u}} &= \hat{\boldsymbol{u}}(s,n,\phi,t)\text{exp}(ik(s)\bar{s} + \lambda(s)\bar{t}) + c.c.,\\
\tilde{p} &= \hat{p}(s,n,\phi,t)\text{exp}(ik(s)\bar{s} + \lambda(s)\bar{t}) + c.c.,\\
\tilde{R} &= \hat{R}(s,\phi,t)\text{exp}(ik(s)\bar{s} + \lambda(s)\bar{t}) + c.c.,\\
\tilde{\boldsymbol{X}} &= \hat{\boldsymbol{X}}(s,t)\text{exp}(ik(s)\bar{s} + \lambda(s)\bar{t}) + c.c.,
\end{aligned} \tag{6.77}$$

where $\hat{\boldsymbol{u}} = \hat{u}\mathbf{e_s} + \hat{v}\mathbf{e_n} + \hat{w}\mathbf{e}_{\boldsymbol{\phi}}$, $\hat{\boldsymbol{X}} = \hat{X}\mathbf{i} + \hat{Z}\mathbf{k}$, $c.c.$ denotes complex conjugate, $k(s)$ is the wavenumber and $\lambda(s)$ is the wave frequency. Looking for solutions by expanding the remaining unknowns (in the variables with 'hats') in Fourier series in ϕ, it is possible to find a countably infinite set of eigenvalue relationships, each associated with $\cos(n\phi)$ or $\sin(n\phi)$ for each integer n. After some lengthy algebra it can be determined that these are stable modes for $n \geq 1$, plus

one unstable mode, corresponding to $n = 0$, which has the following eigenvalue relation

$$
\begin{aligned}
&-2ik^5\eta_0\mathcal{W}eI_1(\tilde{k}R_0)I_0(kR_0)R_0^2u_0 + k^5\widetilde{\mathcal{R}e_\alpha}I_1(kR_0)I_1(\tilde{k}R_0)R_0^2 \\
&+k^4\mathcal{W}e\widetilde{\mathcal{R}e_\alpha}I_0(kR_0)I_1(\tilde{k}R_0)R_0^2u_0^2 - 2ik^4\eta_0\mathcal{W}eI_1(\tilde{k}R_0)I_1(kR_0)R_0u_0 \\
&-2k^4\lambda\eta_0\mathcal{W}eI_1(\tilde{k}R_0)I_0(kR_0)R_0^2 + 4ik^4\tilde{k}\eta_0\mathcal{W}eI_1(kR_0)I_0(\tilde{k}R_0)R_0^2u_0 \\
&+4k^3\tilde{k}\lambda\eta_0\mathcal{W}eI_1(kR_0)I_0(\tilde{k}R_0)R_0^2 - 2ik^3\tilde{k}^2\eta_0\mathcal{W}eI_1(\tilde{k}R_0)I_0(kR_0)R_0^2u_0 \\
&-k^3\widetilde{\mathcal{R}e_\alpha}I_1(kR_0)I_1(\tilde{k}R_0) - 2ik^3\lambda\mathcal{W}e\widetilde{\mathcal{R}e_\alpha}I_0(kR_0)I_1(\tilde{k}R_0)R_0^2 \\
&-2k^3\lambda\eta_0\mathcal{W}eI_1(\tilde{k}R_0)I_1(kR_0)R_0 - k^3\tilde{k}^2\widetilde{\mathcal{R}e_\alpha}I_1(kR_0)I_1(\tilde{k}R_0)R_0^2 \\
&-2k^2\tilde{k}^2\lambda\eta_0\mathcal{W}eI_1(\tilde{k}R_0)I_0(kR_0)R_0^2 + k^2\tilde{k}^2\mathcal{W}e\widetilde{\mathcal{R}e_\alpha}I_0(kR_0)I_1(\tilde{k}R_0)R_0^2u_0^2 \\
&-k^2\lambda^2\mathcal{W}e\widetilde{\mathcal{R}e_\alpha}I_0(kR_0)I_1(\tilde{k}R_0)R_0^2 + 2ik^2\tilde{k}^2\eta_0\mathcal{W}eI_1(\tilde{k}R_0)I_1(kR_0)R_0u_0 \\
&-2ik\tilde{k}^2\lambda\mathcal{W}e\widetilde{\mathcal{R}e_\alpha}I_0(kR_0)I_1(\tilde{k}R_0)R_0^2u_0 + k\tilde{k}^2\widetilde{\mathcal{R}e_\alpha}I_1(kR_0)I_1(\tilde{k}R_0) \\
&+2k\tilde{k}^2\lambda\eta_0\mathcal{W}eI_1(\tilde{k}R_0)I_1(kR_0)R_0 - \tilde{k}^2\lambda^2\mathcal{W}e\widetilde{\mathcal{R}e_\alpha}I_0(kR_0)I_1(\tilde{k}R_0)R_0^2 = 0
\end{aligned}
\tag{6.78}
$$

where

$$
\tilde{k} = \sqrt{k^2 + \frac{\widetilde{\mathcal{R}e_\alpha}(\lambda + iku_0)}{\eta_0}}, \tag{6.79}
$$

and I_n is the modified Bessel function of order n. Note for this mode $\tilde{w} = 0$. Here, R_0, u_0 and η_0 are functions of arclength, s, and depend upon the rotation parameter $\mathcal{R}b$ and satisfy the differential equations (6.57), (6.59), (6.62), (6.63) and (6.65). The Newtonian equivalent is given in Chapter 2. This eigenvalue relationship can be interpreted in two different ways, using a temporal or spatial instability approach. Note that (6.78) reduces to the simpler result of Uddin et al. (2006) in the long wavelength limit $k \to 0$, as shown in Section 6.10. Also, (6.78) reduces to the classical straight jet Newtonian viscous result of Weber (1931) as $\mathcal{R}b \to \infty$ and $\alpha = 1$.

6.7 Spatial instability

Following Keller et al. (1973), the eigenvalue relation is considered in terms of spatial instability. This was shown in Keller et al. (1973) to be physically more realistic than temporal instability. For spatial instability, k is complex, while $\lambda = -i\omega$ is purely imaginary and ω is a real frequency. The eigenvalue relationship (6.78) is then solved for k, describing the wavenumber of the wave, $Re(k)$, and its spatial growth rate $-Im(k)$. The mode is unstable when $Im(k) < 0$. The largest growth rate, $Re(k) = k^*$ will correspond to the most negative value of $Im(k)$ and ω^* is the corresponding frequency.

The eigenvalue relationship (6.78) can be solved computationally. It can be shown graphically how the spatial mode varies for various values of the parameters. Figure 6.4 shows computational solutions to (6.78) at various values of s. In Figure 6.4(a) each line of the graphs has been constructed by varying ω from 0 to 5. As s increases, it can be seen that the most unstable wave has a larger wavenumber, $Re(k)$, yielding shorter wavelength disturbances and a smaller growth rate, $Im(k)$. Figure 6.4(b) presents a graph of the growth rate, $Im(k)$, plotted against the frequency, ω, for various parameters. The wavenumber with the largest growth rate occurs for higher values of ω for greater values of s.

Figure 6.5 shows how the frequency, ω^* (in Figure 6.5(a)), and the growth rate, $|Im(k)|$ (in Figure 6.5(b)), of the most unstable mode given by (6.78), vary along the arclength, s, for different Reynolds numbers. As the Reynolds number increases, the frequency increases along s. For lower Reynolds numbers, the growth rate of the most unstable mode decreases more along s.

Figures 6.6(a) and 6.6(b) show computational solutions to (6.78) at two different values of the arclength, s. The figures describe two different points on the jet and the most unstable mode on each curve occurs at the minimum value. Figures 6.6(a) and 6.6(b) show that decreasing the Reynolds number causes the jet to be less unstable as the waves are more heavily damped. For smaller Reynolds numbers, the most unstable wave occurs at longer wavelengths.

Figure 6.7 shows how varying the Weber number affects the frequency, ω^* (in Figure 6.7(a)),

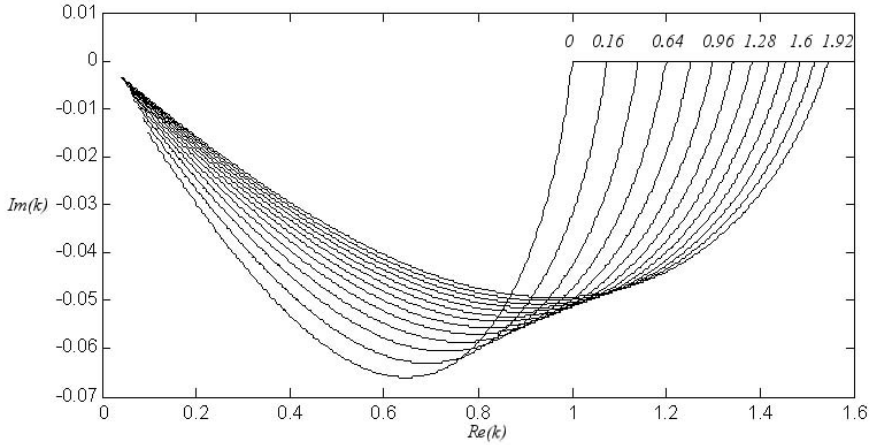

(a)

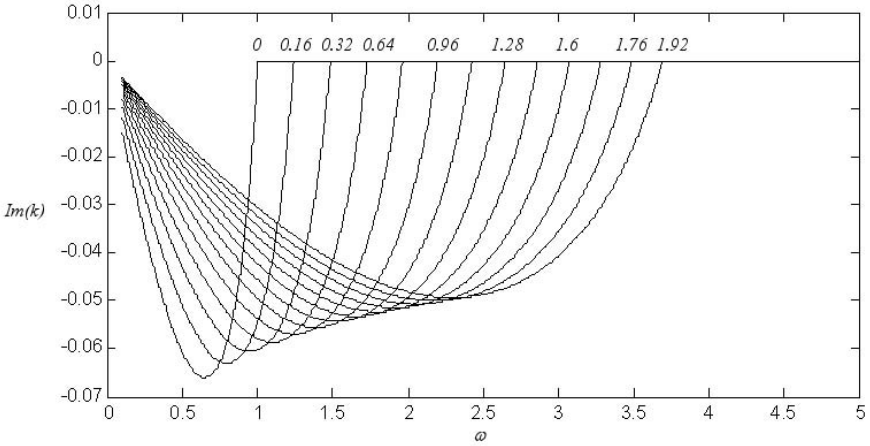

(b)

Figure 6.4: Graph showing (a) $Im(k)$ against $Re(k)$ and (b) $Im(k)$ against ω for various values of s ($\mathcal{W}e = 20, \mathcal{R}b = 1, \alpha = 0.8, \mathcal{R}e_\alpha = 40$).

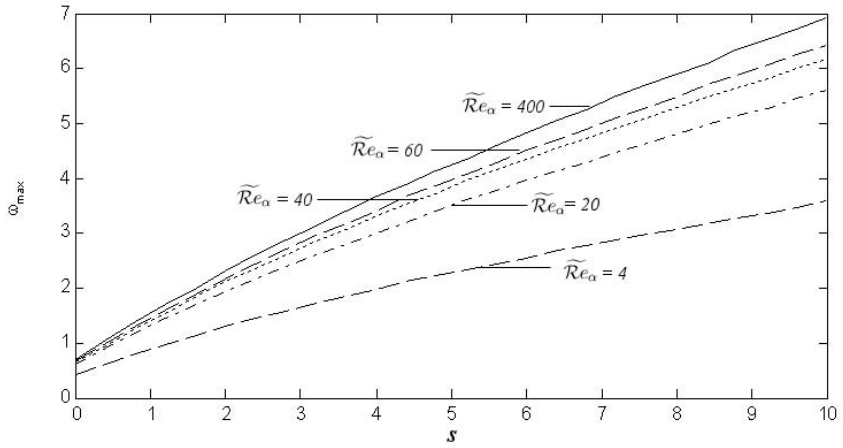

(a)

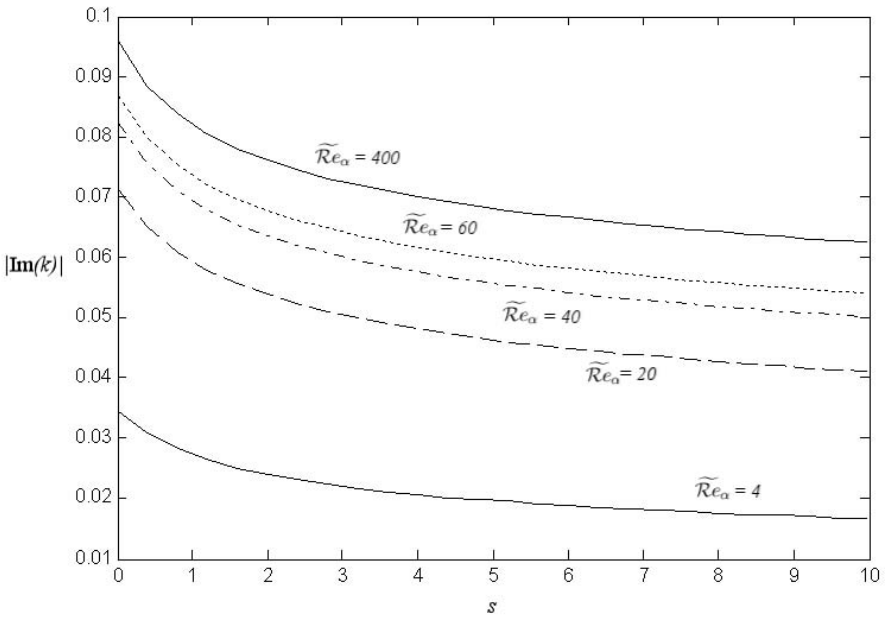

(b)

Figure 6.5: The plot shows (a) the frequency, ω^* and (b) the modulus of growth rate, $|Im(k)|$, of the most unstable mode, as a function of arclength, s, for various Reynolds numbers ($\mathcal{W}e = 13.33, \mathcal{R}b = 1.12, \alpha = 0.92$).

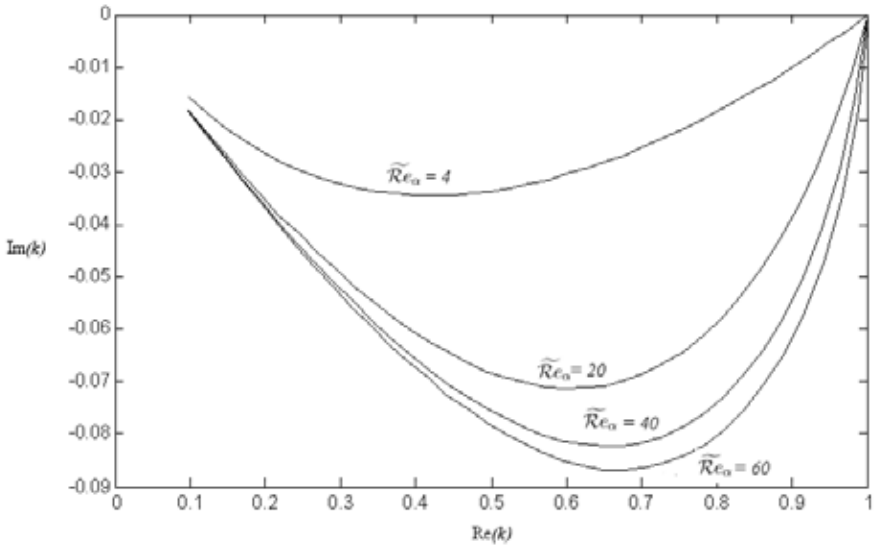

(a)

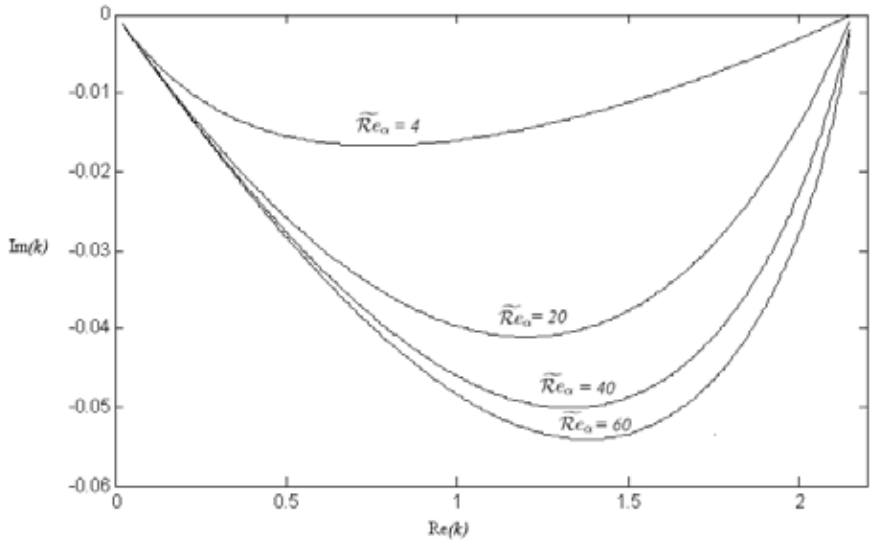

(b)

Figure 6.6: Graph showing $Im(k)$ against $Re(k)$ at (a) $s = 0$ and (b) $s = 10$, for various Reynolds numbers ($\mathcal{W}e = 13.33, \mathcal{R}b = 1.12, \alpha = 0.92$).

and the growth rate, $|Im(k)|$ (in Figure 6.7(b)), of the most unstable mode as a function of the arclength, s. It can be seen in Figure 6.7(a) that the values of the frequency are larger for smaller Weber numbers. Figure 6.7(b) shows that the growth rate of the most unstable mode decreases as s increases, and the smaller values of $|Im(k)|$ correspond to larger Weber numbers.

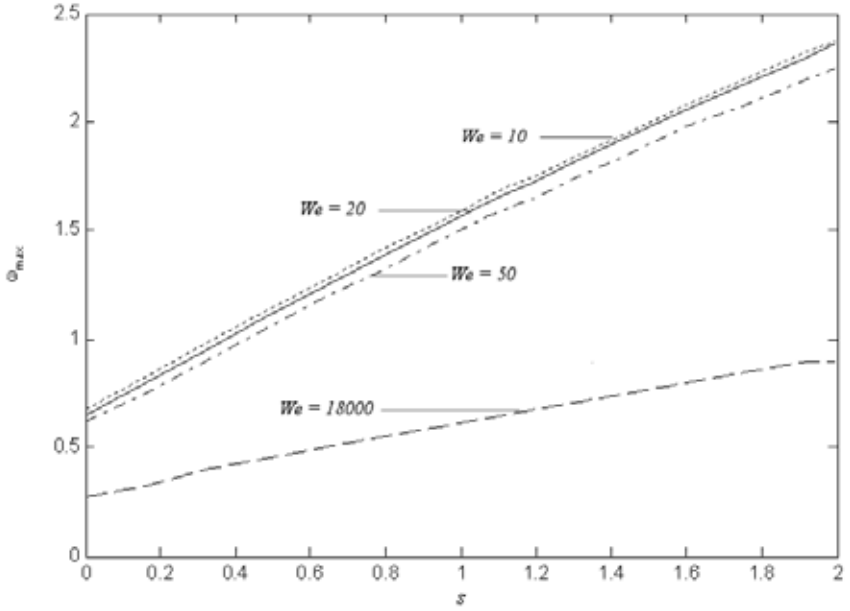

(a)

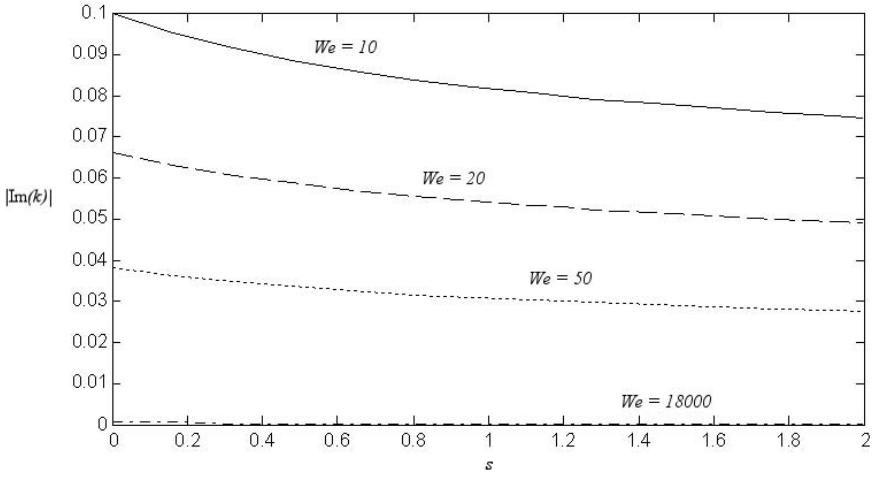

(b)

Figure 6.7: The plot shows (a) the frequency, ω^* and (b) the modulus of growth rate, $|Im(k)|$, of the most unstable mode, as a function of arclength, s, for various Weber numbers ($\widetilde{\mathcal{R}e_\alpha} = 40, \mathcal{R}b = 1, \alpha = 0.8$).

Figure 6.8(a) and Figure 6.8(b) show that $|Im(k)|$ decreases as the arc length, s, increases.

In both cases the wavenumber $Re(k)$ of k^* increases. Therefore the mode of maximum instability has different wavelengths down the jet.

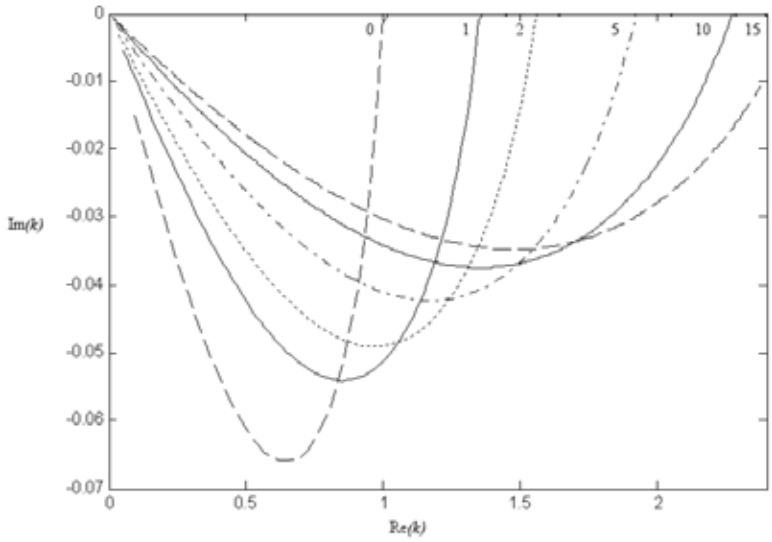

(a) Graph showing $Im(k)$ against $Re(k)$ for various values of s ($\mathcal{W}e = 20, \mathcal{R}b = 1, \alpha = 0.8, \widetilde{\mathcal{R}e_\alpha} = 40$).

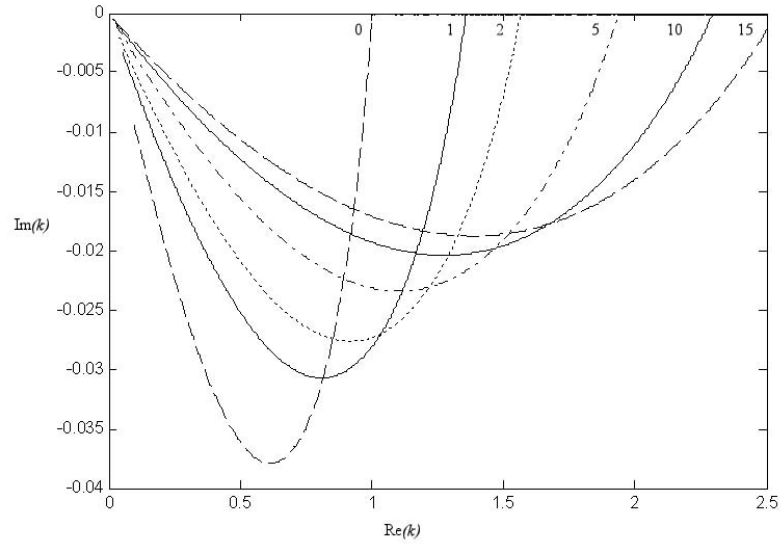

(b) Graph showing $Im(k)$ against $Re(k)$ for various values of s ($\mathcal{W}e = 50, \mathcal{R}b = 1, \alpha = 0.8, \widetilde{\mathcal{R}e_\alpha} = 40$).

Figure 6.8: Graph showing $Im(k)$ against $Re(k)$ for various values of s, (a) when $\mathcal{W}e = 20$ and (b) when $\mathcal{W}e = 50$ ($\mathcal{R}b = 1, \alpha = 0.8, \widetilde{\mathcal{R}e_\alpha} = 40$).

Figures 6.9(a) and 6.9(b) show how the frequency, ω^*, and the growth rate, $|Im(k)|$, of the most unstable mode vary with Rossby number respectively. These graphs show the same trends

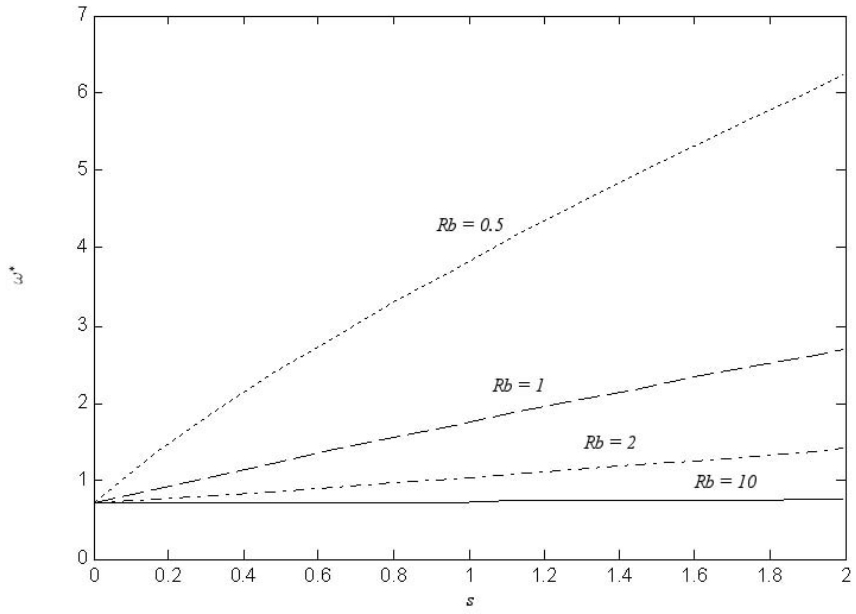

(a)

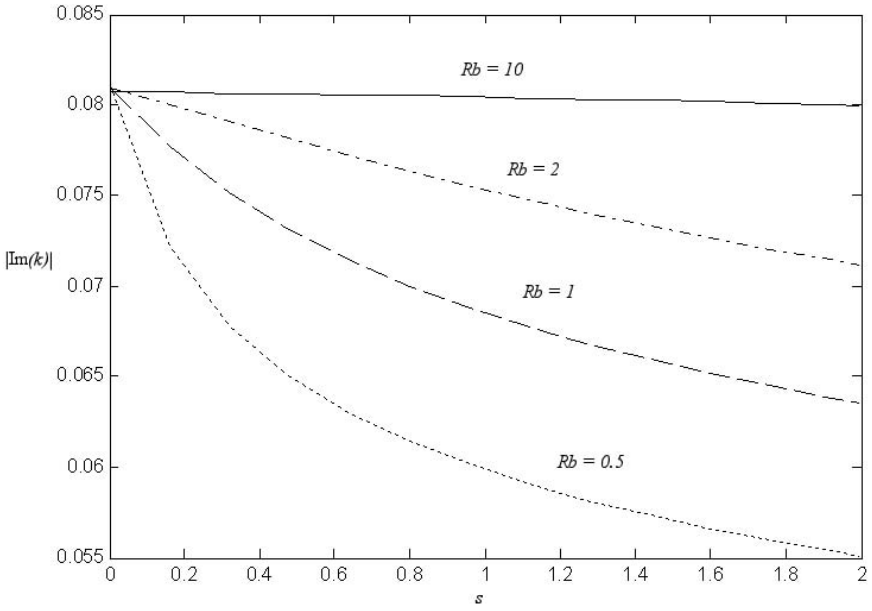

(b)

Figure 6.9: The plot shows (a) the frequency, ω^* and (b) the modulus of growth rate, $|Im(k)|$, of the most unstable mode, as a function of arclength, s, for various Rossby numbers ($\mathcal{R}e_\alpha = 40, \mathcal{W}e = 20, \alpha = 0.8$).

as were found for a fluid of zero viscosity, that for decreasing Rossby number the values of frequency are larger and the growth rate of the most unstable mode reduces.

Figure 6.10 shows how the flow index number, α affects the most unstable mode associated with (6.78). It can be seen that the smaller values of $|Im(k)|$ correspond to increasing values of

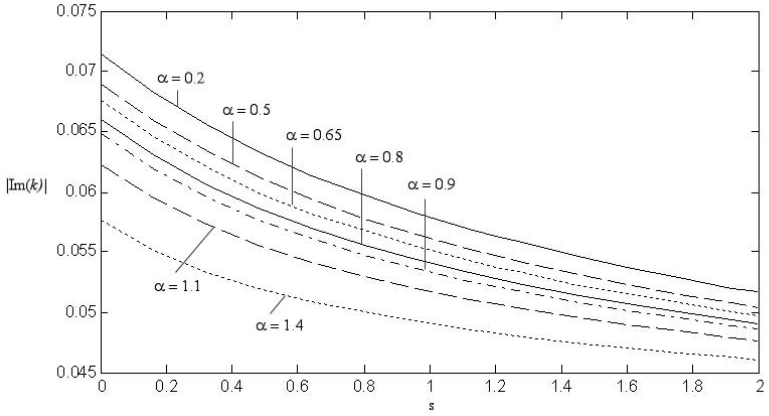

Figure 6.10: The plot shows the modulus of the growth rate, $|Im(k)|$, as a function of arclength, s, for various values of α ($\mathcal{R}e_\alpha = 40, \mathcal{W}e = 20, \mathcal{R}b = 1$).

α. Very little difference was seen in the frequency of the most unstable mode given by (6.78), when plotted against s. Only slightly larger values of ω were found for smaller values of α.

Figures 6.11(a) and 6.11(b) show that decreasing α causes the jet to become more unstable. For larger values of α, the most unstable wave occurs at longer wavelengths.

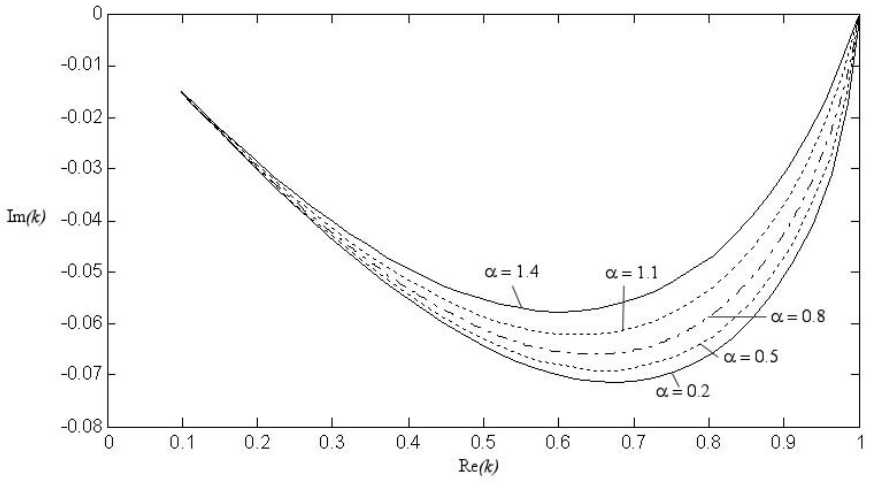

(a)

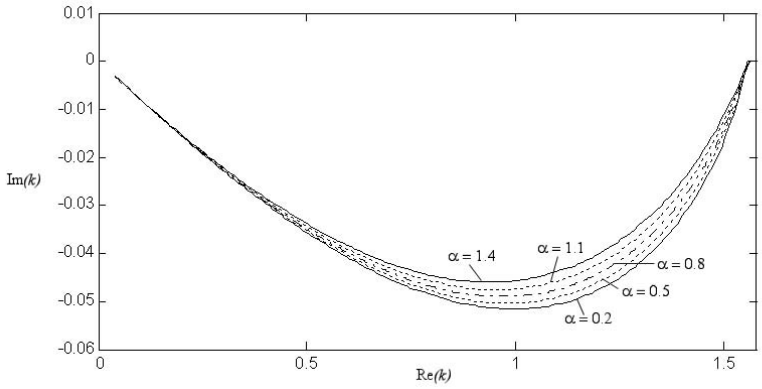

(b)

Figure 6.11: Graph showing $Im(k)$ against $Re(k)$ at (a) $s = 0$ and (b) $s = 10$, for various α ($\mathcal{R}e_\alpha = 40, \mathcal{W}e = 20, \mathcal{R}b = 1$).

6.8 Temporal instability

To interpret (6.78) in terms of temporal stability λ is complex and k is real. Equation (6.78) is then an algebraic equation to be solved for λ, where $Re(\lambda)$ describes the temporal growth of the wave and $Im(\lambda)$ represents its frequency. Instability occurs when $Re(\lambda) > 0$.

In the case of temporal instability it is necessary to determine the most unstable wavenumber $k = k^*(s)$, for which the growth rate, $Re(\lambda)$, is a maximum for each value of the arclength, s. In this way, the growth rate, frequency and the wavelength of the most unstable mode will vary down the jet. The wavenumber, $k = k^*$, is determined numerically, which gives the most unstable mode for each s by solving (6.78) directly.

It can be shown graphically how the temporal mode varies down the jet for various parameters. Figure 6.12 shows computational solutions to (6.78) at various values of s at time $t = 0$. In Figure 6.12(a) each line of the graphs has been constructed by varying k from 0 to ∞. On each line k is real.

It can be seen that the growth rate, $Re(\lambda)$, increases as s increases, which differs to spatial stability. Figure 6.12(b) presents a graph of the wavenumber k, against the growth rate $Re(\lambda)$. Similarly to spatial stability, the maximum growth rate occurs for an increasing wavenumber as s is increased.

Figure 6.13 shows the growth rate, $Re(\lambda)$, of the most unstable mode. The larger values of $\widetilde{\mathcal{R}e_\alpha}$ correspond to larger values of the growth rate. Figure 6.14 shows the wavenumbers, k^*, that correspond to the most unstable wave, plotted against s for various Reynolds numbers.

Figure 6.15 shows how varying the Weber number affects the most unstable mode. Travelling along the arclength of the jet, the growth rate increases, causing the jet to become more unstable. The smaller Weber numbers correspond to the mode being more unstable. This is because smaller Weber numbers correspond to larger surface tension values. Figure 6.16 shows the wavenumbers which correspond to the most unstable mode. The smaller the Weber number the larger the wavenumber.

Figures 6.17 and 6.18 show the growth rate, $Re(\lambda)$, and the most unstable wave number, k^*,

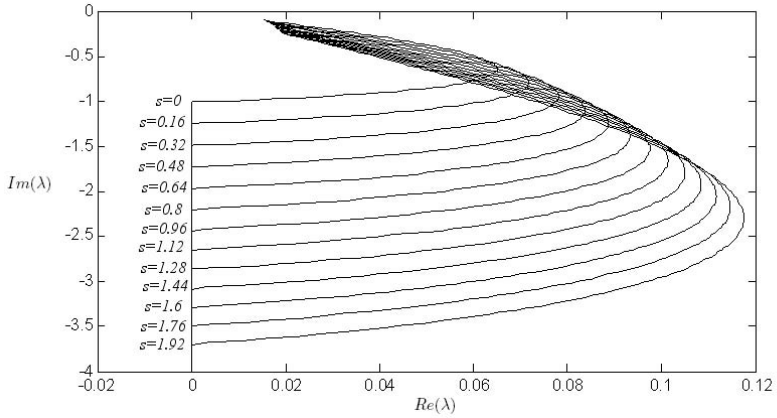

(a) Graph showing $Im(\lambda)$ against $Re(\lambda)$ at $t = 0$ for various s ($\widetilde{\mathcal{R}e_\alpha} = 40, \mathcal{W}e = 20, \mathcal{R}b = 1, \alpha = 0.8$).

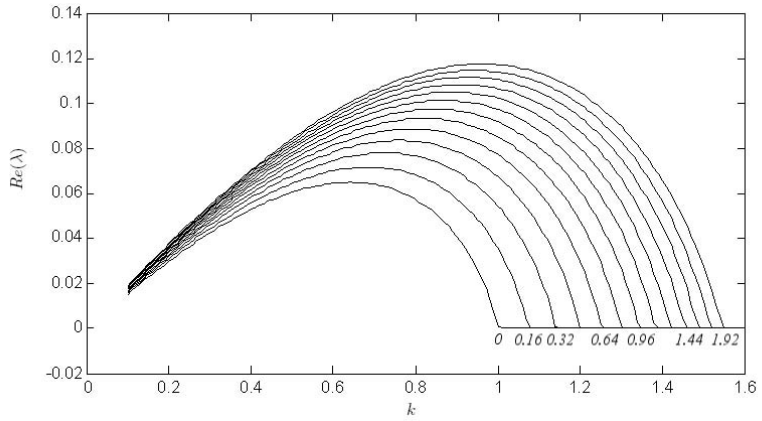

(b) Graph showing the growth rate, $Re(\lambda)$, against k at $t = 0$ for various s ($\widetilde{\mathcal{R}e_\alpha} = 40, \mathcal{W}e = 20, \mathcal{R}b = 1, \alpha = 0.8$).

Figure 6.12: Graph showing (a) the frequency, λ, and (b) the growth rate, $Re(\lambda)$, against k, at $t = 0$ for various s ($\widetilde{\mathcal{R}e_\alpha} = 40, \mathcal{W}e = 20, \mathcal{R}b = 1, \alpha = 0.8$). In (a) k is real on each line, but varies from 0 to ∞ along each line from left to right.

plotted against s for various values of the Rossby number. Figure 6.17 shows that the smaller the value of the Rossby number (which relates to larger rotation rates), the larger the growth rate. In Figure 6.18 it can be seen that the larger wavenumbers correspond to smaller Rossby numbers.

Very little qualitative change is shown if the Rossby, Reynolds and Weber numbers are fixed and α is varied. The growth rate is again seen to increase travelling down the jet, but altering α shows very little variation.

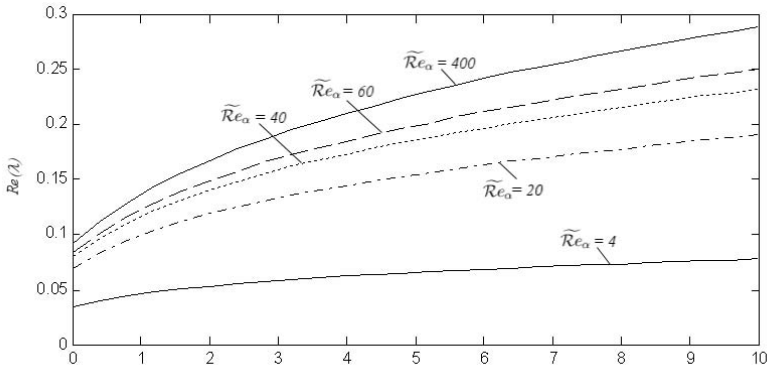

Figure 6.13: Graph showing the growth rate, $Re(\lambda)$, of the most unstable mode against the arclength, s, for various Reynolds numbers ($\mathcal{W}e = 13.33, \mathcal{R}b = 1.12, \alpha = 0.92$).

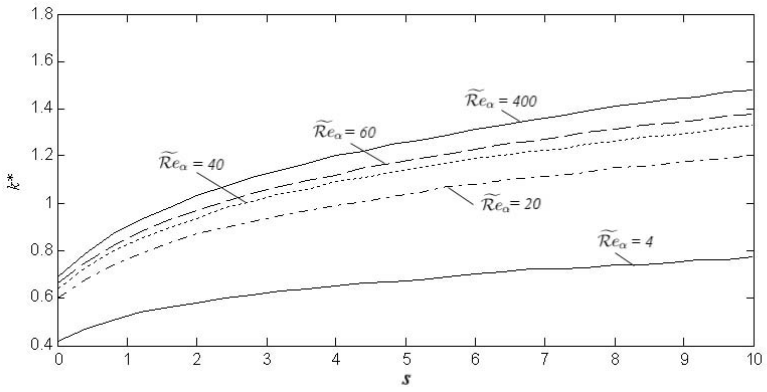

Figure 6.14: Graph showing the wavenumber of the most unstable mode, k^*, against the arclength, s, for various Reynolds numbers ($\mathcal{W}e = 13.33, \mathcal{R}b = 1.12, \alpha = 0.92$).

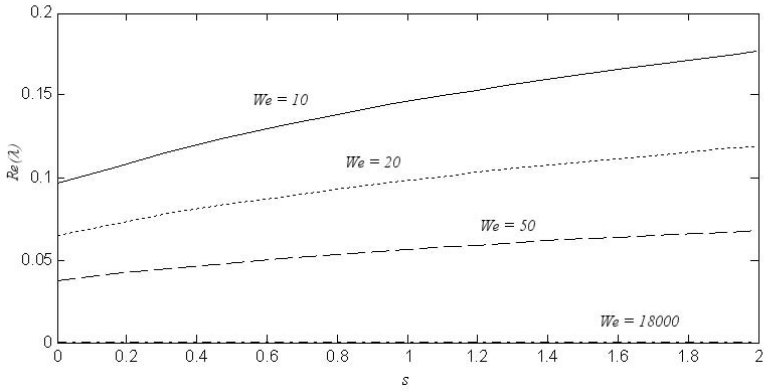

Figure 6.15: Graph showing the growth rate, $Re(\lambda)$, of the most unstable mode against the arclength, s, for various Weber numbers ($\mathcal{R}b = 1, \widetilde{\mathcal{R}e_\alpha} = 40, \alpha = 0.8$).

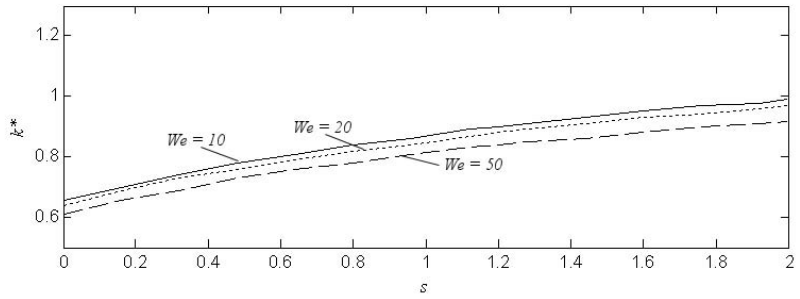

Figure 6.16: Graph showing the wavenumber of the most unstable mode, k^*, against the arclength, s, for various Weber numbers ($\mathcal{R}b = 1, \widetilde{\mathcal{R}e_\alpha} = 40, \alpha = 0.8$).

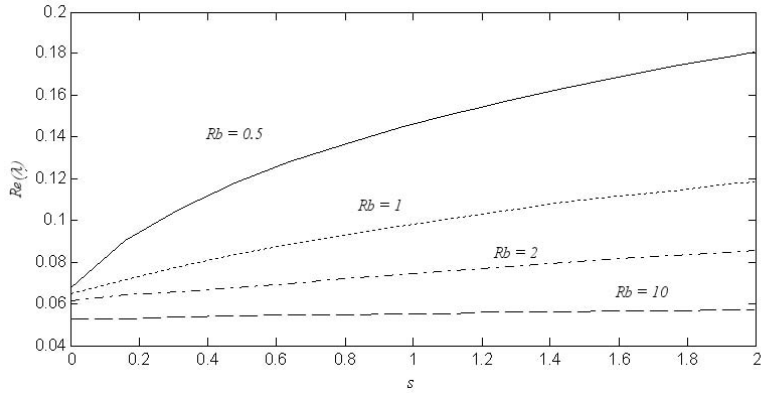

Figure 6.17: Graph showing the growth rate, $Re(\lambda)$, of the most unstable mode against the arclength, s, for various Rossby numbers ($\mathcal{W}e = 20, \widetilde{\mathcal{R}e_\alpha} = 40, \alpha = 0.8$).

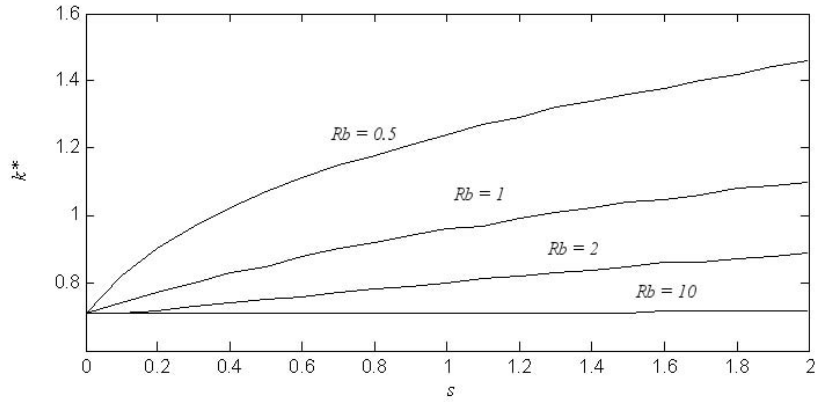

Figure 6.18: Graph showing the wavenumber of the most unstable mode, k^*, against the arclength, s, for various Rossby numbers ($\mathcal{W}e = 20, \widetilde{\mathcal{R}e_\alpha} = 40, \alpha = 0.8$).

6.9 Comparison with experiments

The experiments performed on the pilot scale facility described in Chapter 5 were used to determine the accuracy of the theoretical model in determining primary drop size for shear thinning liquids (CMC solutions). Three different liquid systems were examined as given in Table 3.1.

The break-up length, $s = s_b$, is taken from the experimental measurements and non-dimensionalised with respect to the radius of the drum, s_0. The values of the steady state radius, $R_0(s_b)$, velocity, $u_0(s_b)$, and apparent viscosity $\eta_0(s_b)$ are obtained from the solution to the steady state equations, (6.57) - (6.64). We then substitute $R_0(s_b)$, $u_0(s_b)$ and $\eta_0(s_b)$ into (6.78), adopting the view of spatial instability with $\lambda = -i\omega$. The resulting equations are solved for k numerically for various values of ω to determine the most unstable wavenumber $k^*(s_b)$ as described in section 6.6. From this it is possible to determine the radius of the main droplet produced by this instability by calculating the volume of liquid in the wavelength at the break-up point. As these droplets will be approximately spherical, the main droplet radius can be determined from this volume (see Equation 2.26).

Equation (6.78) was solved computationally using real measured parameters from the experiments in order to determine the wavelength and hence the theoretical drop size at the experimental point of break-up. These results are then compared to drop sizes measured experimentally.

Figures 6.19(a), 6.19(b) and 6.19(c) demonstrate how the velocity, u_0, the radius of the jet, R_0, and the predicted drop size vary with the arclength s in the computations for parameter values corresponding to experiments. The data presented in these graphs only presents numerical predictions for 0.1% CMC, so $\alpha = 0.92$. The same trends are observed for 0.2% CMC and 0.3% CMC.

Figure 6.19(b) shows that the radius of the jet thins as it leaves the orifice. It can also be seen that Rossby number appears to have a greater impact on the rate at which the jet thins than the other experimental parameters. The predicted droplet radius, shown in Figure 6.19(c), indicates how that parameter would vary if the jet breaks at different lengths, s. Thus if the jet

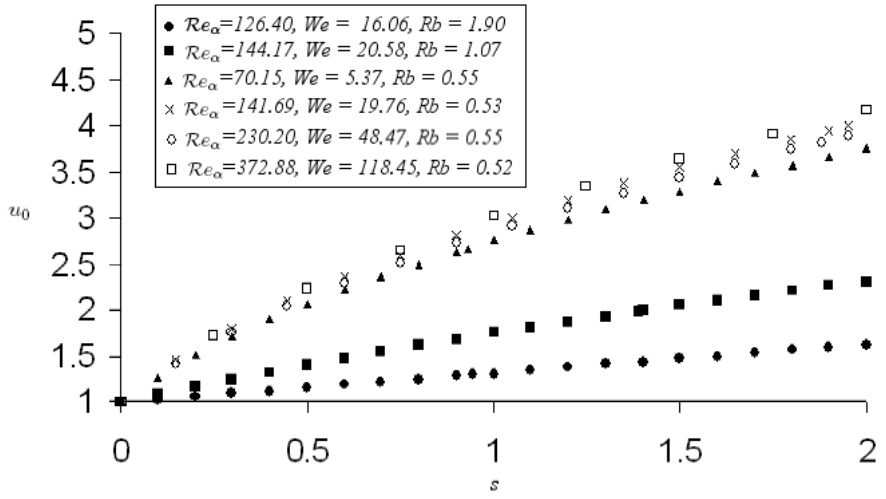

(a)

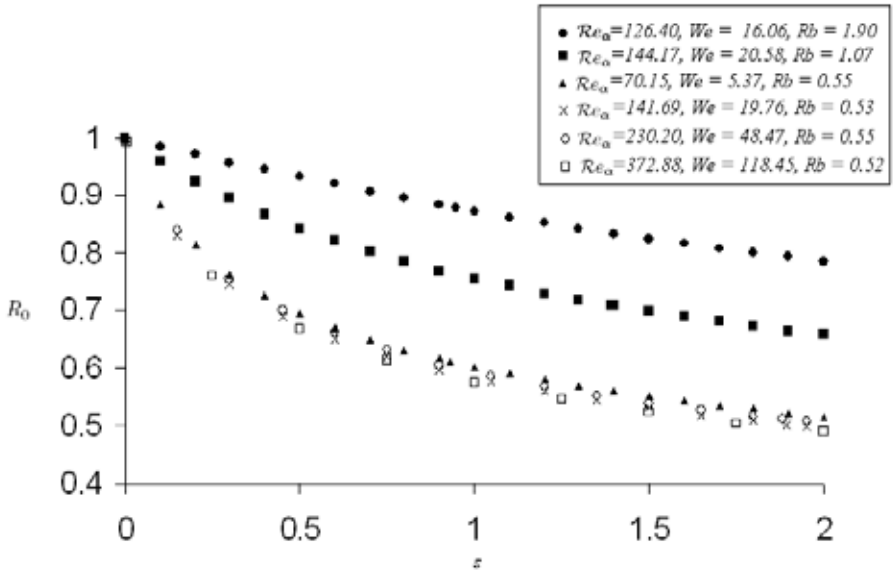

(b)

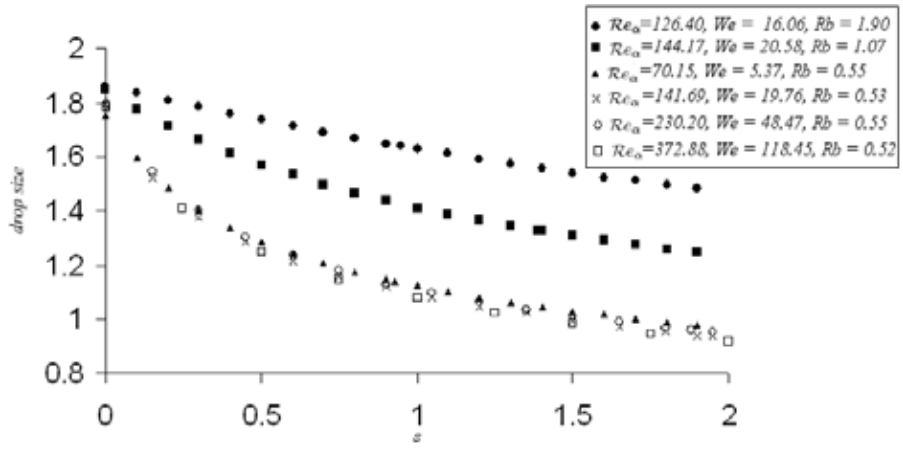

(c)

Figure 6.19: The plot shows (a) u_0, (b) the radius of the jet, R_0, and (c) the predicted drop radius, as a function of arclength, s, for various parameter values. For all solutions, $\alpha = 0.92$.

Table 6.1: Table of normalised drop sizes for experiments and predictions using the numerical model.

k (Pa s$^{\alpha}$)	α	$\mathcal{W}e$	$\mathcal{R}b$	$\mathcal{R}e_{\alpha}$	Experimental value $\pm$ s.d.	Model prediction
0.012	0.92	16.06	1.90	126.39	1.434 ± 0.138	1.6707
0.012	0.92	20.58	1.08	144.17	1.389 ± 0.142	1.3523
0.012	0.92	5.37	0.55	70.15	1.341 ± 0.112	1.1622
0.012	0.92	19.76	0.53	141.69	1.305 ± 0.129	0.9623
0.012	0.92	48.47	0.55	230.20	1.423 ± 0.161	0.9615
0.060	0.748	6.46	1.21	19.16	1.252 ± 0.126	1.5921
0.060	0.748	8.34	0.69	22.49	1.376 ± 0.119	1.995
0.060	0.748	2.91	0.41	11.64	1.104 ± 0.144	1.1928
0.060	0.748	10.41	0.39	25.99	1.248 ± 0.115	0.8356
0.060	0.748	23.50	0.39	43.58	1.020 ± 0.085	0.7321
0.060	0.748	83.21	0.44	95.40	1.161 ± 0.103	0.713
0.060	0.748	14.60	1.10	27.33	1.993 ± 0.178	1.4856
0.060	0.748	38.37	0.89	49.72	1.584 ± 0.133	1.2015
0.060	0.748	44.63	0.65	55.39	1.325 ± 0.123	0.9341
0.199	0.654	10.19	0.38	9.18	1.154 ± 0.094	1.3213
0.199	0.654	13.54	1.08	9.73	1.833 ± 0.156	1.4754
0.199	0.654	26.32	0.75	15.14	1.632 ± 0.129	1.0835
0.199	0.654	60.21	0.59	18.80	1.407 ± 0.125	0.9472
0.199	0.654	20.17	0.66	12.77	1.699 ± 0.194	1.0826
0.199	0.654	32.74	0.56	17.69	1.529 ± 0.145	0.8854
0.199	0.654	46.23	0.49	21.83	1.173 ± 0.126	0.8551
0.199	0.654	66.00	0.47	28.04	1.345 ± 0.158	0.8428

was longer, then the drops would be smaller.

The theoretical drop radii estimated using (6.78) are given in Table 6.1, along with the experimental results and parameters examined. All the drop radii are normalised with respect to the radius of the orifice, a. The value of the break-up length is taken from the experimental observation.

The accuracy of the drop radii predictions are illustrated in Figure 6.20. It can be seen from Figure 6.20, where the theoretical value of the radius is compared to the experimental mean of the primary drop radii, that reasonable agreement between drop sizes acquired experimentally and theoretically is obtained. The results suggest that over the range of Weber numbers treated, the theory under-predicts the droplet radius, more than it over-predicts it and there appears to be some correlation between the Weber number and accuracy of the prediction. As the Weber number increases, the prediction of the droplet radius becomes less accurate.

Experimental images of the jet as the Weber number increases are shown in Figure 6.21 and correlate to the points marked (a),(b) and (c) in Figure 6.20. As the Weber number increases these images show that the jet break-up becomes more complicated. At low Weber numbers

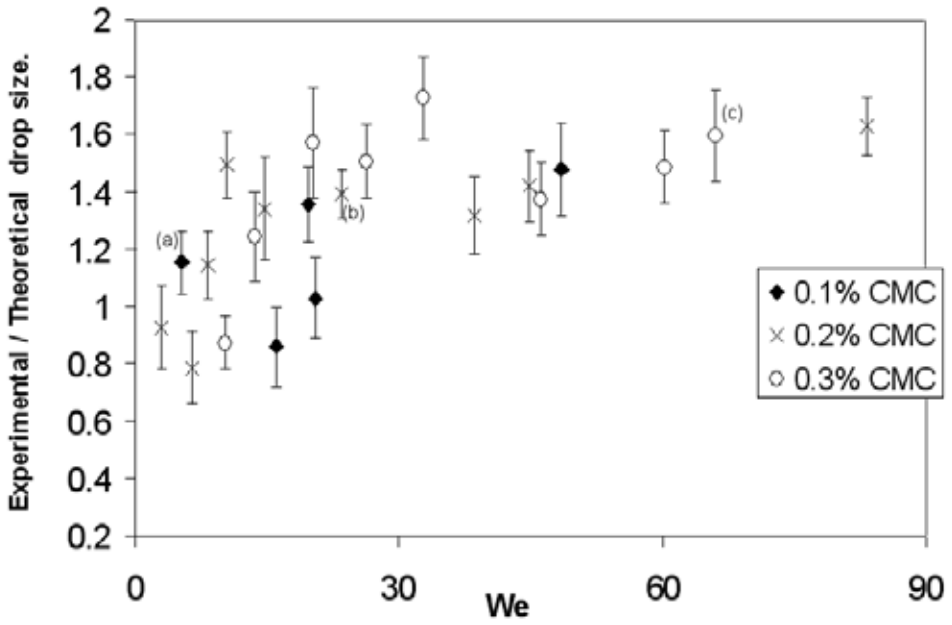

Figure 6.20: Experimental main drop radius/theoretical drop radius predictions for experiments as shown in Table 6.1 plotted against the Weber number. Drop sizes are grouped by liquid system and the error bars represent the standard deviations given by the distribution of primary drop sizes obtained.

(corresponding to low exit velocities) the jet is fairly straight-forward as demonstrated in Figure 6.21(a). As the Weber number increases, so does the Reynolds number and jet break-up becomes more complicated. As can be seen in Figures 6.21(b) and 6.21(c), the jet becomes increasingly complex for increasing Weber number and it is more difficult to accurately predict drop size.

The computations predict that different drop sizes arise depending on where the jet breaks. Figure 6.19(c) shows the drop size that will arise for different break-up lengths, calculated using the steady state and the eigenvalue relationship (6.78). The actual break-up length depends upon the size of the disturbance at the orifice. If we know the size of the disturbance at the orifice, then the theory can be used to predict the break-up length[1]. Experimental work with known forced disturbances at the orifice will follow, but this chapter concerns unforced jets where the size of the disturbance at the orifice is unknown. The results in Table 6.1 are determined by experimentally observing the break-up length and using that value to feed into the computations

[1]It is possible to predict the size of the disturbance at the orifice by matching to experiments. Decent et al. (2009) uses the linear instability calculations to theoretically predict break-up length.

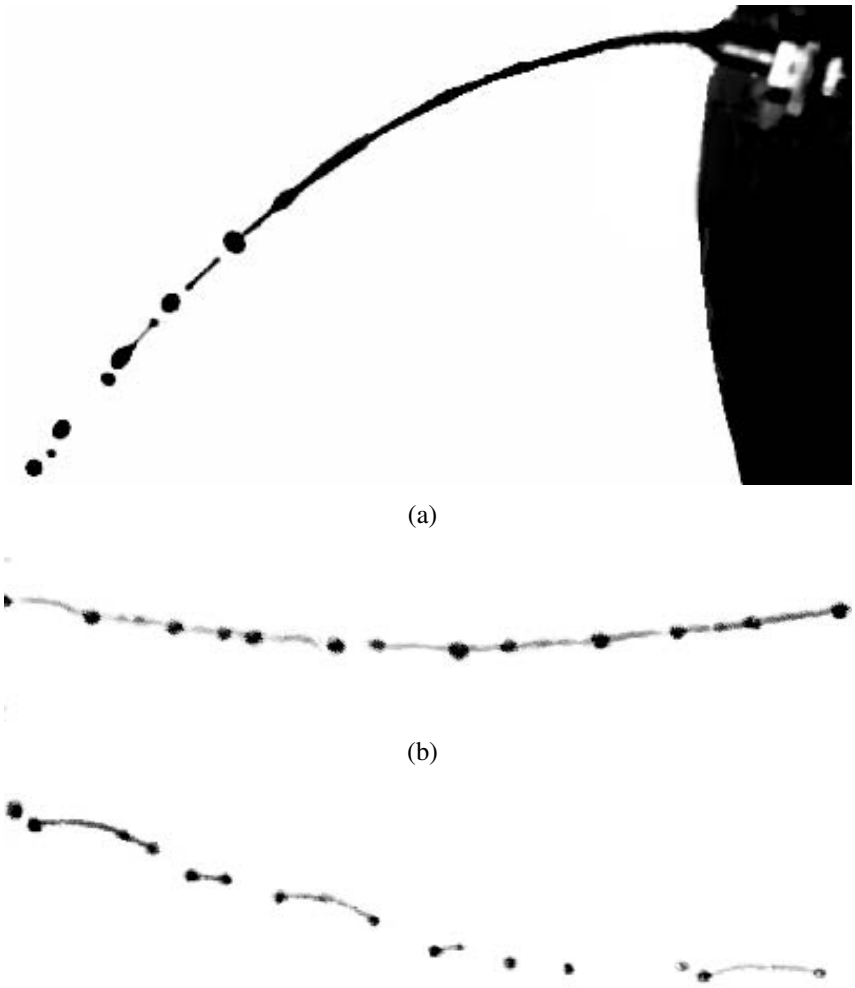

(a)

(b)

(c)

Figure 6.21: Experimental images of the jet (a) $\mathcal{W}e = 5.37, \mathcal{R}b = 0.552, \mathcal{O}h = 0.0229, \mathcal{R}e = 101.00, \rho = 1025$ kg m$^{-3}, k = 0.012$ Pa s$^n, n = 0.920$, (b) $\mathcal{W}e = 23.50, \mathcal{R}b = 0.588, \mathcal{O}h = 0.0356, \mathcal{R}e = 136.11, \rho = 1026$ kg m$^{-3}, k = 0.061$ Pa s$^n, n = 0.748$ and (c) $\mathcal{W}e = 65.99, \mathcal{R}b = 0.473, \mathcal{O}h = 0.0519, \mathcal{R}e = 156.31, \rho = 1027$ kg m$^{-3}, k = 0.199$ Pa s$^n, n = 0.654$.

to predict the resulting drop size. However, at high Weber number, Figure 6.21(c) shows that determining the location of the break-up point experimentally is not straight-forward; there is not always a unique break-up point, but the jet may break at several locations simultaneously. Moreover, while the Weber number at the orifice, which is the Weber number quoted throughout this Chapter, is high, if a local Weber number were to be calculated on the ligament, this would probably be quite small as the speed of the flow within the ligament (not relative to the orifice) will be quite different to the initial speed of the jet, U, and the radius of the ligament is much smaller than a. Therefore, the break-up in 6.21(c) may not be convective, but instead absolute.

6.10 Long-wavelength dispersion relation

It is useful to analyse the stability of the long wavelength approximation $k \to 0$ of the full dispersion relation (6.78). To obtain this we take the non-linear equations from Uddin et al. (2008a), namely

$$\frac{\partial A}{\partial t} = -\frac{\partial}{\partial s}(Au), \tag{6.80}$$

$$\begin{aligned} u_t + uu_s &= -\frac{1}{\mathcal{W}e}\frac{4(2A + (\epsilon A_s)^2 - \epsilon^2 A A_{ss})}{(4A + (\epsilon A_s)^2)^{\frac{3}{2}}} \\ &+ \frac{(X+1)X_s + ZZ_s}{\mathcal{R}b^2} + \frac{3}{A\mathcal{R}e_\alpha}\left(|\sqrt{3}u_s|^{\alpha-1}u_s A\right)_s, \end{aligned} \tag{6.81}$$

where $A = R^2$, and perturb them by unsteady quantities

$$\begin{aligned} R = R_0(s) &= R_0(s) + \delta\tilde{R}(s, \bar{s}, \phi, t, \bar{t}), \\ u = u_0(s) &= u_0(s) + \delta\tilde{u}(s, \bar{s}, \phi, t, \bar{t}), \end{aligned}$$

where δ is a small parameter and $\bar{s} = s/\epsilon$ is a short lengthscale and $\bar{t} = t/\epsilon$ is a small timescale associated with short wavelike disturbances.

Taking terms of $O(\delta)$ and of leading order in ϵ we obtain the equations

$$\begin{aligned}\tilde{R}_t &= \frac{1}{2}R_0\tilde{u}_{\bar{s}} + u_0\tilde{R}_{\bar{s}} \\ \tilde{u}_{\bar{t}} + u_0\tilde{u}_{\bar{s}} &= \frac{1}{\mathcal{W}e}\left(\frac{1}{R_0^2}\tilde{R}_{\bar{s}} + \tilde{R}_{\bar{s}\bar{s}\bar{s}}\right) + \frac{3}{\widetilde{\mathcal{R}e_\alpha}}\left|\sqrt{3}u_{0s}\right| n\tilde{u}_{\bar{s}\bar{s}},\end{aligned}$$

We look for solutions in modes of the form

$$\tilde{R} = \hat{R}(s,\phi,t)\text{ext}(ik(s,t)\bar{s} + \lambda(s,t)\hat{t}), \tag{6.82}$$

$$\tilde{u} = \hat{u}(s,\phi,t)\text{ext}(ik(s,t)\bar{s} + \lambda(s,t)\hat{t}), \tag{6.83}$$

and after some algebra, obtain

$$(\lambda + iu_0k)^2 + \frac{3k^2\alpha}{\widetilde{\mathcal{R}e_\alpha}}\left|\sqrt{3}u_{0s}\right|^{\alpha-1}(\lambda + iu_0k) + \frac{k^2R_0}{2\mathcal{W}e}\left(k^2 - \frac{1}{R_0^2}\right). \tag{6.84}$$

which matches the dispersion relation obtained in Uddin (2007). This can be further simplified to obtain

$$\lambda = -iu_0k - \frac{3}{2}\frac{k^2}{\widetilde{\mathcal{R}e_\alpha}}\left|\sqrt{3}u_{0s}\right| \pm \frac{k}{2}\sqrt{\frac{9k^2\alpha^2}{\widetilde{\mathcal{R}e_\alpha}^2}\left|\sqrt{3}u_{0s}\right|^{2(\alpha-1)} - \frac{2R_0}{\mathcal{W}e}\left(k^2 - \frac{1}{R_0^2}\right)} \tag{6.85}$$

It is now possible to compare the long wavelength dispersion relation (6.85) with the results obtained for the full dispersion relation (6.78). Figures 6.22 and 6.23 present computational solutions to the full dispersion relation by solving (6.78), indicated by the unbroken line, and the long wavelength approximation $k \to 0$ of the full dispersion relation by solving (6.85), indicated by the broken line. Figure 6.22 solves (6.78) and (6.85) in terms of spatial instability and Figure 6.23 in terms of temporal instability.

In all cases in the unstable region quite a good comparison can be seen, although in Figure 6.22(a) it can be seen that the long wavelength theory predicts a smaller growth rate, whereas in Figure 6.23(a) the long wavelength theory predicts a slightly larger growth rate. In addition, in the stable region when $Im(k) > 0$ in the spatial case, or $Re(\lambda) < 0$ in the temporal case,

the long wavelength theory predicts stable modes, whereas the full dispersion relation predicts modes of zero growth rate. However, as we focus on the region for unstable modes, where the correlation is found to be excellent, this means that it is possible to take the long wavelength approximation in future, in order to predict drop size measurements, thus saving significant computational time whilst solving the dispersion relation.

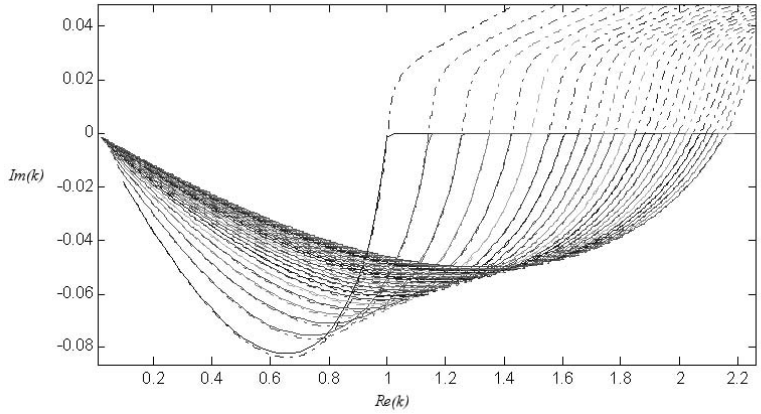

(a) Graph showing $Im(k)$ against $Re(k)$ for various values of s ($\widetilde{\mathcal{R}e_\alpha} = 40, \mathcal{W}e = 13.33, \mathcal{R}b = 1.12, \alpha = 0.92$).

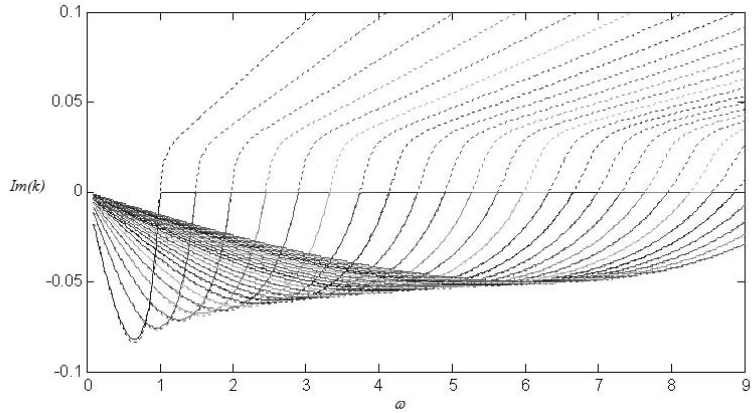

(b) Graph showing $Im(k)$ against w for various s ($(\widetilde{\mathcal{R}e_\alpha} = 40, \mathcal{W}e = 13.33, \mathcal{R}b = 1.12, \alpha = 0.92$).

Figure 6.22: Graph showing (a) $Im(k)$ against $Re(k)$ and (b) $Im(k)$ against w for various values of s shown for (i) the full dispersion relation '-' and (ii) the long wavelength dispersion relation '- -' ($\widetilde{\mathcal{R}e_\alpha} = 40, \mathcal{W}e = 13.33, \mathcal{R}b = 1.12, \alpha = 0.92$). In (a) the frequency, ω, is real on each line, but varies from 0 to ∞ along each line from left to right.

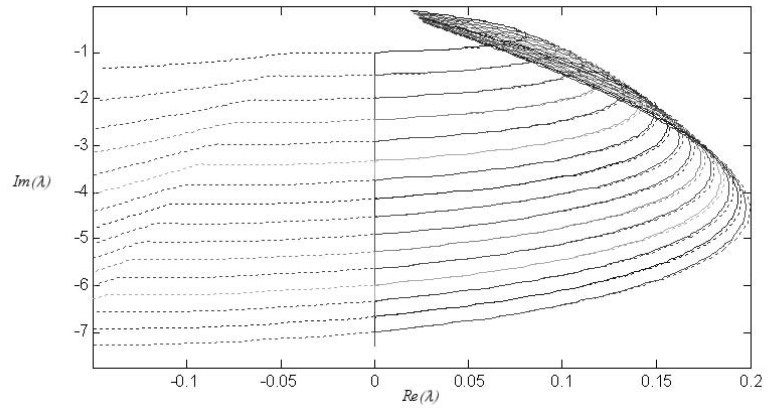

(a) Graph showing $Im(\lambda)$ against $Re(\lambda)$ at $t = 0$ for various s ($\widetilde{\mathcal{R}e_\alpha} = 40, \mathcal{W}e = 13.33, \mathcal{R}b = 1.12, \alpha = 0.92$).

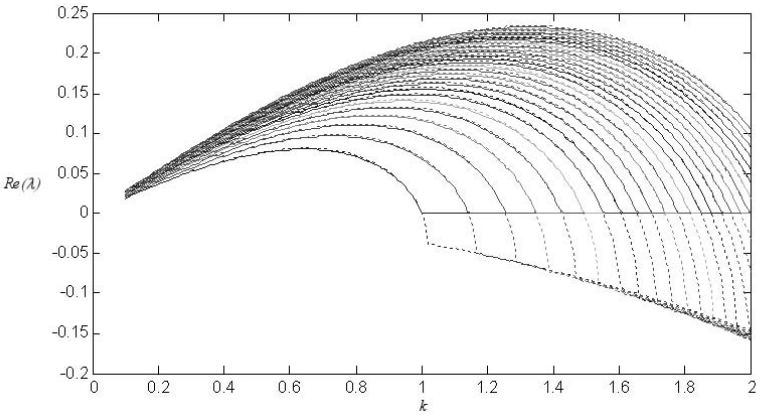

(b) Graph showing the growth rate, $Re(\lambda)$, against k at $t = 0$ for various s ($\widetilde{\mathcal{R}e_\alpha} = 40, \mathcal{W}e = 13.33, \mathcal{R}b = 1.12, \alpha = 0.92$).

Figure 6.23: Graph showing (a) the frequency, λ, and (b) the growth rate, $Re(\lambda)$, against k, at $t = 0$ for various s, shown for (i) the full dispersion relation '-' and (ii) the long wavelength dispersion relation '- -' ($\widetilde{\mathcal{R}e_\alpha} = 40, \mathcal{W}e = 13.33, \mathcal{R}b = 1.12, \alpha = 0.92$). In (a) k is real on each line, but varies from 0 to ∞ along each line from left to right.

6.11 Conclusions

The effect of apparent viscosity on the trajectory of a rotating, slender non-Newtonian liquid jet emanating from a small orifice, has been examined by incorporating the effects of non-Newtonian power-law rheology into the existing steady state equations derived by Wallwork et al. (2002). Apparent viscosity only appears as a higher order (in ϵ) correction to the inviscid steady centreline.

A linear dispersion relation has been obtained that can be solved computationally to estab-

lish the behaviour of wave modes as they propagate along a curved liquid jet. As the arclength, s, increases, the growth rate decreases, and the wavenumber with the largest growth rate occurs for higher values of frequency, ω.

The influence of the parameter, α, appeared to have little effect on the linear modes. Of course, in reality changing α also alters the apparent viscosity of the fluid and hence, the Reynolds number, which does have a dramatic effect on wave behaviour.

The experiments detailed in Chapter 5 were used to determine the trajectory and break-up of slender liquid jets over a wide range of parameters, with measurements of break-up length and drop size being taken. The mean droplet radius produced by instability has been determined using the linear instability calculations and the experimental value of break-up which enables a comparison between experimental and theoretical work. Some good points of agreement have been obtained between theoretical and experimental measurements of the size of the drops produced by instability, particularly at lower Weber numbers. At higher values of the Weber number, break-up may be via absolute instability on the observed slender ligament: this will be the subject of future work by Rachan Bassi, a PhD student in the Mathematics department at the University of Birmingham. All the fluids were tested for viscoelastic effects, however at high Weber number the jet does appear less laminar and there is the possibility that at high Weber number the stresses the fluid are being subjected to are more severe than can be tested accurately in the rheometer, particularly near break-up. It would be interesting to extend this work using the Olroyd-B model to see if there is any hint of viscoelasticity in the experimental results.

A comparison was also made with the approximate long wavelength dispersion relation (Uddin, 2007). It was found that the long wavelength approximation offers comparable results if we focus on the region for unstable modes, where the correlation is found to be excellent. Using this approximation saves significant computational time in predicting primary drop radii.

CHAPTER 7

CONTROLLING BREAK-UP THROUGH THE USE OF A VIBRATING NOZZLE

7.1 Introduction

In Gurney et al. (2010), a thorough comparison of the existing linear and non-linear theories of Decent et al. (2009) and Părău et al. (2007) was performed (Chapter 2.3.3). Experimental work, which is published in Gurney et al. (2010), was also performed on Newtonian liquid jets in order to enable a comparison with the theory in order to fully appreciate the uses and limitations of the mathematical model.[1] The non-linear simulations of jet profiles were examined, by matching the break-up length to that obtained experimentally and primary droplets were compared for both theories (Chapter 2.4). It was found that the two theories differ more for high rotation rates and viscosities, and that the non-linear theory predicts much larger droplets than those obtained experimentally, while the linear theory predicts drop sizes towards the lower end of the distribution.

In Gurney et al. (2010), a secondary disturbance is introduced through the boundary conditions at the orifice in the non-linear model of Părău et al. (2007), which use the method of finite differences to solve the non-linear evolution equations for jet radius and axial velocity, to investigate the possibility of mechanical instabilities affecting the break-up of the liquid jet. Drop size distributions are generated that match those obtained experimentally through the ap-

[1] Some of the experiments and analysis of Partridge et al. (2005) were repeated in order to obtain more focused results. The rig used was as described in Chapter 3 and Newtonian aqueous solutions of glycerol were used as the working fluid ($0.001 < \mu < 0.09$ Pa s). Further details are given in Partridge et al. (2005)

plication of high amplitude secondary disturbances.

It is noted that drop size distributions become more unimodal for the application of certain frequencies and amplitudes and the idea of applying a secondary disturbance in order to force a certain break-up mode is investigated further, by exploiting the results found in Gurney et al. (2010) and applying these.

This Chapter details an attempt to control jet break-up motivated by the results found in Gurney et al. (2010), which are summarised in Sections 7.4 and 7.5. In Section 7.5 it will be established that in order to dominate break-up and obtain M1 behaviour it is necessary to apply a secondary disturbance which has a high amplitude. Modifications were made to the pilot scale rig (Section 7.6) to enable the use of vibrating nozzle to apply forced disturbances. Experimental results are presented in Sections 7.7 and 7.8 and in the latter, it is explored whether it is possible to use the numerical simulations developed in Gurney et al. (2010), to accurately predict conditions using forced disturbances, where satellite droplets are eradicated.

7.2 Previous experimental work

Previous attempts to control jet break-up were made by Partridge (2006), who placed a fully waterproof sub-aqua speaker inside the can. The speaker was connected to a personal computer and a sound wave was generated using signal generator software (Natch Engineering Sigjenny v0.989). The lowest frequency obtainable from the signal generator software was 10 Hz.

Experiments were carried out for water at four different Rossby numbers with three different wave frequencies ($10, 100$ and 200 Hz). At 10 Hz, insonification was found to have a negligible effect on the drop size distributions at all the Rossby numbers. At 100 Hz, at the higher Rossby numbers, insonification appeared to reduce the number of satellite drops. At lower Rossby numbers, insonification produced a negligible effect on the satellite drops. The lower Rossby numbers correspond to higher rotation rates so it appears that at higher rotation rates the sound waves cannot overcome the increased rotational forces. At 200 Hz a number of satellite drops were eliminated again at higher Rossby numbers, but not for the lower ones.

During the experiments the volume of the sound wave generated from the sub-aqua speaker

was perceived to be louder at 100 Hz than 10 Hz, and the volume of the sound wave was louder at 200 Hz than 100 Hz despite the volume setting being the same in all experiments. This suggested that the amplitude of the wave was larger at 200 Hz than 100 Hz and larger at 100 Hz than 10 Hz. This suggests a minimum amplitude of sound wave is required before insonification can be successful, which matches the results of Gurney (2010). These comments are subjective, as the human ear detects sound more easily at some frequencies than others and the ear does not have a uniform frequency response. However the numerical work done both by Partridge (2006) and Gurney (2010) do point to a critical amplitude of the secondary disturbance, above which insonification is more likely to be successful.

Lower Rossby number corresponded to higher rotation rates therefore there were greater rotational forces for the sound wave to overcome at lower Rossby number. So a larger amplitude of sound wave was required for insonification to be successful at lower Rossby numbers.

7.3 Classifying jet break-up

For the purposes of the next section it is important to clarify typical mode behaviour of a theoretical jet and to explore whether the modes identified by Wong et al. (2004) can be attributed to theoretical jets. The non-linear model of Părău et al. (2007), which uses the Lax-Wendroff method, is used to simulate break-up and the modes of break-up are identified through their similarity in behaviour to experimental modes.

Figure 7.1 shows numerical simulations of jet break-up, using parameters from the experimental regime. They illustrate modes of theoretical jet break-up with similar characteristics to the experimental modes M1 - M3. Identifying the mode of break-up can be relatively straight forward, as in Figure 7.1(a), which is distinctly M1 and a single primary droplet can clearly be seen to form . Figure 7.1(b) also shows clear M2 break-up, where formation of the primary and satellite droplets occur either side of break-up. However, Gurney et al. (2010) also identified a transition period between M2 and M3 break-up, where classifying the break-up mode becomes more difficult and quite subjective. Where the simulation does not show secondary pinch off, as in Figure 7.1(c), or if it is unclear if it is a ligament or large satellite droplet, the

jet is assumed to break-up under the M2/M3 regime. If the simulation indicates that multiple primary droplets may form as in Figure 7.1(d), then the jet is classified as M3, where a ligament forms between two main primary droplets. As the numerical model breaks down at the point of break-up (Părău et al., 2007), no information on the behaviour of the jet after break-up can be obtained. Therefore, for M2/M3 and M3 break-up, the frequency and size of satellite droplets cannot be obtained and the theory is limited to examining primary droplets.

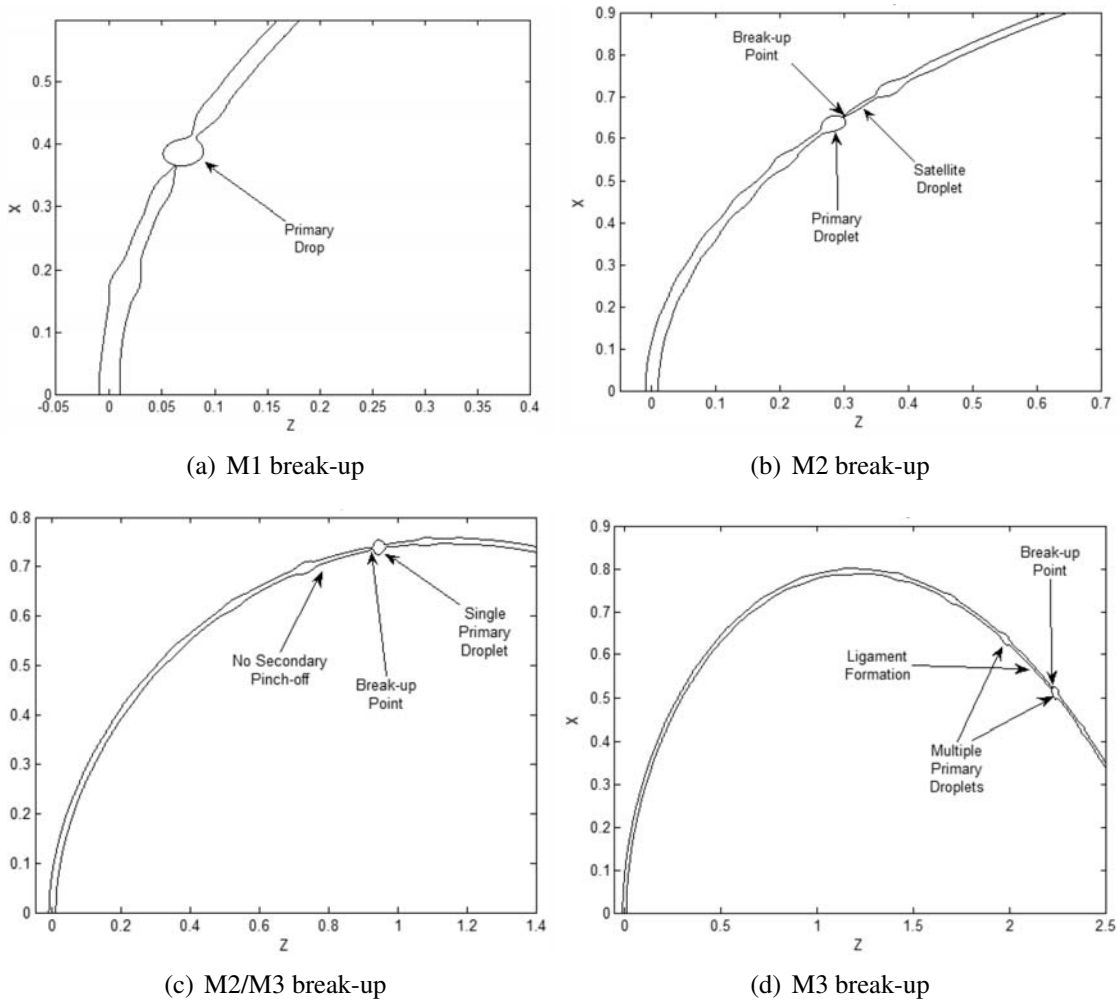

(a) M1 break-up

(b) M2 break-up

(c) M2/M3 break-up

(d) M3 break-up

Figure 7.1: Theoretical mode classifications. (a) Theoretical M1 break-up. $\mathcal{W}e = 20.03, \mathcal{R}b = 2.185, \mathcal{R}e = 1462, \mathcal{O}h = 0.0031, \kappa = 0.705, \delta = 0.01$ and $\epsilon = 0.01$.(b) Theoretical M2 break-up. $\mathcal{W}e = 38.5, Rb = 1.41, \mathcal{R}e = 564, \mathcal{O}h = 0.011, \kappa = 0.699, \delta = 0.01$ and $\epsilon = 0.01$. (c) Theoretical M2/M3 break-up. $\mathcal{W}e = 26.2, \mathcal{R}b = 0.672, \mathcal{R}e = 268, \mathcal{O}h = 0.0191, \kappa = 0.6932, \delta = 0.01$ and $\epsilon = 0.01$. (d) Theoretical M3 break-up. $\mathcal{W}e = 92.3, \mathcal{R}b = 0.73, \mathcal{R}e = 873, \mathcal{O}h = 0.011, \kappa = 0.699, \delta = 0.01$ and $\epsilon = 0.01$. Figures taken from Gurney et al. (2010).

7.4 Introducing a secondary disturbance

While the numerical simulations predict a unique droplet size for given parameters, it has been seen that, experimentally, a distribution is yielded. In Partridge et al. (2005), it was suggested that it is possible that some of the discrepancies between the results from the pilot scale rig and the laboratory scale rig could be due to increased mechanical disturbances in the rig. This could also add to varied distributions in drop sizes. In order to attempt to model this, in Gurney et al. (2010), a secondary disturbance is introduced through the boundary conditions at the orifice,

$$u(0,t) = 1 + \delta \sin(\kappa t/\epsilon) + \gamma \sin(\omega t/\epsilon), \tag{7.1}$$

where γ and ω are the amplitude and frequency of the additional disturbance. Clearly it is unlikely that a singular sinusoidal wave is representative of all vibrations in the rig; this approach merely allows the sensitivity of a jet to additional disturbances to be demonstrated.

To model a distribution in disturbance frequencies at the orifice, a (truncated) Gaussian profile is adopted with the mean chosen to be equal to the frequency of the most unstable wave (so by setting $\kappa = k^*$ in (2.35), so that the most unstable mode at the orifice is imposed), under the assumption that the most unstable wavemode is still a critical factor in jet break-up. The standard deviation of the Gaussian distribution is arbitrarily taken to be equal to the experimental standard deviation in drop size. 200 frequencies (values of ω) are studied to remain consistent with experimental distributions; these are generated using MATLAB's normal distribution function (normrnd).

Inputting 200 different frequencies into the non-linear model is impractical, thus discrete values of ω are chosen (i.e. those shown in Figure 7.2). It is assumed that drop sizes generated by a given frequency fall on the gradient in between the discrete points. In cases where no satellite droplets are produced, such as $\omega = 1.3$, the jet is found to undergo M1 break-up. It is also assumed that no further satellite drops are generated in between the two discrete values. In Figure 7.2, different modes are identified by different symbols.

Using this Gaussian profile a theoretical drop size distribution can be obtained, an example

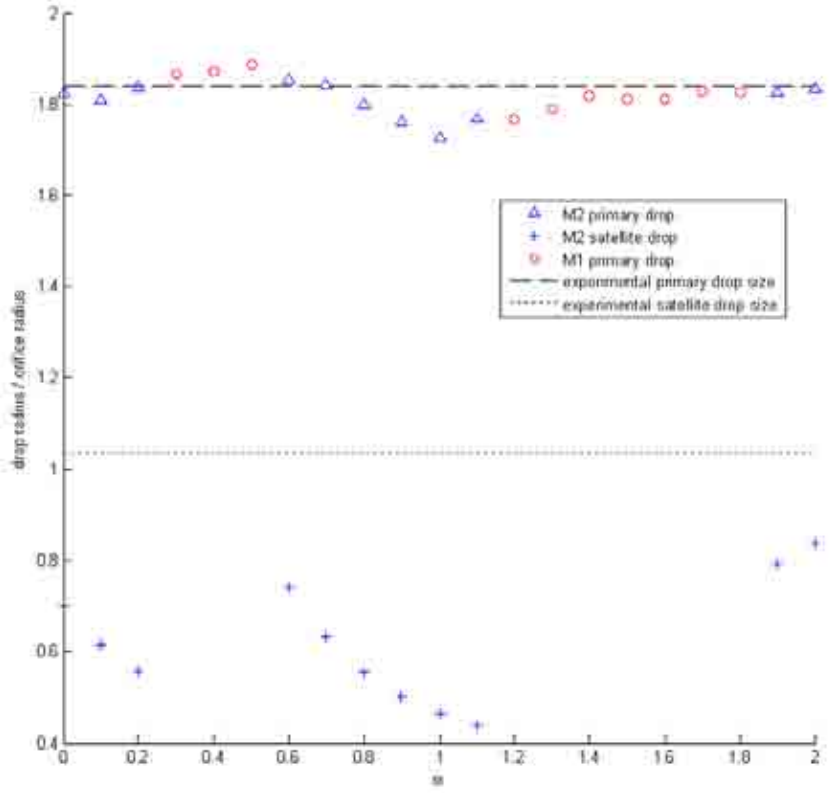

Figure 7.2: Dimensionless drop sizes with varying ω for a jet of water. Here $\mathcal{W}e = 20.03, \mathcal{R}b = 2.189, \mathcal{O}h = 0.003051, \kappa = 0.7048, \delta = 0.00199, \gamma = 0.01$ and $\epsilon = 0.01$. The dotted line shows the experimental mean.

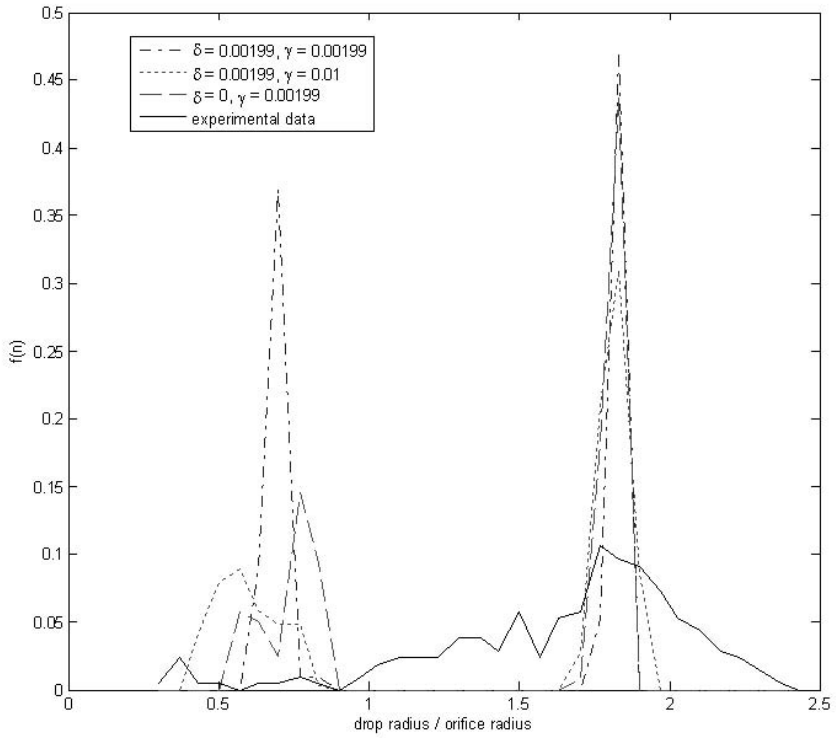

Figure 7.3: Theoretical drop size distributions produced for the different disturbances (1) $\delta = 0.00199, \gamma = 0.00199$, (2) $\delta = 0.00199, \gamma = 0.01$, and (3) $\delta = 0, \gamma = 0.00199$, taken about the frequency of the most unstable wave for a jet of water ($\mathcal{W}e = 20.03, \mathcal{R}b = 2.189, \mathcal{O}h = 0.003051, \kappa = 0.7048, \delta = 0.00199, \epsilon = 0.01$). Also plotted is the experimental data.

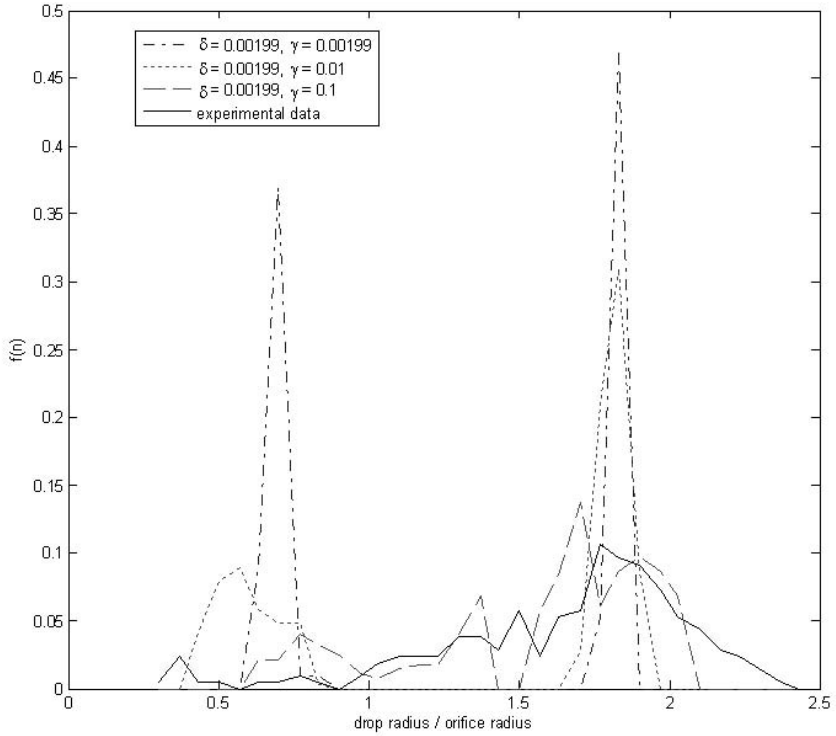

Figure 7.4: Theoretical drop size distributions produced for the different disturbances (1) $\delta = 0.00199, \gamma = 0.00199$, (2) $\delta = 0.00199, \gamma = 0.01$, and (3) $\delta = 0.00199, \gamma = 0.1$, taken about the frequency of the most unstable wave for a jet of water ($\mathcal{W}e = 20.03, \mathcal{R}b = 2.189, \mathcal{O}h = 0.003051, \kappa = 0.7048, \delta = 0.00199, \epsilon = 0.01$). Also plotted is the experimental data.

of which is shown in Figure 7.3 for a jet of water. A Gaussian distribution of frequencies about $\omega = \kappa = 0.7048$ is used. In Gurney et al. (2010), it was found that if the secondary disturbances are of similar magnitude to the most unstable wave ($\gamma = \delta$), then there is a poor correlation with experimental results - a bimodal distribution is generated with too many satellite droplets and the deviation in primary drop sizes is too small. Removing the most unstable wave from the jet had no improved effect upon the variation in main droplet sizes, but had a more dramatic effect on satellite droplets, in a similar fashion to increasing the amplitude of the secondary disturbance by an order of magnitude.

It is necessary for γ to increase by two orders of magnitude, to $\gamma = 0.1$ in Figure 7.4, before good agreement with experimental results are reached and a less bimodal distribution is generated. This indicates the impact of mechanical instabilities that dominate the classical

dynamics of liquid jet break-up.

In order to control jet break-up, it would be necessary to dominate the mechanical instabilities that arise as the rig rotates, regardless of its design.

Gurney et al. (2010) showed that distributions are less comparable for higher rotation rates, for more viscous jets. If there are mechanical instabilities in the pilot scale rig these are more pronounced when the rig is rotating more rapidly and consequently, the experimental jet will be experiencing higher amplitude vibrations at the orifice.

7.5 Controlling jet break-up

The presence of satellite droplets was shown to be reduced in Figure 7.4, when a high amplitude secondary frequency was introduced. A comprehensive theoretical study was undertaken in Gurney (2010), where the impact of altering both the amplitude, γ, and frequency, ω, of the secondary disturbance was investigated. Both the drop size distributions generated and the effect on the jet qualitatively were studied. Key results from this study are presented here.

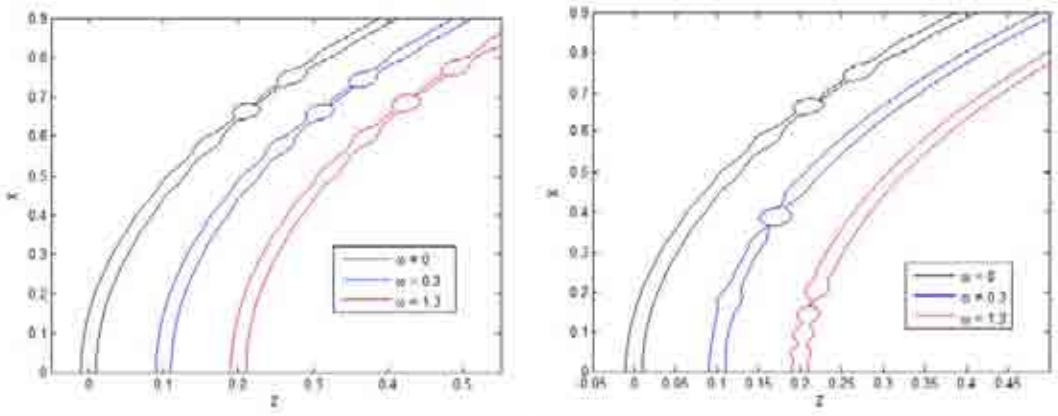

(a) $\gamma = 0.00199$ (b) $\gamma = 0.1$

Figure 7.5: Graphs showing how the jet is affected by changing the frequency, ω of a (a) low amplitude disturbances, $\gamma = 0.00199$, and (b) high amplitude disturbances, $\gamma = 0.1$, for a jet of water ($\mathcal{W}e = 20.03, \mathcal{R}b = 2.189, \mathcal{O}h = 0.003051, \kappa = 0.7048, \delta = 0.00199, \epsilon = 0.01$).

At low amplitude break-up (shown in Figure 7.5(a)), increasing the frequency has little effect on the jet, aside from a slight reduction in break-up length. However, when the amplitude of the jet is increased and then the frequency altered, markedly different behaviour is observed.

Qualitatively in Figure 7.5(b), it appears that as the frequency, ω is increased, not only does the break-up length shorten dramatically, but satellite drop formation is eliminated.

Figure 7.6 shows the different modes of break-up for a theoretical jet of water, which uses experimental parameter values, on the application of the additional disturbance. For low amplitude disturbances (Figure 7.6(a)) break-up is dominated by the most unstable wave. On application of high amplitude disturbances (Figure 7.6(b)), satellite droplets are eradicated in certain frequency ranges and M1 behaviour is generated. With a curved jet, for some value of s, a given value of ω becomes the most unstable wave and if it is applied at large amplitude, this mode dominates break-up (Gurney et al., 2010).

These areas of satellite drop eradication are of a significant industrial interest to prilling. If jet break-up can be controlled through the successful application of a secondary frequency and this can be successfully modelled, this would be very advantageous.

As the viscosity of the liquid is increased these areas of satellite eradication become less frequent and tend to only occur at high amplitude disturbances. In order to regulate jet break-up, the jet must be forced to break-up in regions where the non-linear waves are stable. As the jet becomes more viscous it was shown in Gurney (2010) that, for a given value of s, the frequency of the most unstable wave is larger. The growth rate of a given ω also decreases with s at a greater rate and thus it is harder to regulate break-up with application of a single frequency disturbance. This may explain why it is harder to force M1 for a more viscous jet.

In Figure 7.7 as the secondary frequency is increased break-up moves through the mode boundaries, starting with M2/M3, moving through M2, with the high frequency disturbance actually predicting M1 behaviour. For very high frequency, $\omega > 1.8$, break-up reverts back to M2 behaviour. We know from Gurney et al. (2010), that with a curved jet, for some value of s, a given value of ω becomes the most unstable wave and if it is applied at large amplitude, this mode dominates break-up (Gurney et al., 2010). This may also explain why break-up reverts back to M2 behaviour for larger frequencies; the value of s at which a greater ω becomes unstable is larger, and thus nonlinearities have a chance to grow and influence break-up.

For the most viscous jet, obtained using experimental parameters, Figure 7.8 demonstrates

how the break-up mode changes. As ω is increased, the break-up mode changes from M3 to M2. In this Figure, the ligaments formed are plotted, assuming that the ligament contracts to form a single satellite droplet rater than multiple droplets.

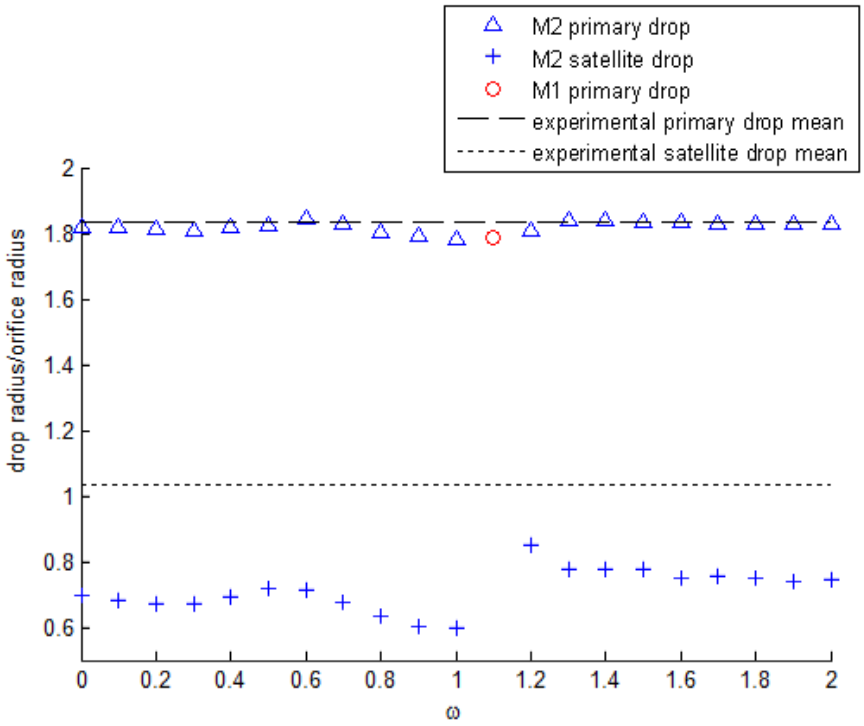

(a) $\gamma = 0.00199$

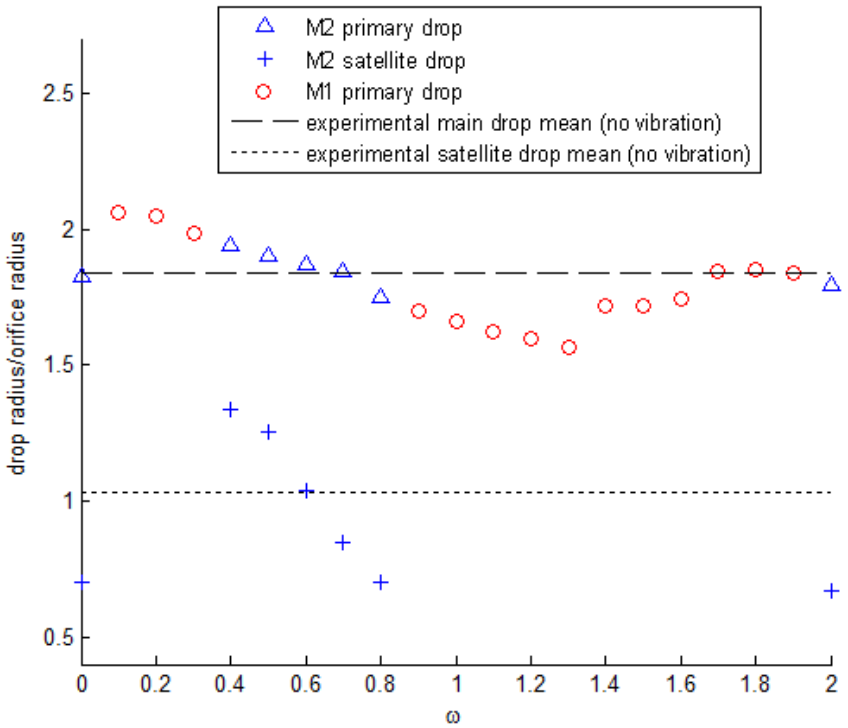

(b) $\gamma = 0.1$

Figure 7.6: Graphs showing how the mode of break-up changes with varying frequency at (a) a low amplitude disturbance of $\gamma = 0.00199$ and (b) a high amplitude disturbance of $\gamma = 0.1$ for a jet of water ($\mathcal{W}e = 20.03, \mathcal{R}b = 2.189, \mathcal{O}h = 0.003051, \kappa = 0.7048, \delta = 0.00199$).

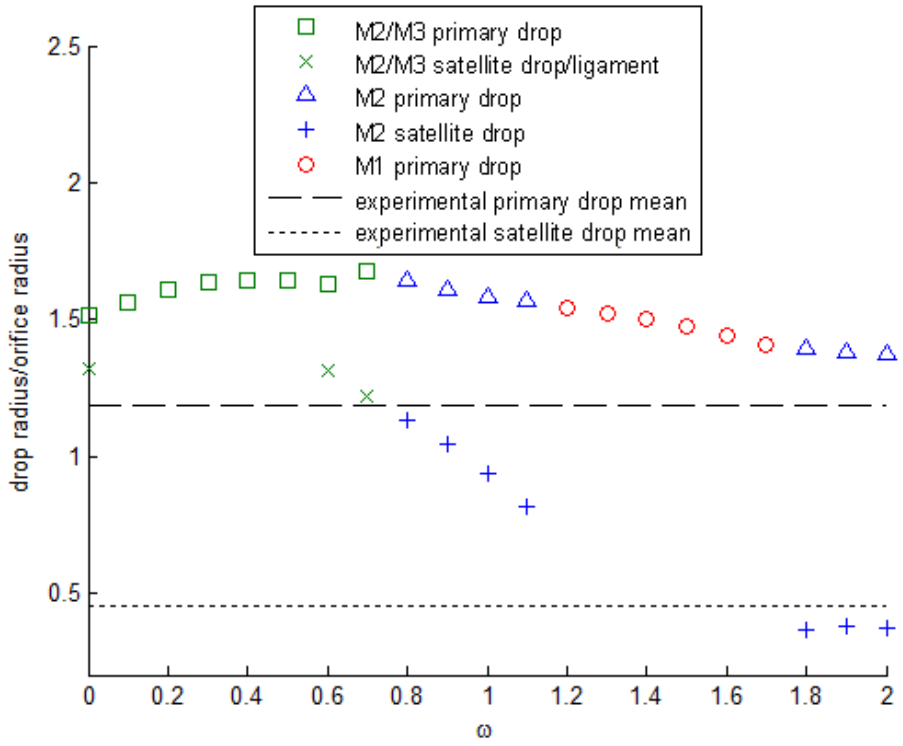

Figure 7.7: Graph showing how the mode of break-up changes with a high amplitude disturbance of $\gamma = 0.1$ for a jet of 40% glycerol ($\mathcal{W}e = 51.86, \mathcal{R}b = 0.522, \mathcal{O}h = 0.01253, \kappa = 0.6972, \delta = 0.0399$).

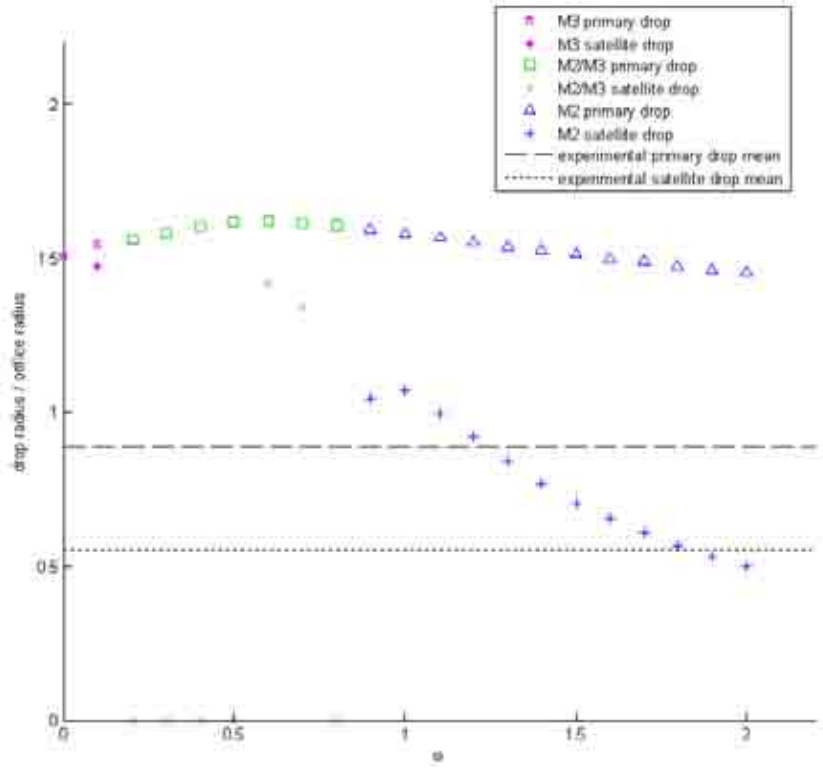

Figure 7.8: Graph showing how the mode of break-up changes with a high amplitude disturbance of $\gamma = 0.1$ for a jet of 80% glycerol ($\mathcal{W}e = 28.78, \mathcal{R}b = 0.336, \mathcal{O}h = 0.1785, \kappa = 0.6022, \delta = 0.058$).

7.6 Modifications to the rig: Vibrating nozzle

The aim of this Chapter is to demonstrate whether the work performed by Gurney et al. (2010) will enable us to control the jets with a greater accuracy than in Partridge (2006). To do this it is necessary to be able to control both the amplitude and frequency of the secondary disturbance. In order to apply such a disturbance and force mechanical vibrations at the orifice, modifications were made to the pilot scale rig, detailed in Chapter 3, to enable a vibrating nozzle to be attached to the can, shown in Figure 7.9, so that both the frequency and the amplitude of the vibration can be controlled. This is important since mechanical vibrations can produce oscillations with

Figure 7.9: Photograph of the vibrating nozzle

a greater amplitude than insonification, and will hopefully be able to control break-up in more viscous jets.

An electrical signal (AC sine wave) is generated using a laptop sound card, using software designed by Andrew Tanner in the combined workshop in the School of Biosciences at the University of Birmingham. This is amplified by a power amplifier and causes the moving magnet coil (speaker driver) at the top of the vibrating nozzle unit to vibrate at the frequency of the applied electrical signal. At the base of the unit is a bar magnet which vibrates with the unit. Below this is a linear output Hall effect sensor attached to a X10 amplifier. This produces an analogue output proportional to magnetic field strength. The device has been calibrated to enable feedback, so that the amplitude of vibration can be determined by the output voltage.

The output voltage is fed back through the National Instruments analogue to digital convertor (ADC) which is connected to the computer and the measured output signal of the speaker is compared to the input signal power to ensure that the amplitude of vibration is correct.

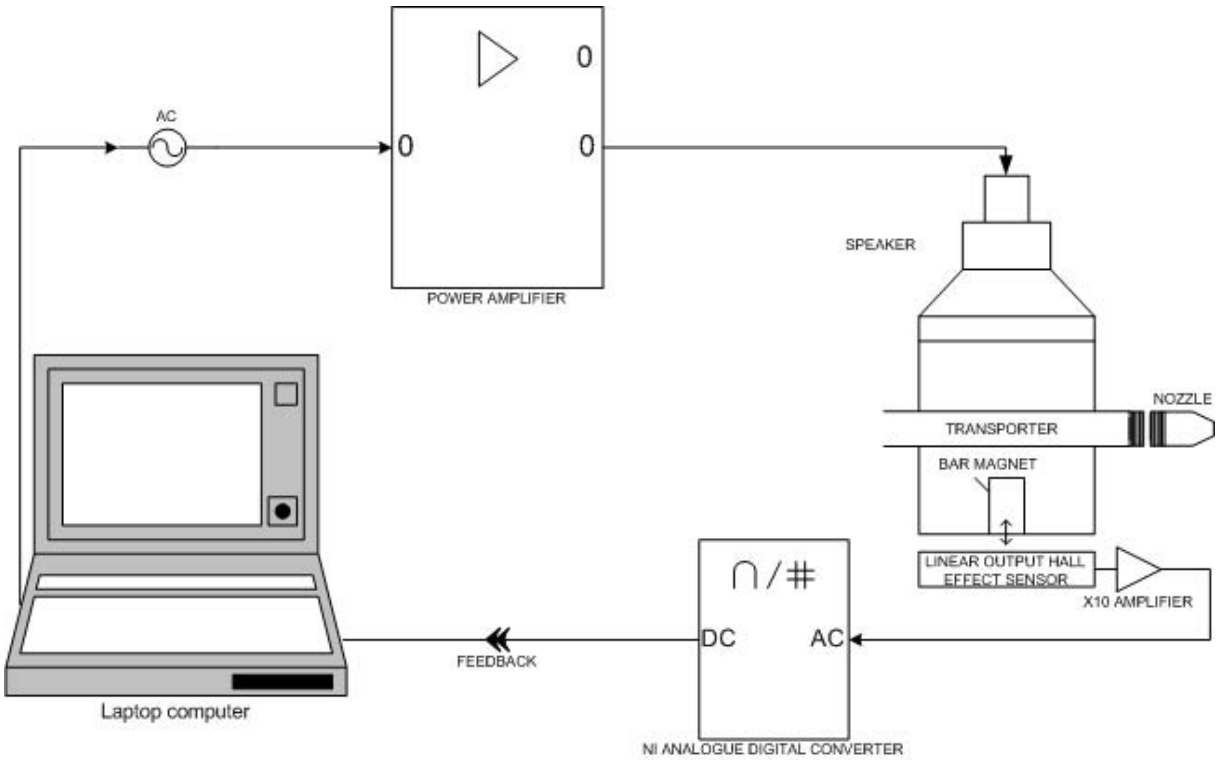

Figure 7.10: Sketch of the vibrating nozzle set-up.

The vibrating nozzle unit is shown in detail in Figure 7.10. At the top of the unit is the speaker driver, which is made from a permanent magnet which interacts with a moving coil of wire on a paper former. When an electrical signal is applied, a magnetic field is induced by the electric current in the coil, and this becomes an electromagnet. The permanent magnet is attracted or repelled, when current flows one way or another, causing vibration. The paper helps amplify the signal. Below the speaker driver is the transporter tube, which has a screw thread at the end to enable different sized nozzles to be used. The liquid flows from the drum through the transporter tube to the nozzle before jetting. The transporter tube is encased in nylon, which has holes drilled in it and the nozzles are made from acrylonitrile butadiene styrene (ABS), as opposed to brass to make the unit as light and easy to vibrate as possible.

The amplitude and frequency are set using the software designed by Andrew Tanner. A

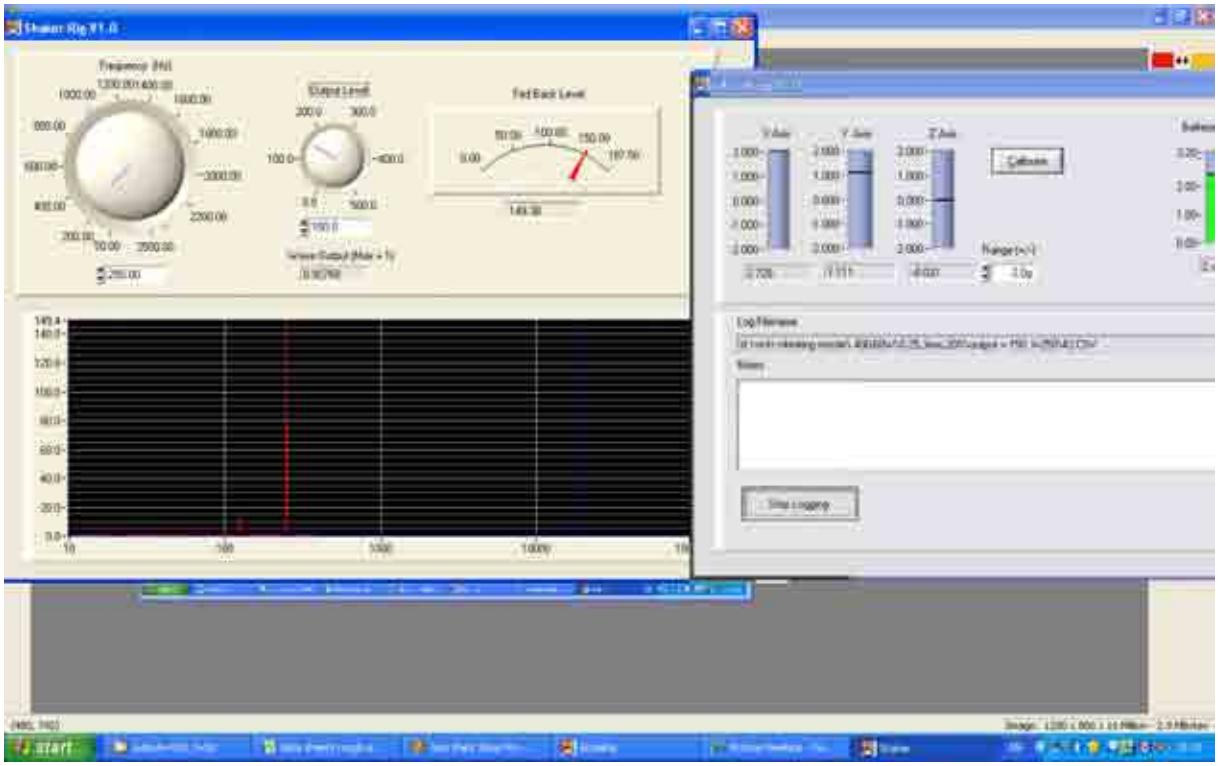

Figure 7.11: A screenshot showing the software used to set the amplitude and vibration of the nozzle and to start logging the motion detected by the accelerometer.

screenshot of the software is shown in Figure 7.11. As can be seen from the Figure, the frequency and amplitude are set using dials. The output represents the amplitude and setting the output to 500 is equivalent to setting the amplitude to 0.5 mm. The information fed back from the Hall effect sensor about the output is shown to the right of this figure. The graph at the bottom of the figure also shows information gathered from the feedback. The x-axis represents the amplitude of the vibration (in terms of output) and the y-axis represent the frequency (Hz). If we overdrive the nozzle this graph shows harmonics. To avoid overdriving the nozzle the 'Wave Output' Figure, shown on the program should be comfortably below unity.

As can be seen in Figure 7.12, attached to the side of the can is an accelerometer. This interacts with the wireless interface board that is attached to the computer and allows for measurement in X, Y and Z directions. The X direction represents motion in the direction of the centrifugal force, the Y direction motion in the direction of gravity and the Z direction indicates smoothness of rotation. The program to the right of the screenshot in Figure 7.11 logs the motion detected by the accelerometer. It is necessary to set the range of g-force which the

accelerometer and nozzle experience at different rotation rates before using the accelerometer at that rotation rate.

7.6.1 Determining the frequency and amplitude of dimensional units

In Section 7.5, jet break-up was caused by applying the following orifice boundary condition

$$u(0,t) = 1 + \delta \sin(\kappa t/\epsilon) + \gamma \sin(\omega t/\epsilon), \tag{7.2}$$

where δ and κ are the amplitude and frequency of the most unstable wave and γ and ω are the amplitude and frequency of the secondary disturbance. This is a perturbation to the velocity of the jet, but a vibrating orifice will cause perturbations to the jet by vibrating in the plane of gravity. This means it is necessary to determine the values of γ and ω physically.

If the problem is considered in terms of the full equations in three dimensions, gravity is perturbed by a small parameter, $g = \bar{g} + G\sin(\omega t)$, such that $G/g << 1$. Therefore, a perturbation expansion in terms of G/g gives, to leading order, the unperturbed long wavelength equations which have a steady solution given by the solution to the three-dimensional steady ODEs (2.31).

To the next order in G/g, a linearised system of equations describing a perturbation of frequency ω are obtained. This yields the viscous dispersion relation (2.23) for a given frequency ω. As long as $G/g << 1$, these linear spatial instability results remain valid. Non-linear theory can be used to determine the behaviour as G/g increases from 0^+, taking a long wavelength approximation of the linear results to a long wavelength dispersion relation, namely

$$\lambda = -iu_0 k - \frac{3k^2}{2\mathcal{R}e} \pm \frac{k}{2}\sqrt{\frac{9k^2}{\mathcal{R}e^2} - \frac{2R_0}{\mathcal{W}e}\left(k^2 - \frac{1}{R_0^2}\right)}. \tag{7.3}$$

This was derived in Decent et al. (2009) by taking the long wavelength limit $k \to 0$ of the full eigenvalue relationship for $\mathcal{O}h = O(1)$. Therefore G/g is small. Alternatively the same results as above are found if we were to apply a small δ expansion of the non-linear equations. Hence, δ would be the amplitude of the velocity perturbation in the above boundary condition

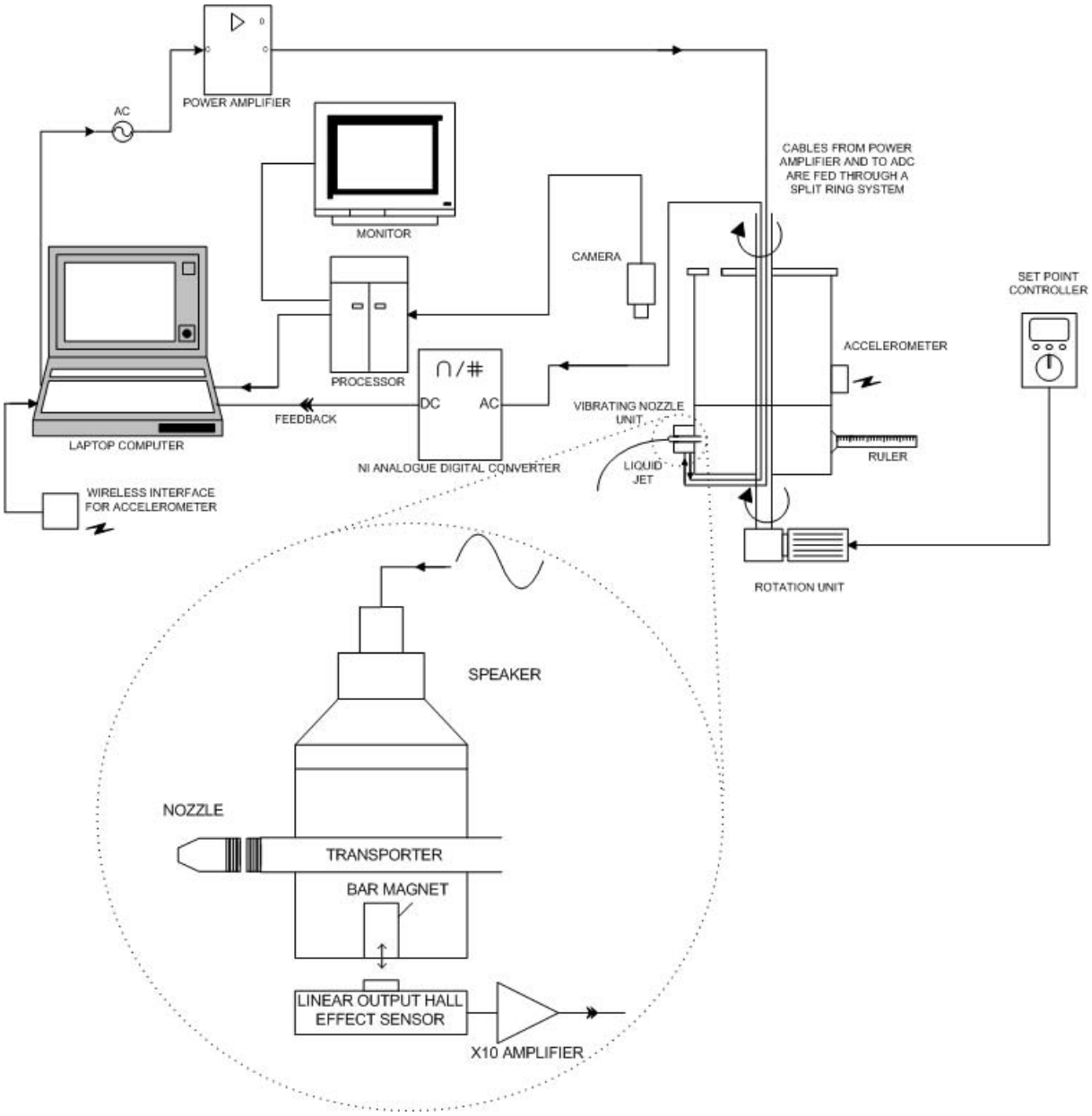

Figure 7.12: Schematic showing vibrating nozzle set-up.

(7.2). Therefore, a perturbation in the plane of gravity and a perturbation of the velocity are equivalent. Therefore, we only need to dimensionalise γ and ω.

In Section 7.5 M1 break-up was found to occur for $\gamma = O(0.1)$ and $\omega = O(1)$. Using the dimensionless parameters introduced in Chapter 2.3.2,

$$t = \frac{U\bar{t}}{s_0} \quad \text{and} \quad \epsilon = \frac{a}{s_0},$$

where t and $\bar{t}$ are the dimensionless and dimensional time respectively, U is the jet exit velocity, a is the orifice radius and s_0 is the radius of the can. Examining (7.2),

$$\frac{\omega}{\epsilon}t = \frac{\omega U}{a}\bar{t}$$

and so the dimensional frequency would be given by

$$\bar{f} = \frac{\omega U}{a}.$$

As $a = O(10^{-3}$ m), $U = O(1$ ms$^{-1})$ and $\omega = O(1)$, $\bar{f} = O(10^3$ Hz).

As the perturbation in the plane of gravity and the perturbation in the velocity can be considered equivalent, the amplitude of the perturbation is given by

$$\bar{\gamma} = \gamma a,$$

and so $\bar{\gamma} = O(0.1$ mm) for $\gamma = O(0.1)$ and $a = O(1$ mm).

Therefore in order to control liquid jet break-up 0.1 mm amplitude disturbances of the order of kHz should be applied to the jet.

7.7 Preliminary Results

Preliminary experiments were performed on a jet of water rotating at just 30 rpm ($\Omega = 3.14$ rad s^{-1}) through a nozzle of $a = 0.0015$ m at an aspect ratio (H/D) of a $1/2$.

The jet was examined by fixing the amplitude and performing experiments, in the same

manner as described in Chapter 3.2.2, at a range of different frequencies to further explore and verify the results of Gurney et al. (2010).

Unfortunately, there were limitations on the frequencies that can be obtained at high amplitude experimentally. As can seen in Figure 7.13, as the amplitude is increased the frequencies obtainable reduce dramatically. Dimensionally, at $\gamma = 0.3$, the nozzle is actually vibrating approximately 0.45 mm.

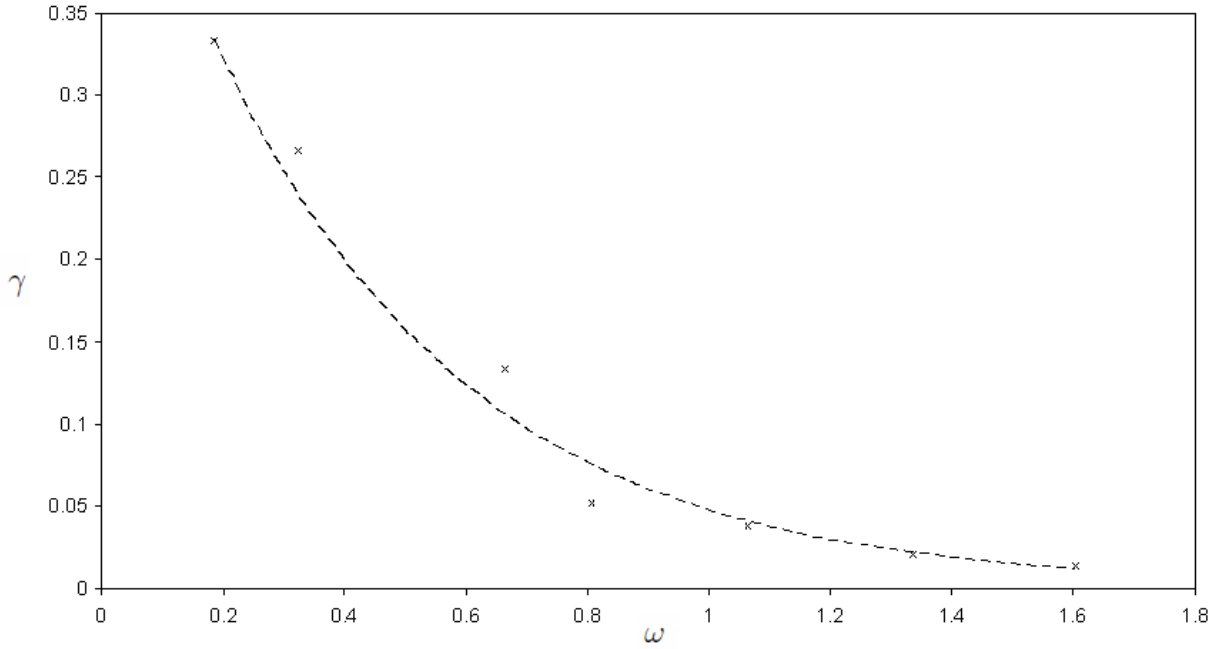

Figure 7.13: Figure showing maximum range of ω and γ.

The jet was first examined by fixing the amplitude, γ, and altering the frequency, ω of the secondary disturbance as can be seen in Figure 7.14. At a low amplitude secondary disturbance, $\gamma = 0.002$ (Figure 7.14(a)), it can be seen that in terms of primary and satellite droplets produced there is little effect. However, at high amplitude disturbances, $\gamma = 0.1$ (Figure 7.14(b)) satellite droplets disappear at high frequencies. This can also be seen in Figure 7.15, where the drop size distribution can be seen to be becoming more unimodal as ω increases.

Figure 7.16 demonstrates that when the amplitude of the secondary disturbance is low, $\gamma = 0.002$, the break-up length of the jet remains relatively consistent, regardless of the frequency applied. However, at high amplitude break-up $\gamma = 0.1$, as ω increases, it can be seen than the

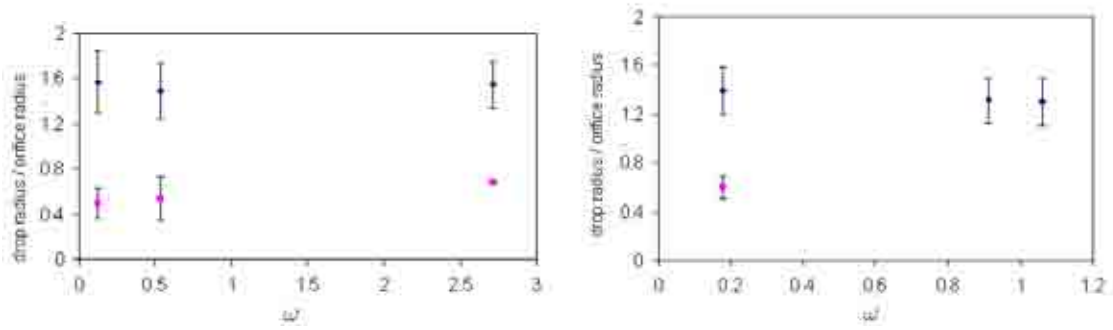

(a) $\gamma = 0.002$ (b) $\gamma = 0.1$

Figure 7.14: Primary and satellite drop sizes obtained for varying ω for a jet of water at (a) $\gamma = 0.00199$, $(4.61 < \mathcal{W}e < 7.62, 1.05 < \mathcal{R}b < 1.34, 703.3 < \mathcal{R}e < 900.2, \mathcal{O}h = 0.003051)$ and (b) $\gamma = 0.1$ $(2.30 < \mathcal{W}e < 3.81, 0.74 < \mathcal{R}b < 0.95, 495.1 < \mathcal{R}e < 637.7, \mathcal{O}h = 0.003051)$.

break-up length decreases.

The jet was then examined by fixing the dimensional frequency for a jet of water ($0.126 < \omega < 0.249$), and altering the amplitude of the secondary disturbance as can be seen in Figure 7.17. The effect this has on drop size is demonstrated in Figure 7.17. Figure 7.17(a) shows that as the amplitude of the secondary disturbance is increased satellite drop sizes disappear. This is also illustrated in Figure 7.17(b), where the drop size distributions appear to become more unimodal as γ increases, then plateau and the distribution actually becomes slightly wider for $\gamma = 0.33$.

Similar results were found for higher frequencies; that it is not until the amplitude of the secondary disturbance increases that satellite drop sizes are affected.

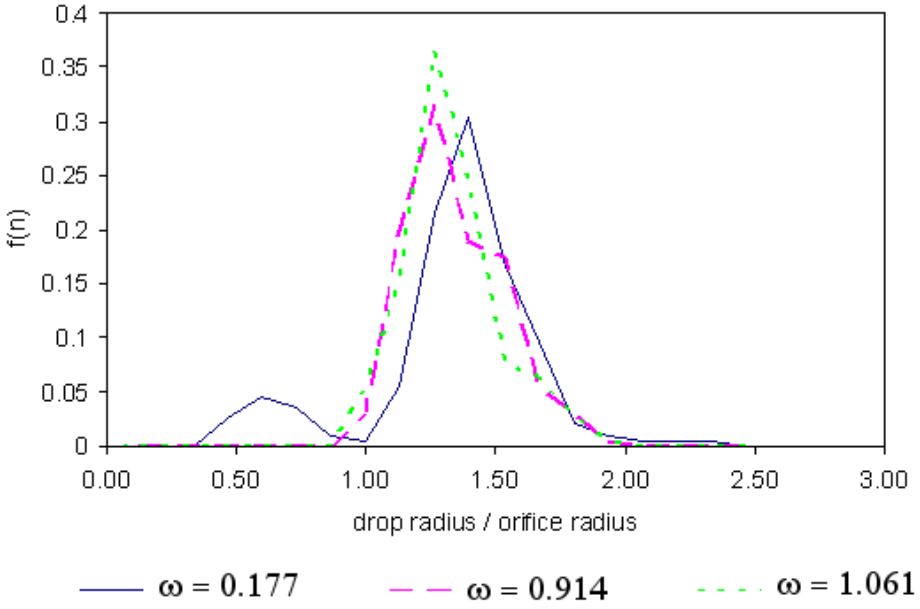

Figure 7.15: Drop size distributions for $\gamma = 0.1$ and increasing ω. ($2.30 < \mathcal{W}e < 3.81, 0.74 < \mathcal{R}b < 0.95, 495.1 < \mathcal{R}e < 637.7, \mathcal{O}h = 0.003051$).

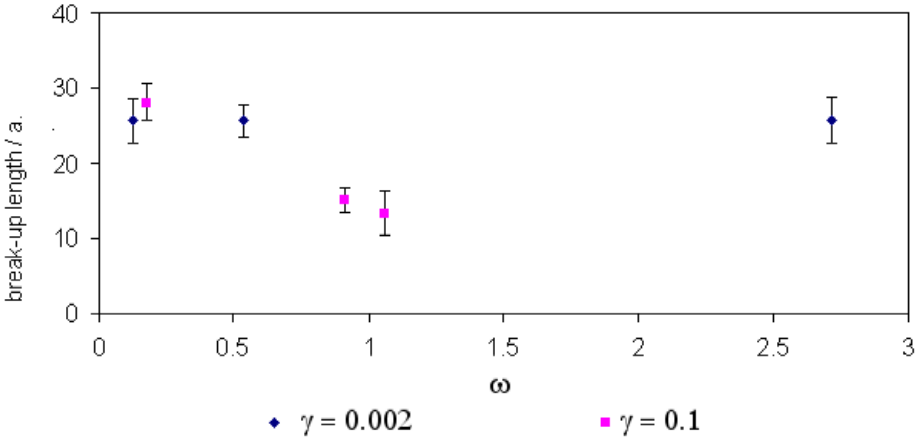

Figure 7.16: Break-up length obtained when varying ω for a jet of water at $\gamma = 0.002$ ($4.61 < \mathcal{W}e < 7.62, 1.05 < \mathcal{R}b < 1.34, 703.3 < \mathcal{R}e < 900.2, \mathcal{O}h = 0.003051$) and $\gamma = 0.1$. ($2.30 < \mathcal{W}e < 3.81, 0.74 < \mathcal{R}b < 0.95, 495.1 < \mathcal{R}e < 637.7, \mathcal{O}h = 0.003051$).

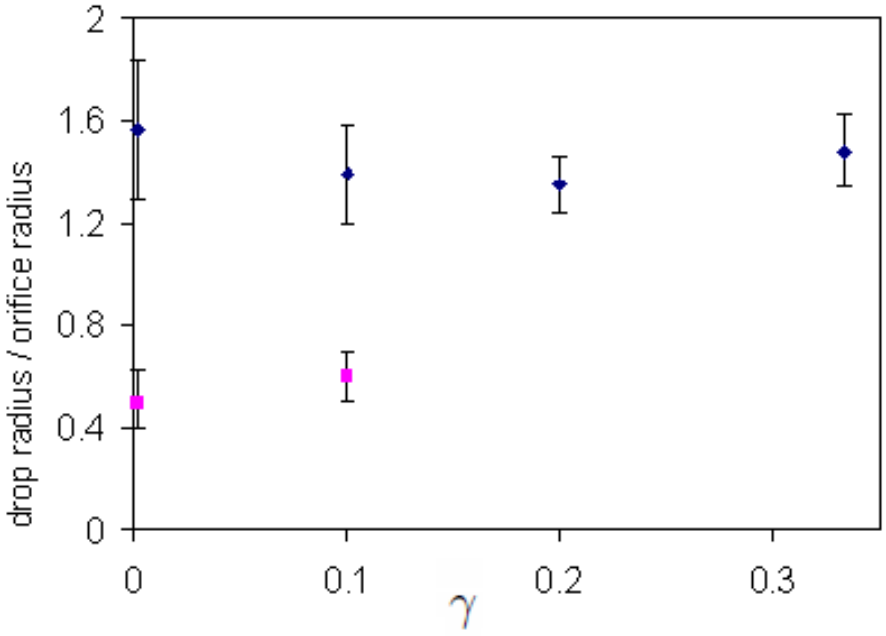

(a)

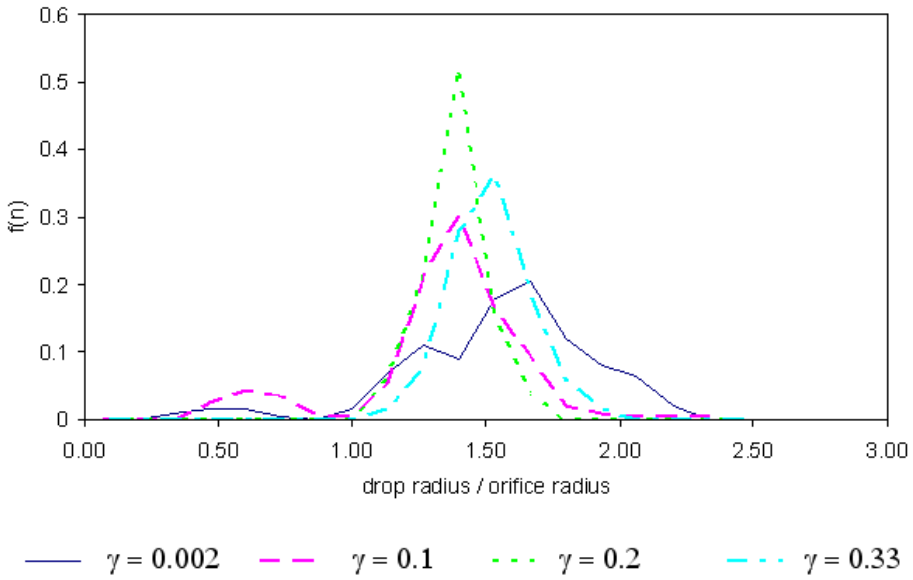

(b)

Figure 7.17: (a) Primary and satellite drop sizes and (b) drop size distributions obtained for varying γ for a jet of water a fixed dimensional frequency ($0.126 < \omega < 0.249$) Here $3.45 < \mathcal{W}e < 7.62, 0.91 < \mathcal{R}b < 1.34, 607.7 < \mathcal{R}e < 900.2, \mathcal{O}h = 0.003051$.

7.8 Results - changing modes

Following the preliminary results, which focused on a jet of water, rotating relatively slowly, a more thorough investigation was performed on aqueous glycerol (0-80% glycerol) solutions of varying viscosity (1 - 65.4 mPa s), at a rotation rate of 120 rpm (12.56 rad s^{-1}), through a nozzle of radius 0.0015 m at an aspect ratio (H/D) of 0.25 to see if it possible to control the mode of break-up. A summary of the full experimental conditions and properties of the fluids examined are given in Table 7.1.

A full range of forced disturbances are applied, varying both the amplitude and frequency of the secondary disturbance. The mode achieved is recorded in order to see the extent to which it is possible to alter the mode of break-up. Selected points are then examined in more detail and the numerical model of Gurney et al. (2010) is applied to enable a comparison to be made. The overall aim is to see if it is possible to use the numerical simulations to accurately predict conditions, using forced disturbances, where satellite droplets are eradicated.

7.8.1 Water

The first fluid to be examined in detail is water. If the experimental parameters in Table 7.1 are applied with no secondary disturbance the normal mode of break-up is M2. Figure 7.18 shows a plot of the mode obtained from the experiments on axes of γ versus ω for water. As can be seen, it is possible to change the mode of break-up by applying a secondary disturbance. As predicted by Gurney et al. (2010), if the amplitude is low, very little happens and the mode of

Table 7.1: Experimental conditions and properties of fluids examined.

	Liquid		
	Water	40% Glycerol	80% Glycerol
Density (ρ) [kg m^{-3}]	997.5	1106.6	1211.7
Viscosity (μ) [Pa s]	0.001	0.00373	0.0654
σ [N m^{-1}]	0.0718	0.0688	0.0645
U [ms^{-1}]	0.56 - 1.05	0.39 - 0.83	0.145 - 0.211
$\mathcal{W}e$	6.50 - 23.10	3.69 - 15.61	1.59 - 2.25
$\mathcal{R}b$	0.312 - 0.588	0.222 - 0.446	0.081 - 0.118
$\mathcal{O}h$	0.0030501	0.0110	0.17845
$\mathcal{R}e$	835.94 - 1575.42	174.04 - 368.16	4.31 - 6.26

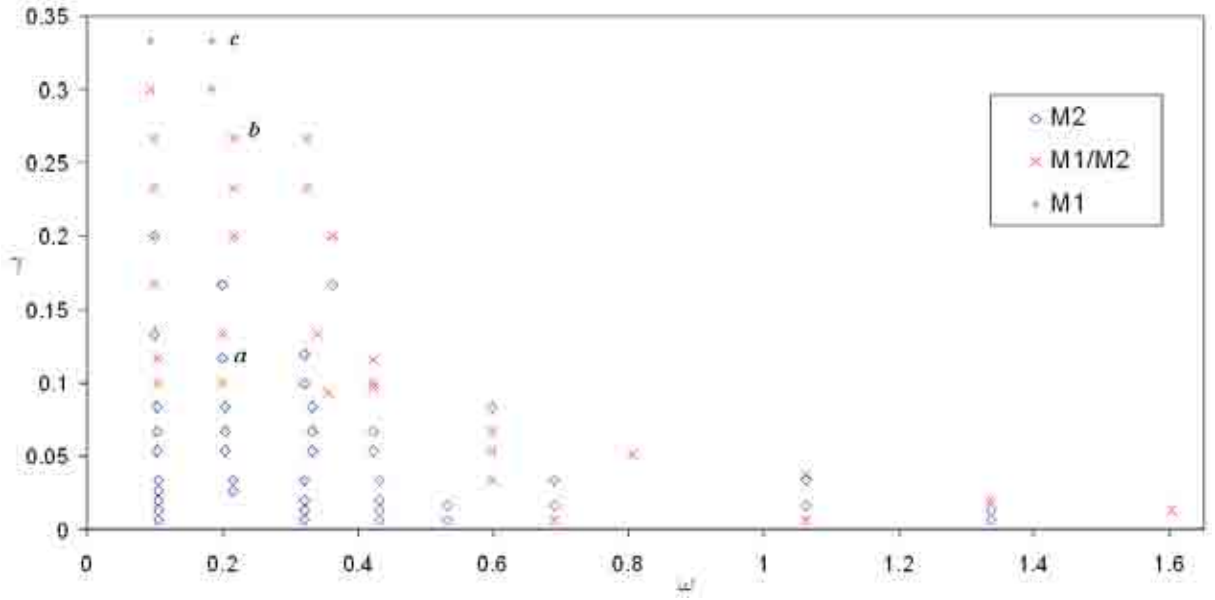

Figure 7.18: Break-up modes obtained when varying ω and γ for a jet of water ($6.50 < \mathcal{W}e < 23.10, 0.312 < \mathcal{R}b < 0.588, 835.94 < \mathcal{R}e < 1575.42, \mathcal{O}h = 0.003051$).

break-up is observed to primarily be M2. However as the amplitude increases, it can be seen that it is possible to obtain M1 on the pilot scale rig. This has never previously been seen at this scale.

To illustrate what is actually happening to the jet experimentally, a few specific points on the graph will be examined in more detail, to show what happens as the amplitude of the forced disturbance is increased. The points to be examined in further detail are marked in Figure 7.18.

At point (a), shown in Figure 7.19(a), M2 behaviour is demonstrated. This is typical of this liquid system operating for these experimental parameters. Satellite droplets are formed singly between the primary droplets and the drop size distribution attributed to this result, The drop size distribution in Figure 7.19(b) is shown to be typically M2 with both primary and satellite droplets occurring.

Figure 7.20(a) demonstrates typical break-up at point (b) in Figure 7.18. This type of break-up has been defined experimentally as M1/M2. The break-up is quite similar to M1, but with occasional satellite droplets appearing. However, these do not consistently appear as with M2 break-up. The drop size distributions associated with this point are as shown in Figure 7.20(b), and it can be seen the break-up is mostly unimodal but with quite a large spread. Close to the

orifice, as the jet emanates from the drum, the jet assumes a sinuous trajectory. This effect is attributed to the effect of the vibrating nozzle, as nothing like this has ever been seen for unforced jets.

Finally, M1 break-up is shown in Figure 7.21(a), which is a typical image from break-up at point (c). Satellite droplets have been eradicated and a unimodal frequency distribution has been achieved, as seen in Figure 7.21(b).

The numerical model developed in Gurney et al. (2010) was then applied to these experimental conditions as a means of comparison. The dimensional frequency was fixed ($0.184 < \omega < 0.217$), in order to move through a range of amplitudes, highlighted in Figure 7.22, with a view to comparing experimental results with the numerical model. For the values highlighted in the Figure, theoretical modes and drop sizes have been calculated. These are then compared to experimental modes observed and drop sizes measured to give an indication of the accuracy of the values predicted by the theory.

As can be seen in Figure 7.23, the theoretical drop sizes predicted are generally too large. However the theoretical modes predicted match those obtained experimentally quite well. The main cross over area is in the area identified as M1/M2 experimentally. This mode is not possible to predict theoretically. This result suggests that the theoretical model could be used quite successfully to identify areas of break-up where it is possible to predict M1 break-up.

(a)

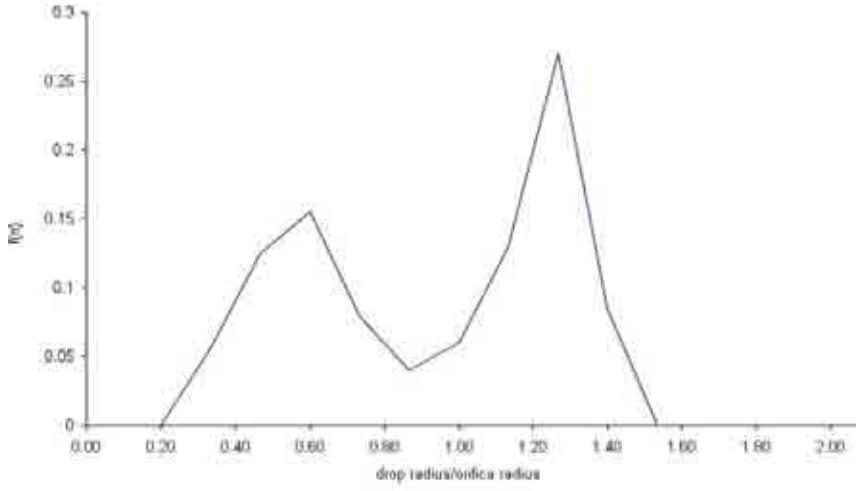

(b)

Figure 7.19: (a) Experimental image and (b) drop size distribution at point (a) on Figure 7.18 demonstrating M2 break-up ($\mathcal{W}e = 11.79, \mathcal{R}b = 0.42, \mathcal{R}e = 1125.30, \mathcal{O}h = 0.003051$).

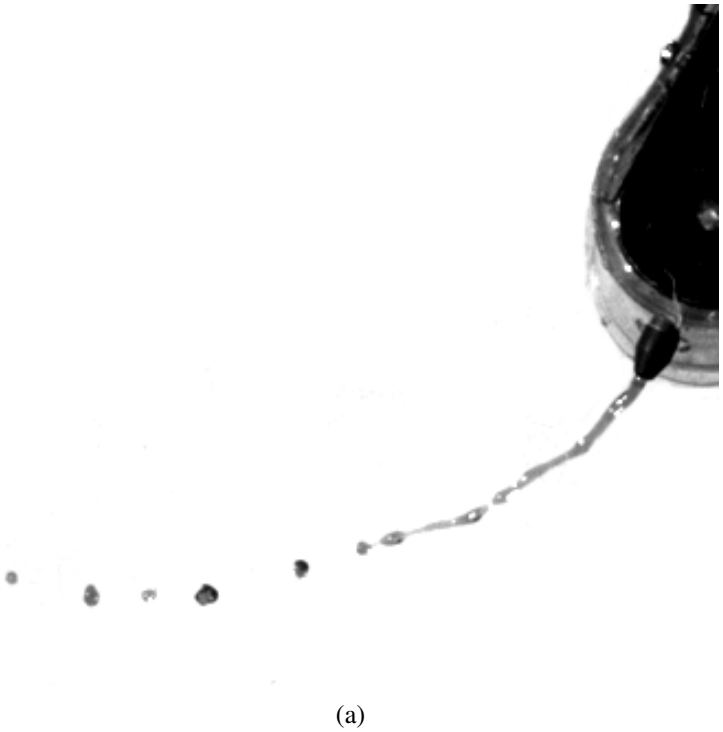

(a)

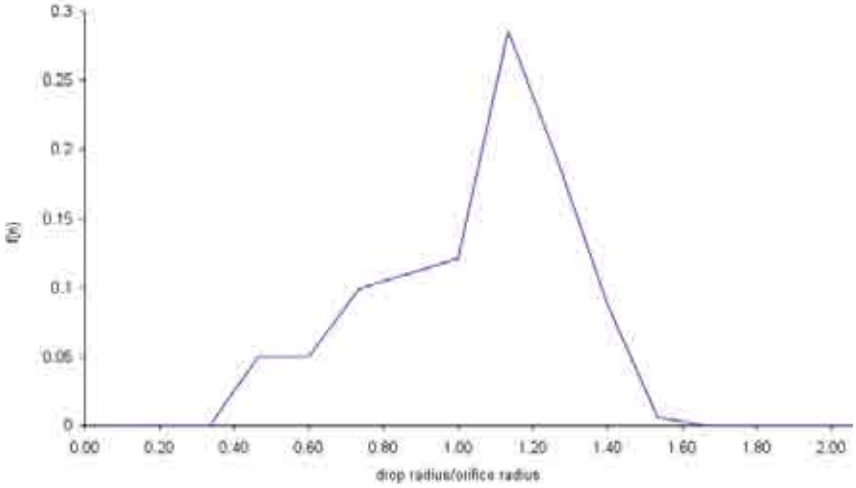

(b)

Figure 7.20: (a) Experimental image and (b) drop size distribution at point (b) on Figure 7.18 demonstrating M1/M2 break-up ($\mathcal{W}e = 9.98, \mathcal{R}b = 0.39, \mathcal{R}e = 1035.28, \mathcal{O}h = 0.003051$).

(a)

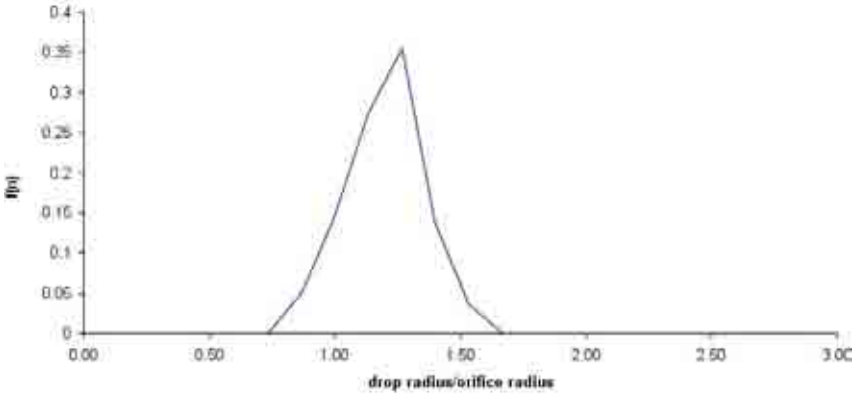

(b)

Figure 7.21: (a) Experimental image and (b) drop size distribution at point (c) on Figure 7.18 demonstrating M1 break-up ($\mathcal{W}e = 13.85, \mathcal{R}b = 0.46, \mathcal{R}e = 1219.69, \mathcal{O}h = 0.003051$).

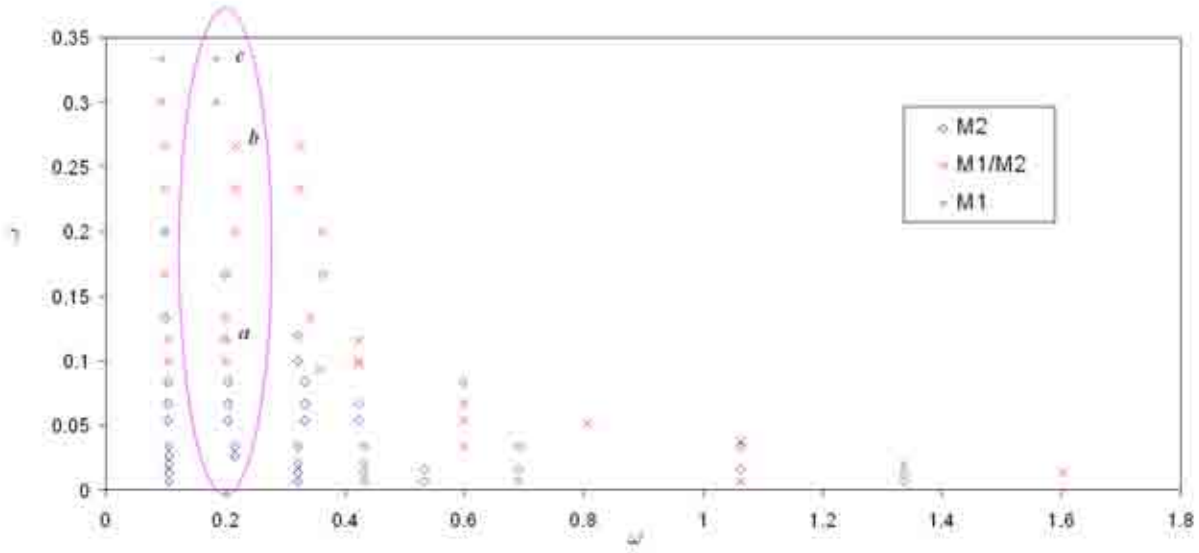

Figure 7.22: Break-up modes obtained when varying ω and γ for a jet of water ($6.50 < \mathcal{W}e < 23.10, 0.312 < \mathcal{R}b < 0.588, 835.94 < \mathcal{R}e < 1575.42, \mathcal{O}h = 0.003051$). The circled points are to be compared to the numerical model.

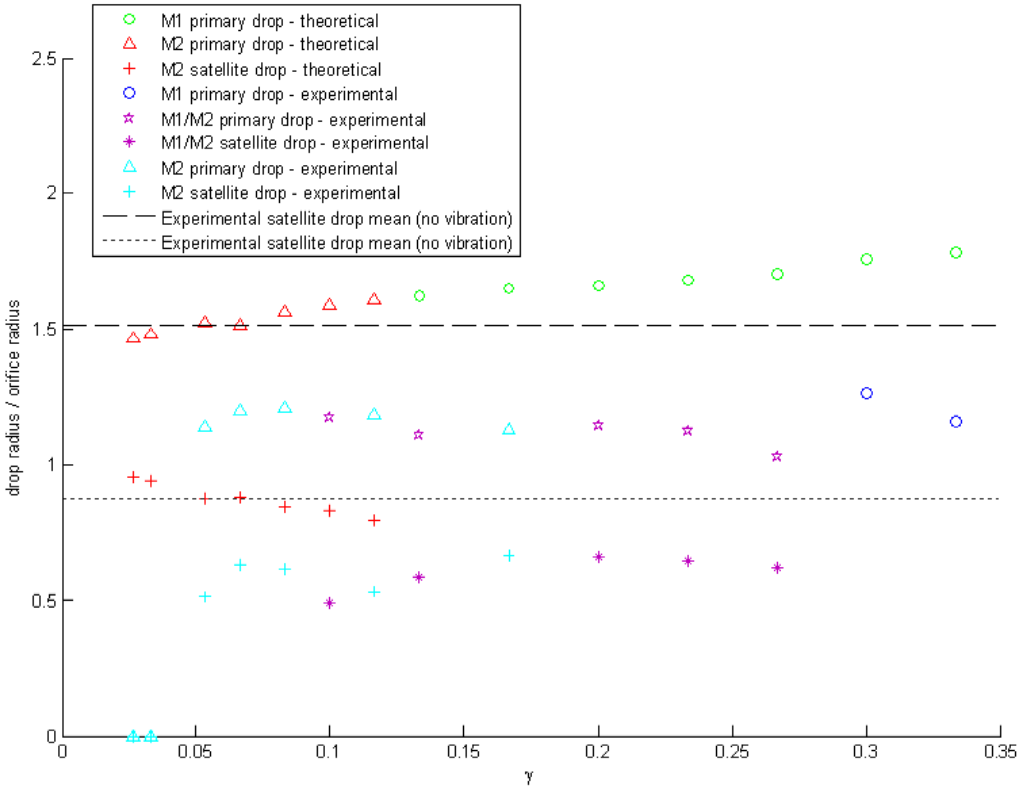

Figure 7.23: Dimensionless drop sizes and break-up modes for experimental and theoretical work with varying γ for a fixed dimensional frequency ($0.184 < \omega < 0.217$). Here, $9.977 < \mathcal{W}e < 13.847, 0.387 < \mathcal{R}b < 0.455, 1035 < \mathcal{R}e < 1220, \mathcal{O}h = 0.003051, \delta = 0.0256, \kappa = 0.702$.

7.8.2 Viscous liquids - 40% Glycerol

It can be seen in Figure 7.24, that it is also possible to change the mode of break-up of a more viscous fluid. Similarly to water, the most dramatic of these changes tends to occur at high amplitude disturbances. The natural mode of break-up for this fluid at these experimental conditions is again M2.

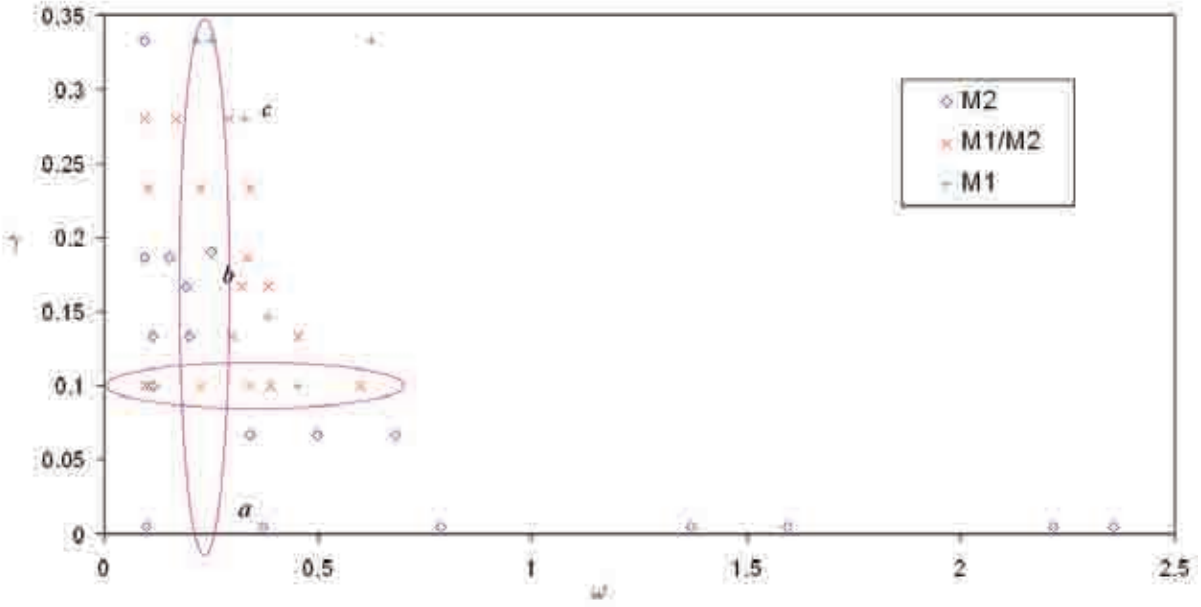

Figure 7.24: Break-up modes obtained when varying ω and γ for a jet of 40% Glycerol ($3.69 < \mathcal{W}e < 15.61, 0.222 < \mathcal{R}b < 0.446, 174.04 < \mathcal{R}e < 368.16, \mathcal{O}h = 0.0110$). The circled points are to be compared to the numerical model.

The specific points marked in Figure 7.24 will be examined in more detail. Typical break-up at point (a) is illustrated in 7.25(a), where M2 behaviour can be observed, although when breaking up, the droplets do appear to cluster together. Satellites are again formed singly in between the main drops, although there do appear to be fewer, as illustrated in Figure 7.25(b).

Figure 7.26(a) is an experimental image of M1/M2 break-up, found at point (b) on Figure 7.24. Figure 7.26(b) demonstrates that few satellite droplets are found at this point, but there is still quite a spread of drop sizes achieved.

An experimental image at point (c) is demonstrated in Figure 7.27(a). It can once again be seen that the break-up mode of the jet is M1 and only primary droplets are achieved. This is

supported by a drop size distribution taken at the same point, shown in Figure 7.27(b), where a narrow distribution of drop sizes can be seen.

It is possible, in this case, to compare numerical simulations with experimental results, not only by fixing the dimensional frequency and moving through a range of amplitudes, but also by fixing the amplitude and moving through a range of frequencies as highlighted in Figure 7.24. Again theoretical modes and drop sizes have been calculated to compare to experimental results.

In Figure 7.28 the dimensional frequency is fixed $(0.153 < \omega < 0.227)$ and theoretical modes and drop sizes are calculated for the range of amplitudes highlighted in Figure 7.24.

Similarly to water, while the drop sizes predicted by the theory are larger than experimental values, the modes predicted match quite well. It is only experimentally in the cross over area of M1/M2, where there are discrepancies.

A similar result can be seen in Figure 7.29, when fixing the amplitude ($\gamma = 0.1$) and moving through the range of frequencies illustrated in Figure 7.24 . Again, it can be seen that main area of ambiguity is where M1/M2 is predicted experimentally.

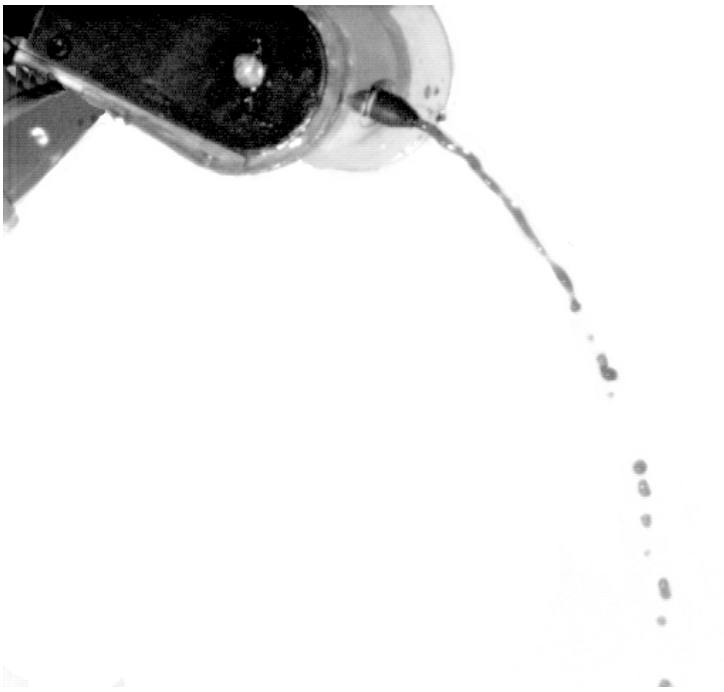

(a)

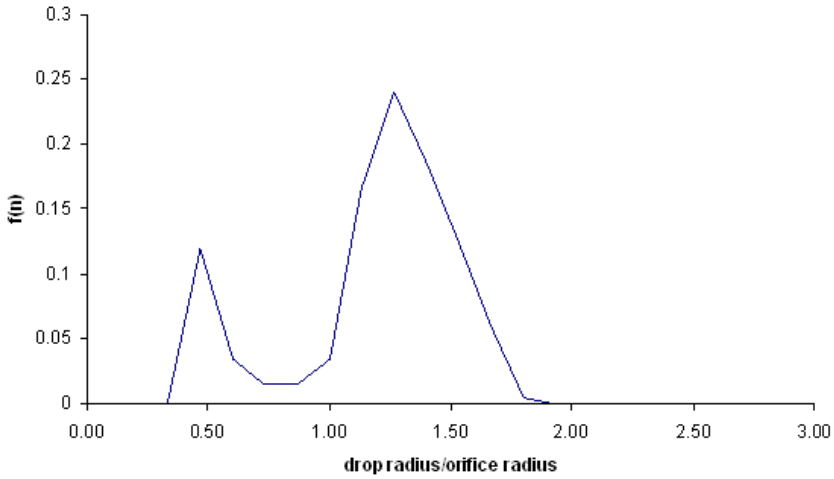

(b)

Figure 7.25: (a) Experimental image and (b) drop size distribution at point (a) on Figure 7.24 demonstrating M2 break-up ($\mathcal{W}e = 13.78, \mathcal{R}b = 0.42, \mathcal{R}e = 334.69, \mathcal{O}h = 0.0110$).

(a)

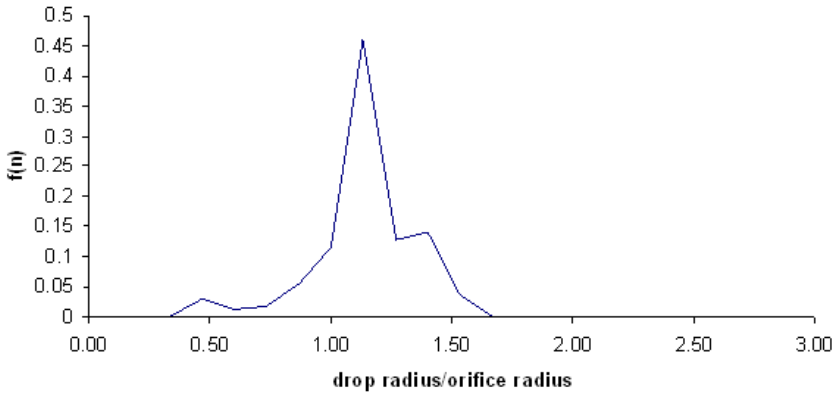

(b)

Figure 7.26: (a) Experimental image and (b) drop size distribution at point (b) on Figure 7.24 demonstrating M1/M2 break-up ($\mathcal{W}e = 11.89, \mathcal{R}b = 0.39, \mathcal{R}e = 312.37, \mathcal{O}h = 0.0110$).

(a)

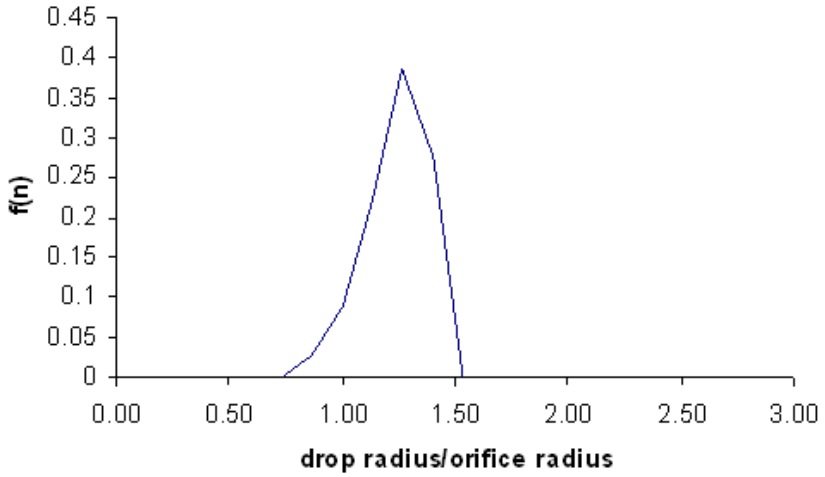

(b)

Figure 7.27: (a) Experimental image and (b) drop size distribution at point (c) on Figure 7.24 demonstrating M1 break-up ($\mathcal{W}e = 9.86, \mathcal{R}b = 0.36, \mathcal{R}e = 284.48, \mathcal{O}h = 0.0110$).

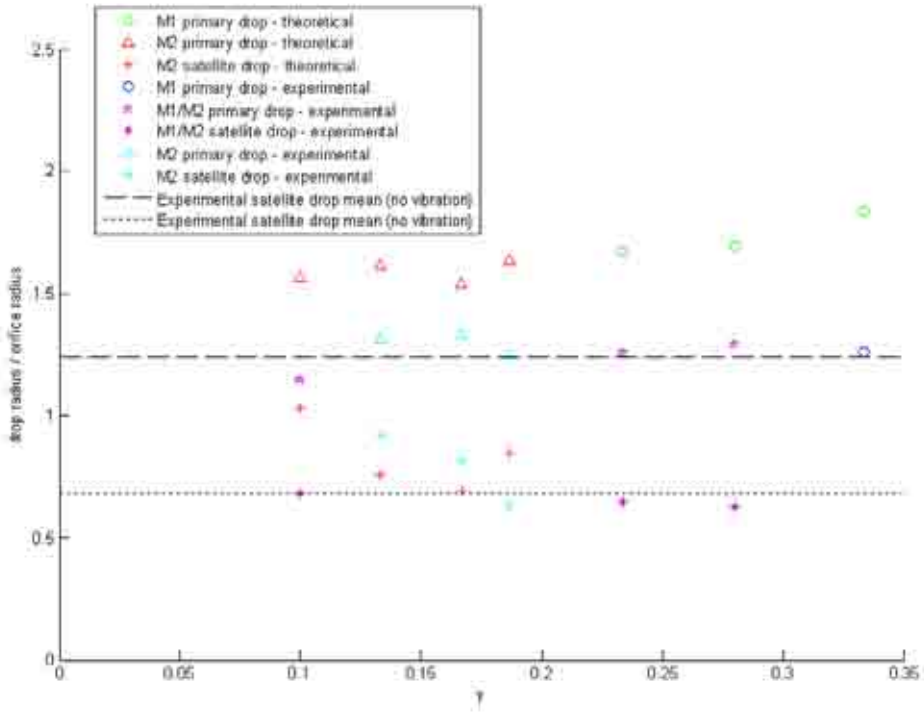

Figure 7.28: Dimensionless drop sizes and break-up modes for experimental and theoretical work with varying γ for fixed dimensional frequency $(0.153 < \omega < 0.227)$. Here, $10.57 < \mathcal{W}e < 16.51, 0.153 < \mathcal{R}b < 0.453, 294.5 < \mathcal{R}e < 334.7, \mathcal{O}h = 0.01104, \delta = 0.0054, \kappa = 0.688$.

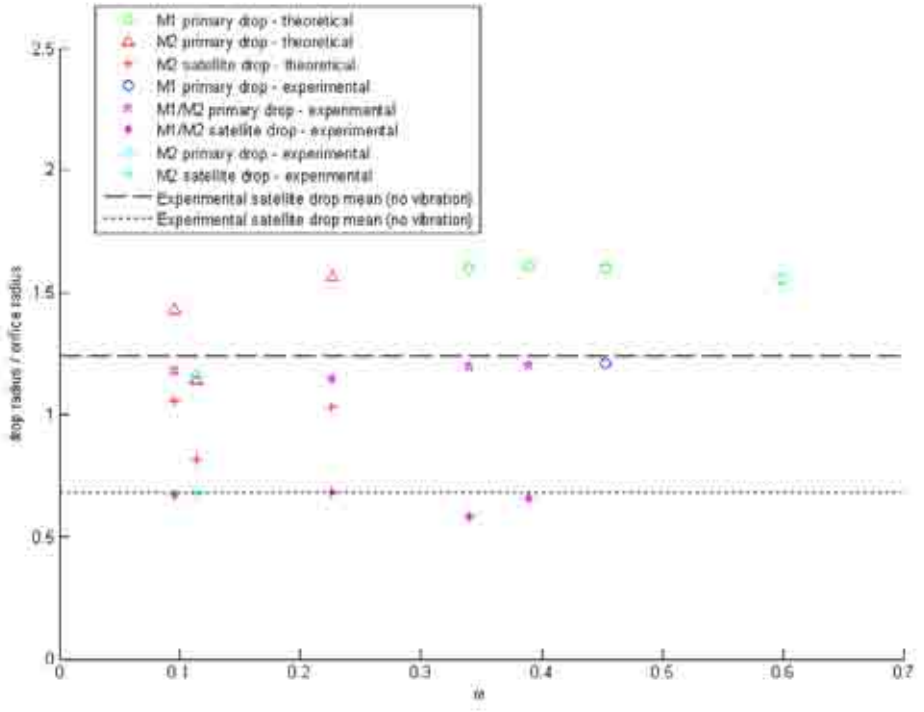

Figure 7.29: Dimensionless drop sizes and break-up modes for experimental and theoretical work with varying ω for fixed $\gamma = 0.1$. Here, $9.49 < \mathcal{W}e < 15.18, 0.35 < \mathcal{R}b < 0.44, 278.91 < \mathcal{R}e < 351.42, \mathcal{O}h = 0.01104, \delta = 0.0054, \kappa = 0.688$.

7.8.3 Very viscous liquids - 80% Glycerol

Finally, an aqueous solution of 80% glycerol is examined. Here the natural mode of break-up when no additional disturbances are applied at the nozzle is that of M3.

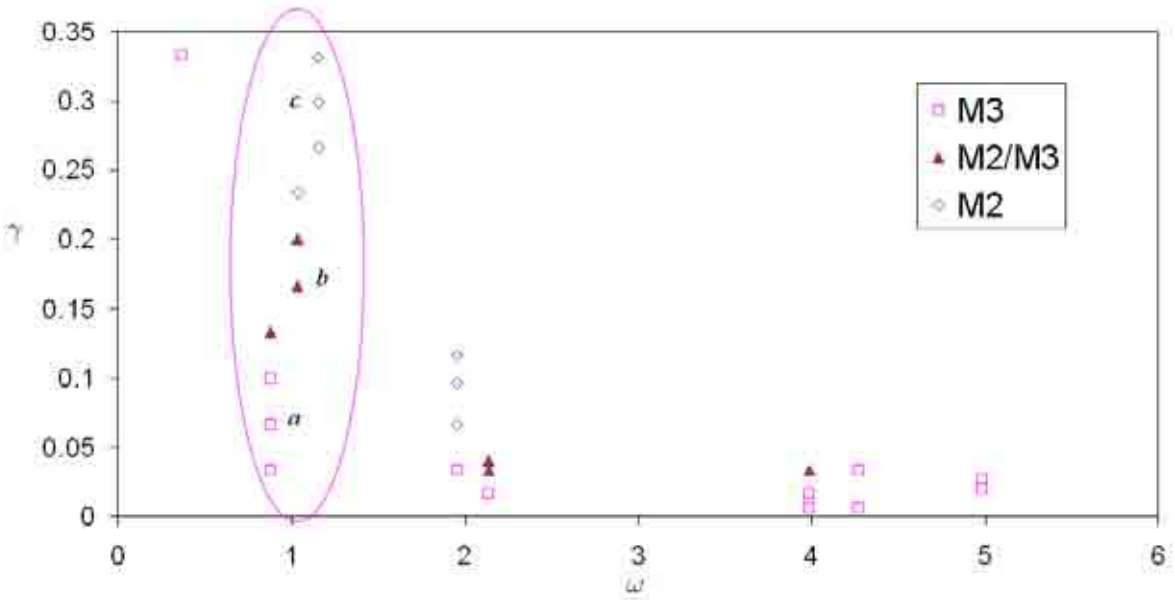

Figure 7.30: Break-up modes obtained when varying ω and γ for a jet of 80% Glycerol ($1.59 < \mathcal{W}e < 2.25, 0.081 < \mathcal{R}b < 0.118, 4.31 < \mathcal{R}e < 6.26, \mathcal{O}h = 0.17845$). The circled points are to be compared to the numerical model.

Figure 7.30 demonstrates that it is possible to change the mode of break-up, even for very viscous liquids, although it should be noted here that M2 has been defined slightly differently, which will be explained more in the following paragraphs.

An experimental image at point (a), shown in Figure 7.31(a), can be seen to be typically M3. Long wavelengths are formed on the surface of the jet, multiple break-up can be observed frequently and satellite droplets are formed by the contraction of long thin ligaments in between the primary droplets. The corresponding drop size distribution can be seen in Figure 7.31(b) and shows a classic bimodal distribution, with roughly equal numbers of primary and satellite drop sizes, that is typical of M3 break-up.

Break-up at point (b) is shown in Figure 7.32(a). Here the break-up has been defined experimentally as M2/M3. This is still long wavelength break-up, but here satellites are sometimes actually formed in their own right, not just from the fragmentation of ligaments. The drop size

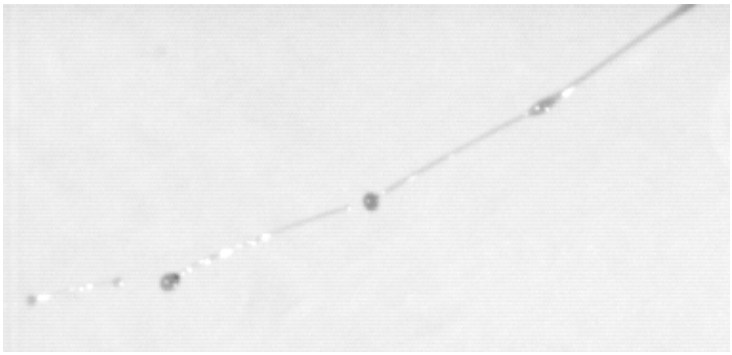

(a)

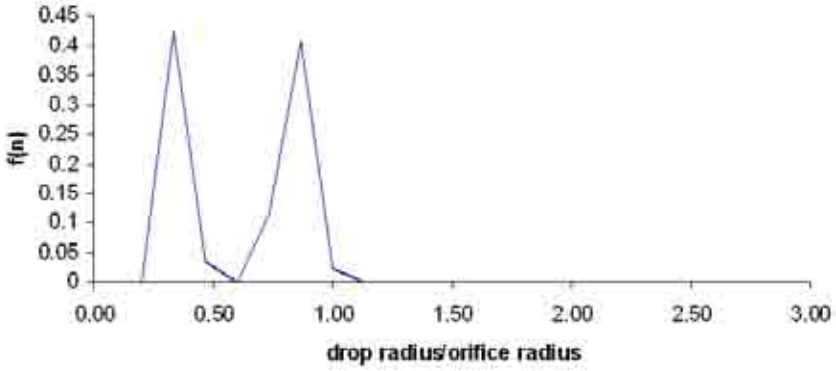

(b)

Figure 7.31: (a) Experimental image and (b) drop size distribution at point (a) on Figure 7.30 demonstrating M3 break-up ($\mathcal{W}e = 1.83, \mathcal{R}b = 0.10, \mathcal{R}e = 5.10, \mathcal{O}h = 0.17845$).

distribution is still bimodal, shown in Figure 7.32(b), but with a reduced number of satellite droplets occurring.

Figure 7.33(a) shown an experimental image at point (a), and it can be seen that the break-up mode has changed again. While this has been defined in this case as M2 break-up, long wavelength disturbances are still visible on the surface of the jet, but ligaments are no longer being formed. The fluid which would normally form ligaments is fragmenting into satellites immediately upon detachment. Multiple break-up is less common, so actual break-up and the formation of primary and satellite droplets is more like M2, hence why it has been defined as such. This Figure also demonstrates how much the break-up length has shortened. It has never previously been possible to capture break-up and the formation of drops simultaneously in one image for a fluid this viscous, at these experimental conditions. The drop size distribution,

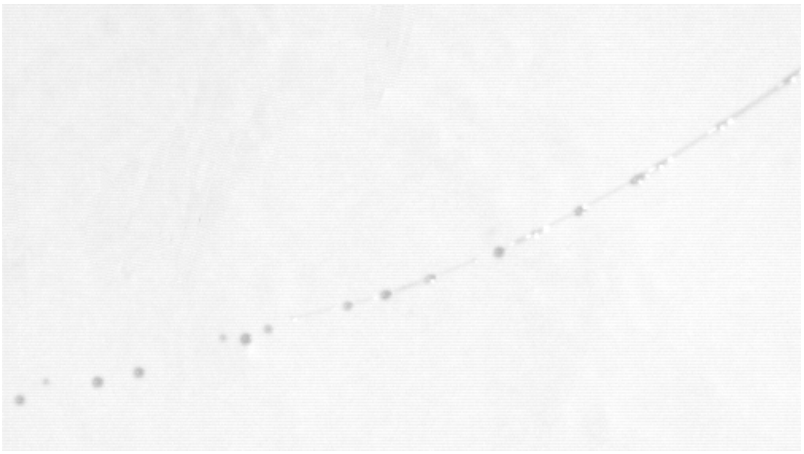

(a)

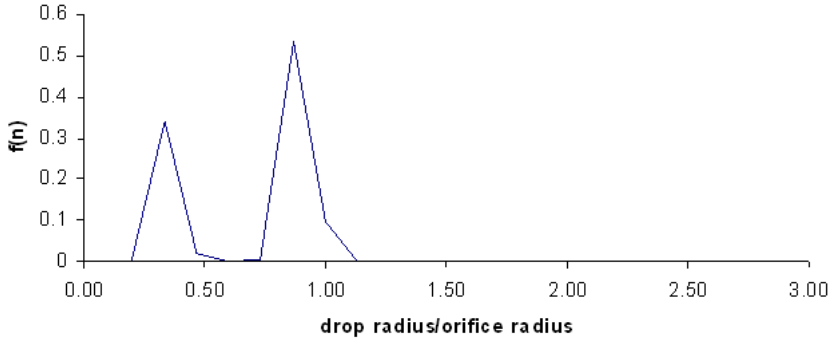

(b)

Figure 7.32: (a) Experimental image and (b) drop size distribution at point (b) on Figure 7.30 demonstrating M2/M3 break-up ($\mathcal{W}e = 1.59, \mathcal{R}b = 0.08, \mathcal{R}e = 4.31, \mathcal{O}h = 0.17845$).

Figure 7.33(b), shows a reduction in the number of satellites droplets formed.

In Figure 7.34, the dimensional frequency is again fixed ($0.875 < \omega < 1.153$) and we move through a range of amplitudes, highlighted in Figure 7.30, to enable a comparison between theoretical and experimental work.

Figure 7.34 shows that the drop sizes predicted are again bigger than those obtained experimentally although the difference between the theoretical and experimental drop sizes is not as great as for the other liquid systems examined. It can also be seen that experimentally, the jet actually transitions to M2 break-up faster than predicted, but there is again a reasonable prediction of break-up modes obtained with the main area's of discrepancies found in the regions defined experimentally by cross over modes.

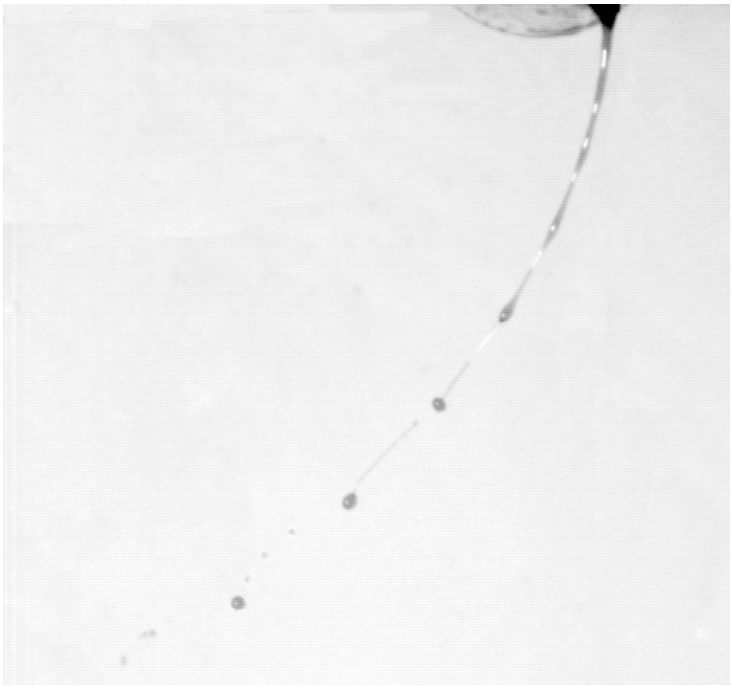

(a)

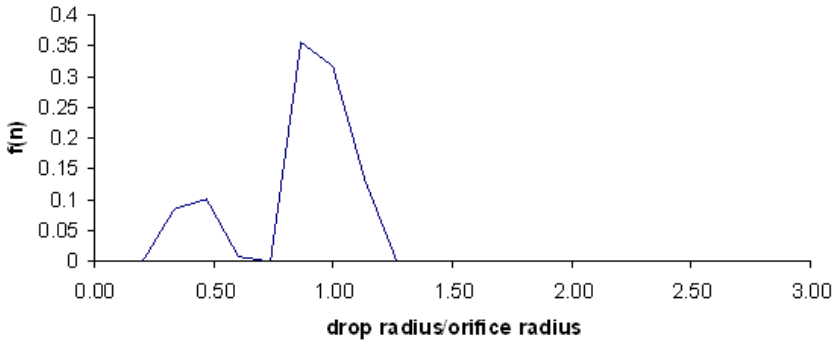

(b)

Figure 7.33: (a) Experimental image and (b) drop size distribution at point (c) on Figure 7.30 demonstrating M2 break-up ($\mathcal{W}e = 1.96, \mathcal{R}b = 0.10, \mathcal{R}e = 5.29, \mathcal{O}h = 0.17845$).

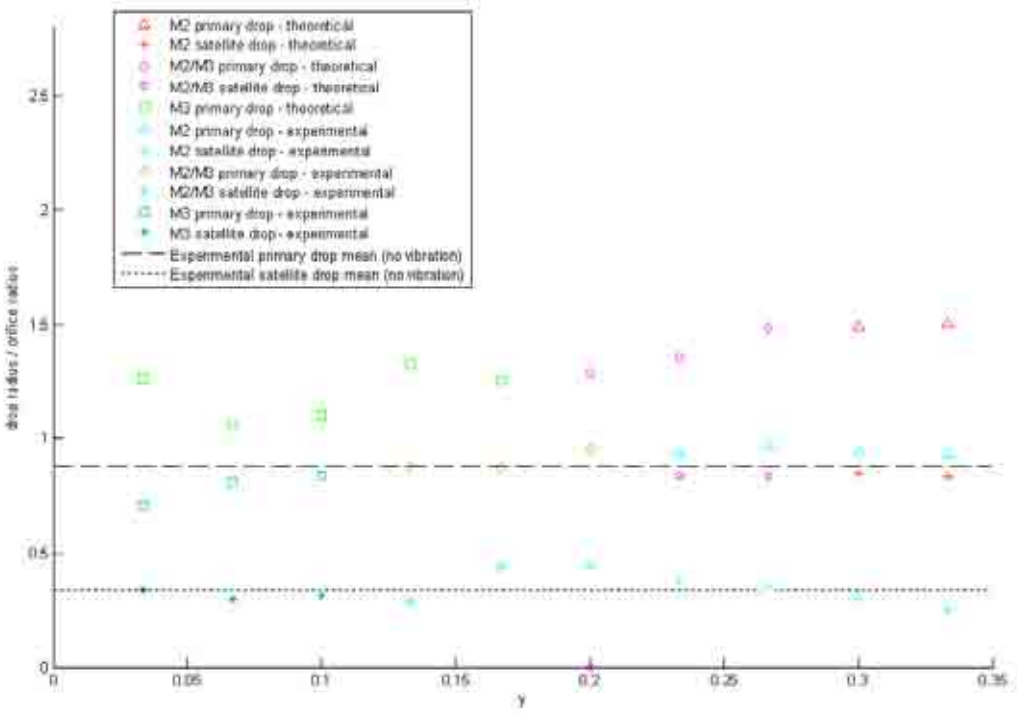

Figure 7.34: Dimensionless drop sizes and break-up modes for experimental and theoretical work with varying γ for a fixed dimensional frequency ($0.875 < \omega < 1.153$). Here, $1.59 < \mathcal{W}e < 1.96, 0.081 < \mathcal{R}b < 0.099, 4.30 < \mathcal{R}e < 5.29, \mathcal{O}h = 0.17845, \delta = 0.058, \kappa = 0.488$.

7.9 Conclusions

Following the theoretical work of Gurney et al. (2010), where it was suggested that it may be possible to dominate break-up using forced disturbances to generate a particular break-up mode and to eradicate satellite droplets through the application of certain frequencies, modifications were made to the pilot scale rig to enable the use of a vibrating nozzle to force mechanical vibrations at the orifice, so that both the frequency and the amplitude of the vibration can be controlled.

Initial experiments were performed on water, with results suggesting that it is possible to reduce the presence of satellite droplets for high amplitude disturbances.

Following this a more thorough investigation was performed on aqueous glycerol (0-80% glycerol) solutions of varying viscosity rotating at a higher rotation rate, with a full range of forced disturbances being applied, varying both the amplitude and frequency of the secondary disturbance. It was found that it was possible to change the break-up mode of a liquid system with M1 break-up being achieved on the pilot scale rig for both water and aqueous glycerol solutions up to 40% glycerol.

Selected points were examined in more detail and the numerical model of Gurney et al. (2010) was applied in order to enable a comparison between the experiments and the theory. While the numerical model, predicted drop sizes that were too big, it was found that it was possible to use the numerical simulations to accurately predict conditions, using forced disturbances, where satellite droplets are eradicated.

Experimentally, there is the possibility to extend this work to encompass different rotation rate and perform a more comprehensive analysis

CHAPTER 8

CONCLUSIONS AND FUTURE WORK

8.1 Conclusions

The dynamics of break-up and drop formation in curved liquid jets has been investigated with a view to better understanding and hence, controlling the interfacial disturbances which lead to rupture. Particular attention was paid to the industrial process of prilling, where control of droplet size is important; a greater understanding of the break-up of curved liquid jets increases the likelihood of being able to manipulate the production of droplets, with a particular view to eliminating waste through the eradication of satellite droplets. This chapter is intended to concisely summarise prominent results from previous chapters. In this thesis, a number of techniques for controlling the break-up of liquid jets were investigated. These include the use of non-Newtonian liquid jets in Chapters 4 and 5, the use of soluble surfactants (Chapter 5) and forcing a particular mode of break-up by the use of a vibrating nozzle (Chapter 7).

Chapter 2 provided an in depth review of previous theoretical and experimental work on straight and curved liquid jets. For Newtonian fluids the linear stability analysis of Decent et al. (2009) was presented, along with the non-linear equations derived by Părău et al. (2007), as well as details of a comparison between these two models (Gurney et al., 2010). Previous experimental work by Wong et al. (2004) and Partridge et al. (2005) was also recapped in detail. For non-Newtonian fluids, the theoretical work of Uddin et al. (2008a) was presented.

In Chapter 3, details of the materials and methods used to carry out the experiments presented in this thesis were given. A new method of data analysis methods, using MATLAB, was

also detailed in this chapter.

In Chapter 4, analysis was performed on the break-up mechanisms and droplet formation of both shear thinning and shear thickening liquid jets at the laboratory scale. The shear thinning fluids examined were found to display unique characteristics of break-up, that differed to those found for Newtonian fluids by Wong et al. (2004). Satellite droplet formation differed and the ligaments were observed to stretch between the main droplets with a curvature normal to the curved central axis of the jet, that became more notable with increasing apparent viscosity and rotation rate. The drop size distributions were found to differ from those achieved for Newtonian fluids, as they appear to progressively change from bimodal to unimodal, as the apparent viscosity and rotation rate increase, with increasing numbers of primary droplets than satellite droplets found. The size of primary droplets decreased with increasing rotation rate, but satellite droplets were found to be only marginally affected. Break-up length was also found to increase with increasing apparent viscosity and rotation rate of the fluid. Shear thickening jets were also examined on this scale, but comparisons between shear thinning and shear thickening liquid jets were difficult to make due to the large difference of dimensionless parameter ranges that the jets were operating in. The 'beads-on-string' phenomena was commonly observed for shear thickening liquid jets, with droplets being noted to be particularly well formed. The drop size distributions were all bimodal, with larger primary droplets found for lower rotation rates due to the tendency of ligaments in between main droplets to contract whilst still attached to the main droplet.

In Chapter 5, where experiments were performed on the pilot scale, the jet shapes at break-up of shear thinning fluids were also markedly different to those observed for Newtonian fluids, again with none of the previously observed Newtonian break-up modes being detected. Extreme curvature of the ligaments between the primary drops, resulting from the growth of long wavelength disturbances, were attributed to the effects of air resistance. This phenomena, together with the formation of pendant droplets, could be predicted on a flow regime map of Ohnesorge number versus Weber number.

Experimental results were compared to the theoretical model of Uddin et al. (2008a), with

some success. For selected experiments, where the theoretical and experimental break-up lengths were matched, good correlation was initially found between the non-linear theory and the experimental image, and main and satellite drop radii were predicted that compared reasonably well to experiments. As the apparent viscosity and rotation rate increased, a less accurate comparison was found, the trajectory appeared displaced, and the droplet predicted was larger than obtained experimentally. Drop sizes were compared for the whole data set, generally the numerical simulations were found to overpredict drop size, however reasonable agreement was found, within 25% for the primary drops and mostly within 50% for the satellite drops, if formed. There are difficulties in the prediction of satellite droplet formation from the theoretical simulations due to the mechanism of satellite formation observed experimentally. Experimentally, satellite formation from the ligaments is either, by contraction of the ligaments to form a single droplet, or by the ligament shattering to form several droplets. Theoretically, satellite droplets are only calculated if a clear minimum in the drop radius is observed either side of the ligament.

When the influence of varying surface tension along the jet through the addition of a soluble surfactant was examined on the pilot scale, in Chapter 5, it was found that, due to weakened surface tension effects, which acts to contract a droplet, such that its surface area is minimised, the droplets produced from break-up are less well formed and appear less spherical than those obtained from both Newtonian and non-Newtonian jets. When the break-up length was examined at lower rotation rates, the surfactant jets were found to be less curved, with a longer break-up length than Newtonian jets of water, which is to be expected, as the surface tension for the surfactant jet should be lower at break-up than the jet of water, hence disturbances due to surface tension are damped. However as the rate of rotation increased, it was found that the surfactant jets actually breaks up sooner than the jet of water. This was attributed to increased mechanical vibration in the rig as the rotation rate increased, with the surface tension forces present in the surfactant jet not being strong enough to hold the jet together.

In Chapter 6, the effects of a power law rheology on the trajectory of curved liquid jets were examined theoretically, with a linear dispersion relation being obtained that was solved

computationally to establish the behaviour of wave modes as they propagate along a curved liquid jet. Apparent viscosity was found to only appear as a higher order (in ϵ) correction to the inviscid steady centreline.

The experiments detailed in Chapter 5 were compared to the theoretical work developed in this chapter, with the sizes of the droplets produced by this instability determined by considering the most unstable wave mode. Some good points of agreement were obtained between theoretical and experimental measurements, particularly at lower Weber numbers. At higher values of the Weber number, break-up may be via absolute instability on the observed slender ligament. All the fluids were tested for viscoelastic effects, however at high Weber number the jet does appear less laminar and there is the possibility that at high Weber number the stresses the fluid are being subjected to are more severe than can be tested accurately in the rheometer, particularly near break-up. It would be interesting to extend this work using the Olroyd-B model to see if there is any hint of viscoelasticity in the experimental results.

A comparison was also made with the long wavelength dispersion relation (Uddin, 2007). It was found that the long wavelength approximation offers comparable results if we focus on the region for unstable modes, where the correlation is found to be excellent. Using this approximation saves significant computational time in predicting primary drop radii.

Finally in Chapter 7, following Gurney et al. (2010), where the possibility of using forced disturbances to dominate break-up mode and eradicate satellite droplets was explored theoretically, modifications made to the pilot scale rig to enable the use of a vibrating nozzle to force mechanical vibrations at the orifice, so that both the frequency and the amplitude of the vibration can be controlled, are described.

An investigation was performed on aqueous glycerol solutions of varying viscosity, with a full range of forced disturbances being applied, varying both the amplitude and frequency of the secondary disturbance. It was found that it was possible to change the break-up mode of a liquid system with M1 break-up being achieved, with satellite droplets being eradicated for both water and aqueous glycerol solutions up to 40% glycerol.

In Gurney et al. (2010) it was suggested that the forced disturbances that are most effective

at controlling jet break-up and causing M1 are ones that are stable at the orifice, but become unstable at some point down the jet. At high amplitude, the sudden onset of a large unstable disturbance ruptures the jet close to the orifice before non-linear waves become unstable. Through the application of initially stable linear frequencies that quickly become unstable, break-up can be controlled to regulate droplet size.

The numerical model of Gurney et al. (2010) was applied to enable a comparison between the experiments and the theory. It was found that it was possible to use the numerical simulations to accurately predict conditions, using forced disturbances, where satellite droplets are eradicated.

8.2 Future work

There is the possibility to extend the work of Chapter 7, to examine different rotation rates and aspect ratios and perform a more comprehensive analysis. This could also include investigating fluids with a more complex rheology. There is also the possibility to modify the non-linear model of Uddin et al. (2008a) to model the effect of forced disturbances on power law fluids, which would enable a comparison to be made with the experiments.

If more sophisticated equipment could be obtained, where a higher frequency can be obtained for high amplitude disturbances it would be useful to repeat some of the experiments on forced disturbances to identify larger regions where it is possible to eradicate satellite droplets.

In Uddin (2007), the break-up of straight compound jets is considered. Such two-fluid systems have numerous applications, particularly in the fields of pharmaceutics and biotechnology when considering encapsulated droplets, however two fluid flows can also be used to stabilise the inner jet and therefore provide the possibility of controlling some features of break-up of the inner jet. Both inviscid-inviscid and power law-power law systems have been considered by Uddin (2007) and some interesting features were found, including the formation of compound jets with multiple cores. When power law fluids were considered it was discovered that the flow index number of the outer fluid dominates break-up and droplet formation. It would be interesting to examine this problem experimentally and to build a rig to do this. It would also

be interesting to examine the effect of applying vibrations to a compound jet.

Rachan Bassi, in the School of Mathematics, has examined absolute instability in curved Newtonian liquid jets, focusing on the M4 break-up identified by Wong et al. (2004). Different types of M4 break-up have been recognised experimentally, that fit well onto a critical curve identified by Lin and Lian (1989). There is the possibility to extend this work to non-Newtonian fluids and perform experiments on the laboratory scale to study absolute instability in this case.

APPENDIX A

DROP SIZE DISTRIBUTIONS

Extensive studies on the drop size distributions obtained for each break-up mode were carried out by both Wong et al. (2004) and Partridge et al. (2005) on the laboratory scale and pilot scale respectively. Viscosity, rotation rate and exit velocity were all found to be important in determining the drop size distributions.

On the pilot scale rig, Partridge et al. (2005) found that all the drop size distributions for the experimental parameters examined were bimodal. For M2 break-up, for lower rotation rates, it was found that there were significantly more primary drops than satellite drops, although by increasing the rotation rate it was possible to change this skew, so that at higher rotation rates there were significantly more satellite drops than primary drops. Increasing the rotation rate not only increases the number of satellite droplets but also leads to a reduction in the size of both primary and satellite drops. For M3 break-up, where the fluid is generally more viscous, there were similar numbers of primary and satellite droplets found for all rotation rates. Again, increasing the rotation rate led to a reduction in both primary and satellite droplet size.

A.1 Laboratory scale

Examples of drop size distributions for non-Newtonian shear thinning fluids on the laboratory scale rig are shown in Figure A.1 as well as in Figure 4.12. The figures show data for three fluids (0.1% CMC, 0.2% CMC and 0.3% CMC) of varying apparent viscosity, properties of which can be found detailed in Table 3.4, at different liquid aspect ratios, $\frac{2}{3}, 1$ or $\frac{5}{4}$, flowing

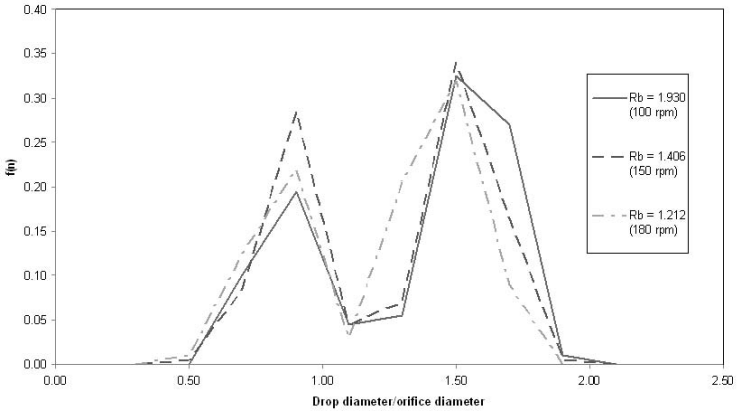

(a)

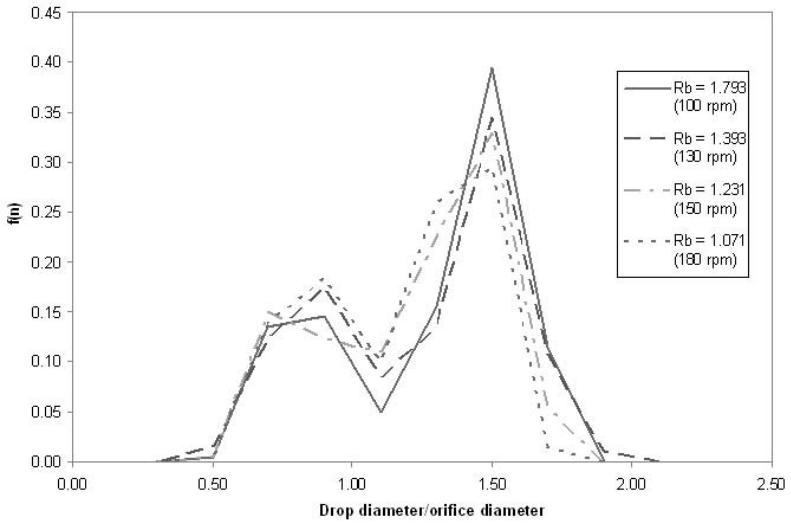

(b)

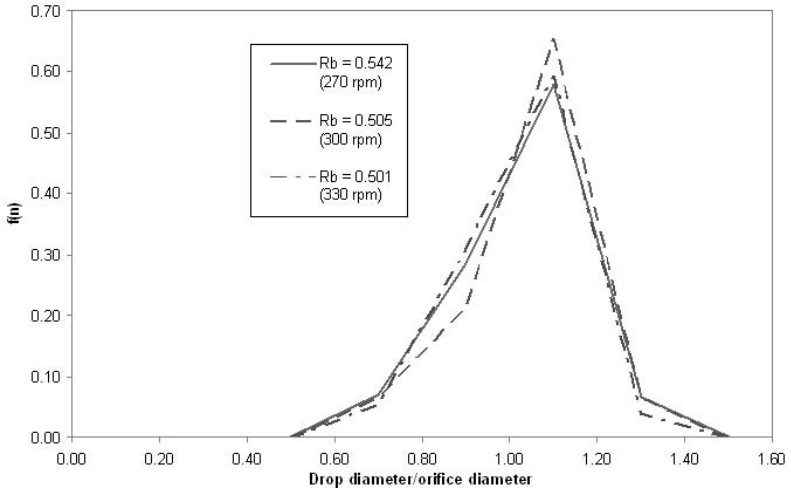

(c)

Figure A.1: Drop size distributions for a solution of (a) 0.1% CMC with a liquid aspect ratio of $2/3$, flowing through a nozzle of diameter 0.002 m, (b) 0.2% CMC with a liquid aspect ratio of $5/4$, flowing through a nozzle of diameter 0.002 m and (c) 0.3% CMC with a liquid aspect ratio of $2/3$, flowing through a nozzle of diameter 0.003 m.

through a nozzle of diameter 0.003 m or 0.002 m. Conditions for experiments appear in the legends of the figures.

In Figure A.1(a), a 0.1% CMC solution, which has the lowest apparent viscosity of the fluids studied, is shown with a liquid aspect ratio (H/D) of $\frac{2}{3}$, flowing through a nozzle of diameter 0.002 m. As the rotation rate increases, the distribution changes from bimodal to one broad peak, although a positive skew is observed. This trend of the drop size distributions becoming more uni-modal with increasing rotational speed, seems to occur throughout all the different shear thinning regimes tested and can also be observed in Figure 4.12(b).

Figure A.1(b) indicates that at low rotational rates the distribution is bimodal, with the smallest peak indicating the size of the satellite droplets and larger peak indicating the size of the main droplets. The ratio of main drops to satellites is approximately 2:1.

All the distributions produced for 0.3% CMC, which has the highest apparent viscosity and is the most strongly shear thinning of the fluids used ($\alpha = 0.654$) were unimodal and exhibited no bimodality, as in Figure A.1(c). However, it was impossible to examine this fluid at low rotation rates on the laboratory scale due to being unable to coherent jets at low Ω.

A.2 Pilot scale

Examples of drop size distributions for non-Newtonian shear thinning fluids on the pilot scale rig are shown in Figures A.2(a) - A.3(b) as well as in Figure 5.12. The figures show data for three fluids (0.1% CMC, 0.2% CMC and 0.3% CMC) of varying apparent viscosity, properties of which can be found detailed in Table 3.5, at different liquid aspect ratios, $\frac{1}{2}$ or $\frac{1}{4}$, flowing through a nozzle of diameter 0.003 m or 0.002 m. Conditions for experiments again appear in the legends of the figures.

In Figure A.2(a), a 0.1% CMC solution, which has the lowest apparent viscosity of the fluids studied, is shown with a liquid aspect ratio (H/D) of $\frac{1}{2}$, flowing through a nozzle of diameter 0.003 m. At low rotational rates the distribution is unsurprisingly bimodal, with the smallest peak indicating the size of the satellite droplets and larger peak indicating the size of the main droplets. The ratio of main drops to satellites is approximately 2:1.

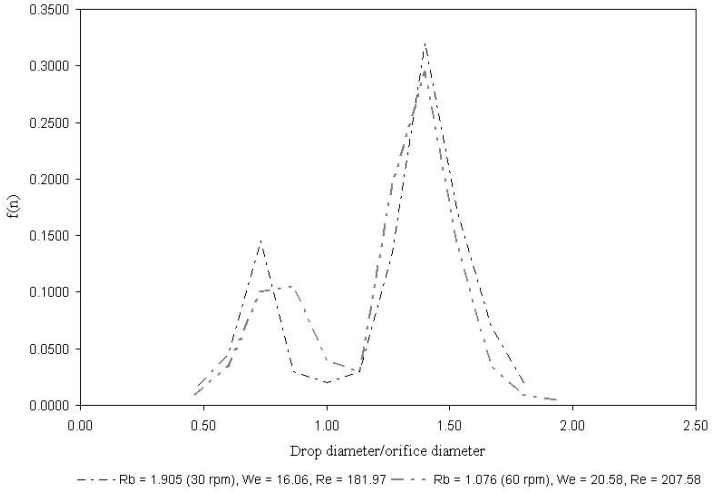

(a)

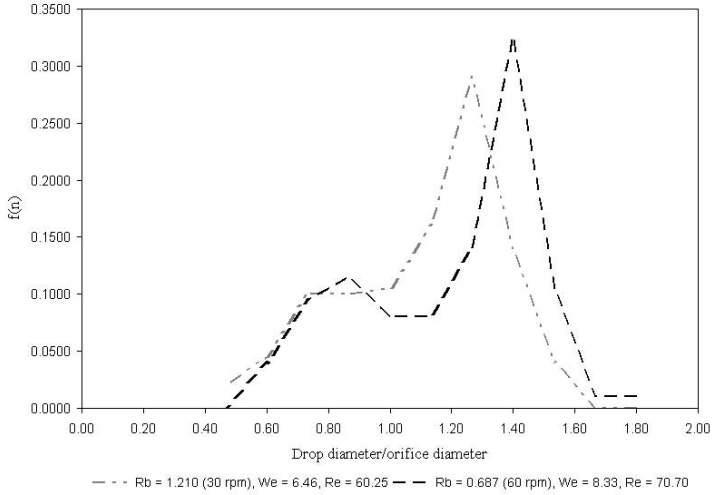

(b)

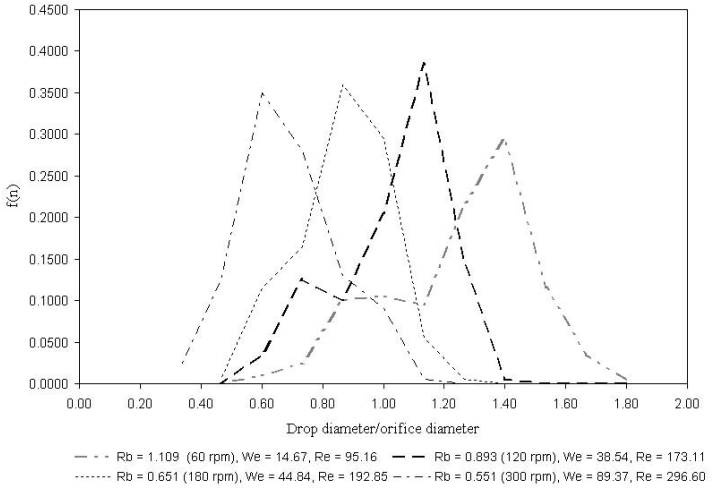

(c)

Figure A.2: Drop size distributions for a solution of (a) 0.1% CMC with a liquid aspect ratio of $1/2$, flowing through a nozzle of diameter 0.003 m, (b) 0.2% CMC with a liquid aspect ratio of $1/2$, flowing through a nozzle of diameter 0.003 m and (c) 0.2% CMC with a liquid aspect ratio of $1/2$, flowing through a nozzle of diameter 0.002 m.

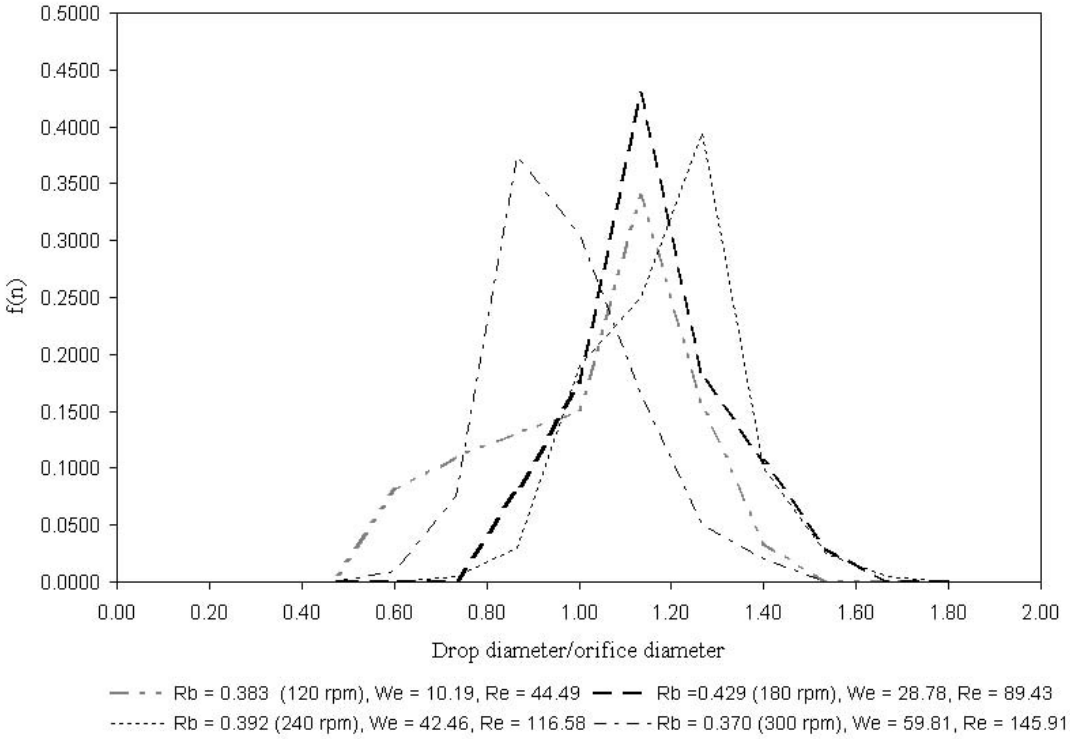

(a)

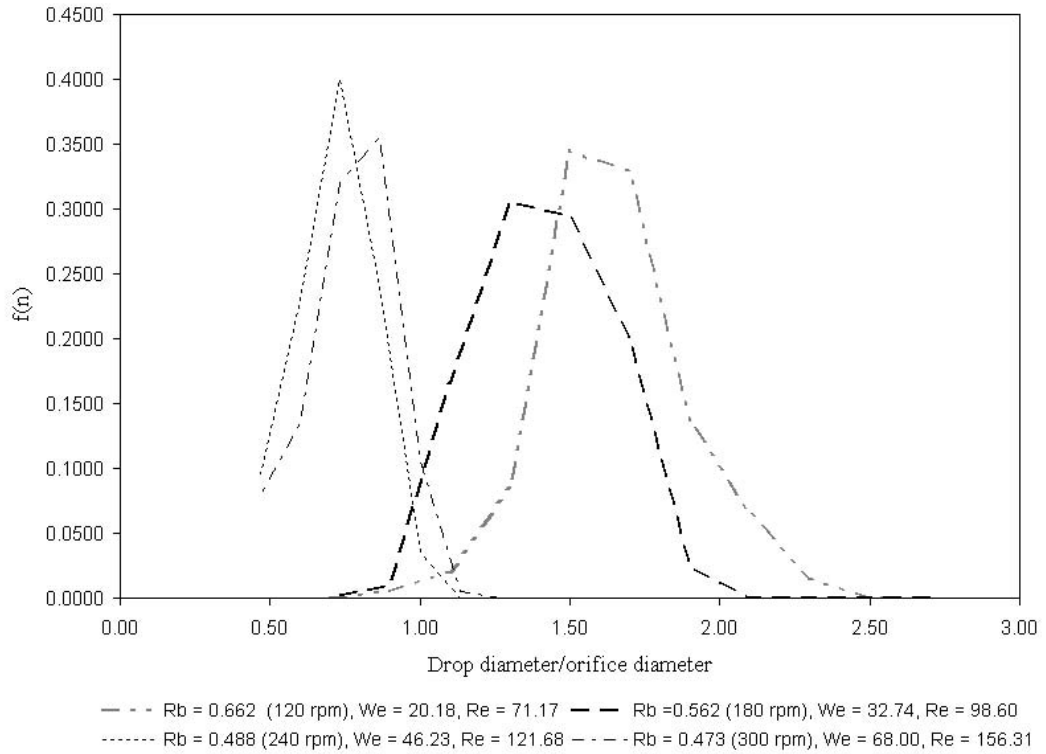

(b)

Figure A.3: Drop size distributions for a solution of 0.3% CMC (a) with a liquid aspect ratio of $1/4$ flowing through a nozzle of diameter 0.003 m and (b) with a liquid aspect ratio of $1/4$ flowing through a nozzle of diameter 0.002 m.

Figures A.2(b) and A.2(c) show drop size distributions produced using 0.2% CMC, varying nozzle size from 0.003 m to 0.002 m respectively (which lowers exit velocity). In Figure A.2(c) as the rotation rate increases, the distribution changes from bimodal to one broad peak, although a positive skew is observed. This trend of the drop size distributions becoming more uni-modal with increasing rotational speed, seems to occur throughout all the different shear thinning regimes tested and can also be observed in Figure A.3(a). The drop size distributions also show evidence of an increase of size with increasing Ω, this is the reverse of what was observed by Wong et al. (2004) and Partridge et al. (2005) for Newtonian fluids.

Figures A.3(a) and A.3(b) illustrate distributions for 0.3% CMC. The effect of nozzle size is again examined. Figure A.3(a) shows results for $a = 0.003$ m, with a liquid aspect ratio of $\frac{1}{4}$, which exhibits no bimodality. As the rotation rate increases the distribution becomes narrower and switches from skewing negatively to skewing positively.

In Figure A.3(b), all the distributions are unimodal and more symmetrical than in Figures A.2(a) - A.3(a). The drop size is again seen to be decreasing with increasing rotation rate and the peak is also seen to be narrow for increasing rotation rate.

An increase in rotation rate always results in an increase of jet exit velocity and a more curved jet trajectory. For Newtonian fluids, Wong et al. (2004) showed that jets that are rotating at a higher rate produce smaller droplets. The same trend has also been observed for the drop size distributions, when we have a unimodal distribution, that as the rotation rate increases so the drop distributions shift left to indicate a smaller drop size (see Figures A.2(c)and A.3(b)).

The drop size distributions observed here are significantly different to those observed for Newtonian fluids. Bimodal distributions are only obtained for lower rotation rates for fluids that are not as strongly shear thinning. As the fluid appears to become more shear thinning (α decreases) a unimodal distribution is expected with the drop size decreasing for increasing rotation rate and the distribution becoming narrower and less negatively skewed for increasing rotation rate. For higher rotation rates it is noted that the break-up mechanism was caused by axisymmetric disturbances. This agrees with the work of Camelot et al. (1999), who found that axisymmetric break-up produced a much narrower size distribution. At higher rotation rates

we also have increased average jet exit velocity and at higher values of U aerodynamic forces and the internal flows within the jet have increased influence (Lin and Lian, 1990; Ohnesorge, 1936); the so-called Taylor or atomisation regime. The primary drops produced in this regime are much smaller. This agrees with the discoveries presented here.

A.3 Surfactants

Examples of drop size distributions for jets containing 0.05% - 0.3% SDS are shown in Figures A.4(a) - A.6 as well as in Figure 5.31. Properties of these experiments can be found detailed in Table 3.3. The experiments are performed at different liquid aspect ratios, $\frac{1}{2}$ or $\frac{1}{4}$ and are flowing through a nozzle of diameter 0.003 m or 0.002 m. Conditions for experiments again appear in the legends of the figures.

In Figure A.4(a), a 0.05% SDS solution, which has the lowest concentration of surfactant of the fluids studied, is shown with a liquid aspect ratio (H/D) of $\frac{1}{2}$, flowing through a nozzle of diameter 0.003 m. At low rotational rates the distributions show only small numbers of satellite droplets. As the rotation rate increases, the distribution becomes more bimodal with numbers of satellite drops increasing.

In Figure A.4(b) quite varied distributions can be seen with a spread of different drop sizes. As rotation rate increases, the drop sizes can be seen to generally decrease. Figure A.4(c) shows main drop sizes decreasing quite drastically with increasing rotation rate.

Figure A.5 shows drop size distributions for a solution of 0.1% SDS. Figure A.5(a) again shows both primary and satellite droplets decreasing in size as the rotation rate increases, but the number of satellites increases. Figure A.5(b) shows a shift from a bimodal distribution, to one that is more unimodal as the rotation rate is increased from 30 to 120 rpm. The main peak has also shifted significantly and there is a reduction in size of all droplets measured.

Figure A.6, which shows drop size distributions for a 0.3% SDS solution is more usual and shows that both primary and satellite droplets decrease in size for increasing rotation rate, however the number of satellite droplets increases with increasing Ω.

Generally, these drop size distributions show that for higher concentrations of surfactant,

there are a greater proportion of primary drops to satellite drops. Craster et al. (2002) found that increasing the surfactant concentration decreased the size of the satellite droplets. To some extent, the same phenomena can be observed here, as the concentration of surfactant increases, both primary and satellite droplets can be seen to decrease in size. However, the number of satellite droplets generally increases with increasing rotation rate, no matter what the concentration of surfactant.

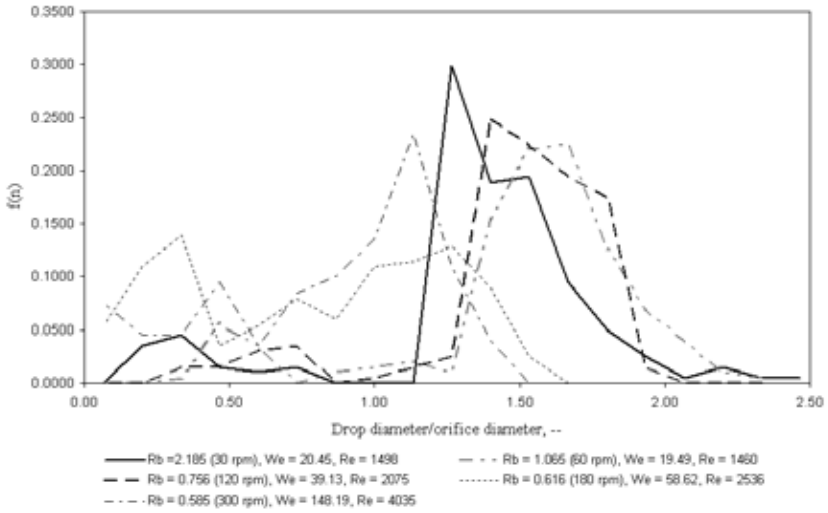

(a)

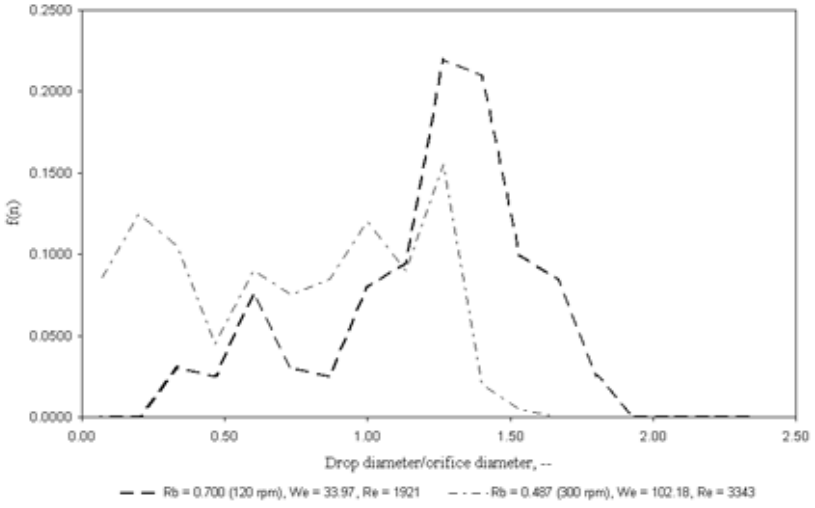

(b)

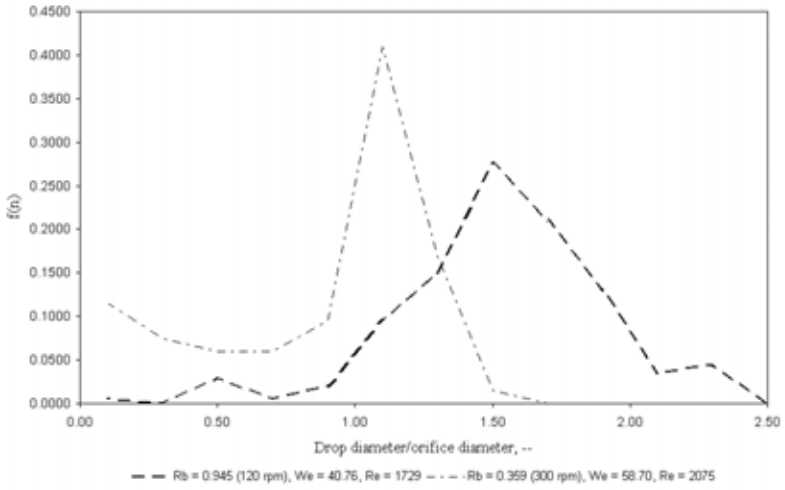

(c)

Figure A.4: Drop size distributions for a solution of 0.05% SDS (a) with a liquid aspect ratio of $1/2$, flowing through a nozzle of diameter 0.003 m, (b) with a liquid aspect ratio of $1/4$, flowing through a nozzle of diameter 0.003 m, (c) with a liquid aspect ratio of $1/2$, flowing through a nozzle of diameter 0.002 m

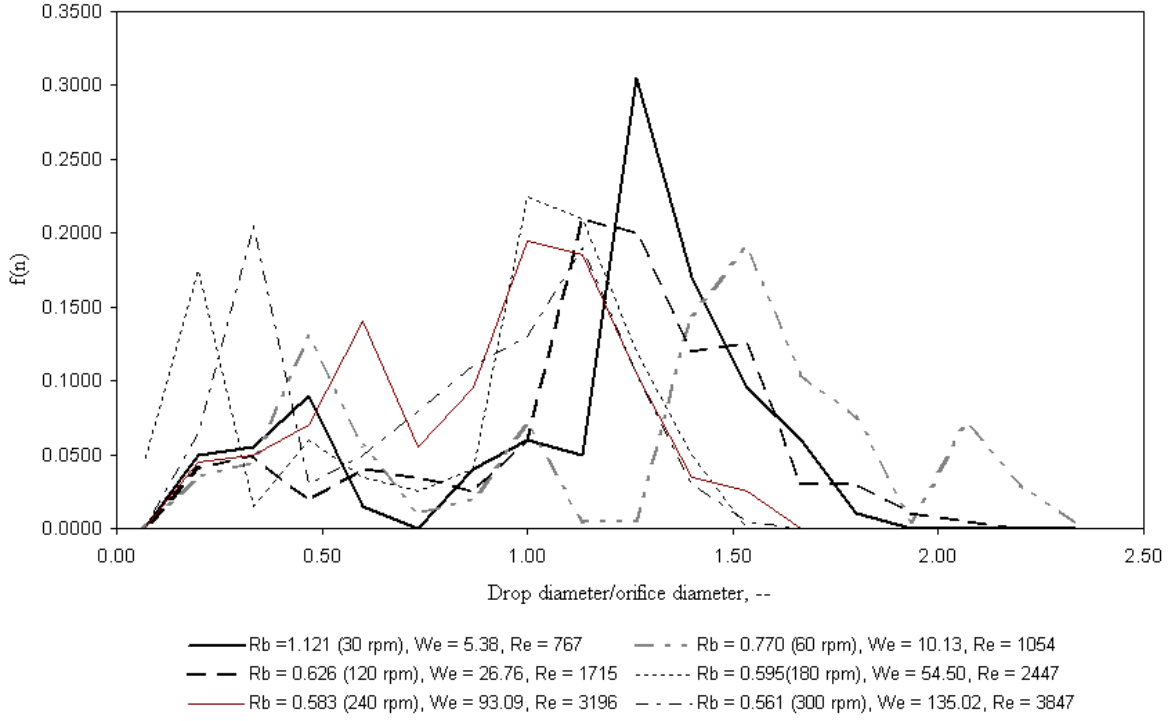

(a)

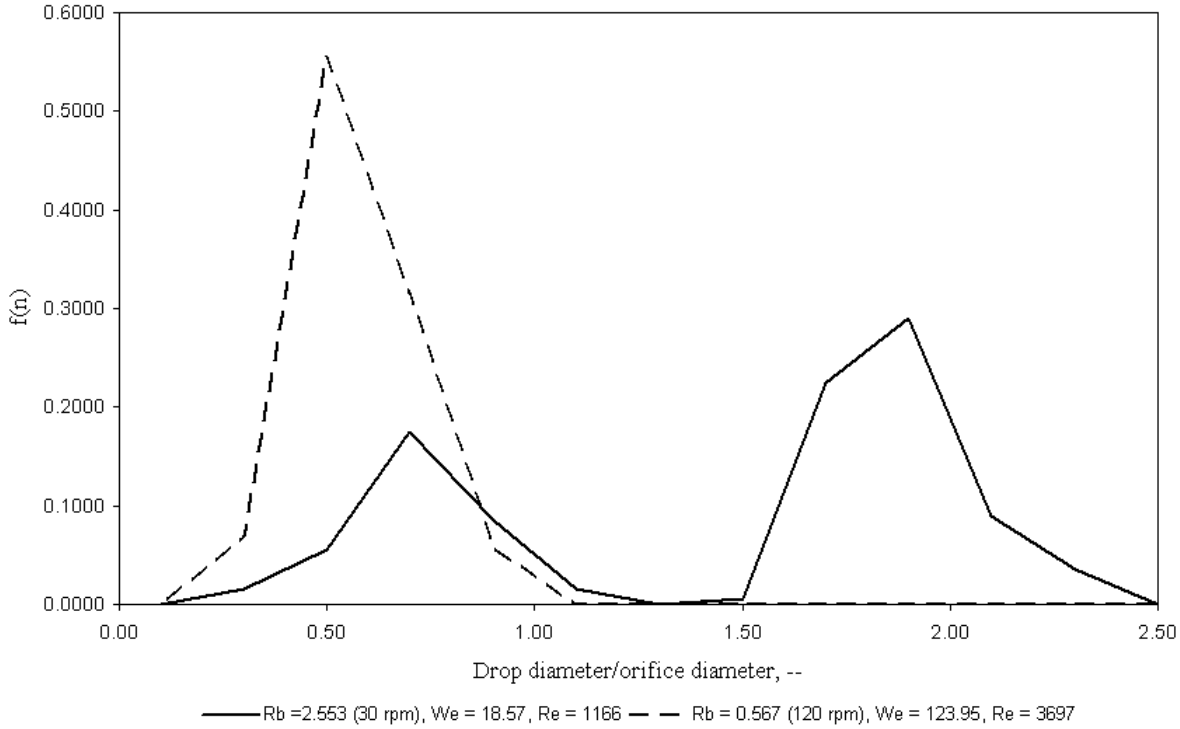

(b)

Figure A.5: Drop size distributions for a solution of 0.1% SDS (a) with a liquid aspect ratio of $1/4$ flowing through a nozzle of diameter 0.003 m and (b) with a liquid aspect ratio of $1/2$ flowing through a nozzle of diameter 0.002 m.

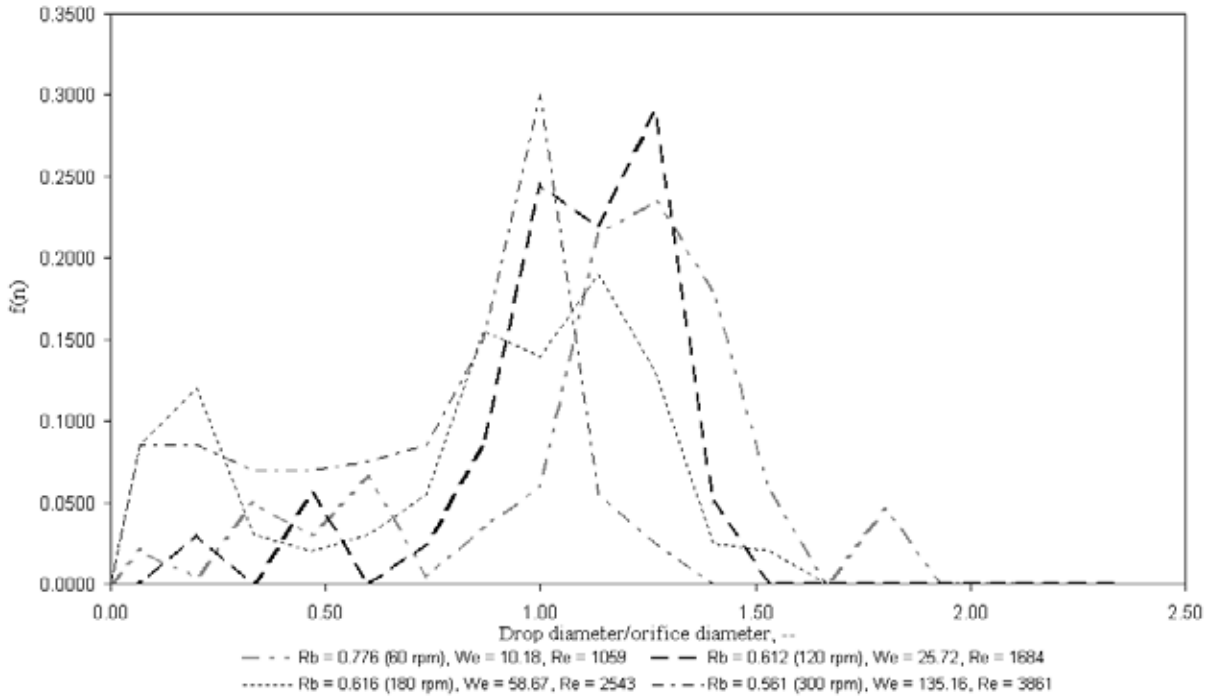

Figure A.6: Drop size distributions for a solution of 0.3% SDS with a liquid aspect ratio of $1/4$ flowing through a nozzle of diameter 0.003 m.

APPENDIX

LIST OF REFERENCES

J.N. Anno. *The Mechanics of Liquid Jets*. Lexington, Mass: Lexington Books., 1977.

M. Aytouna, D. Bartolo, G. Wegdam, D. Bonn, and S. Rafaï. Impact dynamics of surfactant laden drops: dynamic surface tension effects. *Exp. Fluids*, 48(1):49–57, 2010.

M.H.I. Baird and J.F. Davidson. Annular jets-I:: Fluid dynamics. *Chem. Eng. Sci.*, 17(6): 467–472, 1962.

N.J. Balmforth, R.V. Craster, and C. Toniolo. Interfacial instability in non-Newtonian fluid layers. *Phys. Fluids*, 15:3370, 2003.

T. Battal, C.D. Bain, M. Weifl, and R.C. Darton. Surfactant adsorption and Marangoni flow in liquid jets: I. Experiments. *J. Colloid Interface Sci.*, 263(1):250–260, 2003.

E. Becker, W.J. Hiller, and T.A. Kowalewski. Experimental and theoretical investigation of large-amplitude oscillations of liquid droplets. *J. Fluid Mech*, 231:189–210, 1991.

Y.A. Berezin, K. Hutter, and LA Spodareva. Stability analysis of gravity driven shear flows with free surface for power-law fluids. *Arch. Appl. Mech.*, 68(3):169–178, 1998.

R.N. Berglund and B.Y.H. Liu. Generation of monodisperse aerosol standards. *Environ. Sci. Technol.*, 7(2):147–153, 1973.

J.B. Blaisot and S. Adeline. Instabilities on a free falling jet under an internal flow breakup mode regime. *Int. J. Multiphase Flow*, 29:629–653, 2003.

D.B. Bogy. Drop formation in a circular liquid jet. *Ann. Rev. Fluid Mech.*, 11(1):207–228, 1979.

D.W. Bousfield and M.M. Denn. Jet break-up enhanced by an intial pulse. *Chem. Eng. Comm*, 53(1):61–68, 1987.

DW Bousfield, R. Keunings, G. Marrucci, and M.M. Denn. Nonlinear analysis of the surface tension driven break up of viscoelastic filaments. *J. Non-Newtonian Fluid Mech.*, 21(1): 79–97, 1986.

G. Brenn and U. Lackermeier. Drop formation from a vibrating orifice generator driven by modulated electrical signals. *Phys. Fluids*, 9:3658, 1997.

M.P. Brenner, J. Eggers, K. Joseph, S.R. Nagel, and X.D. Shi. Breakdown of scaling in droplet fission at high Reynolds number. *Phys. Fluids*, 9(6):1573–1590, 1997.

D.M.A. Camelot, R.P.A. Hartman, J.C.M. Marijnissen, B. Scarlett, and D. Brunner. Experimental study of the jet break up for electrohydrodynamics atomisation of liquids in the cone-jet mode. *J. Aerosol Sci.*, 30:976–977, 1999.

S. Chandrasekhar. *Hydrodynamic and hydromagnetic stability*. Dover Pubns, 1961.

K.C. Chaudhary and T. Maxworthy. The nonlinear capillary instability of a liquid jet, part 2. experiments on jet behaviour before droplet control. *J. Fluid Mech.*, 96:275–286, 1980a.

K.C. Chaudhary and T. Maxworthy. The nonlinear capillary instability of a liquid jet, part 3. experiments on satellite drop formation and control. *J. Fluid Mech.*, 96:287–297, 1980b.

K.C. Chaudhary and L. Redekopp. The nonlinear capillary instability of a liquid jet, part 1. *J. Fluid Mech.*, 96:263–274, 1980.

A. Chauhan, C. Maldarelli, D.S. Rumschitzki, and D.T. Papageorgiou. An experimental investigation of the convective instability of a jet. *Chem. Eng. Sci.*, 58(11):2421–2432, 2003.

K.H.K. Chung, M.J.H. Simmons, and M. Barigou. Local gas and liquid phase velocity measurement in a miniature stirred vessel using PIV combined with a new image processing algorithm. *Exp. Therm. Fluid Sci.*, 33(4):743–753, 2009.

C. Clanet and J.C. Lasheras. Transition from dripping to jetting. *J. Fluid Mech.*, 383:307–326, 1999.

C. Clasen, J. Eggers, M.A. Fontelos, J. Li, and G. H. McKinley. The beads-on-string structure of viscoelastic threads. *J. Fluid Mech.*, 556:283–308, 2006.

R. Clift, Grace J., and M.E. Weber. *Bubbles, Drops and Particles*. Academic Press, Inc., New York, 1978.

J. J. Cooper-White, R. C. Crooks, and D. V. Boger. A drop impact study of worm-like viscoelastic surfactant solutions. *Colloids and Surfaces A: Physicochemical and Engineering Aspects*, 210(1):105 – 123, 2002.

O. Coronado-Matutti, P.R.S. Mendes, and M.S. Carvalho. Instability of Inelastic Shear-Thinning Liquids in a Couette Flow Between Concentric Cylinders. *J. Fluids Eng.*, 126: 385, 2004.

L. Crane, S. Birch, and P.D. McCormack. The effect of mechanical vibration on the break-up of a cylindrical water jet in air. *Br. J. Appl. Phys.*, 15:743–750, 1964.

R.V. Craster, O.K. Matar, and D.T. Papageorgiou. Pinchoff and satellite formation in surfactant-covered viscous threads. *Phys. Fluids*, 14:1364–1376, 2002.

L.J. Cummings and P.D. Howell. On the evolution of non-axisymmetric viscous fibres with surface tension, inertia and gravity. *J. Fluid Mech.*, 389:361–389, 1999.

E.K. Dabora. Production of monodisperse sprays. *Rev. Sci. Instrum.*, 38(4):502–506, 1967.

M.R. Davidson and J.J. Cooper-White. Pendant drop formation of shear-thinning and yield stress fluids. *J. App. Math. Model.*, 30:1392–1405, 2006.

J.T. Davies and R.W. Makepeace. Measurement of the surface ages of water jets. *AIChE J.*, 24 (3):524–530, 1978.

S.P. Decent, A.C. King, and I.M. Wallwork. Free jets spun from a prilling tower. *J. Eng. Math.*, 42:265–282, 2002.

S.P. Decent, A.C. King, M.J.H. Simmons, E.I. Parau, I.M. Wallwork, C.J. Gurney, and J. Uddin. The trajectory and stability of a spiralling liquid jet: Viscous theory. *Appl. Math. Model.*, 33 (12):4283 – 4302, 2009.

J.N. Dewynne, J.R. Ockendon, and P. Wilmott. A systematic derivation of the leading-order equations for extensional flows in slender geometries. *J. Fluid Mech.*, 244:323, 1992.

J.N. Dewynne, P.D. Howell, and P. Wilmott. Slender viscous fibres with inertia and gravity. *Q. J. Mechanics Appl. Math.*, 47(4), 1994.

F. Dias and J.-M. Vanden-Broeck. Flows emerging from a nozzle and falling under gravity. *J. Fluid Mech.*, 213:465–477, 1990.

R.J. Donnelly and W. Glaberson. Experiments on the capillary instabillity of a liquid jet. *Proc. Royal. Soc. Lond.*, 290:547–556, 1965.

P. Doshi, R.Suryo, O.E. Yildirim, G.H. McKinley, and O.A. Basaran. Scaling in pinch-off of generalized newtonian fluids. *J. Non-Newtonian Fluid Mech.*, 113:1–27, 2003.

V. Dravid, P.B. Loke, C.M. Corvalan, and P.E. Sojka. Drop Formation in Non-Newtonian Jets at Low Reynolds Numbers. *J. Fluids Eng.*, 130:081504, 2008.

H.E. Edgerton, E.A. Hauser, and W.B. Tucker. Studies in drop formation as revealed by the high-speed motion camera. *J. Phys. Chem.*, 41(7):1017–1028, 1937.

J. Eggers. Universal pinching of 3d axisymmetric free-surface flow. *Phys. Rev. Lett.*, 71:3458–3460, 1993.

J. Eggers. Nonlinear dynamics and breakup of free-surface flows. *Rev. Mod. Phys.*, 69:865–929, 1997.

J. Eggers. *A brief history of drop formation, in: Nonsmooth Mechanics and Analysis*. Springer, 2006.

J. Eggers and T. F. Dupont. Drop formation in a one-dimensional approximation of the navier-stokes equation. *J. Fluid Mech.*, 262:205–221, 1994.

J. Eggers and E. Villermaux. Physics of liquid jets. *Rep. Prog. Phys.*, 71:036601, 2008.

M.V. Entov and A.L. Yarin. The dynamics of thin liquid jets in air. *J. Fluid Mech.*, 140:91–111, 1984.

D.S. Finnicum, S.J. Weinstein, and K.J. Rushack. The effect of applied pressure on the shape of a two-dimensional liquid curtain falling under the influence of gravity. *J. Fluid Mech.*, 255: 647–665, 1993.

E.F. Goedde and M.C. Yuen. Experiments on liquid jet instabillity. *J. Fluid Mech.*, 40:495–511, 1970.

M. Goldin, R. Pfeffer, R. Shinnar, and J. Yerushalmi. Breakup of a laminar capillary jet of a viscoelastic fluid. *J. Fluid Mech.*, 38(04):689–711, 1969.

A.E. Green. On the non-linear behaviour of fluid jets. *Int.J. Eng. Sci.*, 14(1):49–63, 1976.

C.J. Gurney. *The stability and control of curved liquid jet break-up*. PhD thesis, School of Mathematics, University of Birmingham, 2010.

C.J. Gurney, M.J.H. Simmons, V.L. Hawkins, and S.P. Decent. The impact of multi-frequency and forced disturbances upon drop size distributions in prilling. *Chem. Eng. Sci.*, 65:3474–3484, 2010.

A. Haenlein. Über den zerfall eines flüssigkeitsstrahls. *Forsch. Geb. Ingenieurwes.*, 2:139, 1931.

S. Hansen, G.W.M. Peters, and H.E.H. Meijer. The effect of surfactant on the stability of a fluid filament embedded in a viscous fluid. *J. Fluid Mech.*, 382(-1):331–349, 1999.

V.L. Hawkins, C.J. Gurney, S.P. Decent, M.J.H. Simmons, and J. Uddin. Unstable waves on a curved non-Newtonian liquid jet. *Journal of Physics A: Mathematical and Theoretical*, 43: 055501, 2010.

J.H. Hilbing and S.D. Heister. Droplet size control in liquid jet breakup. *Phys. Fluids*, 8: 1574–1581, 1996.

M.M. Hohman, M. Shin, G. Rutledge, and M.P. Brenner. Electro-spinning and electrically forced jets. I. Stability theory. *Phys. Fluids*, 13:2201–2220, 2001.

C.C. Hwang, J.L. Chen, J.S. Wang, and J.S. Lin. Linear stability of power law liquid film flows down an inclined plane. *J. Phys. D: Appl. Phys.*, 27:2297–2301, 1994.

J.C. Ijsebaert, K.B. Geerse, J. Marijnissen, J.W.J. Lammers, and P. Zanen. Electro-hydrodynamic atomization of drug solutions for inhalation purposes. *J. App. Physiol.*, 91 (6):2735, 2001.

P.P. Jobert and J. Leblond. Effects of surface active materials on the hydrodynamic development in a liquid jet. *J. Colloid Interface Sci.*, 68(3):478–485, 1979.

J.B. Keller and J. Geer. Flows of thin streams with free boundaries. *J. Fluid Mech.*, 59:417–432, 1973.

J.B. Keller and M.L. Weitz. Upward 'falling' jets and surface tension. *J. Fluid Mech.*, 2: 201–203, 1957.

J.B. Keller, S.I. Rubinow, and Y.O. Tu. Spatial instability of a jet. *Phys. Fluids*, 16:2052–2055, 1973.

Y. Kitamura and T. Takahashi. Breakup of jets in power law non-newtonian liquid systems. *CJChE*, 60(6), 1982.

T.A. Kowaleski. On the separation of droplets from a liquid jet. *Fluid Dyn. Res.*, 17:121–145, 1996.

S. Kwak and C. Pozrikidis. Effect of surfactants on the instability of a liquid thread or annular layer:: Part I: Quiescent fluids. *International Journal of Multiphase Flow*, 27(1):1–37, 2001.

C. M. Van't Land. *Industrial crystallization of melts*. CRC Press, 2004.

H.C. Lee. Drop formation in a liquid jet. *IBM J. Res. Dev.*, 18:364–369, 1974.

S.J. Leib and M.E. Goldstein. The generation of capillary instabilities in a liquid jet. *J. Fluid Mech.*, 168:479–500, 1986.

P. Lenard. Ueber die schwingungen fallender tropfen. *Ann. Phys.*, 266(2):209–243, 1887.

J. Li and M.A. Fontelos. Drop-dynamics on the beads-on-string structure for viscoelastic jets: A numerical study. *Phys. Fluids*, 15:922–936, 2003.

Y.C. Liao, H.J. Subramani, E.I. Franses, and O.A. Basaran. Effects of soluble surfactants on the deformation and breakup of stretching liquid bridges. *Langmuir*, 20:9926–9930, 2004.

S.P. Lin and Z.W. Lian. Absolute instability of a liquid jet in a gas. *Phys. Fluids A*, 1:490–493, 1989.

S.P. Lin and Z.W. Lian. Mechanisms of the break-up of liquid jets. *Amer. Inst. Aeronaut. Astronaut.*, 28:120–126, 1990.

S.P. Lin and R.D. Reitz. Drop and spray formation from a liquid jet. *Ann. Rev. Fluid Mech.*, 30: 85–105, 1998.

N.R. Lindblad and J.M. Schneider. Production of uniform-sized liquid droplets. *Rev. Sci. Instrum.*, 42:635–638, 1965.

G.E. McCreery and Stoots. Drop formation mechanism and size distribution for spray plate orifices. *Int. J. Multiphase Flow*, 22:431–452, 1996.

G.H. McKinley. Visco-elasto-capillary thinning and break-up of complex fluids. *Annual Rheology Reviews*, 3:1–45, 2003.

S. Middleman. *Modeling of axisymmetric flows*. Academic Press, 1995.

V.N. Morozov and T.Y. Morozova. Electrospray deposition as a method for mass fabrication of mono-and multicomponent microarrays of biological and biologically active substances. *Anal. Chem.*, 71(15):3110–3117, 1999.

M.P. Moses, S.H. Collicott, and S.D. Heister. Visualization of liquid jet breakup and droplet formation. *Flow visualization VII: Proceedings of the 7th International Symposium on Flow Visualization*, pages 878–885, 1995.

I. Moulitsas and G. Georgiou. Steady flow of a two-dimensional liquid curtain under pressure. *Eng. App. Comp. Fluid Mech.*, 3(2):271, 2009.

A.H. Nayfeh. Nonlinear stability of a liquid jet. *Phys. Fluids.*, 13:841–847, 1970.

W. Ohnesorge. Formation of drops by nozzles and the break-up of liquid jets. *Z. Agnew. Math. Mech.*, 16:355–358, 1936.

Y. Okubo, K. Ikemoto, K. Koike, C. Tsutsui, I. Sakata, O. Takei, A. Adachi, and T. Sakai. DNA Introduction into Living Cells by Water Droplet Impact with an Electrospray Process. *Angewandte Chemie - International edition in English*, 47(8):1429, 2008.

M. Orme and E. P. Muntz. New technique for producing highly uniform droplet streams over an extended range of disturbance wavenumbers. *Rev. Sci. Instrum.*, 58:279, 1987.

M. Orme and E. P. Muntz. The manipulation of capillary stream breakup using amplitude-modulated disturbances: A pictorial and quantitative representation. *Phys. Fluids A*, 2:1124, 1990.

M. Orme and E. P. Muntz. On the genesis of droplet stream microspeed dispersions. *Phys. Fluids A*, 3:2936, 1991.

D. Ornek, T. Gurkan, and C. Oztin. Prilling of aluminium sulphate. *J. Chem. Technol. Biotechnol*, 75(8):689–694, 2000.

L. Partridge. *An experimental and theoretical investigation into the break-up of curved liquid jets in the prilling process*. PhD thesis, University of Birmingham, 2006.

L. Partridge, D.C.Y. Wong, M.J.H. Simmons, E.I. Părău, and S.P. Decent. Experimental and theoretical description of the break-up of curved liquid jets in the prilling process. *Chem. Eng. Res. Des.*, 83:1267–1275, 2005.

D.H. Peregrine, G. Shoker, and A. Symon. The bifurcation of liquid bridges. *J. Fluid Mech.*, 212:25–39, 1990.

W.T. Pimbley and H.C. Lee. Satellite droplet formation in a liquid jet. *IBM J. Res. Develop*, 21 (1):21–30, 1977.

J. Plateau. *Acad. Sci. Bruxelles Mem.*, 16:3, 1843.

J. Plateau. *Acad. Sci. Bruxelles Mem.*, 23:5, 1849.

J. Plateau. Statique experimentale et theortique des liquides soumis aux seules forces moleculaires. *Gauthier Villars, Paris II*, 319, 1873.

E.I. Părău, S.P. Decent, A.C. King, M.J.H. Simmons, and D.C. Wong. Nonlinear travelling waves on a spiralling liquid jet. *Wave Motion*, 43(7):599–618, 2006.

E.I. Părău, S.P. Decent, M.J.H. Simmons, D.C. Wong, and A.C. King. Nonlinear viscous liquid jets from a rotating orifice. *J. Eng. Math.*, 57(2):159–179, 2007.

S. Rafaï, D. Bonn, and A. Boudaoud. Spreading of non-Newtonian fluids on hydrophilic surfaces. *Journal of Fluid Mechanics*, 513:77–85, 2004.

J.I. Ramos. Upward and downward annular liquid jets: Conservation properties, singularities and numerical errors. *Appl. Math, Modelling*, 20:440–458, 1996.

J.W.S. Rayleigh. On the stability of liquid jets. *Proc. Lond. Math. Soc.*, 10:4–13, 1879a.

J.W.S. Rayleigh. *Proc. Lond. Math. Soc.*, 29:94, 1879b.

L. Rayleigh. On the equilibrium of liquid conducting masses charged with electricity. *Phil. Mag*, 14:184–186, 1882.

L. Rayleigh. Some applications of photography. *Nature*, 44:249–254, 1891.

D.F. Rutland and G.J. Jameson. A non-linear effect in the capillary instability of liquid jets. *J. Fluid Mech.*, 46:267, 1971.

F. Savart. Memoire sur la constitution des veines liquides lancees par des orifices circulaires en mince paroi. *Ann. Chim. Phys*, 53:337–374, 1833.

J.M. Schneider and C.D. Hendricks. Source of uniform-sized liquid droplets. *Rev. Sci. Instrum.*, 35:1349–1350, 1964.

W.R. Schowalter. *Mechanics of Non-Newtonian Fluids*. Pergamon Press, Oxford, 1978.

R.M.S.M. Schulkes. Dynamics of liquid jets revised. *J. Fluid Mech.*, 250:635–650, 1993.

X.D. Shi, M.P. Brenner, and S.R. Nagel. A cascade of structure in a drop falling from a faucet. *Science*, 265(5169):219, 1994.

T.W. Shield, D.B. Bogy, and F.E. Talke. Drop formation by dod ink-jet nozzle: a comparison of experimental and numerical simulation. *IBM J. Res. Dev.*, 31:96–110, 1987.

A.M. Sterling and C.A. Sleicher. The instability of capillary jets. *J. Fluid Mech*, 68(3):477–495, 1975.

H.A. Stone and L.G. Leal. The effects of surfactants on drop deformation and breakup. *J. Fluid Mech.*, 220:161–186, 1990.

H.H. Taub. Investigation of nonlinear waves on liquid jets. *Phys. Fluids*, 19:1124, 1976.

M.L.E. Timmermans and J.R. Lister. The effect of surfactant on the stability of a liquid thread. *Journal of Fluid Mechanics*, 459:289–306, 2002.

S. Tomotika. On the instability of a cylindrical thread of a viscous liquid surrounded by another viscous fluid. *Proceedings of the Royal Society of London. Series A, Mathematical and Physical Sciences*, 150(870):322–337, 1935.

P.A. Torpey. A nonlinear theory for describing the propogation of disturbances on a capillary jet. *Phys. Fluids*, 1:66–71, 1989.

EO Tuck. The shape of free jets of water under gravity. *J. Fluid Mech.*, 76:625–640, 1976.

J. Uddin. *An investigation into methods to control breakup and droplet formation in single and compound liquid jets*. PhD thesis, University of Birmingham, 2007.

J. Uddin and S.P. Decent. Non-newtonian jets curved by gravity. *Mathematics in Industry*, 2008.

J. Uddin and S.P. Decent. Curved non-newtonian liquid jets with surfactants. *J. Fluids Eng.*, 131:901203, 2009.

J. Uddin, S.P. Decent, and M.J.H. Simmons. The instability of shear thinning and shear thickening spiralling liquid jets: Linear theory. *ASME J. of Fluids Eng.*, 128:968–975, 2006.

J. Uddin, S.P. Decent, and M.J.H. Simmons. Non-linear waves along rotating non-Newtonian liquid jets. *Int. J. Eng. Sci*, 46, 2008a.

J. Uddin, S.P. Decent, and M.J.H. Simmons. The effect of surfactants on the instability of a rotating liquid jet. *Fluid Dyn. Res.*, 40:827–851, 2008b.

J.-M. Vanden-Broeck and J.B. Keller. Jets rising and falling under gravity. *J. Fluid Mech.*, 124: 335–345, 1982.

P. Vassallo and N. Ashgriz. Satellite formation and merging in liquid jet breakup. *Proceedings: Mathematical and Physical Sciences*, pages 269–286, 1991.

I.M. Wallwork. *The trajectory and stability of a spiralling liquid jet*. Phd thesis, University of Birmingham, 2001.

I.M. Wallwork, S.P. Decent, A.C. King, and R.M.S.M. Schulkes. The trajectory and stability of a spiralling liquid jet: Part I. Inviscid theory. *J. Fluid Mech.*, 459:43–65, 2002.

C. Weber. Zum zerfall eines Flüssigkeitsstrahles. *Z. Agnew. Math. Mech.*, 11:136–154, 1931.

D.C. Wong, M.J.H. Simmons, S.P. Decent, E.I. Părău, and A.C. King. Break-up dynamics and drop size distributions created from spiralling liquid jets. *Int. J. Multiphase Flow*, 30: 499–520, 2004.

P.K. Wu, R.F. Miranda, and G.M. Faeth. Effects of initial flow conditions on primary break-up of non turbulent and turbulent round liquid jets. *Atom. Sprays*, 5:175–176, 1995.

A.L. Yarin. *Free liquid jets and films: hydrodynamics and rheology*. Longman Pub Group, 1993.

M.C. Yuen. Non-linear capillary instability of a liquid jet. *J. Fluid Mech.*, 33:151–163, 1968.

X. Zhang and O.A. Basaran. An experimental study of dynamics of drop formation. *Phys. Fluids*, 7:1184, 1995.